Department of Spatial Sciences

Estimation of Tropospheric Wet Delay from GNSS Measurements

Johnny Su Hau Lo

This thesis is presented for the degree of
Doctor of Philosophy
of
Curtin University of Technology

October 2011

DECLARATION

This thesis contains no material which has been accepted for the award of any other degree or diploma in any university. To the best of my knowledge and belief this thesis contains no material previously published by any other person except where due acknowledgement has been made.

Signature: .....

Date: .....

ABSTRACT

The determination of the zenith wet delay (ZWD) component can be a difficult task due to the dynamic nature of atmospheric water vapour. However, precise estimation of the ZWD is essential for high-precision Global Navigation Satellite System (GNSS) applications such as real-time positioning and Numerical Weather Prediction (NWP) modelling.

The *functional* and *stochastic* models that can be used for the estimation of the tropospheric parameters from GNSS measurements are presented and discussed in this study. The focus is to determine the ZWD in an efficient manner in static mode. In GNSS, the estimation of the ZWD is directly impacted by the choice of stochastic model used in the estimation process. In this thesis, the rigorous Minimum Norm Quadratic Unbiased Estimation (MINQUE) method was investigated and compared with traditional models such as the equal-weighting model (EWM) and the elevation-angle dependent model (EADM). A variation of the MINQUE method was also introduced. A simulation study of these models resulted in MINQUE outperforming the other stochastic models by at least 36% in resolving the height component. However, this superiority did not lead to better ZWD estimates. In fact, the EADM provided the most accurate set of ZWD estimates among all the models tested. The EADM also yielded the best ZWD estimates in the real data analyses for two independent baselines in Australia and in Europe, respectively.

The study also assessed the validity of a baseline approach, with a reduced processing window size, to provide good ZWD estimates at Continuously Operating Reference Stations (CORS) in an efficient manner. Results show that if the *a-priori* station coordinates are accurately known, the baseline approach, along with a 2-hour processing window, can produce ZWD estimates that are statistically in good agreement with the estimates from external sources such as the radiosonde (RS), water vapour radiometer (WVR) and International GNSS Service (IGS) solutions. Resolving the ZWD from GNSS measurements in such a timely manner can aid NWP model in providing near real-time weather forecasts in the data assimilation process.

In the real-time kinematic modelling of GNSS measurements, the first-order Gauss-Markov (GM) autocorrelation model is commonly used for the dynamic model in Kalman filtering. However, for the purpose of ZWD estimation, it was found that the GM model consistently underestimates the temporal correlations that exist among the ZWD measurements. Therefore, a new autocorrelation dynamic model is proposed in a form similar to that of a hyperbolic function. The proposed model initially requires a small number of autocorrelation estimates using the standard autocorrelation formulations. With these autocorrelation estimates, the least-squares method is then implemented to solve for the model's parameter coefficients. Once solved, the model is then fully defined. The proposed model was shown to be able to follow the autocorrelation trend better than the GM model. Additionally, analysis of real data at an Australian IGS station has showed the proposed model performed better than the random-walk model, and just as well as the GM model. The proposed model was able to provide near real-time (i.e. 30 seconds interval) ZTD estimates to within 2 cm accuracy on average.

The thesis also included an investigation into the several interpolation models for estimating missing ZWD observations that may take place during temporary breakdowns of GNSS stations, or malfunctions of RS and WVR equipments. Results indicated marginal differences between the polynomial regression models, linear interpolation, fast-Fourier transform and simple Kriging methods. However, the linear interpolation method, which is dependent on the two most recent data points, is preferable due to its simplicity. This result corresponded well with the autocorrelation analysis of the ZWD estimates where significant temporal correlations were observed for at most two hours.

The study concluded with an evaluation of several trend and smoothing models to determine the best models for predicting ZWD estimates, which can help improve real-time kinematic (RTK) positioning by mitigating the tropospheric effect. The moving average (MA) and the single-exponential smoothing (SES) models were shown to be the best-performing prediction models overall. These two models were able to provide ZWD estimates with forecast errors of less 10% for up to 4 hours of prediction.

ACKNOWLEDGEMENTS

Firstly, I would like thank my supervisor, Dr. Ahmed El-Mowafy for his guidance and support throughout the course of my study. Special mention also for my co-supervisors Prof. Will Featherstone and Dr. Joseph Awange. This would not be possible without their advice and support. I would also like to extend my appreciation to Dr. Nigel Penna for his supervision early on in my study. Furthermore, I would like to express my appreciation to Dr. Congwei Hu for providing the PPP program needed to perform the analysis of the dynamic models. Special thanks also go to the Head of the Department of Spatial Sciences, Prof. Bert Veenendaal, Associate Prof. Jon Kirby and the rest of the staff members for the encouragement and help during my study.

I am grateful to my colleagues and friends, Dr. Kwang-Ho Bae and Dr. David Belton for their continuing support. I am also thankful to Dr. Ritu Gupta at the Department of Mathematics and Statistics for her mentoring and support, and for providing me with employment opportunities during my time at the Curtin University of Technology.

I would also like to thank Prof. Gunnar Elgered (Onsala Space Observatory), Mr. Walter Schwarz (Fundamentalstation Wettzell), and the Bureau of Meteorology for providing all the radiosonde and water vapour radiometer data that were necessary to complete my analysis.

I would like to acknowledge Curtin University and the Bureau of Meteorology for awarding me with the Australian Postgraduate Award Industry (APAI) scholarship.

I would like to sincerely thank my brother Jeff, my sisters Karen and Susan, and in particular, my parents for their encouragement and patience. Finally, I am eternally grateful to my wife, Wendy, for all her love and support during these past few years.

TABLE OF CONTENTS

CHAPTER 7: INTERPOLATION AND PREDICTION OF ZENITH WET DELAYS

CHAPTER 8: CONCLUSIONS AND RECOMMENDATIONS

LIST OF FIGURES

LIST OF TABLES

LIST OF SYMBOLS AND NOTATIONS

A	observation design matrix
d	dry air
D_c	double-differenced correlation matrix
$D_d(\theta_z)$	Dry delay at the zenith angle
$D_{wv}(\theta_z)$	Wet delay (due to water vapour) at the zenith angle
e_j^k	GNSS observation residual error from receiver j and satellite k
E_F	forecast error
E_I	interpolation error
$F_{i,i-1}$	transition matrix from state i-1 to i
g_m^0	mean gravity at mean sea level
g_m	mean gravity
g_s	surface gravity
H	height
H_0	null hypothesis
H_A	alternative hypothesis
I	identity matrix
I_j^k	ionospheric delay between receiver j and satellite k
k_{mis}	number of missing observations
L	misclosure vector
L_c	a curve path
L_g	straight line geometric Euclidean path
L_p	length of a curve path
Lv_t	level component at time t
$m(\theta)$	mapping function value at angle θ
$m_H(\theta)$	hydrostatic mapping function value at angle θ
$m_W(\theta)$	wet mapping function value at angle θ

m_{zwd}	number of ZWD observations
M_d	molecular weight of dry air
M_{wv}	molecular weight of water vapour
n	number of observations
n_d	number of moles of dry air
$n_{refr}(s)$	index of refraction
n_{wv}	number of moles of water vapour
$\tilde{N}$	normal matrix
$N_{refr}(s)$	atmospheric refractivity
N_d	refractivity due to dry air
N_{wv}	refractivity due to water vapour
N_j^k	integer carrier phase ambiguity from receiver j and satellite k
p	number of unknown parameters
P	total air pressure
P_d	partial pressure of dry air
P_s	surface air pressure
P_{wv}	partial pressure of water vapour
P_{wv}^s	surface partial pressure of water vapour
$P_{wv,I}$	saturation water vapour pressure over ice
$P_{wv,s}$	saturation vapour pressure
P_j^k	pseudorange observation from receiver j to satellite k
q_{wv}	specific humidity
r_s	mean geocentric radius
R_E	Earth's equatorial radius
R_d	specific gas constant for dry air
R_{reg}	regression correlation coefficient
R_u	universal gas constant
Q	cofactor matrix

Sn_t	seasonal component at time t
t	time
t_{α_s}	t-statistic at α_s level of significance
T	height-dependent temperature
T_{Bg}	brightness temperature of the cosmic background radiation
T_f	freezing temperature
T_m	weighted mean temperature
Tr_t	trend component at time t
T_s	surface temperature
T_{sky}	sky brightness temperature
T_j^k	tropospheric delay between receiver j and satellite k
U	relative humidity
v	residual vector
V	accompanying matrix
wv	water vapour
W	weight matrix
X	state vector
X^0	initial state vector
$\hat{X}$	estimated vector coefficients
Z_d	compressibility factor of dry air
Z_{wv}	compressibility factor of water vapour

α	lapse rate
α_s	level of significance
α_w	weight for the level component
δt_j	receiver clock error from receiver j
δt^k	satellite clock error from satellite k
Δm	differential mapping function
Δx	x-coordinate partial
Δy	y-coordinate partial
Δz	z-coordinate partial
$\overline{\phi}$	a set of zero-difference GNSS observations
$\overline{\phi}_{DD}$	a set of doubled-difference GNSS observations
ϕ_j^k	carrier-phase observation from receiver j and satellite k
γ_w	weight for the trend component
χ_q	volume mixing ratio
Π	conversion factor
λ	wavelength of the carrier frequency
θ	elevation angle
θ_z	zenith angle
ρ	total air density
ρ_d	density of dry air
ρ_{wv}	density of water vapour
ρ_j^k	geometric distance from receiver j and satellite k
σ^2	*a-priori* error variance of the observation
$\hat{\sigma}_0^2$	*a-posteriori* unit variance
$\sum$	variance-covariance matrix
τ	correlation time
υ	opacity
ϖ	seasonal period
ω_{wv}	mass mixing ratio

$\omega_{wv,s}$	saturation mixing ratio
ζ_w	weight for the seasonal component
ℓ	geocentric latitude

LIST OF ABBREVIATIONS

AFN	Australian Fiducial Network
ARIMA	Auto-regressive integrated moving average
BoM	Bureau of Meteorology
CHP	Cubic Hermite polynomial
CI	Confidence interval
C/N	Carrier-to-noise ratio
CORS	Continuously Operating Reference Stations
CS	Cubic spline
DCP	Decomposition
DD	Double-difference
DES	Double exponential smoothing
DOY	Day of year
EADM	Elevation-angle-dependent model
ECMWF	European Centre for Medium-range Weather Forecast
EGT	Exponential growth trend
EOP	Earth Orientation Parameters
EWM	Equal-weighting model
FFT	Fast Fourier transform
GM	Gauss-Markov
GMF	Global mapping functions
GNSS	Global Navigation Satellite Systems
GPS	Global Positioning System
GPSMet	GPS Meteorology
IGRA	Integrated Global Radiosonde Archive
IGS	International GNSS Service
IM	Interpolation model
IMF	Isobaric mapping function
ITRF	International Terrestrial Reference Frame
IWV	Integrated water vapour
KF	Kalman filter
LCL	Lower control limit

LI	Linear interpolation
LP	Lagrange polynomial
LT	Linear trend
LS	Least-squares
MA	Moving average
MF	Mapping function
MINQUE	Minimum norm quadratic unbiased estimation
MLE	Maximum likelihood estimation
MMR	Mass mixing ratio
MSE	Mean squared error
NCEP	National Centres for Environmental Prediction
NEQ	Normal equations
NMF	Niell mapping function
NND_MINQUE	Non-negative definite MINQUE
NOAA	National Oceanic and Atmospheric Administration
NSSD	No statistical significant difference
NWP	Numerical weather prediction
OTL	Ocean tide loading
PPP	Precise point positioning
PWV	Precipitable water vapour
QC	Quality control
QIF	Quasi-Ionosphere-Free
QT	Quadratic Trend
RI	Relative improvement
RMSE	Root mean squared error
RO	Radio occultation
RS	Radiosonde
RTK	Real-time kinematic
RW	Random Walk
SimZWD	Simulated ZWD
SE	Standard error
SCP	Sum of cross-products
SD	Single-difference
SES	Single exponential smoothing

SLS	Sequential least squares
SMINQUE	Simplified MINQUE
SNR	Signal-to-noise ratio
SSQ	Sum of squares
SWD	Slant wet delay
TPD	Total path delay
TS	Time series
UCL	Upper control limit
VCV	Variance covariance
VLBI	Very long baseline interferometry
VMF	Vienna mapping function
VMR	Volume mixing ratio
WM	Winter's method
WV	Water vapour
WVR	Water vapour radiometer
ZD	Zero-difference
ZHD	Zenith hydrostatic delay
ZTD	Zenith total delay
ZWD	Zenith wet delay

CHAPTER 1

INTRODUCTION

1.0 BACKGROUND

Water vapour is the major greenhouse gas in the atmosphere and contributes enormously to cloud and precipitation processes. It is extremely variable both spatially and temporally, and is dependent on surface and air temperature. Given its role in the hydrological cycle, a better understanding of the distribution of atmospheric water vapour will ultimately improve precipitation forecasts worldwide. Atmospheric water vapour is a difficult entity to measure due to its dynamic behaviour. Therefore, any new water vapour measurement techniques should be welcome.

In Global Satellite Navigation Systems (GNSS), a signal delay caused by the atmospheric water vapour is referred to as the wet delay. Initially considered as a nuisance factor in GNSS data processing, the wet delay can be determined in the estimation process. Once the wet delay is estimated, it can then be used to determine the amount of precipitable water vapour (PWV) in the atmosphere (section 2.3.1). Over the years, traditional sensors such as radiosonde (RS) and water vapour radiometer (WVR) have provided the benchmark for quantifying PWV. However, the performances of these sensors can be affected by unfavourable weather conditions, and especially at times of precipitation. The large costs of RS (long-term) and WVR (immediate) can also be disadvantageous. Other water vapour sensing techniques such as radio occultation (RO) and Very Long Baseline Interferometry (VLBI) also have their disadvantages. Although RO can provide greater coverage than the other methods, especially over the oceans, its accuracy is restricted to 5 km above the Earth's surface. The cost of constructing and maintaining VLBI stations, on the other hand, are too great to ensure adequate spatial coverage over the land. However, the flexibility and reasonable cost of GNSS, as well as its all-weather

operation capability can provide an additional dimension to the conventional methods of atmospheric sensing in a cost-effective manner.

In GNSS post-processing, the tropospheric delay is often estimated, for instance, using least-squares (LS), in the zenith direction as a parameter, along with the differential coordinates and the carrier-phase integer ambiguities. Due to its small magnitude in comparison to other parameters, the precision (i.e. LS standard error estimates) of the zenith tropospheric delay solutions provided by GNSS is heavily dependent on how effectively other measurement errors can be removed or mitigated prior to the LS estimation process. The majority of these measurement errors, such as the clock errors and the ionospheric delay, can be effectively accounted for through the use of dual-frequency (L1 and L2) measurements, differencing techniques and external models (e.g., Klobuchar, 1986). Once estimated, the zenith tropospheric delay, or zenith total delay (ZTD), can then be divided into its hydrostatic and wet components.

The zenith hydrostatic delay (ZHD) can be estimated with external models to within a millimetre in accuracy (e.g., Saastamoinen, 1972), and be subtracted from the estimated total tropospheric delay, leaving behind the zenith wet delay (ZWD) component, which is mostly due to the atmospheric water vapour. The ZWD can then be used to determine the precipitable water vapour (PWV) for a given site (see section 2.3.1). A receiver at a nearby location can also make use of this ZWD estimates for accurate positioning by correcting for the atmosphere related errors. The accuracy and precision of LS tropospheric estimates are also dependent of the choice of *stochastic model*, which describes the quality of the observed GNSS signals and the correlations among these measurements. An appropriately defined model can lead to quality tropospheric estimates and error estimates.

One of the applications of GNSS PWV estimates is in aiding Numerical Weather Prediction (NWP) models to provide better weather forecasts. The impact of GNSS PWV estimates on weather forecasting is well documented (e.g., Kuo *et al.*, 1996; Vedel and Huang, 2003; Gutman *et al.*, 2004; Vedel and Huang, 2004; Vedel *et al.*, 2004; Macpherson *et al.*, 2007). These studies reported improvements in the humidity and precipitation forecasts when GNSS PWV estimates are assimilated into

NWP models. Comparisons between the estimates from a NWP model with and without GNSS PWV estimates assimilation were made and the improvement in relative humidity (RH) forecasts lead to a 40% reduction of forecast errors (Gutman *et al.*, 2001). The impact of GNSS PWV estimates was further emphasised by a multi-year experiment over the period from 1999-2004 by Smith *et al.* (2006), whereby improvements were evident in the 6-h and 12-h RH forecasts. An experiment for a three month period (March-May 2004) in the corresponding campaign also witnessed the strongest improvements in the 3- and 6-hr forecasts.

Properly-defined error estimates for the GNSS PWV estimates are also essential in the realisation of their true impact on the NWP. The estimation of the observation error covariance matrices is still a very challenging prospect in data assimilation (Buehner *et al.*, 2005). The true impact of GNSS PWV estimates on NWP cannot be realised unless the error covariance matrix is correctly defined (Kuo *et al.*, 1996). Even if the quality of the assimilated data is poor, improvement in the NWP analysis can be expected as long as the error information is given correctly (Huang and Vedel, 2003). Along with the actual GNSS tropospheric estimates, the use of the corresponding ZTD error estimates (i.e. square root of the LS error variances of the ZTD estimates) in the assimilation process was found to have improved the NWP forecast skill in precipitation (Vedel and Huang, 2004). It was also noted, however, that the optimal error estimates to be used in the assimilation need to be "significantly" greater than the standard errors of the LS ZTD, which was in the order of around 3 mm (at one standard deviation). Therefore, a strategy to provide more realistic LS tropospheric error estimates are needed, in addition to quality tropospheric estimates.

The benefits of good GNSS tropospheric solutions can also extend to near real-time or real-time kinematic (RTK) GNSS applications. If a network of reference stations (or a single reference station) is able to provide accurate and precise ZWD estimates in a timely manner, these estimates can then be used by a mobile or static user at an unknown location to improve ambiguity resolution, and ultimately, the position solutions. Furthermore, these GNSS ZWD estimates and error estimates can be used to predict or forecast ZWD estimates ahead of time. These predicted values can be

useful for real-time positioning, as well as for aiding NWP models to provide dependable short-term weather forecasts.

1.1 RESEARCH OBJECTIVES

Factors that can affect the determination of the ZTD (and accordingly the ZWD), and the corresponding error estimates include the *parameterisation of the observation equation*, the *processing strategy*, the *choice of stochastic model used*, the *observation redundancy level*, and the *degree in which the measurement noises have been mitigated*. To evaluate the significance of their roles in the estimation of the ZWD, the following tasks were undertaken in this study:

- Parameterisation of ZWD from GNSS observations through functional and stochastic modelling;
- Investigate the achievable accuracies and precisions of GNSS tropospheric estimates;
- Assess the impact of stochastic modelling on the estimation of the GNSS tropospheric estimates and their corresponding error estimates with simulated and real data at reference stations. The study also includes the comparisons between the Minimum Norm Quadratic Unbiased Estimator (MINQUE) and the other more traditional models;
- Investigate using t-tests to determine whether the error estimates from the LS adjustment process are a dependable source of error information for corresponding GNSS tropospheric solutions;
- Study the impact of a reduced processing window size and a reduced network (i.e. smaller number of stations) on the estimation of the GNSS tropospheric estimates and the corresponding error estimates;
- Investigate the temporal correlations that exist among the ZWD estimates and propose an autocorrelation function that can represent the trend of these correlations. The impact of the proposed autocorrelation model on the estimation of ZWD in RTK mode will also be studied;

- Investigate the best interpolation models for the purpose of estimating missing ZWD values, which can be used during breaks in GNSS, RS or WVR data;
- Test a number of prediction models to provide reliable short-term forecast of ZWD estimates, which can be used for real-time kinematic applications, as well as for NWP models.

1.2 THESIS OUTLINE

The remainder of this thesis comprises seven chapters.

Chapter 2 reviews the modelling of atmospheric water vapour and, briefly, its role in the atmosphere the major greenhouse gases. It also discusses a number of existing methods, other than GNSS, that can be used to quantify the atmospheric water vapour.

Chapter 3 details the procedure in which the atmospheric wet delays can be estimated with GNSS using the least-squares approach in static mode. This Chapter also discusses the GNSS measurement noises that can affect the wet delay estimation process, and the manner in which they can be mitigated to minimise the residual errors from filtering through to the wet delay estimates. The Kalman filter (KF) process is also outlined as a technique that allows the determination of the wet delays in near real-time. The first-order Gauss-Markov (GM) KF process which models consecutive state vectors with respect to the GM autocorrelation function, is examined closely. A new autocorrelation function is then proposed to better represent the decaying trend of the autocorrelations among the ZWD measurements.

Chapter 4 discusses the importance of the choice of the stochastic model on the quality of the determined tropospheric parameter and its error estimates. Some conventional stochastic models, such as the equal-weighting model, the elevation-angle dependent model, and the signal-to-noise model are discussed. In addition, one of the more rigorous spatial models, the MINQUE model, is reviewed along with its

limitations. A modification to this spatial model is proposed to overcome some of its limitations.

Chapter 5 presents the t-test approach to determine the effectiveness of the error estimates of the GNSS ZWD solutions as one of the sources for assessing the quality of the actual ZWD estimates for periods where there are no external data available to determine the accuracy of these estimates. This chapter also examines the consequences of a processing strategy, which involves a network of reference stations with a 24-h or longer processing windows, on the estimation of the LS ZWD estimates and their error estimates.

Chapter 6 provides all the results and analyses of the methods discussed in the previous chapters related to the ZWD estimation and error analysis. One of the primary focuses of Chapter 6 is to investigate the impact of MINUQE stochastic model on the tropospheric solutions from the LS adjustment process in static positioning. This chapter is divided into four sections. The first section provides the analysis of GNSS stations that cover all of Australia to demonstrate the capability of GNSS to provide accurate tropospheric estimates. Through the use of simulation data, the second section tests a number of proposed stochastic models on the determination of the ZWD values and their error estimates. This study also analyses the effects of varying the processing window sizes on the error estimates with the statistical procedure outlined in Chapter 5. The investigation is then carried over to a real data analysis of a long baseline between two Australian stations. The PWV estimates resulting from this baseline analysis are compared and validated with the RS data sets. However, as the number of RS data was limited to a maximum of two per day, the number of comparisons was limited. Therefore, data from a baseline between two European stations with co-located WVRs were investigated. The WVRs are able to provide ZWD estimates at a higher resolution than RS, and thus, more of the GNSS ZWD estimates can be validated. The results of the European campaign are presented in the Section 6.4. The other focus of Chapter 6 is to evaluate the performance of the proposed autocorrelation model against two of the more established random process model, i.e. the random walk and the Gauss-Markov models, in the near real-time determination of the ZWD in the KF process. The results of these comparisons are presented in the final section of Chapter 6.

Chapter 7 analyses the significance of the temporal correlations that exist among the ZWD estimates over different time lags. This chapter also outlines and demonstrates the performance of a number of proposed ZWD interpolation methods that can be used to estimate missing ZWD data in an effective manner. This chapter also outlines and tests a number of ZWD prediction models that may prove useful in real-time kinematic applications and NWP models by forecasting short-term ZWD estimates.

Finally, Chapter 8 summarises the findings and conclusion of the study, and presents some recommendations for future research.

CHAPTER 2

BACKGROUND – ZENITH WET DELAY IN THE ATMOSPHERE

2.0 INTRODUCTION

The Earth's atmosphere is primarily composed of Nitrogen (N_2, ~78%) and Oxygen (O_2, ~21%). Traces of other gaseous constituents are also present, which include water vapour (H_2O), methane (CH_4), hydrogen (H_2), carbon dioxide (CO_2), and noble gases such as argon (Ar), helium (He) and neon (Ne). The degree of contribution of these gases to the atmosphere is very small, and is difficult to quantify with any precision. However, adequate measurements may be obtained with an appropriate apparatus at a specific time and location (Jacobson, 1999).

The atmosphere is divided into five layers according to the difference in temperature. From the lowest to the highest altitude, these layers are the troposphere, the stratosphere, the mesosphere, the thermosphere and the exosphere. These atmospheric layers are illustrated in Figure 2.1.

The troposphere is a layer that extends from the Earth's surface to about 10 km over the North and South poles and about 16 km over the equator. The temperature of the troposphere decreases as the altitude increases. The temperature reduction rate (lapse rate) is approximately 6.5^0C/km. The temperature stops decreasing at the upper boundary of the troposphere, known as the tropopause. Nearly 90% of the atmospheric mass is below 16 km (Möller, 1973), and more than 80% of this is within the troposphere. Therefore, nearly all of the Earth's weather activities occur in the troposphere. The troposphere also contains most of the water vapour in the atmosphere. By studying the troposphere, meteorologists are able to forecast weather.

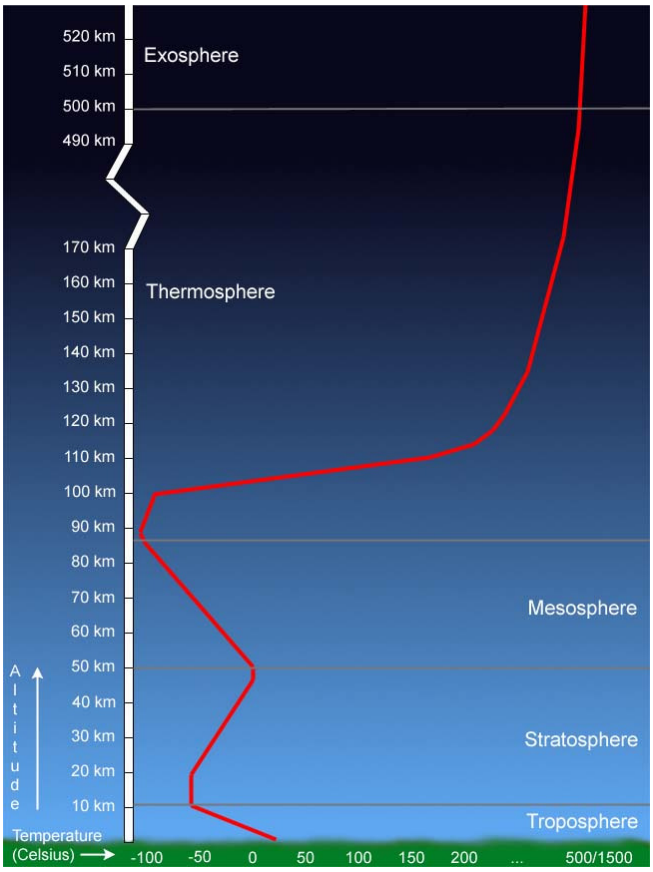

Figure 2.1 The Earth's atmospheric structures (source: UCAR, 2008)

The stratosphere extends from the tropopause to about 50 km from the Earth's surface. It is also where the ozone layer is found. The stratosphere contains very little moisture and thus, clouds are rare, as well as any weather disturbances. The top of the stratosphere is known as the stratopause. All of the gaseous mixtures in the troposphere and the stratosphere are virtually electrically uncharged, and therefore, it is commonly referred to as the *neutral atmosphere*. Nearly 99% of the atmospheric mass is below 30 km (Möller, 1973), therefore the neutral region of the atmosphere contains virtually all of the water vapour.

From the stratopause to about 86 km above the Earth's surface is the mesosphere. The temperature in the mesosphere decreases with altitude. The lowest temperature in the Earth's atmosphere occurs at the top of the mesosphere, called the mesopause. The average temperature at the mesopause is -90^0 C and may reach as low as -100^0 C. The mesosphere is also the layer of the atmosphere where most meteors are vaporised when entering the atmosphere

The thermosphere extends from the mesopause to about 500 km above the Earth's surface. When radiation from the Sun and other sources in the outer space enters the thermosphere, ionization of the atoms and molecules occur, producing ions. Most of the ionization takes place in the lower layer of the thermosphere, and hence, is called the ionosphere. Technically, the ionosphere is not an atmospheric layer but rather, it is an extension of the thermosphere. The ionosphere represents less than 0.1% of the total atmospheric mass. The ionization process requires the presence of short-wave radiation from the Sun and therefore, little or no ionization would take place below the lower boundary of the ionosphere.

Beyond the upper layer of the thermosphere is known as the exosphere. The exosphere is the upper limit of the Earth's atmosphere and is the only atmospheric layer where atoms and molecules can, to some extent, escape into space.

2.1 MOIST AIR

Moist air is a mixture of dry air and various phases (i.e., liquid, solid and gas) of water. As such, the Earth's atmosphere can be viewed as the *moist* atmosphere. Dry air refers to all gases in the atmosphere, except water vapour (WV). The major constituents of dry air are nitrogen, oxygen, argon and carbon dioxide. These four gases account for 99.99% of the pressure exerted by dry air, therefore the concentration of all other dry or trace gases, such as neon, helium and methane, can be ignored in the calculation of the total dry air pressure without much loss in accuracy (Jacobson, 1999).

When the water in the *moist* atmosphere is in the gaseous state, it behaves like the dry air (Satoh, 2004). WV is the gaseous form of water. It is the result of evaporations from soil, lakes, rivers, oceans, sublimation from glaciers, transpiration from plants, or through chemical reactions. Approximately 85% of the atmospheric water is due to ocean surface evaporation (Jacobson, 1999). The distribution of WV in the atmosphere varies with time and location. The atmosphere may contain up to 4% or 40,000 ppmv (parts per million by volume) of WV over the equatorial regions.

In comparison, the WV concentration is almost zero over the Earth's poles. Mid-latitude regions will experience seasonal changes in the water vapour distribution.

WV is a major greenhouse gas and it plays a major role in the climate change process. In addition to providing radiative feedback of the greenhouse effect due to CO_2, its phase changes and transportation through the atmosphere is vital in forming clouds and the precipitation processes. An improved understanding of how water vapour re-distributes itself in the atmosphere will ultimately lead to superior short-term (daily-weekly) weather forecasts, as well as better long-term (yearly) climate prediction (Jacobson, 1999). Therefore, this underlines the need for its study, thereby forming the basis of the present work.

2.1.1 Mixing Ratio

The mixing ratio is a relative quantity that defines the abundance of a gas with respect to the dry air either by volume or mass. The volume mixing ratio (VMR), χ_q, is the number of gas molecules per molecule of dry air (d), and for a gas q it is expressed as (Jacobson, 1999):

$$\chi_q = \frac{P_q}{P_d} = \frac{n_q}{n_d} \tag{2.1}$$

where P_d and P_q are the partial pressures (kPa) of dry air and gas q; n_d and n_q are the number of moles (in mol) of dry air and gas q, respectively.

The mass mixing ratio (MMR) is mass of a gas per mass of dry air and is defined by:

$$\omega_q = \frac{\rho_q}{\rho_d} = \frac{M_q}{M_d}\frac{P_q}{P_d} = \frac{M_q}{M_d}\frac{n_q}{n_d} = \frac{M_q}{M_d}\chi_q \tag{2.2}$$

where M_d and M_q are defined as the molecular weight (or molar mass) of dry air and gas q, respectively; ρ_d and ρ_q denote the density of dry air and gas q.

From Eq. (2.2), the mass mixing ratio of water vapour can be defined as:

$$\omega_{wv} = \frac{M_{wv}}{M_d}\chi_{wv} = \frac{18.0}{28.9}\chi_{wv} = 0.622\chi_{wv} \tag{2.3}$$

where M_{wv} and χ_{wv} are the molecular weight and VMR of water vapour; The values for M_d and M_{wv} in Eq. (2.3) can be found in standard chemistry textbooks. (e.g., Peixoto and Oort, 1992).

2.1.2 Humidity

The water vapour content in the atmosphere can also be expressed in terms of specific humidity. Specific humidity is quantified in a similar way to the mass mixing ratio, except it expresses the mass of water vapour per mass of moist air. The equation for specific humidity q_{wv} can be given as (Jacobson, 1999):

$$q_{wv} = \frac{\rho_{wv}}{\rho_m} = \frac{\rho_{wv}}{\rho_d + \rho_{wv}} = \frac{0.622P_{wv}}{P_d + 0.622P_{wv}} \tag{2.4}$$

where P_{wv} and ρ_{wv} are the partial pressure and density of water vapour, with P_m and ρ_m being the pressure and density of moist air, respectively. The mass density of moist air is:

$$\rho_m = \rho_d + \rho_{wv} \tag{2.5}$$

and thus, Eq. (2.4) can be rewritten as:

$$q_{wv} = \frac{0.622P_{wv}}{(P_m - P_{wv}) + 0.622P_{wv}} = \frac{0.622P_{wv}}{P_m - 0.378P_{wv}} \approx \frac{0.622P_{wv}}{P_m} \tag{2.6}$$

Specific humidity can also be expressed in terms of the mass mixing ratio (Jacobson, 1999), i.e.

$$q_{wv} = \omega_{wv} \frac{\rho_d}{\rho_m} \tag{2.7}$$

The mixing ratio is always greater than the specific humidity, the difference is however negligible in most instances. The discrepancy between the mixing ratio and specific humidity is generally less than 2% (Saucier, 1955).

There is a maximum value for water vapour pressure P_{wv} known as the *saturation vapour pressure*, $P_{wv,s}$, which is a function of the temperature T. The saturation vapour pressure over a liquid surface is given as (Jacobson, 1999):

$$P_{wv,S} = 6.112 \times \exp\left[6816\left(\frac{1}{T_f} - \frac{1}{T}\right) + 5.1309 \times \ln\left(\frac{T_f}{T}\right)\right] \tag{2.8}$$

where $P_{wv,s}$ and T are given in millibars and Kelvin respectively. T_f is the freezing temperature of water and has a constant value of 273.16 K (0^0C). For the temperature range $-35^0\text{C} < T_c < 35^0\text{C}$, Bolton (1980) provides an alternative expression,

$$P_{wv,s} = 6.112 \times \exp\left(\frac{17.67 T_c}{T_c + 243.5}\right) \tag{2.9}$$

The relationship between T and T_c is given as

$$T = T_f + T_c \tag{2.10}$$

Correspondingly, the equation for the saturation vapour pressure over ice, $P_{wv,I}$, is (Jacobson, 1999):

$$P_{wv,I} = 6.112 \times \exp\left[4648\left(\frac{1}{T_f} - \frac{1}{T}\right) - 11.64 \times \ln\left(\frac{T_f}{T}\right) + 0.02265\left(T_f - T\right)\right]$$

(2.11)

The saturation vapour pressure equations above are central in determining whether water vapour condenses as liquid or deposits as ice particles. If the air temperature is below T_f and $P_{wv} > P_{wv,I}$, water vapour deposits as a solid and snow. If the air temperature is above T_f and $P_{wv} > P_{wv,s}$, water vapour generally condenses to liquid.

The relationship between P_{wv} and $P_{wv,s}$ gives rise to another commonly used humidity parameter, *relative humidity*, U. That is,

$$U = \frac{\omega_{wv}}{\omega_{wv,s}} \times 100\% \tag{2.12}$$

where

$$\omega_{wv,s} = 0.622\left(\frac{P_{wv,s}}{P_d}\right) \tag{2.13}$$

which can be referred to as the *saturation mixing ratio*.

2.2 ATMOSPHERIC EFFECTS ON L-BAND GNSS SIGNAL PROPAGATION

As a GNSS signal propagates towards a receiver on Earth, its path lengths and velocities are significantly compromised due to the presence of the atmosphere. Efforts to correct the ranges between the satellites and receivers are essential in precise GNSS positioning. A slight distortion, in the order of a nanosecond, in the signal travel times may result in inaccuracies of a few decimetres in the determination of the range, which in turn dilutes the accuracy of the determined position. Outer space is a largely resistance-free environment, and as such, the electromagnetic GNSS signals are assumed to propagate in a direct path at the speed of light.

The direct signal propagation routes imply, by definition, that the travelling medium of the electromagnetic waves has an index of refraction, n_{ref}, value of 1. Any

deviations from this value are attributed to the Earth's atmospheric effect, as well as other error sources and biases (e.g., Nicholson *et al.*, 2005). These error sources include satellite orbital errors (Pervan and Chan, 2003; Beutler *et al.*, 2006), antenna phase centre offsets and variations (Schmid and Rothacher, 2003; Schmid, 2005), ocean tide loading (e.g., Penna and Baker, 2002; Khan and Scherneck, 2003; Urschl *et al.*, 2005), atmospheric loading (Sun *et al.*, 1995; Kaniuth and Vetter, 2006) and multipath (Van Nee, 1992; Bétaille *et al.*, 2006; Larson *et al.*, 2007), which individually can incur an inaccuracy of a millimetre to a few centimetres to the GNSS solutions. The combined effects can be even more dramatic.

The Earth's atmosphere, more specifically the ionosphere and the troposphere, is largely responsible for the GNSS signal propagation error. The *refraction effect* due to the atmosphere not only affects the traversing speed of a GNSS signal, curvature is also introduced to its intended straight-line path. The associated excess length due to the *bending* of the signal propagation path is about one centimetre at 15° elevation angle (Bevis *et al.*, 1992; Ichikawa, 1995). The bending effect is usually ignored as it corresponds to approximately 0.1% of the total path delay. The refraction effect is seen as an important source of information for atmospheric science, however in GNSS positioning, refraction is generally considered as a nuisance factor. Subsequently, the atmospheric effects are often mitigated from the observables in order to ensure solutions of high precision (Bevis *et al.*, 1992; Musa *et al.*, 2004). The height component of coordinates is most affected by unmodelled atmospheric refraction (Bock *et al.*, 2001). A path delay has to be resolved to an accuracy of about 0.3mm in order to secure 1 mm accuracy in the height component of differential GNSS measurements. Such level of accuracy is currently unachievable on a consistent basis (Schön *et al.*, 2004; Satirapod and Chalermwattanachai, 2005).

2.3 TROPOSPHERIC DELAY

Signal delays induced by the troposphere are generally known as *tropospheric refractions* or *tropospheric delays*. In practice, tropospheric effects on GNSS measurements refer to the delays induced by the troposphere, and the stratosphere (i.e. the neutral atmosphere). Although the troposphere is smaller than the

stratosphere, GNSS signals experience greater refractions in the troposphere as it contains the majority of the atmospheric mass.

Signal delay occurs in the troposphere by the slowing of the signal velocity and bending of the propagation path. Thus, the measured distance (based on timed signals) will be greater than the geometric range. The troposphere is a non-dispersive medium for GNSS frequencies or for any radio frequencies below 15 GHz (Hay and Wong, 2000). Delays on the code and phase observables are therefore identical.

Signals received at low elevations pass through more of the atmosphere than those of higher elevations and therefore, experience greater tropospheric effects. Tropospheric refraction can reach 2.3 m in the zenith direction of an observing receiver at sea level (Bevis *et al.*, 1992; Rocken *et al.*, 1995; Businger *et al.*, 1996; Dodson *et al.*, 1996; Duan *et al.*, 1996; Leick, 2004). The measured signal range error for an elevation of a few degrees could be in the order of several metres (El-Rabanny, 2002; Xu, 2003). A difference up to a factor of four can be seen between a delay at the zenith and at the an elevation angle of 15^0 (Bevis *et al.*, 1992).

The tropospheric delay cannot be mitigated using the L1/L2 combination, as it is for the ionospheric effects (e.g., Seeber, 2003). Therefore, it has to be properly modelled or estimated. For short baselines (<10-20 km), each GNSS station/receiver will be subject to virtually identical tropospheric biases, thus, the effect can be differenced away without the need to introduce external aid from meteorological data or models. This approach works best provided the stations are at comparable altitudes, i.e. the amount of atmosphere above each of the stations is similar. When larger baselines are being considered, or when the height differences between the stations are, adequate modelling of the tropospheric delays is essential (Seeber, 2003). However, acquiring highly precise tropospheric estimates still remains difficult due to the dynamic nature of the atmospheric gases, more specifically, the atmospheric water vapour (e.g. Bevis *et al.*, 1994; Rocken *et al.*, 1997; Snajdrova *et al.*, 2006).

2.3.1 Modelling the Tropospheric Delay

A medium with a refractive index (not equal to one) impacts a signal's propagation path length and its velocity. The difference between the calculated range and the geometric range can be defined as:

$$\Delta L_c = \int_{L_c} n_{refr}(s)ds - L_g \tag{2.14}$$

where $n_{refr}(s)$ is the index of refraction as a function of position s along a curved path L_c, and L_g is the straight line geometric Euclidean path between a satellite and a receiver. Equivalently, (2.14) can be expressed as (Bevis *et al.*, 1992):

$$\Delta L_c = \int_{L_c} [n_{refr}(s) - 1]ds + [L_p - L_g] \tag{2.15}$$

where L_p is the path length of the curve L_c. The first term of the right-hand side of Eq. (2.15) is attributed to the change in signal velocity, while the second term represents the *bending* of the ray path. As mentioned previously, this bending effect is usually ignored as it corresponds to approximately 0.1% of the total path delay. Thus, following Eq. (2.15), the excess path between a station i and a satellite j as a result of signal retardation due to the troposphere is modelled as:

$$T_j^k = \int_{L_c} [n_{refr}(s) - 1]ds \tag{2.16}$$

The quantity $n_{refr}(s)$ is often described in terms of the atmospheric refractivity $N_{refr}(s)$. The relationship between $n_{refr}(s)$ and $N_{refr}(s)$ is defined as:

$$n_{refr}(s) - 1 = 10^{-6} N_{refr}(s) \tag{2.17}$$

Thus, Eq. (2.16) becomes

$$T_i^j = 10^{-6} \int_{L_c} N_{refr}(s) ds \tag{2.18}$$

The degree of tropospheric refraction on a GNSS signal depends directly on the density of the atmospheric air. In turn, the air density is dependent on temperature, atmospheric pressure and the air humidity (or water vapour pressure). Smith and Weintraub (1953) proposed a two-term formula to describe the air refractivity as:

$$N_{refr} = 77.6\frac{P}{T} + 3.73\times10^5 \frac{P_{wv}}{T^2} \tag{2.19}$$

The first term in Eq. (2.19) is considerably larger than the second in most circumstances. Under normal atmospheric conditions, the proposed formulation is considered accurate to about 0.5% (Resch, 1984). A more refined, three-term formula for refractivity was also offered by Smith and Weintraub (1953):

$$N_{refr} = k_1\left(\frac{P_d}{T}\right)Z_d^{-1} + k_2\left(\frac{P_{wv}}{T}\right)Z_{wv}^{-1} + k_3\left(\frac{P_{wv}}{T^2}\right)Z_{wv}^{-1} \tag{2.20}$$

where Z_d and Z_{wv} is the compressibility factor of dry air and water vapour, respectively; k_1, k_2, k_3 are the pre-determined coefficients based on theory and experimental observations. Table 2.1 provides the values for these coefficients.

Table 2.1 Values for Coefficients k_1, k_2 and k_3

	k_1(Kmbar^{-1})	k_2(Kmbar^{-1})	k_3(K^{2}mbar^{-1})
Smith and Weintraub (1953)	77.607 ± 0.013	71.60 ± 8.50	3.747 ± 0.031
Thayer (1974)	77.604 ± 0.014	64.79 ± 0.08	3.776 ± 0.004
Bevis *et al.*(1994)	77.600 ± 0.050	70.40 ± 2.20	3.739 ± 0.012

Although water vapour represents less than 1% of the total atmospheric volume, it is extremely variable and difficult to quantify. Most of the water in the air is from the atmospheric water vapour (e.g., Leick, 2004). Liquid water does contribute slightly to the overall refractivity; however it is not parameterised in Eq. (2.20). Elgered (1993) evaluates a maximum of about 0.75 cm path delay can be introduced by liquid

water, which amounts to even less than that of the bending effect. It is as such treated similarly and is ignored in the formulation. The compressibility factors, Z_d and Z_{wv}, take into account small departures in the behaviour of the atmospheric gases from the ideal gas laws (Bevis *et al.*, 1992). Both parameters differ from unity only a few parts per thousand (Owens, 1967), and therefore are usually set to one. The first and second terms of Eq. (2.20) describe the sum of distortions of the dry and wet atmospheric constituents under the influence of an applied magnetic field. The third term refers to the refractivity due to the permanent dipole moment of the water vapour molecule, which is independent of the GNSS frequency (Bevis *et al.*, 1992).

In Table 2.1, the coefficients k_1, k_2, and k_3 of Thayer (1974) are more widely used than Smith and Weintraub (1953) because of their high nominal precisions. The accuracy of the refractivity computed via Eq. (2.20) is limited to around 0.02%, as a result of the uncertainties in Thayer's constant coefficients (Davis *et al.*, 1985). However, there were arguments against the derivation of these coefficients by Hill *et al.* (1982), who argued that the methodology of Thayer (1974) as theoretically unjustifiable. The main issue here is with the k_2 constant, which is determined through extrapolation of the optical frequencies. Another set of values for the k_1, k_2, and k_3 constants were later suggested by Bevis *et al.* (1994). Bevis *et al.* (1994) are confident that the proposed set of coefficients has a 95% probability that their true values lie within two standard deviations.

The first term of Eq. (2.20) can be further split into two terms, one that reflects the refractivity of an ideal gas in hydrostatic equilibrium and another that is dependent of the partial water vapour pressure (Leick, 2004). By introducing the equation for the ideal gas with respect to its density

$$P_i = \frac{Z_i \rho_i R_u T}{M_i}, \qquad \text{for } i = d \text{ (dry), wv (water vapour)} \qquad (2.21)$$

and applying P_d from (2.21) to the first term of (2.20) results in,

$$k_1\left(\frac{P_d}{T}\right)Z_d^{-1} = \frac{k_1\rho_d R_u}{M_d} \tag{2.22}$$

where R_u denotes the universal gas constant and is given as 8.31434 $Jmol^{-1}K^{-1}$ (Jacobson, 1999).

Defining the relationship between the total air mass density ρ with its partial densities due to the dry and wet air constituents as:

$$\rho = \rho_d + \rho_{wv} \tag{2.23}$$

and substituting it into Eq. (2.22) and combining it with the other terms of Eq. (2.20) gives

$$\begin{aligned} N_{refr} &= \frac{k_1\rho R_u}{M_d} + k_2^{'}\frac{P_{wv}}{T}Z_{wv}^{-1} + k_3\frac{P_{wv}}{T^2}Z_{wv}^{-1} \\ &= k_1\frac{P_d}{T} + \left[k_2^{'}\frac{P_{wv}}{T} + k_3\frac{P_{wv}}{T^2}\right]Z_{wv}^{-1} \end{aligned} \tag{2.24}$$

where

$$k_2^{'} = k_2 - k_1\frac{M_{wv}}{M_d} \tag{2.25}$$

A value of 22.1 ± 2.2 $Kmbar^{-1}$ for $k_2^{'}$ is given in Bevis *et al.* (1994).

The total refractivity N_{refr} can now be expressed in terms of the hydrostatic (N_d) and wet (N_{wv}) components. That is,

$$N_d = k_1\frac{P_d}{T}, \text{ and} \tag{2.26}$$

$$N_{wv} = \left[k_2^{'}\frac{P_{wv}}{T} + k_3\frac{P_{wv}}{T^2}\right]Z_{wv}^{-1} \tag{2.27}$$

However, the wet delay component (i.e. Eq. (2.27)) due to water vapour is more elaborate than the dry component (i.e. Eq. (2.26)). When Eqs. (2.26) and (2.27) are integrated along the zenith direction, the zenith hydrostatic delay (ZHD) and the zenith wet delay (ZWD) are finally computed respectively as:

$$\mathrm{ZHD} = 10^{-6} \int_{\text{zenith}} \mathrm{N_d}(\mathrm{h})\mathrm{dh} \tag{2.28}$$

$$\mathrm{ZWD} = 10^{-6} \int_{\text{zenith}} \mathrm{N_{wv}}(\mathrm{h})\mathrm{dh} \tag{2.29}$$

with the zenith total delay (ZTD) defined as

$$\mathrm{ZTD} = \mathrm{ZHD} + \mathrm{ZWD} \tag{2.30}$$

When *surface pressure* and *surface temperature* data are available, the ZWD may be expressed in terms of precipitable water vapour (PWV) measurement. PWV is often identified as the Integrated Water Vapour (IWV). Thus, the relationship between the two entities is defined by the dimensionless conversion factor Π (e.g., Bevis *et al.*, 1992; Glowacki *et al.*, 2006):

$$\mathrm{PWV} = \Pi \times \mathrm{ZWD} \tag{2.31}$$

with

$$\Pi = 10^{6} \rho_{\mathrm{w}} \mathrm{R_{wv}} \left(\mathrm{k}_2' + \frac{\mathrm{k}_3}{\mathrm{T_m}} \right) \tag{2.32}$$

and

$$\mathrm{T_m} = \frac{\int_{\mathrm{H_s}}^{\infty} \frac{\mathrm{P_{wv}}}{\mathrm{T}} \mathrm{dh}}{\int_{\mathrm{H_s}}^{\infty} \frac{\mathrm{P_{wv}}}{\mathrm{T}^2} \mathrm{dh}} \tag{2.33}$$

where $\mathrm{R_{wv}}$ and ρ_{w} are the specific gas constant of water vapour and the density of liquid water, respectively; $\mathrm{T_m}$ is the weighted mean temperature; $\mathrm{P_{wv}}$ denotes the partial pressure of water vapour with T denoting the height-dependent temperature

reading. The integration is performed from the surface through the entire atmosphere. The factor Π is sometimes approximated as 6.5 (Kleijer, 2004), but it varies spatially and temporally. The parameter T_m can be approximated using a linear regression equation, which is derived from the radiosonde profiles acquired within the USA (Bevis *et al.*, 1992):

$$T_m = 70.2 + 0.72T_s \tag{2.34}$$

where T_s is the surface temperature in Kelvin. Bevis *et al.* (1992) mentioned that Π can be evaluated to within 2% accuracy with Eq. (2.34). A study into the estimation of T_m over 53 global stations in a 23-year period has found that the appropriateness of the coefficients in Eq. (2.34) are limited to the continental US (Ross and Rosenfeld, 1997). However, using a linear regression model of the same form as Eq. (2.34), it was found in most cases that site-specific coefficients can evaluate T_m to within 2% accuracy, corresponding to an absolute PWV error of 0.1-0.5 mm.

2.3.2 Hydrostatic and Wet Delays

The hydrostatic delay is much larger than the wet delay as it represents 90% of the total tropospheric refraction (Dodson *et al.*, 1996; Duan *et al.*, 1996). Changes in the ZHD, given in Eq. (2.28) at a specific location are mainly due to surface pressure changes accompanying synoptic-scale motions of the atmosphere. Variations in the ZHD are usually at the order of 2-3 cm during the year at mid-latitudes (Janes *et al.*, 1991), but may reach 5 cm on a daily basis, or over a few days. The hydrostatic delay is not difficult to account for and can be estimated with a high degree of accuracy when precise surface meteorological measurements are incorporated in its modelling. Current models can estimate the hydrostatic delay with an accuracy that is within 1% of actual delay (Seeber, 2003). Moreover, if the atmosphere is in hydrostatic equilibrium and if the atmospheric pressure is measured with an error less than 0.3 mbar, then the ZHD can be retrieved within 1 mm using for example, the Saastamoinen (1973) hydrostatic model (Mendes and Langley, 1999). This ensures that minimal hydrostatic errors propagate through to the wet delay estimates.

Although the wet delay, given in Eq. (2.29) accounts for only 10% of the total delay, it is far more difficult to model or remove due to the lack of knowledge regarding the distribution of the water vapour in the atmosphere. The temporal and spatial variability of the water vapour ensures that the wet delay cannot be consistently modelled with millimetre precision. The wet delay can vary from a few centimetres in arid places to 35 cm in tropical and humid regions (Bevis *et al.*, 1992).

2.4 TROPOSPHERIC MODELS

Tropospheric models are often used to model the state of the atmosphere with varying degrees of accuracy. Surface meteorological measurements such as pressure, temperature and humidity are generally required as inputs for these models. Other inputs may include station height, surface gravity and temperature lapse rate. Models such as the Hopfield (1971) and Baby *et al.* (1988) can be used to estimate the ZHD accurately to within 3-4 mm whilst Saastamoinen (1973) can produce results with sub-millimetre bias (Mendes and Langley, 1999).

On the other hand, acquiring highly-precise measurements of ZWD consistently with current tropospheric models is difficult, as the correlation between wet delay and surface measurements is weak (Mendes and Langley, 1999). Under standard atmospheric conditions (1,010 mbar for atmospheric pressure, 20^0C for temperature, and 50% humidity), most existing models generate acceptable estimates for weather forecast application. However, such conditions are rare, especially over long periods of time. Thus, many of these models are inadequate in capturing the absolute wet delay estimates (El-Rabanny, 2002). The residual wet delay resulting from existing models ranges from a couple to several centimetres (e.g., Mendes and Langley, 1999; Kim *et al.*, 2004; Farah *et al.*, 2005; Satirapod and Chalermwattanachai, 2005). This inaccuracy may rise to 5-8 cm during the passage of weather fronts (Elgered, 1993; Ichikawa, 1995). In humid conditions such as that on the Indian subcontinent, a mean absolute difference of up to 6.4 cm between the true ZWD and the widely used Hopfield (1971) model can be observed (Saha *et al.*, 2007). The European Geostationary Navigation Overlay Service (EGNOS) tropospheric model was reported to produce vertical tropospheric errors of up to 17.8 cm for a UK-based network (Dodson *et al.*, 1999; Penna *et al.*, 2001). Although tropospheric models

such as EGNOS and Saastamoinen (1973) are considered as global models, the meteorological data used to generate these models are primarily from Northern Hemisphere. Thus, it is not surprising that these models do not perform well under vastly different conditions and locations. The situation is worse for airborne applications as accurate meteorological measurements are difficult to obtain (Mendes and Langley, 1999).

The following sub-sections will discuss in detail some of the more widely used tropospheric models, namely the Saastamoinen (1973) model, the modified Saastamoinen (1973) model and the modified Hopfield (1969) model. These models are included the Bernese GNSS software package V4.2 (Hugentobler *et al.*, 2001), which is the main processing software package used in this study.

2.4.1 Saastamoinen Model

Under the assumption of hydrostatic equilibrium, Saastamoinen (1973) modelled the integral solution to the ZHD formula in Eq. (2.28) as a function of mean gravity g_m (Saastamoinen, 1973):

$$\mathrm{ZHD} = 10^{-6} \mathrm{k}_1 \mathrm{P}_s \frac{\mathrm{R}_d}{\mathrm{g}_m} \tag{2.35}$$

with

$$\mathrm{g}_m = \mathrm{g}_m^0 (1 - 0.00266 \cos 2\ell - 0.00028\mathrm{H}) \tag{2.36}$$

where P_s is the surface air pressure; g_m^0 is the mean gravity at mean sea level and is defined by a constant value of 9.784 ms^{-2}; ℓ is the geocentric latitude of observing site, whilst H is the station orthometric height in km. By applying the refractivity constant provided by Essen and Froome (1951), the Saastamoinen model is thus given as

$$\mathrm{ZHD} = \frac{0.002277 \mathrm{P}_s}{1 - 0.00266 \cos 2\ell - 0.00028\mathrm{H}} \tag{2.37}$$

The corresponding Saastamoinen ZWD model is outlined as:

$$\mathrm{ZWD} = 0.002277\left(\frac{1255}{\mathrm{T_s}} + 0.05\right)\mathrm{P_{wv}^s} \tag{2.38}$$

where the surface partial pressure of water vapour, $\mathrm{P_{wv}^s}$, can be obtained with in situ measurements of surface temperature $\mathrm{T_s}$ (K) and relative humidity $\mathrm{U_s}$ (in %) via the following expression (Xu, 2003);

$$\mathrm{P_{wv}^s} = \mathrm{U_s} \times \exp\left(-37.2465 + 0.213166\mathrm{T} - 0.000256908\mathrm{T}^2\right) \tag{2.39}$$

When Eqs. (2.37) and (2.38) are combined, the resulting Saastamoinen ZTD model is:

$$\mathrm{ZTD_{Saas}} = 0.002277\left[\mathrm{P_s} + \left(\frac{1255}{\mathrm{T_s}} + 0.05\right)\mathrm{P_{wv}^s}\right] \tag{2.40}$$

A more general Saastamoinen formula, which allows for the calculation of the total path delay (TPD), is given by multiplying Eq. (2.40) by the secant function, such that:

$$\mathrm{TPD_{Saas}} = \frac{0.002277}{\cos(\theta_z)}\left[\mathrm{P_s} + \left(\frac{1255}{\mathrm{T_s}} + 0.05\right)\mathrm{P_{wv}^s}\right] \tag{2.41}$$

where θ_z is the zenith angle from a station on the Earth's surface..

2.4.2 Modified Saastamoinen Model

The modified Saastamoinen (1973) model introduces two correction terms to Eq. (2.41), B and $\delta\mathrm{R}$, which are dependent on H and θ_z, respectively. The calculation of the TPD via the modified Saastamoinen model can be summarised by:

$$\mathrm{TPD_{ModSaas}} = \frac{0.002277}{\cos(\theta_z)}\left[\mathrm{P_s} + \left(\frac{1255}{\mathrm{T_s}} + 0.05\right)\mathrm{P_{wv}^s} - \mathrm{B}\tan^2(\theta_z)\right] + \delta\mathrm{R} \tag{2.42}$$

Both δR and B can be linearly interpolated using Tables (2.2) and (2.3) for any given H and θ_z (Xu, 2003).

Table 2.2 Coefficients of B at various heights H

H (km)	0	0.5	1	1.5	2	2.5	3	4	5
B (mbar)	1.156	1.079	1.006	0.938	0.874	0.813	0.757	0.654	0.563

Table 2.3 Coefficients of δR heights H and θ_z

H (km)	θ_z												
	60.00	66.00	70.00	73.00	75.00	76.00	77.00	78.00	78.50	79.00	79.50	79.75	80.00
0.0	0.003	0.006	0.023	0.020	0.032	0.039	0.050	0.065	0.075	0.087	0.102	0.111	0.121
0.5	0.003	0.006	0.011	0.018	0.028	0.035	0.045	0.059	0.068	0.079	0.093	0.101	0.110
1.0	0.002	0.005	0.010	0.017	0.025	0.032	0.041	0.054	0.062	0.072	0.085	0.092	0.100
1.5	0.002	0.005	0.009	0.015	0.023	0.029	0.037	0.049	0.056	0.065	0.077	0.083	0.091
2.0	0.002	0.004	0.008	0.013	0.021	0.026	0.033	0.044	0.051	0.059	0.070	0.076	0.083
3.0	0.002	0.003	0.006	0.011	0.017	0.021	0.028	0.036	0.042	0.049	0.058	0.063	0.068
4.0	0.001	0.003	0.005	0.009	0.014	0.017	0.022	0.030	0.034	0.040	0.047	0.052	0.056
5.0	0.001	0.002	0.004	0.007	0.011	0.014	0.018	0.024	0.028	0.033	0.037	0.043	0.047

Actual pressure, temperature and relative humidity measurements or those from a standard atmospheric model may be used in Eq. (2.42). These meteorological estimates may alternatively be obtained via the following expressions (Xu, 2003):

$$P_s = P_0\left[1 - 0.000226(H - H_0)\right]^{5.225} \tag{2.43}$$

$$T_s = T_0 - 0.0065(H - H_0) \tag{2.44}$$

$$U_s = U_0 \exp\left[-0.000639(H - H_0)\right] \tag{2.45}$$

where $P_0 = 1013.25\,\text{mbar}$, $T_0 = 291.16\,\text{K}$, $H_0 = 0.00\,\text{m}$ and $U_0 = 50\%$. P_{wv}^s is defined earlier by Eq. (2.39).

2.4.3 Modified Hopfield Model

Denoting the tropospheric TPD at θ_z by:

$$\text{TPD}(\theta_z) = D_d(\theta_z) + D_{wv}(\theta_z) \tag{2.46}$$

where $D_d(\theta_z)$ and $D_{wv}(\theta_z)$ are the tropospheric dry and wet delay at the zenith angle θ_z, respectively, the modified Hopfield (1971) model for calculating the TPD are summarised by:

$$D_i(\theta_z) = N_i \sum_{k=1}^{9} \frac{\xi_{k,i}}{k} r_i^k, \text{ for } i = d, wv \tag{2.47}$$

with

$$r_i = \sqrt{(R_E + H_i)^2 - R_E^2 \sin^2(\theta^z)} - R_E \cos(\theta_z) \tag{2.48}$$

$$\xi_{1,i} = 1 \tag{2.49}$$

$$\xi_{2,i} = 4a_i \tag{2.50}$$

$$\xi_{3,i} = 6a_i^2 + 4b_i \tag{2.51}$$

$$\xi_{4,i} = 4a_i\left(a_i^2 + 3b_i\right) \tag{2.52}$$

$$\xi_{5,i} = a_i^4 + 12a_i^2 b_i + 6b_i^2 \tag{2.53}$$

$$\xi_{6,1} = 4a_i b_i\left(a_i^2 + 3b_i\right) \tag{2.54}$$

$$\xi_{7,i} = b_i^2\left(6a_i^2 + 4b_i\right) \tag{2.55}$$

$$\xi_{8,i} = 4a_i b_i^3 \tag{2.56}$$

$$\xi_{9,i} = b_i^4 \tag{2.57}$$

$$a_i = -\frac{\cos(\theta_z)}{H_i^e} \tag{2.58}$$

$$b_i = -\frac{\sin^2(\theta_z)}{\left(2H_i^e R_E\right)} \tag{2.59}$$

$$N_d = \frac{77.64P_s}{T_s} \text{ (in Kmb}^{-1}\text{)} \tag{2.60}$$

$$N_{wv} = \frac{-12.96P_{wv}^s}{T_s} + \frac{371800P_{wv}^s}{T_s^2} \tag{2.61}$$

and

$$R_E = 6378137\text{m} \tag{2.62}$$

$$H_d^e = 40136 + 148.72(T_s - 273.16) \tag{2.63}$$

$$H_{wv}^e = 11000\,\text{m} \tag{2.64}$$

where the quantity R_E is the Earth's equatorial radius.

There are several hydrostatic models available to users, other than the Saastamoinen models in Sections 2.4.1 and 2.4.2. Some of these are presented in Table A1 in the Appendix, including the hydrostatic model given by Davis *et al.* (1985), Baby *et al.* (1988) and Hopfield (1969). Table A2 in the Appendix also provides other available wet delay models, including Askne and Nordius (1987), Baby *et al.* (1988), Hopfield (1971) and Ifadis (1986) wet delay models.

2.5 ATMOSPHERIC SENSORS OTHER THAN GNSS

Precise profiling of the atmospheric delay is arduous and complex matter. This desire to understand the atmosphere has led to the development of several atmospheric sensors. Radiosondes (RS) and water vapour radiometers (WVR) are traditional sensors that are able to provide direct measurement of the atmospheric delays. Radio occultation (RO) is a remote sensing system which is also capable of quantifying the physical properties of the atmosphere. Initially deployed for geodetic purposes, measurements from Very Long Baseline Interferometry (VLBI) are now routinely used to provide comparable atmospheric measurements. The RS has however over the years established itself as the benchmark and its values are frequently used to validate that of its counterparts. The RS is not without its limitations, as is with the other approaches. In this section, the aforementioned sensors will be briefly outlined, along with their advantages and disadvantages.

2.5.1 Radiosonde

RS is an electronic instrument that comprises a set of weather sensors and hangs around 20 m below a hydrogen or helium balloon (see Figure 2.2). When a RS is released, the onboard sensors provide direct measurements of the temperature, relative humidity and air pressure profiles as it travels through the atmosphere (Wang *et al.*, 2003; Soden *et al.*, 2004; Miloshevich *et al.*, 2006; McMillin *et al.*, 2007). The sensors are battery powered and are linked to a 300 milliwatt radio transmitter. The transmitter sends the atmospheric data to a receiver at a monitoring station at a frequency ranging from 1668.4-1700.0 MHz. A RS flight lasts approximately 2 hours and the RS can ascend to more than 35 km above the Earth's surface and drift more than 200 km from the release point.

During its flight, the radiosonde's balloon will expand as the atmospheric pressure decreases. Once the balloon reaches its elastic limit and bursts, a small parachute is employed on the RS to reduce damage to lives and properties during its descent. Although RS are expendable, their impending costs limit the number of launches to at most twice daily at most weather stations. Thus, it is almost impossible to profile the distribution of water vapour based solely on RS measurements. Direct RS measurements also have sensor-icing problem in the upper atmosphere (>10km) due to decreased atmospheric temperature (Fu *et al.*, 2007). Additionally, RS provides poor spatial coverage over the oceans as most launch sites are inland-based. The RS coverage in the Southern Hemisphere is also not as comprehensive as the Northern Hemisphere.

Although RS is perceived as the most reliable sensor by many researchers, biases still exist in the instrument. The Vaisala RS, for example, is one of the most widely used radiosondes worldwide. It has however been shown to exhibit a dry bias in PW of 3-4 mm when compared to GNSS analyses and an independent RS model (Nakamura *et al.*, 2004). Wang and Zhang (2008) indicated that the dry bias in Vaisala (RS80A, RS80H, RS90 and RS92 models) RS increases linearly with PWV and a relative bias (RS-GNSS) of less than 10% is observed for PWV range of ~5-40 mm. The dry bias in Vaisala RS at daytime also tends to be greater than of night-time (e.g., Kwon *et al.*, 2007; Wang and Zhang, 2008; Yoneyama *et al.*, 2008). Wang and Zhang (2008) noted that the daytime and night-time relative dry bias for the RS92 model is about 10% and 5%, respectively.

Figure 2.2 A radiosonde being released (http://www.ncdc.noaa.gov/)

2.5.2 Ground-Based Water Vapour Radiometer

A ground-based WVR is a device that measures the intensity of the electromagnetic energy at a certain frequency. It is able to measure integrated water vapour (IWV) contents as well as the wet delay along a given direction, when operated under infrared bands, by measuring the sky brightness temperature, T_{sky} (e.g., Rocken *et al.*, 1991; Coster *et al.*, 1996; Basili *et al.*, 2001; Aonashi *et al.*, 2004; Haefele *et al.*, 2004; Liu *et al.*, 2005; Mattioli *et al.*, 2005; Wang *et al.*, 2007). Ground-based WVRs are typically operated at 22 GHz in order to quantify a line-of-sight (LoS) IWV measurement. A second measurement at 31 GHz is often simultaneously observed so as to correct the signal for possible cloud liquid water. Once retrieved, a sky brightness temperature measurement is then used to calculate the opacity υ via the following expression (Haefele *et al.*, 2004):

$$\upsilon = \ln\left(\frac{T_{Bg} - T_m}{T_{sky} - T_m}\right) \tag{2.49}$$

where T_{Bg} is the brightness temperature of the cosmic background radiation and has a pre-set value of 2.7 K; T_m is the weighted mean atmospheric temperature which can be determined from surface meteorological measurements. The relationship between the IWV and opacity is characterized by (Haefele *et al.*, 2004):

$$IWV = a + b\upsilon_{22GHz} + c\upsilon_{31GHz} \tag{2.50}$$

The coefficients a, b and c are predetermined from a climatology database. Eq. (2.50) allows IWV to be estimated with an accuracy of 0.5 kg/m^2 (Haefele *et al.*, 2004). Once an IWV value is obtained, the ZWD can in turn be calculated by means of:

$$ZWD = \frac{IWV}{\Pi} \tag{2.51}$$

where Π is defined by Eq. (2.32). The ZWD can be calculated with an accuracy of <0.3 mm if T_m is resolved within 1 Kelvin (Haefele *et al.*, 2004).

The drawbacks of WVR are the high cost, poor spatial coverage, and that its performance is degraded by the presence of heavy cloud covers and moisture on the equipment due to rain or morning dew. Under favourable non-precipitating atmospheric conditions, WVR and RS measurements have been consistently found to greatly agree with one another by less than 2 mm in the average PWV differences (e.g., Basili *et al.*, 2001; Haefele *et al.*, 2004; Martin *et al.*, 2006).

2.5.3 Radio Occultation

Radio Occultation (RO) is a technique that takes advantage of the current satellite constellation by directing the GNSS signals to a GNSS receiver onboard a low Earth orbiter (LEO), shown in Figure 2.3. Using the precise locations of the GNSS and LEO satellites, the ray path and the tangent point accurately determined. Based on the information of the tangent point, the radius "r" and the asymptotic ray miss-distance "α" can be obtained, after which the bending angle "a" can be calculated (e.g., Awange *et al.*, 2004; Fu *et al.*, 2007). The curvature or bending of a GNSS signal allows for the determination of atmospheric refractivity profiles at different heights. By assuming spherical symmetry in the occulting atmosphere, the index of refractivity from LEO to the Earth's surface can be calculated. In turn, temperature, pressure and water vapour in the troposphere and electron density in the ionosphere can be resolved effectively (e.g., Hajj *et al.*, 2002; Fu *et al.*, 2007; Zhang, Biadeglgne *et al.*, 2007; Zhang, Fu *et al.*, 2007).

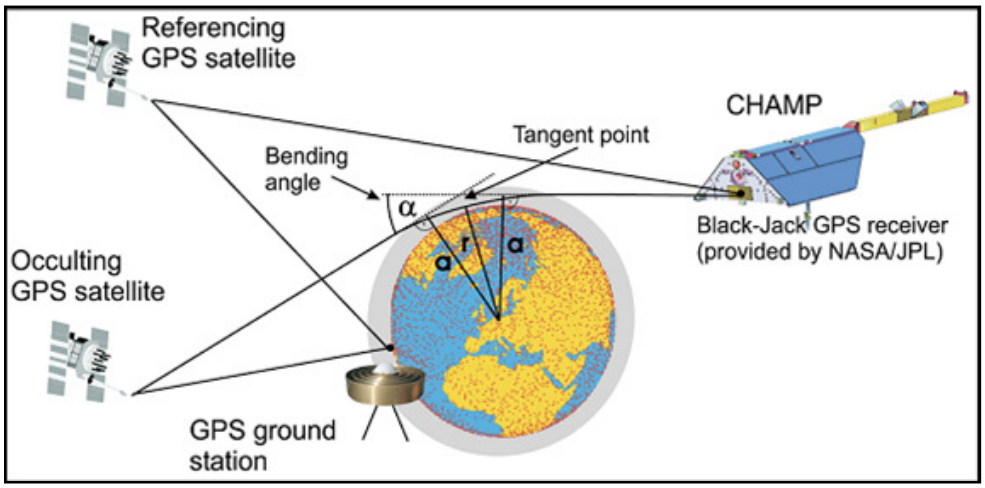

Figure 2.3 GNSS radio occultation geometry

The atmospheric readings provided by RO are most accurate between the altitude of 5-25km (Kuo *et al.*, 2005). RO atmospheric soundings become less reliable in comparison to RS below the specified altitude and the incorporation of such measurements to weather forecasting is unlikely to yield any significant improvement (Healy *et al.*, 2005). As the majority of the atmospheric water vapour is below 5 km, the RS and WVR are the preferred sensors in this study. Figure 2.4 demonstrates the effectiveness of RO for atmospheric profiling at various altitudes in comparison to data from the European Center for Medium-range Weather Forecast (ECMWF) and National Centers for Environmental Prediction (NCEP).

The advantages of RO over RS and WVR are that it provides global coverage, high vertical resolution, high accuracy and all-weather capability (Fu *et al.*, 2007).

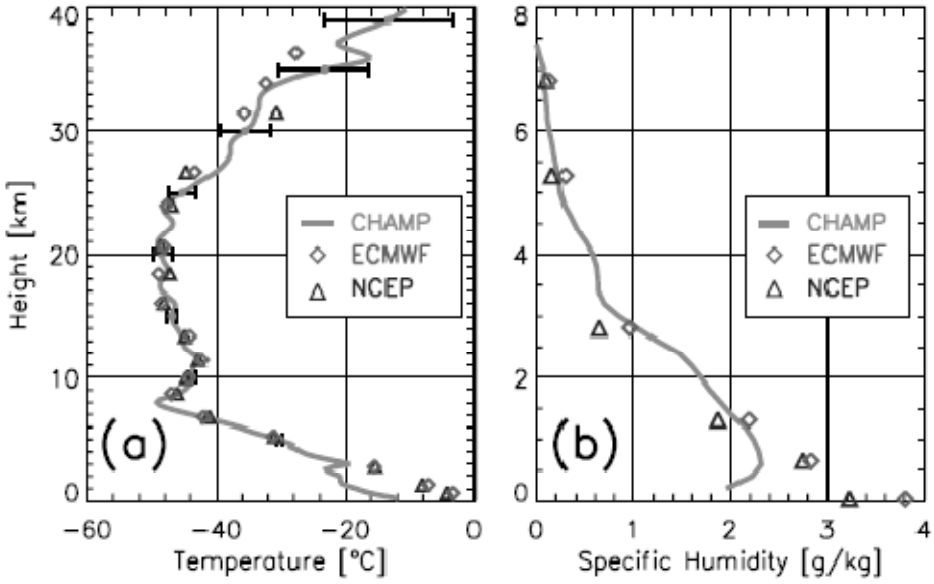

Figure 2.4 Vertical temperature and specific humidity profiles derived from CHAMP's (CHAllenging Minisatellite Payload) occultation measurements compared with data from the ECMWF and NCEP (source: Wickert *et al.*, 2001)

2.5.4 Very Long Baseline Interferometry

The VLBI technique was initially developed to study radio sources in the distant cosmos. The technique itself can be reversed to perform precise geodetic studies on Earth and provide insight into the planet's orientation in the universe. VLBI involves two or more exceptionally sensitive radio telescopes tracking a single natural source such as a quasi-stellar object known as a *quasar* (see Figure 2.5). A quasar will

appear motionless when observed from the Earth's surface due to its great distance from the planet, thus making it a suitable candidate as a reference point. When multiple quasars are observed, a celestial reference frame is formed. By simultaneously observing several quasars over multiple time periods with a network of radio telescopes worldwide, scientists are able to use the collected data and determine the relative times of the arriving signals to within a few picoseconds. These time differences can then be used to determine the distance between each pair of telescopes to within a millimetre across the network (e.g., Pradel *et al.*, 2006). These data also allow scientists to monitor, among others, the Earth's size, shape and variation in its rotational speed. Meteorological studies with VLBI have also been gaining momentum in recent times and have played a significant role in providing reliable atmospheric delay estimates (e.g., Snajdrova *et al.*, 2006; Heinkelmann *et al.*, 2007; Krügel *et al.*, 2007; Steigenberger *et al.*, 2007) and the development of improved mapping functions (e.g., Niell, 2000; Boehm and Schuh, 2004; Boehm *et al.*, 2006; Tesmer *et al.*, 2007). The construction and maintenance costs of a VLBI base station ensure that its numbers are limited on a global scale. Therefore, it does not provide the spatial coverage as comprehensive as that of GNSS.

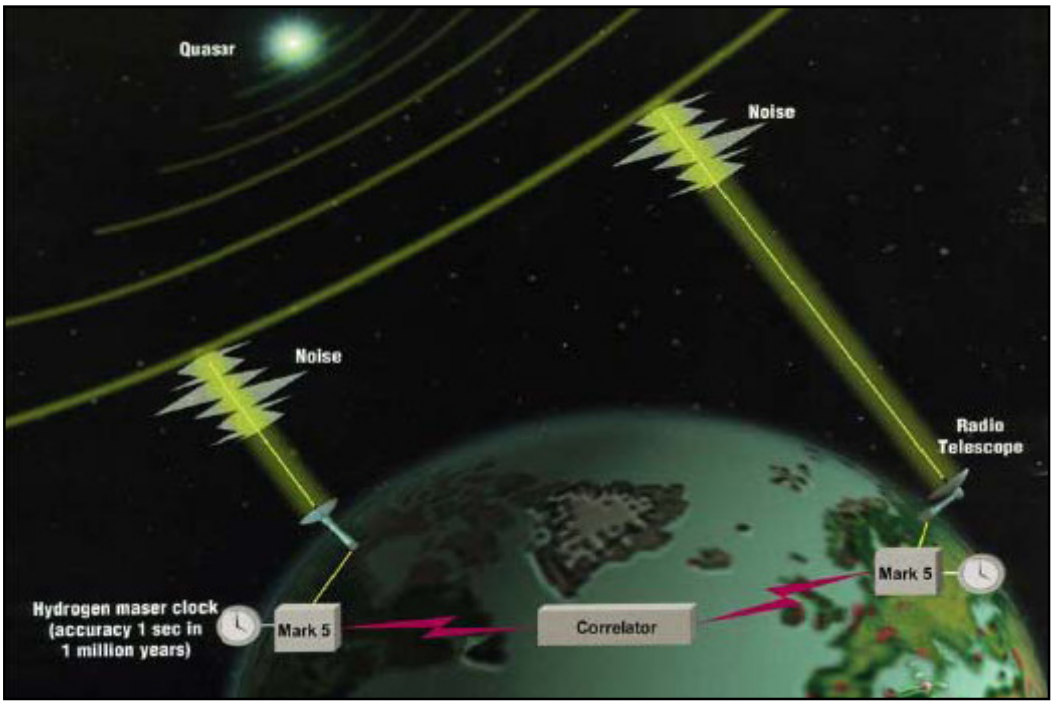

Figure 2.5 A quasar tracked by multiple radio telescopes (http://www.nasa.gov/)

2.6 CHAPTER SUMMARY

Atmospheric WV is a difficult entity to quantify due to its variability and dynamic behaviour. Existing tropospheric models are only able to provide WV estimates to within a few centimetres in accuracy, a level unacceptable in many GPS applications such as precise point positioning and NWP models. Atmospheric sensor such as RS, WVR, RO and VLBI can be used to provide WV estimates at a given station. However, the associated costs of RS (long-term), WVR and VLBI limit the number of these instruments that can be deployed at a given area, and thus, resulting in poor spatial coverage. Although spatial coverage is not an issue with RO, its performance is restricted to the mid and upper troposphere. This is not ideal as majority of the atmospheric WV are found in the lower troposphere (<5 km). On the other hand, GNSS is able to continuously provide 24-h WV estimates virtually anywhere on Earth.

Unlike RS and WVR, the performance of GNSS is also unaffected by heavy cloud cover, precipitation, or moisture on the equipments. The advantages of GNSS over the other WV sensing techniques also include its long-tem stability and relatively low cost. However, GNSS is not a perfect atmospheric sensing tool. In Chapter 3, a detailed discussion on the estimation of the atmospheric WV with GNSS is provided. This chapter will also outline factors that can affect the final GNSS WV solutions.

CHAPTER 3

ZENITH WET DELAY ESTIMATION FROM GNSS

3.0 INTRODUCTION

A GNSS signal propagating from a satellite to a receiver has its journey impeded from the line-of-sight (LoS) path as it enters and passes through the Earth's atmosphere (see Figure 2.1). The retrieved GNSS signal is also affected by other error sources such as satellite and receiver clock errors, ocean tide loading (OTL), atmospheric loading, *a priori* station coordinates, satellite coordinates, multipath, receiver noise, and other equipment errors. The Majority of these errors can be mitigated by differencing techniques. Others can be accounted for by using precise products from International GNSS Service (IGS) or a Continuously Operating Reference Stations (CORS) network. Once these errors are modelled out of the signal, only the variables of interest (generally the coordinates, the ambiguity and/or the tropospheric parameters) remain. These variables can then be estimated with millimetre precision when sufficient observations are available (e.g., Wang *et al.*, 2007).

Recent comparative studies between the RS, WVR and GNSS PWV (derived from ZWD) have shown that a difference of 2.5mm or less can be achieved consistently (e.g., Pottiaux *et al.*, 2003; Mattioli *et al.*, 2005; Wang *et al.*, 2007). However, these studies are generally conducted over mid-latitudes. The mean PWV differences between GNSS and other sensors may reach 4 mm or more over the regions that are closer to the tropics (e.g., Takiguchi *et al.*, 2000; Sapucci *et al.*, 2007).

Unlike WVRs, the performance of GNSS is unaffected by precipitation or cloud cover. Additionally, the satellite constellations ensures that at least four satellites are visible anywhere worldwide and virtually anytime. GNSS can therefore provide continuous 24-hr solutions at any specified time period, an attribute that radiosondes do not possess. The long-term stability of GNSS is also an advantageous attribute that allows it to be used to verify other PWV sensors (e.g., Wang and Zhang, 2008).

In this Chapter, the process for estimating the tropospheric effect with GNSS is outlined. The association between the tropospheric delay and the GNSS observations will be briefly described in Section 3.1. The adjustment methods to process these observations are presented in Section 3.2. The error sources that can impact the final parameter/tropospheric solution are discussed in Section 3.3, along with the methods to minimise their impact. The tropospheric parameter is often expressed in the zenith direction through mapping functions. Section 3.4 will outline a number of mapping functions currently available to help derive the ZTD and reduce any mapping errors. Once estimated, the ZTD can then be used to determine the corresponding ZWDs.

3.1 MODELLING OF THE GNSS OBSERVATIONS

The zero-difference (ZD) GNSS pseudorange (P_{R1}^{i}) and carrier-phase (ϕ_{R1}^{i}) observations from station R1 to satellite *i* are modelled in accordance with the station position, clock offsets, ionosphere, troposphere, and the ambiguity parameters via the following simplified observation equations (e.g., Hofmann-Wellenhof *et al.*, 2001; Leick, 2004):

$$P_{R1}^{i} = \rho_{R1}^{i} + c\left(\delta t_{R1} - \delta t^{i}\right) + I_{R1}^{i} + T_{R1}^{i} + e_{R1}^{i} \tag{3.1}$$

$$\phi_{R1}^{i} = \frac{1}{\lambda}\rho_{R1}^{i} + \frac{c}{\lambda}\left(\delta t_{R1} - \delta t^{i}\right) + N_{R1}^{i} - \frac{1}{\lambda}I_{R1}^{i} + \frac{1}{\lambda}T_{R1}^{i} + e_{A}^{i} \tag{3.2}$$

where ρ_{R1}^{i} is the geometric distance obtained from the satellite position and a approximate receiver position; c is the velocity of light; λ is the wavelength of the carrier frequency L1 or L2; δt_{R1} is the receiver clock error; δt^{i} is the satellite clock error; N_{R1}^{i} is the integer carrier phase ambiguity; I_{R1}^{i} is the ionospheric delay; T_{R1}^{i} is the total tropospheric path delay (TPD) and e_{R1}^{i} represents the errors associated with multipath, satellite orbits and other equipment-related errors.

A single differenced (SD) observation in relative positioning involves the subtraction between two observations with one commonality. The situation generally calls for two GNSS stations, say R1 and R2, tracking the same satellite i at identical epochs of

time. Using the ZD pseudoranges and phase observations defined by Eqs. (3.1) and (3.2), respectively, differencing the observations at R1 and R2 will result in the following SD observation equations (e.g., Leick, 2004):

$$P^{i}_{R1R2} = \rho^{i}_{R1R2} + c\delta t_{R1R2} + I^{i}_{R1R2} + T^{i}_{R1R2} + e^{i}_{R1R2} \tag{3.3}$$

$$\phi^{i}_{R1R2} = \frac{1}{\lambda}\rho^{i}_{R1R2} + \frac{c}{\lambda}\delta t_{R1R2} + N^{i}_{R1R2} - \frac{1}{\lambda}I^{i}_{R1R2} + \frac{1}{\lambda}T^{i}_{R1R2} + e^{i}_{R1R2} \tag{3.4}$$

In the SD scenario, the satellite clock error is removed, and thus, reducing the number of parameters to be estimated. If the baseline of station R1 and station R2 is relatively short as compared to the altitude of the satellite, then the orbital and atmospheric errors are reduced. Another situation where single differencing can be applied is when two or more satellites are simultaneously tracked by one receiver at a particular time t. The receiver clock error, rather than the satellite clock error, will be eliminated in this case.

The double differencing technique is generally applied in GNSS processing as it further reduces errors without sacrificing significant information. The double differencing scenario requires two stations, R1 and R2, and two satellites, i and j. A double differenced (DD) observable can be produced initially generating two SD observations with respect to each of the two satellites and differencing them afterwards, thus resulting in the following DD functional model (e.g., Leick, 2004),

$$P^{ij}_{R1R2} = \rho^{ij}_{R1R2} + I^{ij}_{R1R2} + T^{ij}_{R1R2} + e^{ij}_{R1R2} \tag{3.5}$$

$$\phi^{ij}_{R1R2} = \frac{1}{\lambda}\rho^{ij}_{R1R2} + N^{ij}_{R1R2} - \frac{1}{\lambda}I^{ij}_{R1R2} + \frac{1}{\lambda}T^{ij}_{R1R2} + e^{ij}_{R1R2} \tag{3.6}$$

Both the satellite and receiver clock errors are eliminated from Eqs. (3.5) and (3.6). The ionospheric and tropospheric error terms, as well as satellite-based errors, have been further reduced. Furthermore, the ambiguity term, N^{ij}_{R1R2}, becomes an integer. However, solving the ambiguity term is not a trivial matter. For a relatively short observation window, the highest possible precision in relative positioning can only

be achieved if all the ambiguities of the DD observations are resolved to their integer values (Hofmann-Wellenhof *et al.*, 2001).

However, the gain in baseline precision by resolving the ambiguities becomes smaller when longer window span is used (Teunissen *et al.*, 1997).

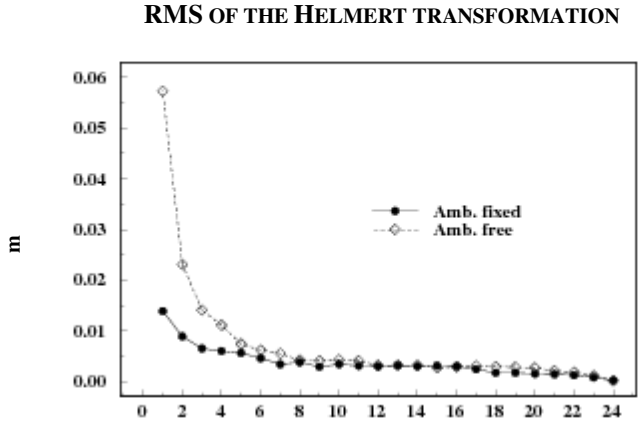

Figure 3.1 RMS of a 7-parameter Helmert transformation with respect to the actual coordinate set (source: Mervart, 1995)

Mervart (1995) investigated the impact of fixing ambiguities on the solved coordinate set with varying window session lengths over a network of 13 stations. Since only one station (Wettzell) was fixed in the analysis, the network solution may be corrupted by rotation errors (Mervart, 1995). Thus, for each session length, the solved coordinate set was transformed to the reference set via the Helmert transformation method. The study has found that there were minimal RMS differences between the positioning solutions of fixed and float ambiguities when the observing window is greater than five hours. The result of the study is illustrated in Figure 3.1. Based on these findings, the real data for the baseline studies, given in Sections 6.3 and 6.4, are processed with float ambiguities.

3.2 ADJUSTMENT MODEL FOR THE ESTIMATION OF ZWD

The functional model for GNSS observations is well known and fairly well defined (e.g., Teunissen and Kleusberg, 1998; Seeber, 2003). To process these observations, adequate adjustment techniques are required to estimate the ZTD/ZWD, the station

coordinates and the integer ambiguity set. The adjustment methods discussed here are the least squares (LS), the sequential least squares (SLS) and Kalman filtering (KF). The LS and SLS adjustment processes are generally applied in static positioning mode whereas KF is often implemented in kinematic positioning.

3.2.1 Least Squares Adjustment

Post-processing of GNSS data is predominantly implemented via the LS principles. Modelling of LS is formulated according to the positioning technique used. For instance in precise point positioning (PPP), suppose at a particular station R1, the satellite clock errors were removed from a set of n ionosphere-free ZD phase signals ϕ via IGS products. A linearised system of ionosphere-free equations can be constructed to represent the relationship between the ZD misclosure vector L, which is a function of ϕ and the *a-priori* parameters X^0, i.e. $L = f(X^0, \phi)$, and the remaining p unknown parameters *X* such that (e.g., Leick, 2004):

$$L = AX + v \tag{3.7}$$

with v being a vector of residuals, and A as the design matrix. Parameterising the total delay (slope) significantly increases the number of unknowns in the observation equations in the manner that will lead to a matrix rank deficiency. Therefore to avoid this problem, the tropospheric parameter T_{R1}^i in matrix A is generally expressed in terms of the ZTD and a mapping function, $m_{R1}(\theta_i)$, such that:

$$T_{R1}^i = m_{R1}(\theta_i) * ZTD \tag{3.8}$$

where θ_i is the elevation angle. A number of mapping functions will be discussed later in Section 3.4. Mapping all LoS delays to the zenith direction will ensure that the system of equations in Eq. (3.7) is not under-determined.

The design matrix A is:

$$A = \begin{bmatrix} \frac{\partial f_1}{\partial x_{R1}} & \frac{\partial f_1}{\partial y_{R1}} & \frac{\partial f_1}{\partial z_{R1}} & \frac{\partial f_1}{\partial t_{R1}} & \frac{\partial f_1}{\partial T_{R1}} & \frac{\partial f_1}{\partial N_{R1}^j (j=1,\cdots n)} \\ \frac{\partial f_2}{\partial x_{R1}} & \frac{\partial f_2}{\partial y_{R1}} & \frac{\partial f_2}{\partial z_{R1}} & \frac{\partial f_2}{\partial t_{R1}} & \frac{\partial f_2}{\partial T_{R1}} & \frac{\partial f_2}{\partial N_{R1}^j (j=1,\cdots n)} \\ \vdots & \vdots & \vdots & \vdots & \vdots & \vdots \\ \frac{\partial f_n}{\partial x_{R1}} & \frac{\partial f_n}{\partial y_{R1}} & \frac{\partial f_n}{\partial z_{R1}} & \frac{\partial f_n}{\partial t_{R1}} & \frac{\partial f_n}{\partial T_{R1}} & \frac{\partial f_n}{\partial N_{R1}^j (j=1,\cdots n)} \end{bmatrix} \tag{3.9}$$

where

$$\frac{\partial f_i}{\partial x_{R1}} = \frac{x^0 - x}{\rho_{R1}^i}, \quad \frac{\partial f_i}{\partial y_{R1}} = \frac{y^0 - y}{\rho_{R1}^i}, \quad \frac{\partial f_i}{\partial z_{R1}} = \frac{z^0 - z}{\rho_{R1}^i}, \quad \frac{\partial f_1}{\partial t_{R1}} = c,$$

$$\frac{\partial f_i}{\partial T_{R1}} = m(\theta_i), \quad \frac{\partial f_n}{\partial N_{R1}^j (j=1,\cdots n)} = 0 \text{ or } 1. \tag{3.10}$$

The corresponding set of unknown parameters to be estimated is:

$$X = \begin{bmatrix} \Delta x \\ \Delta y \\ \Delta z \\ \delta t \\ ZTD \\ N^j (j = 1, \cdots, n) \end{bmatrix} \tag{3.11}$$

When surface pressure and temperature data are available, the ZWD can be the extracted from the estimated ZTD value via Eq. (2.30) by accounting for the ZHD using the Saastamoinen (1973) dry model given by Eq. (2.35). Figure 3.2 illustrates the extraction process.

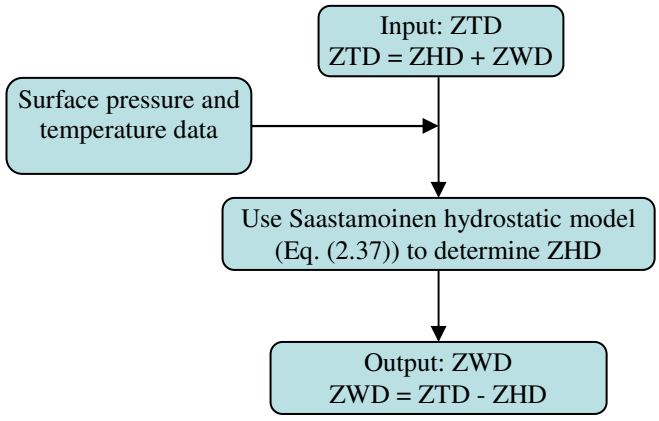

Figure 3.2 Process to determine the ZWD from the ZTD estimates

Apart from the absence of the ambiguity term N^j, the modelling of the design matrix and unknown parameter set for the pseudoranges are identical to that of the phase observations.

In relative positioning, the design matrix differs to that of PPP in that the tropospheric and ambiguity parameters are defined in relative terms. The clock errors are also eliminated in the DD process. The design matrix A for the ionosphere-free DD observations at stations R1 (assumed to be known and is fixed) and R2 can be formulated as:

$$A = \begin{bmatrix} \frac{\partial f_1}{\partial x_{R2}} & \frac{\partial f_1}{\partial y_{R2}} & \frac{\partial f_1}{\partial z_{R2}} & \frac{\partial f_1}{\partial T_{R1R2}} & \frac{\partial f_1}{\partial N_{R1R2}^{n_{amb}}(n_{amb}=1,\cdots,n-1)} \\ \frac{\partial f_2}{\partial x_{R2}} & \frac{\partial f_2}{\partial y_{R2}} & \frac{\partial f_2}{\partial z_{R2}} & \frac{\partial f_2}{\partial T_{R1R2}} & \frac{\partial f_2}{\partial N_{R1R2}^{n_{amb}}(n_{amb}=1,\cdots,n-1)} \\ \vdots & \vdots & \vdots & \vdots & \vdots \\ \frac{\partial f_n}{\partial x_{R2}} & \frac{\partial f_n}{\partial y_{R2}} & \frac{\partial f_n}{\partial z_{R2}} & \frac{\partial f_n}{\partial T_{R1R2}} & \frac{\partial f_n}{\partial N_{R1R2}^{n_{amb}}(n_{amb}=1,\cdots,n-1)} \end{bmatrix} \tag{3.12}$$

where

$$\frac{\partial f_i}{\partial T_{R1R2}} = m_{R1R2}(\theta_i, \theta_j), \ \frac{\partial f_1}{\partial N_{R1R2}^{n_{amb}}(n_{amb}=1,\cdots,n-1)} = 0 \text{ or } 1. \tag{3.13}$$

The vector of unknowns X is:

$$X = \begin{bmatrix} \Delta x_{R2} \\ \Delta y_{R2} \\ \Delta z_{R2} \\ T_{R1R2} \\ N_{R1R2}^{n_{amb}}(n_{amb}=1,..,n-1) \end{bmatrix} \tag{3.14}$$

The differential tropospheric delay parameter of the unknown vector X in Eq. (3.14) between stations R1 and R2 for satellites i and j, can be rewritten as (Collins and Langley, 1997):

$$T_{R1R2}^{ij} = T_{R2}^{j} - T_{R2}^{i} - T_{R1}^{j} + T_{R1}^{i} \tag{3.15}$$

Substituting Eq. (3.8) into Eq. (3.15) results in (Zhang and Lachapelle, 2001):

$$\begin{aligned} T_{R1R2}^{ij} &= ZTD_{R2}\left(m_{R2}^{j} - m_{R2}^{i}\right) - ZTD_{R1}\left(m_{R1}^{j} - m_{R1}^{i}\right) \\ &= ZTD_{R2} * \Delta m_{R2} - ZTD_{R1} * \Delta m_{R1} \end{aligned} \tag{3.16}$$

The design matrix A and the vector of unknowns X are, respectively, given by:

$$A = \begin{bmatrix} \frac{\partial f_1}{\partial x_{R2}} & \frac{\partial f_1}{\partial y_{R2}} & \frac{\partial f_1}{\partial z_{R2}} & -\left(m_{R1}^{j_1} - m_{R1}^{i_1}\right) & -\left(m_{R2}^{j_1} - m_{R2}^{i_1}\right) & \frac{\partial f_1}{\partial N_{R1R2}^{n_{amb}}\left(n_{amb}=1,\cdots,n-1\right)} \\ \frac{\partial f_2}{\partial x_{R2}} & \frac{\partial f_2}{\partial y_{R2}} & \frac{\partial f_2}{\partial z_{R2}} & -\left(m_{R1}^{j_2} - m_{R1}^{i_2}\right) & -\left(m_{R2}^{j_2} - m_{R2}^{i_2}\right) & \frac{\partial f_2}{\partial N_{R1R2}^{n_{amb}}\left(n_{amb}=1,\cdots,n-1\right)} \\ \vdots & \vdots & \vdots & \vdots & \vdots & \vdots \\ \frac{\partial f_n}{\partial x_{R2}} & \frac{\partial f_n}{\partial y_{R2}} & \frac{\partial f_n}{\partial z_{R2}} & -\left(m_{R1}^{j_n} - m_{R1}^{i_n}\right) & -\left(m_{R2}^{j_n} - m_{R2}^{i_n}\right) & \frac{\partial f_n}{\partial N_{R1R2}^{n_{amb}}\left(n_{amb}=1,\cdots,n-1\right)} \end{bmatrix} \tag{3.17}$$

and

$$X = \left[\Delta x \;\; \Delta y \;\; \Delta z \;\; ZTD_{R1} \;\; ZTD_{R2} \;\; N_{R1R2}^{n_{amb}}\left(n_{amb}=1,..,n-1\right)\right]^{T} \tag{3.18}$$

By redefining the differential tropospheric estimate in this manner, the absolute ZTD at stations R1 and at station R2 can be estimated separately using the LS approach. Once the GNSS-estimated zenith tropospheric delay is obtained, it can then be used to determine ZWD (see Figure 3.2), and consequently the PWV via Eq. (2.31).

The LS problem for Eq. (3.7), with a *a-priori* observation weight matrix W, is given by:

$$A^{T}WL = \left(A^{T}WA\right)X \tag{3.19}$$

Eq. (3.19) is often referred to as a system of normal equation (NEQ). For the quantity $A^{T}WA$ in Eq. (3.19), if the weight matrix W is a diagonal matrix, that is,

$$W = \begin{bmatrix} w_{11} & 0 & \cdots & 0 \\ 0 & w_{22} & \ddots & \vdots \\ \vdots & \ddots & \ddots & 0 \\ 0 & \cdots & 0 & w_{nn} \end{bmatrix} \tag{3.20}$$

then $A^T WA$ can be represented as

$$A^T WA = \begin{bmatrix} \sum_{i=1}^{n} a_{i1}^2 w_{ii} & \sum_{i=1}^{n} a_{i1} a_{i2} w_{ii} & \cdots & \sum_{i=1}^{n} a_{i1} a_{ik} w_{ii} \\ \sum_{i=1}^{n} a_{i1} a_{i2} w_{ii} & \sum_{i=1}^{n} a_{i2}^2 w_{ii} & \cdots & \sum_{i=1}^{n} a_{i2} a_{ik} w_{ii} \\ \vdots & \vdots & \ddots & \vdots \\ \sum_{i=1}^{n} a_{i1} a_{ik} w_{ii} & \sum_{i=1}^{n} a_{i2} a_{ik} w_{ii} & \cdots & \sum_{i=1}^{n} a_{ik}^2 w_{ii} \end{bmatrix} \tag{3.21}$$

where a_{ij} is the element of the design matrix A at row i and column j. Each diagonal entry j (for $j = 1, 2, .., k$) of the $A^T WA$ in (3.21) can be viewed as the sum of squares (SSQ) of the elements of column j of design matrix A, whilst each off-diagonal entry (i, j) is the sum of the cross-products (SCP) between the elements of column i and column j (for $i \neq j,$) of A (Walpole *et al.*, 2007). SSQ can also be regarded as the SCP between the two identical columns, i.e. ($SSQ_i = SCP_{ii}$).

If the weight matrix is a non-diagonal matrix, i.e.,

$$W = \begin{bmatrix} w_{11} & w_{12} & \cdots & w_{1n} \\ w_{12} & w_{22} & \ddots & \vdots \\ \vdots & \ddots & \ddots & w_{(n-1)n} \\ w_{1n} & \cdots & w_{(n-1)n} & w_{nn} \end{bmatrix} \tag{3.22}$$

$A^T WA$ becomes

$$A^T WA = \begin{bmatrix} \sum_{i=1}^{n}\sum_{j=1}^{n} a_{i1}a_{j1}w_{ij} & \sum_{i=1}^{n}\sum_{j=1}^{n} a_{i1}a_{j2}w_{ij} & \cdots & \sum_{i=1}^{n}\sum_{j=1}^{n} a_{i1}a_{jk}w_{ij} \\ \sum_{i=1}^{n}\sum_{j=1}^{n} a_{i1}a_{j2}w_{ij} & \sum_{i=1}^{n}\sum_{j=1}^{n} a_{i2}a_{j2}w_{ij} & \cdots & \sum_{i=1}^{n}\sum_{j=1}^{n} a_{i2}a_{jk}w_{ij} \\ \vdots & \vdots & \ddots & \vdots \\ \sum_{i=1}^{n}\sum_{j=1}^{n} a_{i1}a_{jk}w_{ij} & \sum_{i=1}^{n}\sum_{j=1}^{n} a_{i2}a_{jk}w_{ij} & \cdots & \sum_{i=1}^{n}\sum_{j=1}^{n} a_{ik}a_{jk}w_{ij} \end{bmatrix} \tag{3.23}$$

$$= \begin{bmatrix} SCP_{11} & SCP_{12} & \cdots & SCP_{1k} \\ SCP_{12} & SCP_{22} & \cdots & SCP_{2k} \\ \vdots & \vdots & \ddots & \vdots \\ SCP_{1k} & SCP_{2k} & \cdots & SCP_{kk} \end{bmatrix} \tag{3.24}$$

The solution for Eq. (3.19) is then:

$$\hat{X} = \left(A^T WA\right)^{-1} A^T WL = Q_{\hat{X}} A^T WL \tag{3.25}$$

Therefore, the final solution in relation to the *a-priori* parameters X^0 is given by vector X is such that:

$$X = X^0 + \hat{X} \tag{3.26}$$

The *a-posteriori* variance-covariance (VCV) of the estimated parameters $\hat{X}$ is:

$$\sum_{\hat{X}} = \hat{\sigma}_0^2 \left(A^T WA\right)^{-1} \tag{3.27}$$

where,

$$\hat{\sigma}_0^2 = \frac{v^T Wv}{n-p}, \text{ and} \tag{3.28}$$

$$v = L - A\hat{X} \tag{3.29}$$

The quantity $\hat{\sigma}_0^2$, often referred to as the a-*posterior* unit variance or variance factor, is an unbiased estimate of σ^2 and is an indicator of the accuracy of the observations in the LS adjustment process. The formal errors of Eq. (3.27) are generally too optimistic, depending on the data sampling and the complexity of the error modelling

used in defining the weight matrix W (e.g., Kouba, 2009). Therefore, the precision of the parameter estimates are often defined by the square root of the variance parameters given in Eq. (3.27), i.e. the standard deviation, multiplied by a factor k. If the normal distribution is assumed for the parameter estimates, k is often given a value of three as it represents 99.7% probability that true estimate for each individual unknown X_i is within $\pm k * \text{stdev}(\hat{X}_i)$. That is,

$$\text{Prob}\left(-k*\text{stdev}(\hat{X}_i) < X_i < k*\text{stdev}(\hat{X}_i)\right) = 1-\alpha \tag{3.30}$$

where α is the probability that $|X| > k * \sqrt{\text{var}(\hat{X}_i)}$.

If the station coordinates are known beforehand in both the PPP and relative positioning cases, then the matrix A and vector X, respectively, simplify to:

$$A = \begin{bmatrix} \frac{\partial f_1}{\partial t_{R1}} & \frac{\partial f_1}{\partial T_{R1}} & \frac{\partial f_1}{\partial N^j_{R1}(j=1,\cdots n)} \\ \frac{\partial f_2}{\partial t_{R1}} & \frac{\partial f_2}{\partial T_{R1}} & \frac{\partial f_2}{\partial N^j_{R1}(j=1,\cdots n)} \\ \vdots & \vdots & \vdots \\ \frac{\partial f_n}{\partial t_{R1}} & \frac{\partial f_n}{\partial T_{R1}} & \frac{\partial f_n}{\partial N^j_{R1}(j=1,\cdots n)} \end{bmatrix}; \quad X = \begin{bmatrix} \delta t \\ ZTD \\ N^j(j=1,\cdots,n) \end{bmatrix} \tag{3.31}$$

and

$$A = \begin{bmatrix} \frac{\partial f_1}{\partial T_{R1R2}} & \frac{\partial f_1}{\partial N^{n_{amb}}_{R1R2}(n_{amb}=1,\cdots,n-1)} \\ \frac{\partial f_2}{\partial T_{R1R2}} & \frac{\partial f_2}{\partial N^{n_{amb}}_{R1R2}(n_{amb}=1,\cdots,n-1)} \\ \vdots & \vdots \\ \frac{\partial f_n}{\partial T_{R1R2}} & \frac{\partial f_n}{\partial N^{n_{amb}}_{R1R2}(n_{amb}=1,\cdots,n-1)} \end{bmatrix}; \quad X = \begin{bmatrix} T_{R1R2} \\ N^{n_{amb}}_{R1R2}(n_{amb}=1,..,n-1) \end{bmatrix} \tag{3.32}$$

The LS solutions to these systems of equations are as given by Eq. (3.25). The LS approach, outlined above can be seen as a special case of filtering in static mode.

3.2.2 Sequential Least Squares

Over successive observation epochs, consider n_e number of sequential observation equation systems given by:

$$L_1 = A_1X + v_1,\ L_2 = A_2X + v_2,\ \ldots,\ L_{n_e} = A_{n_e}X + v_{n_e} \tag{3.33}$$

with weight matrices $W_1, W_2, \ldots, W_{n_e}$ respectively. The systems have a common unknown vector X. In GNSS processing, these systems are often assumed to be uncorrelated. In this instance, the batch solution to the equation systems, given by

$$\hat{X} = \left(A_1^T W_1 A_1 + \cdots + A_{n_e}^T W_{n_e} A_{n_e}\right)^{-1}\left(A_1^T W_1 L_1 + \cdots + A_{n_e}^T W_{n_e} L_{n_e}\right) \tag{3.34}$$

with

$$\begin{aligned} v^T W v &= v_1^T W_1 v_1 + \cdots + v_{n_e}^T W_{n_e} v_{n_e} \\ &= \left(L_1^T W_1 L_1 + \cdots + L_{n_e}^T W_{n_e} L_{n_e}\right) - \left(A_1^T W_1 L_1 + \cdots + A_{n_e}^T W_{n_e} L_{n_e}\right)\hat{X} \end{aligned} \tag{3.35}$$

Using the formula (Gotthardt, 1978; Cui *et al.*, 1982)

$$\left(E + BCD\right)^{-1} = E^{-1} - E^{-1}BFDE^{-1} \tag{3.36}$$

where B and D are any matrices, C and E are any invertible matrices, and

$$F = \left(C^{-1} + DE^{-1}B\right)^{-1} \tag{3.37}$$

the inverse of the accumulated normal matrices in Eq. (3.34) can be represented as $\tilde{Q}$ such that (Xu, 2003):

$$\tilde{Q} = \left(I - Q^*_{n_e-1} A_{n_e}^T \tilde{K} A_{n_e}\right) Q^*_{n_e-1} \tag{3.38}$$

with

$$Q^*_{n-1} = \left(\sum_{i=1}^{n_e-1} A_i^T W_i A_i\right)^{-1} \tag{3.39}$$

and

$$\tilde{K} = \left(W_{n_e}^{-1} + A_{n_e} Q_{n_e-1}^{*} A_{n_e}^{T}\right)^{-1} \tag{3.40}$$

where I is an identity matrix. Then the batch solution in Eq. (3.34) can be rewritten in terms of Q_{n-1}^{*}, which is the cofactor matrix of the previous $(n_e - 1)$ epochs of observations, and its corresponding estimated solution $\hat{X}_{n_e-1}$ such that (Xu, 2003):

$$\hat{X} = \left(I - Q_{n_e-1}^{*} A_{n_e}^{T} \tilde{K} A_{n_e}\right) \hat{X}_{n_e-1} + \tilde{Q}\left(A_{n_e}^{T} W_{n_e} A_{n_e}\right) \tag{3.41}$$

Eq. (3.41) is known as the SLS solution. The SLS method is often used in GNSS positioning as it reduces to the storage capacity required for a standard LS approach.

3.2.3 Kalman Filtering

Kalman filtering (KF) is a technique that allows the state vector of a moving object, which is characterized by its non-stationary position and velocity, to be computed as a function of time. A Kalman filter is, in a sense, a general form of the SLS adjustment with time updates of the state vector and its VCV matrix (Hofmann-Wellenhof *et al.*, 2001). KF is often applied in real-time GNSS applications such as navigation.

Suppose for the initial epoch t_0, the state vector $X(t_0) = X_0$, which includes the ZWD, and its cofactor matrix Q_{X_0} (see Eq. (3.29)) are assumed to be known. The state transition matrix that relates two consecutive state vectors reads (Xu, 2003):

$$X_i = \Phi_{i,i-1} X_{i-1} + u_i, \quad \text{for } i = 1, 2, \ldots \tag{3.42}$$

$\Phi_{i,i-1}$ is known as the transition matrix. The system noise u_i is assumed to follow a normal distribution with zero mean and a known VCV matrix, Q_u. Using the covariance propagation law, the cofactor matrix for the state vector in Eq. (3.42) is given by (Xu, 2003):

$$Q_{X_i} = \Phi_{i,i-1} Q_{X_{i-1}} \Phi_{i,i-1}^T + Q_u \tag{3.43}$$

Eqs. (3.42) and (3.43) are called the predicted values for the state vector at epoch t_i. By applying the SLS principle to correct for the predicted values, the estimated values of the ZWD, along with the other parameters of the state vector, in this epoch can be calculated by:

$$\hat{X}_i = X_i + K\left(L_i - A_i X_i\right) \tag{3.44}$$

$$\hat{Q}_i = \left(I - KA_i\right) Q_i \tag{3.45}$$

where

$$K = Q_i A_i^T \left(A_i Q_i A_i^T + Q_{v_i}\right)^{-1} \tag{3.46}$$

where I is the identity matrix; A_i and L_i are the design matrix and misclosure vector at epoch t_i; Q_{v_i} is the corresponding cofactor (covariance for the unit weight) matrix of residuals v_i (resulting from the SLS principle), which is often defined as W^{-1}. The KF outlined above is of the classical case. There are several other more refined versions of the KF, such as the extended KF, the robust KF and the adaptively robust KF (e.g., Wang, 2000; Geng and Wang, 2008). Interested readers are referred to Hofmann-Wellenhof *et al.*, (2003), Xu (2003), Leick (2004) and other relevant texts for more details.

In static positioning, the positional state vector, X_i does not change with time, i.e. $X_i = X_{i-1}$, which implies that $\Phi_{i,i-1} = I$ in Eq. (3.42) and also, Q_u is assumed to be zero. This also means that the solutions of the KF will be identical to that of SLS. However, the ZWD estimates will vary with time due to the fluctuations of the water vapour in the atmosphere. In this instance, an appropriate representation of the transition between adjacent ZWD measurements of sampling interval Δt is needed.

3.2.3.1 Random Walk Model

A random walk (RW) model (e.g. Xu, 2003) defines a random process whereby the value of the current variable, say X_i is composed of the past variable X_{i-1} plus an

error term defined as a white noise ε_i with zero mean and unit variance. Mathematically, a RW model is given by:

$$X_i = X_{i-1} + \varepsilon_i \tag{3.47}$$

The associated variance of the RW process noise ε_i is:

$$E(\varepsilon_i^2) = \sigma^2 \Delta t^2 \tag{3.48}$$

where σ^2 is the variance of the RW process.

3.2.3.2 First-Order Gauss Markov Model

Assuming that the correlations among the GNSS observations decays smoothly with time, the first-order Gauss Markov (GM) model (e.g. Xu, 2003) can be called upon to describe the temporal dependence of the adjacent GNSS measurements, such that the dynamic model of the state vector is:

$$X_i = e^{\frac{-1}{\tau_{GM}}\Delta t} X_{i-1} + u_i \tag{3.49}$$

where τ_{GM} is the correlation time of the GM model, and u_i is a white noise with zero mean and covariance Q_u. The value for τ_{GM} can be directly estimated from the GM autocorrelation function:

$$\rho(\Delta t) = e^{\frac{-1}{\tau_{GM}}\Delta t} \tag{3.50}$$

given at the $\rho = 1/e$ point where $\tau_{GM} = \Delta t$. Figure 3.3 illustrates the behaviour of the GM autocorrelation function given by Eq. (3.50), for $\tau_{GM} = 1$-h (curve) and $\tau_{GM} = 2$-h (broken curve).

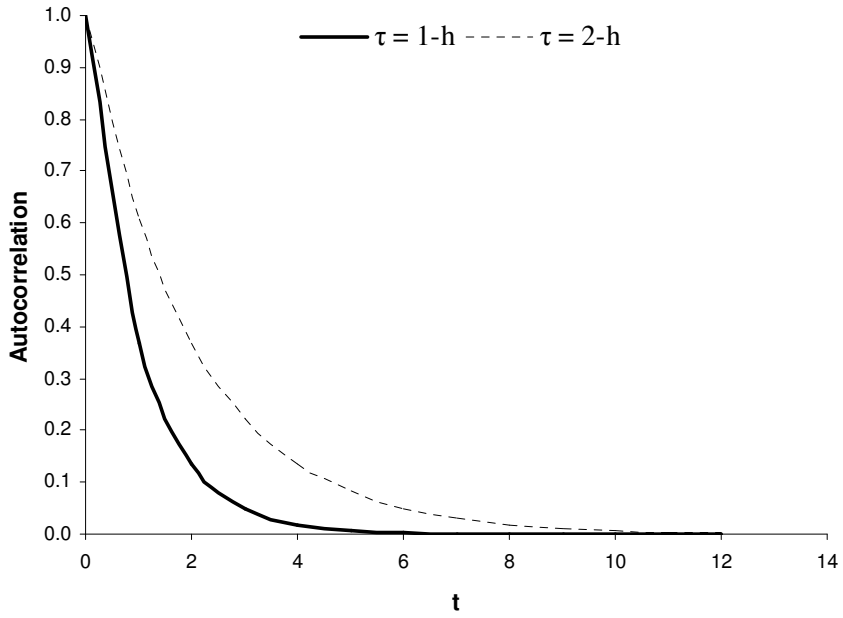

Figure 3.3 Autocorrelation function of the Gauss-Markov process

Without loss of generality, suppose that the positional solutions are known and are fixed or tightly constrained, and that the remaining parameters, i.e. ambiguities, clock errors and etc., are also estimated or modelled out of the observation equation beforehand. In addition, the ZHD is determined via the Saastamoinen hydrostatic model and subtracted from the ZTD parameter prior to the estimation process. Therefore, the estimated tropospheric parameter is that of the ZWD component, and the GM model in Eq. (3.49) can then be expressed as:

$$ZWD_i = e^{\frac{-1}{\tau_{GM}}\Delta t} ZWD_{i-1} + u_i \tag{3.51}$$

The associated variance of the GM process noise, u_i, can be derived by firstly rearranging Eq. (3.51) to give:

$$u_i = ZWD_i - e^{\frac{-1}{\tau_{GM}}\Delta t} ZWD_{i-1} \tag{3.52}$$

Then by squaring and taking the expectation of both sides of Eq. (3.52), this results in:

$$
\begin{aligned}
E\left(u_i^2\right) &= E\left[\left(ZWD_i - e^{\frac{-1}{\tau_{GM}}\Delta t} ZWD_{i-1}\right)^2\right] \\
&= E\left[ZWD_i^2 - 2e^{\frac{-1}{\tau_{GM}}\Delta t} ZWD_i ZWD_{i-1} + e^{\frac{-2}{\tau_{GM}}\Delta t} ZWD_{i-1}^2\right] \\
&= E\left[ZWD_i^2 - 2e^{\frac{-1}{\tau_{GM}}\Delta t}\left(e^{\frac{-1}{\tau_{GM}}\Delta t} ZWD_{i-1}\right) ZWD_{i-1} + e^{\frac{-2}{\tau_{GM}}\Delta t} ZWD_{i-1}^2\right] \\
&= E\left[ZWD_i^2 - 2e^{\frac{-1}{\tau_{GM}}\Delta t}\left(e^{\frac{-1}{\tau_{GM}}\Delta t} ZWD_{i-1}\right) ZWD_{i-1} + e^{\frac{-2}{\tau_{GM}}\Delta t} ZWD_{i-1}^2\right] \\
&= E\left[ZWD_i^2 - e^{\frac{-2}{\tau_{GM}}\Delta t} ZWD_{i-1}^2\right] \\
&= E\left[ZWD_i^2\right] - e^{\frac{-2}{\tau_{GM}}\Delta t} E\left[ZWD_{i-1}^2\right] \\
&= \sigma_{GM}^2 - e^{\frac{-2}{\tau_{GM}}\Delta t} \sigma_{GM}^2 \\
&= \sigma_{GM}^2\left(1 - e^{\frac{-2}{\tau_{GM}}\Delta t}\right)
\end{aligned}
\tag{3.53}
$$

where σ_{GM}^2 is the steady-state variance of the GM process.

In practice, a single value for the ZWD parameter is generally estimated for a 1-h or 2-h interval (Kouba, 2009). This is due to the fact that the ZWDs generally do not vary significantly from their mean value during these short time intervals. In other words, the ZWD data behaves like a stationary process (Wei, 2006). As an example, Figure 3.4 provides an illustration of the ZWD variation around its mean for a 2-h period. The ZWD data in this figure is estimated from WVR at the Onsala station on the 10th of September in 2003.

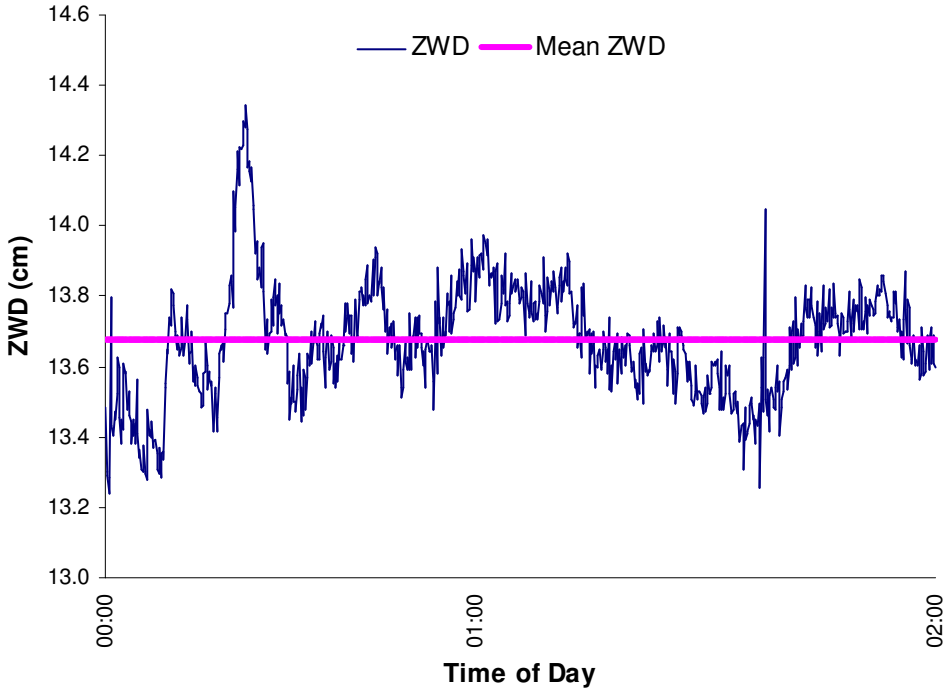

Figure 3.4 A plot of the WVR ZWD data at the Onsala station in a 2-h period on 10 Sept 2003.

By assuming a constant mean, $\overline{\mathrm{ZWD}}$, over a short time-period, the ZWD component can be given as:

$$\mathrm{ZWD} = \overline{\mathrm{ZWD}} + \Delta\mathrm{ZWD} \tag{3.54}$$

The mean parameter $\overline{\mathrm{ZWD}}$ in Eq. (3.54) can be estimated via empirical wet delay models. However, a more rigorous approach would be to estimate $\overline{\mathrm{ZWD}}$ along with $\Delta\mathrm{ZWD}$ in the Kalman filtering process. In this manner, the GM model given by Eq. (3.51) can then be expressed as:

$$\begin{aligned} \mathrm{ZWD}_i &= \overline{\mathrm{ZWD}} + e^{\frac{-1}{\tau_{GM}}\Delta t}\,\Delta\mathrm{ZWD}_{i-1} + \tilde{u}_i \\ &= \overline{\mathrm{ZWD}} + \Phi_{i,i-1}\Delta\mathrm{ZWD}_{i-1} + \tilde{u}_i \end{aligned} \tag{3.55}$$

where $\tilde{u}_i$ is a white noise with zero mean and variance $Q_{\tilde{u}}$. The associated variance $Q_{\tilde{u}}$ for ΔZWD is identical to that given by Eq. (3.53).

3.2.3.3 A New Autocorrelation Model

The GM autocorrelation function given by Eq. (3.52) is dependent on the empirical value given to the correlation time τ_{GM}, which in turn, is determined by a specific point in time t where significant ZWD autocorrelation is observed. For instance, from Figures 7.1 to 7.6, τ can be determined by finding the intersection between the autocorrelation trend line and the confidence interval (broken red line). However, the dependence of τ_{GM} on a single observation at a specific time t may result in an autocorrelation function that does not reflect the true autocorrelations among all the ZWD observations. In other words, the transition of the ZWD from times t_{i-1} to t_i may not be adequately represented by a GM process. Therefore, an alternative autocorrelation function is proposed in this study.

A set of *n* autocorrelation estimates for the *a-priori* ZWD data set can be determined by the following standard autocorrelation formula (e.g., Walpole *et al*., 2007):

$$\rho(\Delta t) = \frac{\hat{Z}(\Delta t)}{\hat{Z}(0)} \tag{3.56}$$

with

$$\hat{Z}(\Delta t) = \frac{1}{n}\sum_{i=1}^{n-\Delta t}\left(ZWD(t) - \overline{ZWD}\right)\left(ZWD(t+\Delta t) - \overline{ZWD}\right) \tag{3.57}$$

where $\overline{ZWD}$ is the empirical mean.

The motivation for the GM is that in a typical situation, one expects that the correlation function $\rho(\Delta t)$ in Eq. (3.56) asymptotically exhibits an exponential behaviour for large lag Δt (Brandt, 1999). That is, $\rho(\Delta t) \sim \exp\left(-\frac{\Delta t}{\tau_{GM}}\right)$. However, it will be shown later on in Figures 3.5 to 3.8 that autocorrelation values determined from the GM model deviates or decays too rapidly as compared to the actual autocorrelation values from Eq. (3.56). Hence in this thesis, an autocorrelation

function was proposed. The hyperbolic function $f(\Delta t)=\frac{1}{\Delta t}$, which also deviates (but not as rapidly) to zero for large positive lag Δt, is the motivation for the proposed autocorrelation model. The hyperbolic function was then divided by the correlation time τ so that it becomes a unit-less measure. A shift was then applied to ensure that the function value is one at zero time lag, i.e. $\Delta t = 0$. A power component is then introduced to the function to control the decaying rate of the hyperbolic function. It will be shown later the proposed autocorrelation model provides a better fit to the autocorrelation model given by Eq. (3.56). The proposed autocorrelation function between the ZWDs at epochs i and i-k, i.e. a lag $\Delta t = k$, is given by:

$$\text{Correlation}\left(ZWD_i, ZWD_{i-k}\right)=\rho(\Delta t)=\frac{1}{\left(\frac{\Delta t}{\tau_{PM}}+1\right)^{\left(\frac{\Delta t}{\tau_{PM}}\beta\right)}} \tag{3.58}$$

where τ_{PM} is the correlation time of the proposed model, and the parameter β is to be determined.

Taking the natural logarithm of both sides of Eq. (3.58) results in the linearised form:

$$\ln(\rho)=\left[-\left(\frac{\Delta t}{\tau_{PM}}\right)\times\ln\left(\frac{\Delta t}{\tau_{PM}}+1\right)\right]\beta \tag{3.59}$$

Therefore, an estimate for β, i.e. $\hat{\beta}$, can then be calculated by performing LS analysis on the first two autocorrelation values, generated by Eqs. (3.56) and (3.57), using the linear relationship defined by Eq. (3.59). As it will be shown in Chapter 7 that the tropospheric estimates are correlated for at most 2 h, it is necessary to ensure that the proposed model is able to follow the autocorrelation trend within a 2-h period. Hence, a LS estimates for β is achieved with the first two autocorrelation values (assuming that the lag Δt in measured in hours). Once $\hat{\beta}$ has been determined, the proposed model given by Eq. (3.58) is then fully defined.

Figures 3.5 to 3.8 demonstrate the capability of the proposed model in following the trend of the estimated PWV autocorrelations, which were calculated via Eq. (3.56). The plots are given at four different locations (Alice Springs, Broome, Burnie and Ceduna) across Australia. The GM model is also included in these figures for comparison purposes. For the GM model, the value of τ_{GM} is determined at a time lag t (in hours) where statistically significant autocorrelation is observed using the Ljung-Box Q statistic (Ljung and Box, 1978). For the proposed model, $\tau_{PM} = \tau_{GM}$.

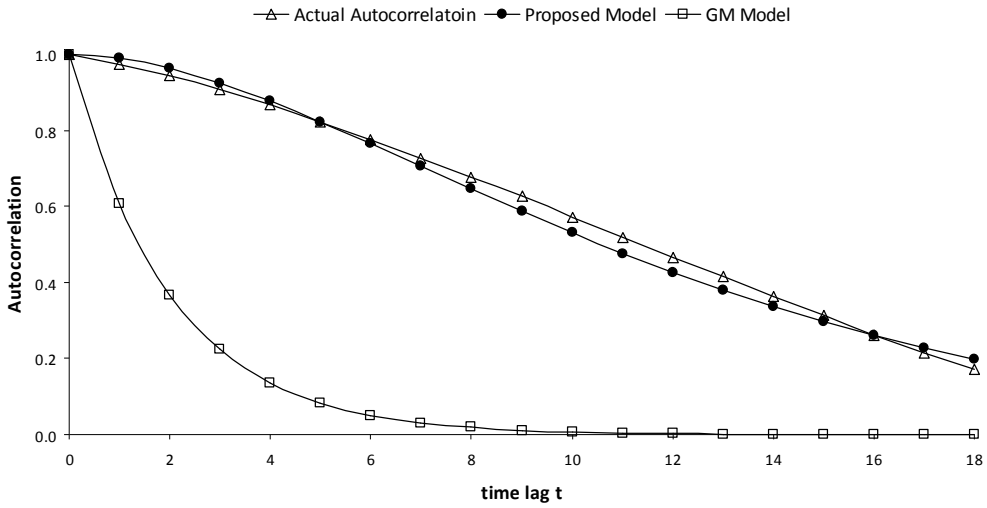

Figure 3.5 Comparison between the performances of the proposed model (solid circles) and the GM model (squares) in estimating the estimated PWV autocorrelations (triangles) at Alice Springs in Northern Territory

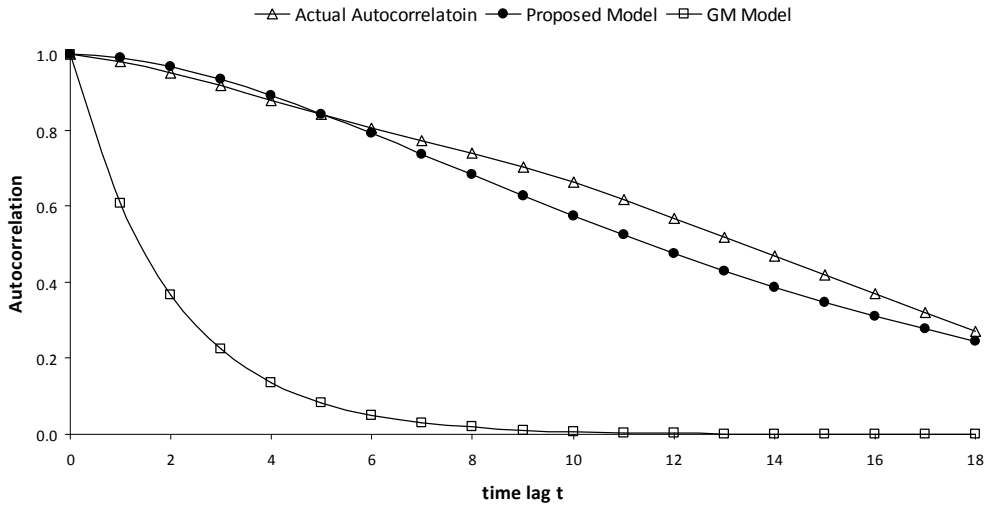

Figure 3.6 Comparison between the performances of the proposed model (solid circles) and the GM model (squares) in estimating the estimated PWV autocorrelations (triangles) at Broome in Western Australia

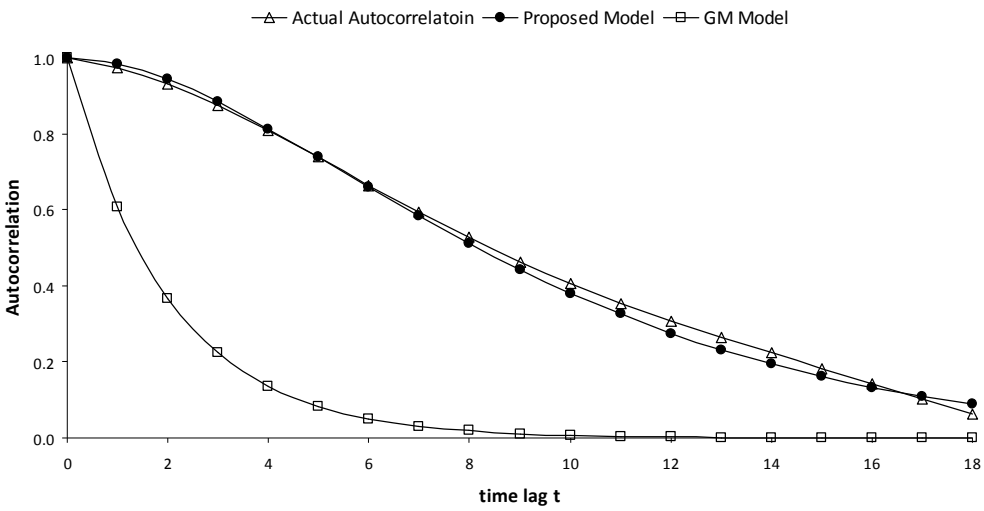

Figure 3.7 Comparison between the performances of the proposed model (solid circles) and the GM model (squares) in estimating the estimated PWV autocorrelations (triangles) at Burnie in Tasmania.

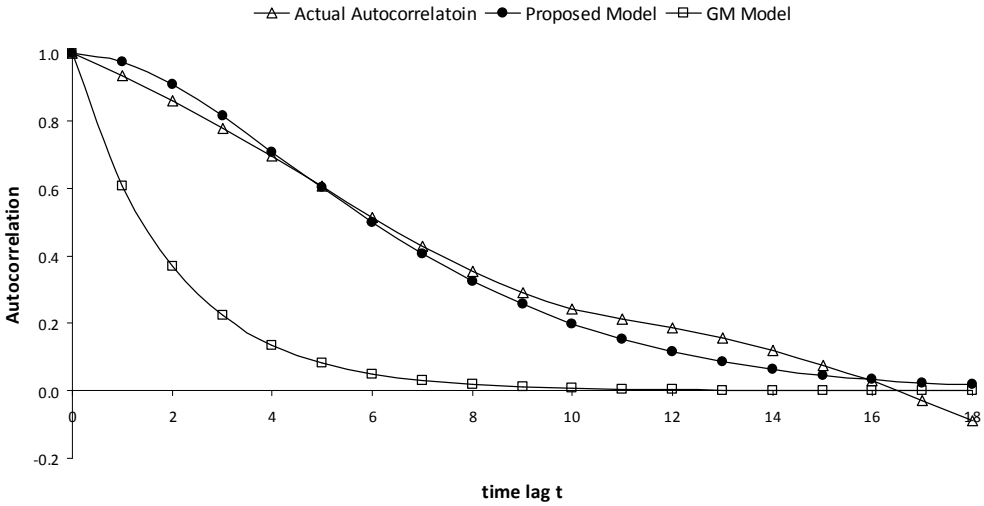

Figure 3.8 Comparison between the performances of the proposed model (solid circles) and the GM model (squares) in estimating the estimated PWV autocorrelations (triangles) at Ceduna in South Australia

From Figures 3.5 to 3.8, it can be seen that the GM function did not adequately represent the actual PWV autocorrelations. In fact, the GM function consistently over-estimates the rate at which the PWV autocorrelation values decreases. Conversely, the proposed model, given by Eq. (3.58) is able to provide autocorrelation values that closely follow the actual autocorrelation values for a significant length of time.

For the proposed autocorrelation model, the state vector of the ZWD at time t_i can be represented by:

$$ZWD_i = \frac{1}{\left(\frac{\Delta t}{\tau_{PM}}+1\right)^{\left(\frac{\Delta t}{\tau_{PM}}\beta\right)}} \times ZWD_{i-1} + u_i \tag{3.60}$$

To determine the variance of the process noise Q_u, the quantity u_i in Eq. (3.60) is once again isolated. Then taking the expectation of its square gives:

$$E\left(u_i^2\right) = E\left[\left(ZWD_i - \frac{1}{\left(\frac{\Delta t}{\tau_{PM}}+1\right)^{\left(\frac{\Delta t}{\tau_{PM}}\beta\right)}} \times ZWD_{i-1}\right)^2\right]$$

$$= E\left[\left(ZWD_i^2 - \frac{2}{\left(\frac{\Delta t}{\tau_{PM}}+1\right)^{\left(\frac{\Delta t}{\tau_{PM}}\beta\right)}} ZWD_i ZWD_{i-1} + \frac{1}{\left(\frac{\Delta t}{\tau_{PM}}+1\right)^{\left(\frac{\Delta t}{\tau_{PM}}\beta\right)}} ZWD_{i-1}^2\right)\right]$$

$$= E\left[\left(ZWD_i^2 - \left(\frac{2}{\left(\frac{\Delta t}{\tau_{PM}}+1\right)^{\left(\frac{\Delta t}{\tau_{PM}}\beta\right)}}\right)\left(\frac{1}{\left(\frac{\Delta t}{\tau_{PM}}+1\right)^{\left(\frac{\Delta t}{\tau_{PM}}\beta\right)}}\right) ZWD_{i-1}^2 + \frac{1}{\left(\frac{\Delta t}{\tau_{PM}}+1\right)^{\left(\frac{2\Delta t}{\tau_{PM}}\beta\right)}} ZWD_{i-1}^2\right)\right]$$

$$= E\left[\left(ZWD_i^2 - \left(\frac{2}{\left(\frac{\Delta t}{\tau_{PM}}+1\right)^{\left(\frac{\Delta t}{\tau_{PM}}\beta\right)}}\right) ZWD_{i-1}^2 + \frac{1}{\left(\frac{\Delta t}{\tau_{PM}}+1\right)^{\left(\frac{2\Delta t}{\tau_{PM}}\beta\right)}} ZWD_{i-1}^2\right)\right]$$

$$= E\left[\left(ZWD_i^2 - \left(\frac{1}{\left(\frac{\Delta t}{\tau_{PM}}+1\right)^{\left(\frac{2\Delta t}{\tau_{PM}}\beta\right)}}\right) ZWD_{i-1}^2\right)\right]$$

$$= \sigma^2 - \left(\frac{1}{\left(\frac{\Delta t}{\tau_{PM}} + 1 \right)^{\left(\frac{2\Delta t}{\tau_{PM}} \beta \right)}} \right) \sigma^2$$

$$= \sigma^2 \left[1 - \left(\frac{1}{\left(\frac{\Delta t}{\tau_{PM}} + 1 \right)^{\left(\frac{2\Delta t}{\tau_{PM}} \beta \right)}} \right) \right] \tag{3.61}$$

where σ^2 is the variance of the process.

The ZWD state vector, given in Eq. (3.60), can also be represented in the form described in Eq. (3.55). In this thesis, the performances of the RW and GM models, and the proposed model will only be assessed in the Kalman filtering process in PPP mode. The results are given Section 6.5.

3.3 ERROR SOURCES AFFECTING GNSS PARAMETER ESTIMATION

In the PPP approach, the estimation of the ZWD and other unknowns can be negatively affected by unmodelled errors sources. Many of the residual errors have small values. However, since the ZWD values are comparatively small, ignoring the errors will impact the precision of the ZWD estimation. Although the differencing techniques mitigate majority of these errors, the combined effects of the residual errors may still be significant. Dealing with these errors is thus, essential if precise ZWD is required. This section will discuss these possible error sources and the degree to which they can be dealt with through the differencing techniques, IGS products and external models.

3.3.1 Satellite Ephemeris Error

The satellite orbital paths are influenced by the solar wind, radiation pressure and forces caused by the celestial bodies in the outer-space. Errors in the modelling of the forces acting on the GNSS satellites are known as ephemeris errors. To achieve high accuracy in GNSS positioning, it is vital that the position of the satellite is accurately known. In the case where the satellite position error is 5m and the baseline length is

20km, and assuming the satellite has an altitude of 20,000km, then the effect of ephemeris error on the baseline error is expected to be around 5mm (Wells *et al.*, 1987). In relative positioning over a short baseline, the stations will view a particular satellite at almost identical angles, and the errors in the satellite position can be removed by differencing the observations.

However, over longer baselines, though it is highly reduced through the differencing method, errors will still be present. To ensure the effect of ephemeris error on the parameter estimation is minimal, several institutions, such as the International GNSS Service (IGS; http://igscb.jpl.nasa.gov/), use a global GNSS network to provide precise ephemeris data with the GNSS data. The IGS ephemeris data are currently available in three different packages: Final Orbits, Rapid orbits and Ultra-Rapid orbits. The Final orbits are post-processed, and are generally available every 2-3 weeks. The expected accuracy of the Final orbits are around 2.5 cm (Kouba, 2009). The latency for the Rapid (approximately 17-h) and Ultra-Rapid orbit (3-h to 9-h) products are much shorter. The expected accuracy of these packages is in the 2.3 cm and 3 cm level, respectively (Kouba, 2009).

3.3.2 Satellite Clock Error

Although onboard satellite clocks are extremely accurate, they are not perfect. The stability of an atomic clock is about one to two parts in 10^{13} over a period of one day, which corresponds to a clock error of about 8.64 to 17.28 nano-seconds per day (El-Rabanny, 2002). When this error is multiplied by the speed of light, a range error of 2.59 m to 5.18 m is the product. As the signal transmission is steered by its individual satellite time, the necessary shift to GNSS time is another component of satellite clock error. The satellite clock correction products are included in the IGS ephemeris data. Even after applying the clock correction to the satellite time frame, an error of several nanoseconds still remains, which, may correspond to a significant range error (Kaplan, 1996). Thus, the estimation of the ZWD can be negatively impacted as a result. Fortunately, the satellite clock errors can be eliminated by differencing the observations, as shown by Eqs. (3.5) and (3.6).

3.3.3 Satellite Antenna Phase Centre Offset

The satellite ephemeris data describes the path in which a particular satellite would undertake with reference to the centre of mass of the satellite. However, the geometric distance between a satellite and a receiver is in fact the distance between the phase centres of the two antennas. The phase centre offset for most satellite are in the *Z*-coordinate direction (see Figure 3.9), which is towards the Earth. Therefore, a correction for this offset needs to be applied to the satellite coordinates to obtain high precision GNSS tropospheric solution. Moreover, the offsets and variations in the phase centre itself needs to be addressed. As of November 2006, the IGS convention has adopted the *absolute* phase centre offset and variation approach (Schmid *et al.*, 2007) for all satellite and station antennas.

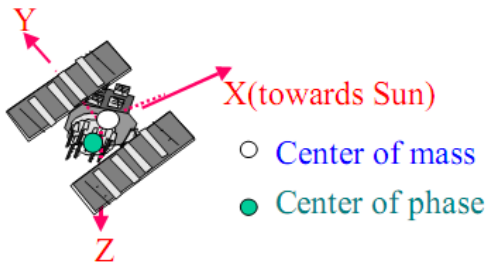

Figure 3.9 Orientation of the satellite offset with respect to the satellite body fixed reference frame in *XYZ*-coordinate

3.3.4 Receiver-Based Errors

Much like the satellites, ground-based receivers are subject to clock errors and antenna phase offsets and variations. The receiver clock error is usually estimated as an additional parameter in the observation equation, or differenced away between satellites as shown in Eqs. (3.3) and (3.4). The receiver antenna phase offset depends on the intensity, the frequency and elevation angle of the received satellite signal, and to a small extent, on the azimuth as well (Schupler and Clark, 1991). The largest offset is generally in the height component, which may be as much as 10 cm (Leick, 2004). An offset of such magnitude can impact the precision of the ZWD estimation by as much as 3 cm (Bock *et al.*, 2001). In addition, the phase centre pattern varies for different antenna types.

In GNSS network processing, the phase centre offsets and variations can be significantly reduced with the differencing process, provided that the identical

receiver-antenna combination are used within the observation session. However, such situations are uncommon. It is therefore mandatory that phase centre offsets and variation products are included in any network processing as exclusion of these data may incur a height and tropospheric error of up to 10 cm (Kouba, 2009). The use of the antenna phase centre products is especially important in PPP (Ebner and Featherstone, 2008). A relative calibration of the antenna is at least required for precise estimation. Absolute calibrations is however, recommended. Fortunately, these are freely available at the IGS centre.

3.3.5 Multipath Effects

Signal can be received in two manners; through a path of direct LoS or through reflections off objects surrounding the receiver antenna. The effect due to the latter is known as the *multipath* effect and it is one of the chief error sources for GNSS measurements (Wells *et al.*, 1987). The presence of multipath errors can be verified using a day-to-day correlation of the estimated residuals (Hofmann-Wellenhof *et al.*, 2001). A reflected signal always travels along a longer path and therefore is delayed en route to the receiver. The amplitude of the reflect signal is also reduced. The magnitude of the amplitude reduction depends on the reflectivity of the reflecting object, the angle of deflection and the polarization.

Multipath affects both code and carrier phase measurements, though the impact is greater for code observables (Lachapelle, 1990). An error of around 4.8 cm (a quarter of a cycle) for L1 carrier phase observables can result from this effect, whilst its influence on the C/A-code measurements may be several tens of metres (El-Rabanny, 2002). Van Nee (1992) reported that a code pseudorange error of up to 100m may result from multipath if the receiver is located near buildings. If the multipath in a signal is unmodelled, the corresponding ZWD parameter will most likely be significantly overestimated due to the longer signal path.

The multipath effect can be estimated by using the L1/L2 pseudorange measurement as it is frequency dependent. As the size of the effect is also dependent of the sensitivity and design of the antenna, a well-designed receiver component can also reduce its impact, such as a *choke ring* antenna. As multipath is a localised effect, the simplest, and possibly the best option, is to select an observation site in a local

environment where there are no reflecting objects in the vicinity of the antenna (Xu, 2003).

3.3.6 Cycle Slips

Resolving the ambiguity of the phase observations, the initial number of integer cycles, is one of the main issues in precise GNSS positioning. The problem can be made even more complicated when a cycle slip interrupts the signal transmission.

A cycle slip occurs when there is a sudden discontinuity or jump in the carrier phase observables by an integer number of cycles, as a result of signal loss. The main culprits for cycle slips are low signal-to-noise (SNR) due to bad atmospheric conditions, multipath or low satellite elevation, malfunction in the receiver firmware, and obstructions of the receiver line of sight due to trees, buildings, mountains and so on. The triple differencing technique is often used to detect cycle slips (e.g., Hofmann-Wellenhof *et al.*, 2001).

3.3.7 A-Priori Positional Error

The analysis of a GNSS network involves the coordinates-fixing (or constraining) of at least one reference station. The International Terrestrial Reference Frame (ITRF) solution is generally used for such cases and although it is accurate, it is not perfect. Errors resulting from positional fixing will filter through to the estimates of the unknown station(s), the tropospheric/ZWD parameter, as well as other remaining variables. Therefore, known stations are often constrained, rather than fixed to their positions in order to minimize the unmodelled errors filtering through to the ZWD and other parameter estimates.

3.3.8 Earth Body Loading

The Earth tides are caused by the temporal variation of the gravitational force due to the orbital motions of the Moon and the Sun, and to a lesser extent the other celestial bodies, resulting in the deformation of the Earth's elastic body. The structure and motion of the Earth also play a role in the magnitude of the deformation of its body. Depending on the latitude and longitude of the station, the solid Earth tides can generate a periodic site displacement of up to 30 cm and 5 cm in the vertical and in the horizontal position components (Leick, 2004), respectively. This resulting offset

in the vertical component can significantly reduce the accuracy of the ZWD estimates. If the Earth body loading is left unmodelled, the difference in ZTD solution may reach 2-4 mm (Watson *et al.*, 2006). The deformation also causes changes in the Earth's gravitational potential and thus, the velocity of the satellites varies with time as a result. Low-orbiting satellites are affected more than the GNSS satellites, which lie approximately 20,000 km above the Earth's surface.

3.3.9 Ocean Tide Loading

An ocean tide is the cyclic rise and fall of the seawater along the coastlines. The time-varying geometric alignment of the Earth, Moon and the Sun is responsible for the changing gravitational attraction between the bodies, which in turn causes, and dictates the rhythm and height of the tides. The cyclical behaviour of the tides is primarily due to the Earth's rotation and orbits. As the tide redistributes and rises along the coastal land, the earth's crust succumbs under the pressure and the weight of the tidal water. The displacement of the sea floor and the coastline due to this phenomenon is called the *ocean tide loading* effect. In-land stations are less affected than stations near the coast, with a maximum displacement of less than a centimetre, whereas a deformation of up to 10 cm can be felt for the latter over the course of just 6 hours (Baker *et al.*, 1995; Penna and Baker, 2002). However, the average value of the loading effects on the GNSS stations is generally small over 24 hours, a sign that the OTL effect can be removed through daily averaging (Khan and Scherneck, 2003). Presently there are several existing ocean tide models, such as GOT00.2, FES04, NAO99b and NEA2004 (e.g., Lyard *et al.*, 2006; Melachroinos *et al.*, 2008). Ocean tide solutions based on these models are often incorporated into GNSS data processing to minimise OTL effects on the errors of the estimated parameters. Incidentally, the versatility of GNSS has allowed it to be conversely used to validate several ocean tide loading models (Urschl *et al.*, 2005).

3.3.10 Atmospheric Pressure Loading

The pressure exerted by the Earth's atmosphere causes crustal deformation. The magnitude of the displacement due to this effect varies with location of the site and the weather status of the atmosphere. A vertical displacement of up to 1cm can result from the time-dependent effects of atmospheric loading (Van Dam and Wahr, 1987). It was shown that up to 24% of the total variance in the GNSS height estimates is

explained by surface deformations due to the atmospheric pressure (Van Dam *et al.*, 1994; Tregoning and Van Dam, 2005). Sun *et al* (1995) indicated that the atmospheric effect can bring about a surface vertical displacement of 2-5 cm in some cases in Europe. The perturbation due to this effect is found to be correlated with the latitude of the observing site. Atmospheric pressure loading on the surface displacements tends to be larger at higher latitude, where pressure variations are greater (Van Dam *et al.*, 1994).

In relative positioning over short baselines, the atmospheric pressure loading may not differ much from site to site, therefore, the effect can be significantly minimised by differencing the observables. Although the atmospheric loading can be effectively modelled, it is often ignored as its impact is significant only for baseline lengths of several thousands of kilometres (Beamson, 1995).

3.4 MAPPING FUNCTIONS

The TPD terms in Eqs. (3.1) and (3.2) vary according to the location of the observed satellite, which changes with time. However, the TPD can be redefined with respect to the zenith total delay (ZTD) over the observing receiver as in Eq. (3.8). The determination of the ZTD is based on the average of the delays of visible satellites observed at various elevation angles multiplied by a *mapping function* (MF) that describes the dependence on the elevation angle. This relationship was established by Marini (1972) as an alternative to the more complex traditional method of series expansion of integrals. The choice of mapping function is crucial for precise GNSS applications such as ZWD estimation. A correctly chosen MF is especially important when low-elevation satellites are observed, to ensure minimal errors from filtering through to the parameter estimates (Mendes, 1999).

If the mapping functions for the hydrostatic (m_H) and wet (m_W) delays are treated separately, then the total tropospheric delay can be expressed as:

$$T_A^i = m_H(\theta)\,\mathrm{ZHD} + m_W(\theta)\,\mathrm{ZWD} \tag{3.62}$$

where θ is the elevation angle from station A to satellite i. Marini (1972) also provided an empirical MF in the form of a continuous fraction. It was determined that the elevation dependence of any horizontally stratified atmosphere can be approximated by expanding in a continued fraction in terms of a cosecant function:

$$m(\theta) = \cfrac{1}{\sin(\theta) + \cfrac{a}{\sin(\theta) + \cfrac{b}{\sin(\theta) + \cfrac{c}{\cdots}}}} \tag{3.63}$$

where the coefficients a, b and c are either constants or linear functions which are dependent on pressure, temperature, humidity, latitude and height. The proposed formulation provided the foundation from which several later mapping functions (e.g., Chao, 1974; Davis *et al.*, 1985; Ifadis, 1986; Herring, 1992) are based upon. Table A3 in the Appendix provides a summary of these established models.

Most MFs assume a fairly homogeneous atmosphere and have varying degrees of accuracy. Mendes and Langley (1999) provided the most comprehensive assessments and comparisons of the MFs developed prior to its publication. It was found that for elevation angles above 10 degrees, there is not one specific MF that stood out as being significantly superior to the others. However, for data observed below 10 degrees, the majority of the mapping functions are found to be inadequate for precise positioning. For lower elevation angles, Mendes (1999) mentioned that the Niell (1996) mapping functions (NMFs) are only one of the few MFs deemed adequate for high-precision applications.

The form adopted by Niell (1996) hydrostatic and wet MF is the continued fraction given by Eq. (3.63). However, the hydrostatic NMF includes a height-dependent correction term to account for the variation in the thickness of the atmosphere at different altitudes. In addition to the station height (H), the hydrostatic NMF is also dependent on the day of year (DOY) and station latitude (ℓ). The wet MF on the other hand, is solely dependent on the latitude. The mathematical hydrostatic and wet delay models for the NMFs are (Niell, 1996):

$$m_H(\theta) = \frac{1 + \dfrac{a_{dry}}{1 + \dfrac{b_{dry}}{1 + c_{dry}}}}{\sin(\theta) + \dfrac{a_{dry}}{\sin(\theta) + \dfrac{b_{dry}}{\sin(\theta) + c_{dry}}}} + \Delta H \tag{3.64}$$

with

$$\Delta H = \frac{H}{1000}\left(\frac{1}{\sin\theta} - \frac{1 + \dfrac{a_{ht}}{1 + \dfrac{b_{ht}}{1 + c_{ht}}}}{\sin(\theta) + \dfrac{a_{ht}}{\sin(\theta) + \dfrac{b_{ht}}{\sin(\theta) + c_{ht}}}} \right) \tag{3.65}$$

$$m_W(\theta) = \frac{1 + \dfrac{a_{wet}}{1 + \dfrac{b_{wet}}{1 + c_{wet}}}}{\sin(\theta) + \dfrac{a_{wet}}{\sin(\theta) + \dfrac{b_{wet}}{\sin(\theta) + c_{wet}}}} \tag{3.66}$$

where $(a_{ht},\ b_{ht},\ c_{ht})$ are given as $(2.53\times10^{-5}, 5.49\times10^{-3}, 1.14\times10^{-3})$km. Each of the coefficient x_{dry} for $(x = a,\ b,\ c)$ is a function of the latitude and day of year, i.e.

$$x_{dry}(\ell, DOY) = x_{avg}(\ell) + x_{amp}(\ell)\cos\left(2\pi\frac{DOY - 28}{365.25}\right) \tag{3.67}$$

The corresponding values for x_{avg} and x_{amp} for five latitudes can be determined from Table 3.1. The values for other latitudes can be computed by linear interpolation between the appropriate tabulated coefficients. These quantities remain constant for latitudes at and below 15^0 elevation. The values for a_{wet}, b_{wet} and c_{wet} are treated similarly.

Table 3.1 Coefficients for Niell's dry and wet mapping (Mendes, 1999)

Coefficients	Latitude				
	15^0	30^0	45^0	60^0	75^0
$a_{avg} \times 10^{-3}$	1.2769934	1.2683230	1.2465397	1.2196049	1.2045996
$b_{avg} \times 10^{-3}$	2.9153695	2.9152299	2.9288445	2.9022565	2.9024912
$c_{avg} \times 10^{-3}$	62.610505	62.837393	63.721774	63.824265	64.258455
$a_{amp} \times 10^{-5}$	0	1.2709626	2.6523662	3.4000452	4.1202191
$b_{amp} \times 10^{-5}$	0	2.1414979	3.0160779	7.2562722	11.723375
$c_{amp} \times 10^{-5}$	0	9.0128400	4.3497037	84.795348	170.37206
$a_{wet} \times 10^{-4}$	5.8021897	5.6794847	5.8118019	5.9727542	6.1641693
$b_{wet} \times 10^{-3}$	1.4275268	1.5138625	1.4572752	1.5007428	1.7599082
$c_{wet} \times 10^{-2}$	4.3472961	4.6729510	4.3908931	4.4626982	5.4736038

The appealing feature of the NMFs is that they require no meteorological data as input parameters (Niell, 1996). The reduction in computational effort ensures that the NMFs are more practical in most instances, whilst providing comparable, if not better, solutions than other established MFs. Therefore, the NMFs are the only MFs considered in this study. Recent MFs such as the Vienna mapping functions (VMF, Boehm and Schuh (2004) and VMF1, Boehm *et al.* (2006)) and the Isobaric mapping functions (IMF, Niell (2003)) provide more realistic modelling of the state of the atmosphere as they allow input data from numerical weather models. The formulae for IMF and VMF1 are summarized in Table A4 in the Appendix. The Global mapping functions (GMF, Boehm, *et al.* (2006)) was later developed as an approximation to VMF1, but without the need for external input data.

3.5 CHAPTER SUMMARY

Although the estimation of the ZWDs is fairly straight forward in the LS process, the quality of the ZWD solutions is dependent on how well the other "nuisance" factors have been handled (as discussed in Section 3.4 and 3.5) in the functional model. Furthermore, the final ZWD estimates are dependent on the choice of stochastic model used in the LS analysis. Some of the more commonly used stochastic models will be discussed in the following Chapter, along with a well-known spatial model known as the Minimum Norm Quadratic Unbiased Estimator.

CHAPTER 4

STOCHASTIC MODELLING OF THE GNSS OBSERVATIONS

4.0 INTRODUCTION

GNSS measurements are characterised by a functional model and a stochastic model in LS. The functional model represents the mathematical relationship between the GNSS observables and the parameters of interest. The stochastic model is defined by an appropriate covariance matrix describing the precision (variance) and the spatial and/or temporal correlation among the measurements (covariance). As shown by Eqs. (3.1) and (3.2) in Chapter 3, the functional model is well defined as factors such as station coordinates, ambiguities, atmospheric delays, clock errors, multipath, etc., have been investigated and identified in many literatures (e.g., Teunissen and Kleusberg, 1998; Hofmann-Wellenhof *et al.*, 2001; Xu, 2003; Leick, 2004). On the other hand, the stochastic model is generally chosen in a relatively simple form for practical purposes (Wang *et al.*, 2002).

Stochastic modelling of GNSS observations is one of the more challenging aspects in precise GNSS positioning. LS possesses an attractive property in that the mean square error (MSE) is minimised. However, an inadequately defined covariance matrix will result in LS losing its optimality property (Dodson, 1993). Many of the existing stochastic models implemented in GNSS data processing, are uncomplicated for practical purposes. For real-time kinematic (RTK) data processing where results are needed almost instantaneously, a simple stochastic model can ease the time delay (e.g., Fuller *et al.*, 2005). A wrongly chosen stochastic model however may result in faulty cycle slip detection, thereby incurring biases into the ambiguity resolution. The quality of the other parameter estimates, including the ZTD, will also suffer as a result (Fuller *et al.*, 2005). Some GNSS processing software often employ a simple stochastic model that assumes all raw observations have the same variance. Such an assumption is too presumptuous as studies have shown that systematic errors caused by the atmosphere and multipath have varying degrees of impact on GNSS signals

(e.g., Barnes and Cross, 1998). It was also demonstrated with statistical analysis that the assumption of constant variances can be inappropriate (Bischoff *et al.*, 2006). Beutler *et al.* (1987) reported that erroneous modelling of the correlations causes millimetres level error in the coordinate estimates. Han and Rizos (1995) concluded that the solved parameter estimates are always over-optimistic when independence is assumed between the observations. Satirapod *et al.* (2002) further demonstrated that an improper stochastic model may incur a height offset of 8-10 mm. Jin *et al.* (2005) similarly reported an offset of up to 2 cm in the height component of the baseline solution. Error in the height determination will ultimately have an impact on the tropospheric delay estimates (e.g., Mendes and Langley, 1999; Tregoning and Herring, 2006).

Modern GNSS software do however provide other alternatives such as the elevation-angle-dependent model and the signal-to-noise ratio model (e.g., Hugentobler *et al.*, 2001; King and Bock, 2002). Although these models do somewhat reflect the quality of the observed GNSS signals, correlations between the raw measurements are again ignored. Nevertheless, the elevation-angle-dependent model for example, has been shown to produce reliable LS ZTD/PWV estimates (e.g., Penna *et al.*, 2005; Steigenberger *et al.*, 2007). Although more rigorous stochastic modelling techniques are available (e.g., Wang *et al.*, 1998; Tiberius and Kenselaar, 2003; Teunissen and Amiri-Simkooei, 2007), the complexity of these models generally demands greater processing time. Additionally these more complicated models have predominantly been used to derive positional and ambiguity estimates, and the effects on ZTD estimates are still relatively unknown. Though one may hypothesise that better coordinates would lead to better ZTD estimates, the significance of the impact is still speculative. One of the objectives of this thesis therefore aims to answer this question.

In this Chapter, details of various existing stochastic models that can be used to estimate ZTD/ZWD will be outlined. Emphasis will be on the more rigorous stochastic modelling technique known as the Minimum Norm Quadratic Unbiased Estimation (MINQUE). Developed by Rao (1970, 1971, 1979), MINQUE was successfully applied in GNSS data processing and has been shown to improve short baseline solutions, as well as ambiguity resolution (Wang *et al.*, 1998; Wang *et al.*,

2002). It has not yet, however, been implemented over long baselines and with large processing windows, or for the purpose of ZWD recovery. The simplified MINQUE (SMINQUE) model (Satirapod *et al.*, 2002), a variation of the original MINQUE approach which was shown to produce similar results to that of its predecessor with limited data, will also be discussed. All the stochastic models outlined in the subsequent sections will be implemented in the study. Although it is discussed, the signal-to-noise model will not be used in the data analysis as it is receiver dependent and tedious to estimate.

4.1 CONVENTIONAL STOCHASTIC MODELS

The choice of stochastic model is an important factor in determining the final outcome of the LS ZTD and parameter solution. The following sub-sections will examine some of the conventional models that are commonly implemented in GNSS applications.

4.1.1 Equal-weighting Model

The equal-weighting model (EWM) refers to the simplest of all stochastic models. The EWM is constructed with the assumption that all ZD GNSS observations are independent from one another (i.e. have no correlations) and have the same variance, i.e.:

$$\text{EWM} = \Sigma_{zd} = \begin{bmatrix} \sigma^2 & 0 & \cdots & 0 \\ 0 & \sigma^2 & \ddots & \vdots \\ \vdots & \ddots & \ddots & 0 \\ 0 & \cdots & 0 & \sigma^2 \end{bmatrix} = \sigma^2 \begin{bmatrix} 1 & 0 & \cdots & 0 \\ 0 & 1 & \ddots & \vdots \\ \vdots & \ddots & \ddots & 0 \\ 0 & \cdots & 0 & 1 \end{bmatrix} = \sigma^2 \mathrm{I} \tag{4.1}$$

Suppose there are n satellites being observed for a given epoch at stations R1 and R2. In addition, satellite s_1 was chosen as the reference satellite at both locations. The corresponding set of ZD phase observations $\bar{\phi}$ can then be mapped to the DD observations $\bar{\phi}_{DD}$ via the *double-differenced correlation matrix* D_c such that:

$$\bar{\phi}_{DD} = D_c \bar{\phi} \tag{4.2}$$

where

$$D_c = \begin{bmatrix} 1 & -1 & 0 & 0 & \cdots & 0 & -1 & 1 & 0 & 0 & \cdots & 0 \\ 1 & 0 & -1 & 0 & \cdots & 0 & -1 & 0 & 1 & 0 & \cdots & 0 \\ 1 & 0 & 0 & -1 & \ddots & \vdots & -1 & 0 & 0 & 1 & \ddots & \vdots \\ \vdots & \vdots & \vdots & \ddots & \ddots & 0 & \vdots & \vdots & \vdots & \ddots & \ddots & 0 \\ 1 & 0 & 0 & \cdots & 0 & -1 & -1 & 0 & 0 & \cdots & 0 & 1 \end{bmatrix} \tag{4.3}$$

$$\bar{\phi} = \begin{bmatrix} \phi_{R1}^{1} & \phi_{R1}^{2} & \phi_{R1}^{3} & \phi_{R1}^{4} & \cdots & \phi_{R1}^{n} & \phi_{R2}^{1} & \phi_{R2}^{2} & \phi_{R2}^{3} & \phi_{R2}^{4} & \cdots & \phi_{R2}^{n} \end{bmatrix}^{T} \tag{4.4}$$

Under the error propagation law, the construction of the variance-covariance (VCV) matrix for the (*n*-1) DD observations is (Hofmann-Wellenhof *et al.*, 2001):

$$\Sigma_{DD} = D_c \Sigma_{zd} D_c^T = \sigma^2 D_c D_c^T = \sigma^2 V = \sigma^2 \begin{bmatrix} 4 & 2 & \cdots & 2 \\ 2 & 4 & \ddots & \vdots \\ \vdots & \ddots & \ddots & 2 \\ 2 & \cdots & 2 & 4 \end{bmatrix} \tag{4.5}$$

4.1.2 Elevation-Angle-Dependent Model

The elevation-angle-dependent model (EADM) is modelled on the basis that the GNSS measurement noise is dependent on satellite elevation, which can be attributed to the receiver antenna's gain pattern, atmospheric refraction and multipath (e.g., Kim and Langley, 2001). Modelling the observational noise as a function of the satellite elevation can take on many forms. Jin and de Jong (1996) described how the standard deviation σ of the code observations can be modelled quite well by a satellite elevation dependent exponential model. The model was expressed as:

$$\sigma = a_0 + a_1 \exp\left(\frac{-\theta}{\delta_0}\right) \tag{4.6}$$

The constants a_0, a_1 and δ_0 are dependent on the type of receiver and observations being used; θ is the observed satellite elevation angle.

The other EADMs are often defined in terms of a geometric function such as the cosine and sine function to capture the severity of the noise induced by the

atmosphere, much like the approach taken in constructing modern mapping functions in Section 3.4. One of these elevation-angle-based models used to describe the variance of a raw GNSS measurement has the general form (Wang, 1999):

$$\sigma_{\phi_i}^2 = a^2 + b^2 f^2\left(\theta^i\right) \tag{4.7}$$

where a^2 and b^2 are constant coefficients and $f^2\left(\theta^i\right)$ is the function that is defined with respect to θ^i, which is the elevation angle for observation i. In the GAMIT Version 4.2 software package (King and Bock, 2002), the variances of the ZD measurements are defined by a sine function of the elevation angle θ^i such that:

$$\sigma_{\phi_i}^2 = a^2 + b^2\left(\frac{1}{\sin^2\left(\theta^i\right)}\right) \tag{4.8}$$

The coefficients are given as $a = 4.3$ mm and $b = 7$ mm. The Bernese Version 4.2 GNSS software package (Hugentobler *et al.*, 2001) on the other hand, utilizes the cosine function of the elevation angle θ^i. The corresponding formula reads:

$$\sigma_{\phi_i}^2 = a^2 + b^2 \cos^2\left(\theta^i\right) \tag{4.9}$$

The coefficients a and b are simply given as 0 and 1. The raw observations are also assumed to be spatially and temporally uncorrelated in the EADMs.

4.1.3 Signal-to-Noise Ratio Model

Signal to noise (SNR) is defined as the ratio between signal strength and the associated background noise. The lower the noise is, the higher the ratio. SNR is a popular signal quality indicator and has been frequently used to construct multipath mitigation models. The relationship between multipath and SNR or carrier-to-noise (C/N) ratio is a subject that has been investigated widely and these studies revealed a strong correlation between the quantities (e.g., Comp and Axelrad, 1996; Brunner *et al.*, 1999; Bétaille *et al.*, 2006; Lau and Cross, 2007). Modern receivers generally

have built-in firmware that is able to estimate SNR. The SNR values can vary from receiver to receiver as the manufacturers may use different algorithms. To a lesser extent, SNR has also been used to produce stochastic models for high-precision GNSS applications (e.g., Özlüdemir, 2004). The relationship between the phase noise (σ_ϕ) and the SNR is (Spilker, 1996):

$$\sigma_\phi^2 \cong \frac{1}{\mathrm{SNR}_\phi} \tag{4.10}$$

The SIGMA-ε weight model (Hartinger and Brunner, 1999) links the phase noise with the C/N observable through a model parameter C_i [m^2Hz], and it reads

$$\sigma_\phi^2 = C_i . 10^{\frac{-C/N}{10}} \tag{4.11}$$

Wieser and Brunner (2000) argued that some antenna-receiver combinations require an additional term, T_i [m^2]. The revised SIGMA-ε model was given as:

$$\sigma_\phi^2 = T_i + C_i . 10^{\frac{-C/N}{10}} \tag{4.12}$$

For the Rogue SNR8000/DORNE MARGOLIN B antenna/receiver combination, the corresponding values given to the constants are estimated to be $T_{L1} = 0$, $C_{L1} = 0.244$ for L1 signals, and $T_{L2} = 0.88 \times 10^{-6}$, $C_{L2} = 0.77 \times 10^{-3}$ for L2 signals respectively (Wieser and Brunner, 2000). Lau and Mok (1999) and Satirapod and Wang (2000) also highlighted the close relationship between SNR and the satellite elevation angle.

Using the phase variances ($\sigma_{\phi_i}^2$) for a ZD observation i, the corresponding weight is calculated via the following equation:

$$w_{\phi_i} = \frac{\sigma^2}{\sigma_{\phi_i}^2} \tag{4.13}$$

where σ^2 is the *a-priori* variance of the GNSS observations.

The coefficients for the SNR models are not of a general nature as they are receiver-dependent, and can be tedious to estimate. Thus, the SNR models are not implemented in this study.

4.2 MINIMUM NORM QUADRATIC UNBIASED ESTIMATION

The stochastic models, given in Section 4.1, assume that the correlations among the ZD observations are negligible when generating the VCV matrix. However, such assumption may lead to unreliable results (Wang *et al.*, 2002). The Minimum Norm Quadratic Unbiased Estimation (MINQUE) method (Rao, 1971) is a popular stochastic estimation procedure and is often called upon in many practical situations to generate dynamic estimates for VCV (e.g., Satirapod *et al.*, 2002; Mäkinen *et al.*, 2003; Musa *et al.*, 2003; Fuller *et al.*, 2005; Erol *et al.*, 2008).

To illustrate the MINQUE process, consider the linear model given by Eq. (3.7). The VCV matrix of the measurement vector L, can be expressed in the form:

$$\Sigma = \sum_{i=1}^{q} C_i = \sum_{i=1}^{q} \sigma_i V_i \tag{4.13}$$

where σ_1, σ_2, .., σ_q are the VCV components to be estimated and V_1, V_2, .., V_q are the so-called *accompanying matrices*. The structure of these matrices will be discussed later. The problem here is one of estimating q unknown elements of Σ.

According to Rao (1971), the MINQUE of the linear function of σ_i $(i = 1, 2, .., q)$, i.e. $a_1\sigma_1 + a_2\sigma_2 + .. + a_q\sigma_q$, is the quadratic function $L^T Y L$, where Y is estimated such that:

$$\text{Trace}(Y\Sigma\Sigma Y) \text{ is a minimum} \tag{4.14}$$

subject to

$$YA = 0 \tag{4.15}$$

and

$$\text{Trace}(YC_i) = \alpha_i, \quad i = 1, 2, ..., q \tag{4.16}$$

with

$$\Sigma = C_1 + C_2 + \cdots + C_q \tag{4.17}$$

Using Eqs. (4.14), (4.15) and (4.16), the MINQUE of $\sum_{i=1}^{q} \sigma_i V_i$ is then

$$\gamma^T M = \sum_{i=1}^{q} \gamma_i M_i, \quad M_i = L^T U V_i U L \tag{4.18}$$

where the vector γ is a solution of

$$\sum_{i=1}^{q} \gamma_i \text{Trace}(UV_i UV_j) = \alpha_{j,} \quad j = 1, 2, ..., q \tag{4.19}$$

and

$$U = W\left[W^{-1} - A(A^T W A)^{-1} A^T\right] W, \text{ where } W = \Sigma^{-1} \tag{4.20}$$

The symmetric U matrix can be partitioned as

$$U = \begin{bmatrix} U_{11} & U_{12} & \cdots & U_{1n_e} \\ U_{21} & U_{22} & \cdots & U_{2n_e} \\ \vdots & \vdots & \ddots & \vdots \\ U_{n_e 1} & U_{n_e 2} & \cdots & U_{n_e n_e} \end{bmatrix} \tag{4.21}$$

where n_e is the number of epochs in a GNSS processing window session.

By expressing Eq. (4.19) as $S\gamma = \kappa$, where the (i,j) entry of matrix S is given by:

$$S_{ij} = \text{Trace}(UV_i UV_j) \tag{4.22}$$

this leads to $\gamma = S^{-1}\kappa$.

Since the MINQUE of $\sum_{i=1}^{q} \sigma_i V_i$ is

$$\gamma^T M = \kappa^T \left(S^{-1}\right)^T M = \kappa^T S^{-1} M = \kappa^T \hat{\sigma} \tag{4.23}$$

Therefore, $\hat{\sigma} = \left(\hat{\sigma}_1, \hat{\sigma}_2, .., \hat{\sigma}_q\right)$ is a solution of

$$S\sigma = M \tag{4.24}$$

M can alternatively be defined as:

$$M_i = L^T U V_i U L = v^T W V_i W v \tag{4.25}$$

One of the criticisms of MINQUE is that it is only locally optimal (Rao, 1971; Rao, 1979; Fotopoulos, 2005). This means that different *a priori* VCV estimates will result in different MINQUE solutions. However, it can be observed from Eqs. (4.18) to (4.22) that both S and M are dependent on the VCV matrix, Σ, via the matrix *U*. Since the elements of Σ are the direct result of $\hat{\sigma}$, an iterative process can be performed. Given an initial estimate $\hat{\sigma}_{(0)}$, a $(j+1)^{th}$ approximation is generated with the following iterative procedure:

$$\hat{\sigma}_{(j+1)} = S^{-1}_{(j)} M_{(j)}, \quad j = 0, 1, \ 2, \ldots \tag{4.26}$$

The number of iterations in Eq. (4.26) can be set to a pre-defined finite value or until the difference between the i^{th} and $(i-1)^{th}$ elements is less than a pre-specified tolerance value, for example, 10^{-5}. An example of how MINQUE can be used to estimates the VCV of the DD observations will be given later in Section 4.4.

Another problem with MINQUE is that it does not ensure the estimated variances will always be positive (Rao and Kleffe, 1988). However, if all the matrices $V_1, V_2, .., V_q$ are non-negative definite, Rao and Kleffe (1988) proposed an alternative iterative scheme

$$\hat{\sigma}^i_{(j+1)} = \hat{\sigma}^i_j \frac{L^T U_{\hat{\sigma}_i} V_i U^T_{\hat{\sigma}_i} L}{\text{Trace}(U_{\hat{\sigma}_i} V_i)}, \quad i = 1, \ 2, .., q \tag{4.27}$$

where the $(j+1)^{th}$ approximation to the i^{th} component of $\hat{\sigma}$ can be computed. This modified scheme ensures $\hat{\sigma}^i$ will remain non-negative throughout the iterations when $\hat{\sigma}^i_{(0)} \geq 0$. It is also computationally simpler than Eq. (4.26), which requires the calculation of the S matrix.

One should note, however, that the convergence in MINQUE is not guaranteed (Rao, 1971; Rao and Kleffe, 1980, 1988). The likelihood of convergence in MINQUE largely depends on the number of observations compared to the number of parameters (i.e., observation redundancy increases the chances of achieving convergence), and/or the pre-defined structure of the stochastic model (Sjöberg, 1984). Another positive consequence of high redundancy is that negative variances occur less frequently (Fotopoulos, 2005).

4.3 SIMPLIFIED MINQUE

The execution of MINQUE, given in Section 4.2, requires a processor with substantial computer power and memory as the number of observations becomes large, and this is mostly due to the computation and storage of the U matrix in Eq. (4.21). For example, suppose fifteen satellites are observed over a certain time period. From these satellites, fourteen distinct satellite-pairs can be constructed. Therefore, a 14×14 VCV matrix needs to be constructed, with each variance σ_i^2 (for i = 1, 2, .., 14) describing the spatial variability of each of the satellite-pair i.

The U matrix is dependent on the weight matrix, which is taken as the inverse of the VCV matrix. Since the VCV matrix is not a diagonal matrix, the calculation of the inverse matrix can be time consuming. For a longer observing time period, the number of distinct satellite-pairs will increase and thus, the determination of the inverse of the VCV will become more complex. Additionally the dimension of matrix U is of $n_{DDobs} \times n_{DDobs}$, where n_{DDobs} is the number of DD observations in the specified observing window. The required storage capacity can therefore be quite significant as n_{DDobs} becomes large.

The notion behind the simplified MINQUE (Satirapod *et al.*, 2002), which will be referred to here as SMINQUE, is to reduce the complexity of the U matrix, resulting in the efficient computation of the MINQUE process. The proposed simplification of MINQUE disregards the off-diagonal block entries of U and gives rise to a block-diagonal matrix U^* as its replacement in the procedure. The U^* matrix is expressed as:

$$U^* = \begin{bmatrix} U_{11} & 0 & \cdots & 0 \\ 0 & U_{22} & \ddots & \vdots \\ \vdots & \ddots & \ddots & 0 \\ 0 & \cdots & 0 & U_{n_e n_e} \end{bmatrix} \tag{4.28}$$

Subsequently, Eq. (4.21) can be simplified to

$$S_{ij} = \sum_{t=1}^{n_e} \text{Trace}\left(U_{tt} V_{it} U_{tt} V_{jt}\right) \tag{4.29}$$

where V_{it} is the block-diagonal element of V_i for epoch t and $V_{it} = V_{jt}$.

The theoretical basis of the simplified approach offered by Satirapod *et al.* (2002) is unclear and was not discussed. It does, however, empirically ensure the operation of the procedure is more efficient when computation time is of concern. The consequence of the simplification of U (see Eq. (4.21)), nevertheless, can be demonstrated.

Given that

$$Wv = UL \tag{4.30}$$

$$\begin{bmatrix} W_1 & 0 & \cdots & 0 \\ 0 & W_2 & \ddots & \vdots \\ \vdots & \ddots & \ddots & 0 \\ 0 & \cdots & 0 & W_{n_e} \end{bmatrix} \begin{bmatrix} v_1 \\ v_2 \\ ... \\ v_{n_e} \end{bmatrix} = \begin{bmatrix} U_{11} & U_{12} & \cdots & U_{1n_e} \\ U_{21} & U_{22} & \cdots & U_{2n_e} \\ \vdots & \vdots & \ddots & \vdots \\ U_{n_e 1} & U_{n_e 2} & \cdots & U_{n_e n_e} \end{bmatrix} \begin{bmatrix} L_1 \\ L_2 \\ \vdots \\ L_s \end{bmatrix} \tag{4.31}$$

$$W_i v_i = U_{ii} L_i + \sum_{j=1}^{n_e} U_{ij} L_j \quad \text{for } i \neq j \text{ and } i = 1, 2, ..., n_e \tag{4.32}$$

then using Eq. (3.23),

$$\hat{\sigma}_0^2 = \frac{\hat{v}^T W \hat{v}}{n - p} = \frac{\sum_{i=1}^{n_e} v_i^T U_{ii} L_i + \sum_{i=1}^{n_e} \sum_{j=1}^{n_e} v_i^T U_{ij} L_j}{n - p} \quad \text{for } i \neq j. \tag{4.33}$$

If matrix U^* was used, then $\sum_{i=1}^{n_e} \sum_{j=1}^{n_e} v_i^T U_{ij} L_j = 0$ and thus, the resulting VCV matrix from the SMINQUE process will be wrongly estimated. Hence, the LS solutions for the tropospheric parameter in Eq. (3.26), as well as the corresponding error estimate in Eq. (3.28), may be unrealistic. Results from Satirapod *et al.* (2002) show that both the MINQUE and SMINQUE yielded similar results in the resolved GNSS ambiguity set. The difference in coordinate solutions produced by MINQUE and its simplified counterpart were in the sub-millimetre range. The investigation was carried out over shorter baselines (15 m, 215 m, 870 m, and 13,300 m), each with 30 min of data. Although MINQUE and SMINQUE were shown to have negligible differences in these instances, whether or not such remark will hold true under difference circumstances (e.g., longer baseline lengths > 20 km) is still unknown. The impact of the simplification on the convergence likelihood was also not discussed.

It has also been indicated by Satirapod *et al.* (2002) that it is "possible" that the effect of changing satellites can be handled simply by processing Eq. (4.28) on an epoch-by-epoch basis when the SMINQUE is used. However, a demonstration was not provided. On closer inspection, the modification has, in fact, failed to overcome this issue of changing satellites. Since the matrix U is dependent on the VCV matrix Σ, the latter has to be constructed appropriately first, in order yield U and eventually U^*. As the problem regarding the formation of the VCV matrix was not addressed, U^* cannot be defined as result. In the following section, an alternative approach to the construction of the VCV is proposed to overcome the issue of changing satellites.

4.4 A MODIFIED APPROACH TO MODELLING WITH MINQUE

MINQUE was only ever used on relatively small processing windows, and over a relatively short baseline (<15km) due to its computational demands. However, there are other limitations to MINQUE. Satirapod *et al.* (2002) stated that MINQUE requires equal number of satellites in every epoch of the window session. Hence, the method was only used for sessions that were less than 1 hour long (e.g., Wang *et al.*, 1998; Satirapod *et al.*, 2002; Wang *et al.*, 2002) and requires the same satellites to be tracked all throughout the session without any cycle slips. In this section, a more general approach will be taken in the construction of the VCV matrix in the estimation step and thus, the effect of having a variable satellite distribution from epoch to epoch can now be handled. This will be illustrated with a simple scenario and an example.

Suppose m_i satellites are tracked at epoch t_i by two receivers. Denote the raw GNSS carrier-phase measurements collected from receiver R1 and receiver R2 at epoch t_i as:

$$\begin{aligned}\bar{\phi}_{R1} &= \left(\phi_{R1}^{1},\ \phi_{R1}^{2},\ ...,\phi_{R1}^{m_i}\right)^T \\ \bar{\phi}_{R2} &= \left(\phi_{R2}^{1},\ \phi_{R2}^{2},\ ...,\phi_{R2}^{m_i}\right)^T\end{aligned} \tag{4.34}$$

Then, the DD measurements $L(t_i)$ between satellite j and satellite k at epoch t_i is:

$$L_{R1R2}^{jk}(t_i) = D_c\bar{\phi}(t_i), \quad i = 1, 2, \ldots, n_e \tag{4.35}$$

where n_e is the number of epochs in the processing session and the matrix D_c is as defined in Eq. (4.3). Let n_s be the number of distinct satellite-pairs in the session. Therefore, a $n_s \times n_s$ VCV matrix can be constructed and represented as:

$$\Sigma = \begin{bmatrix} \sigma_{11} & \sigma_{12} & ... & \sigma_{1n_s} \\ \sigma_{21} & \sigma_{22} & ... & \sigma_{2n_s} \\ ... & ... & ... & ... \\ \sigma_{n_s1} & \sigma_{n_s2} & ... & \sigma_{n_sn_s} \end{bmatrix} = \sum_{j=1}^{q} \sigma_j V_{\sigma_j} \tag{4.36}$$

where

$$q = n_s(n_s + 1)/2 \tag{4.37}$$

$$\sigma = (\sigma_1, \sigma_2, .., \sigma_q)^T \tag{4.38}$$

$$= (\sigma_{11}, \sigma_{22}, .., \sigma_{n_sn_s}, \sigma_{12}, \sigma_{13}, .., \sigma_{1n_s}, \sigma_{23}, .., \sigma_{(n_s-1)n_s})^T \tag{4.39}$$

$$V_{\sigma_1} = \begin{bmatrix} 1 & 0 & ... & 0 \\ 0 & 0 & ... & 0 \\ ... & ... & ... & ... \\ 0 & 0 & ... & 0 \end{bmatrix}, V_{\sigma_2} = \begin{bmatrix} 0 & 0 & ... & 0 \\ 0 & 1 & ... & 0 \\ ... & ... & ... & ... \\ 0 & 0 & ... & 0 \end{bmatrix}, ..., V_{\sigma_{n_s}} = \begin{bmatrix} 0 & 0 & ... & 0 \\ 0 & 0 & ... & 0 \\ ... & ... & ... & ... \\ 0 & 0 & ... & 1 \end{bmatrix}, \ldots, \tag{4.40}$$

$$V_{\sigma_{n_s+1}} = \begin{bmatrix} 0 & 1 & 0 & ... & 0 & 0 \\ 1 & 0 & 0 & ... & 0 & 0 \\ 0 & 0 & 0 & ... & 0 & 0 \\ ... & ... & ... & ... & ... & ... \\ 0 & 0 & 0 & ... & 0 & 0 \\ 0 & 0 & 0 & ... & 0 & 0 \end{bmatrix}, \quad V_{\sigma_{n_s+2}} = \begin{bmatrix} 0 & 0 & 1 & ... & 0 & 0 \\ 0 & 0 & 0 & ... & 0 & 0 \\ 1 & 0 & 0 & ... & 0 & 0 \\ ... & ... & ... & ... & ... & ... \\ 0 & 0 & 0 & ... & 0 & 0 \\ 0 & 0 & 0 & ... & 0 & 0 \end{bmatrix}, ... \tag{4.41}$$

$$V_{\sigma_q} = \begin{bmatrix} 0 & 0 & 0 & ... & 0 & 0 \\ 0 & 0 & 0 & ... & 0 & 0 \\ 0 & 0 & 0 & ... & 0 & 0 \\ ... & ... & ... & ... & ... & ... \\ 0 & 0 & 0 & ... & 0 & 1 \\ 0 & 0 & 0 & ... & 1 & 0 \end{bmatrix} \tag{4.42}$$

Note that the variances, denoted as $\sigma_{ii} = \sigma_i^2$, can only be calculated if and only if, the number of occurrences for each distinct satellite-pair is at least two in the selected processing window.

If the same set of satellites were tracked throughout the session, and assuming that the satellite-pairs do not vary from epoch to epoch, then $m_1 = m_2 = ... = m_{n_e}$ for a session with n_e epochs of data. Therefore, the full VCV matrix of all DD observations is:

$$\Sigma_{DD} = \sum_{j=1}^{q} \sigma_j V_{\sigma_j}^{*}, \tag{4.43}$$

where,

$$V_{\sigma_j}^{*} = \mathrm{diag}\left(V_{\sigma_j}(i)\right), \tag{4.44}$$

$$V_{\sigma_j}(i) = V_{\sigma_j}, \quad i = 1, 2, ..., n_e \tag{4.45}$$

This was the case considered in Wang *et al.* (1998). The problem occurs when the number of observed satellites varies from epoch to epoch, that is, $m_i \neq m_j, \ \forall i, j$ such that, $i \neq j$. In order to overcome the problem, the necessary adjustment only involves simple manipulation of the VCV matrix. Consider a scenario where there are four variables, $x1$, $x2$, $x3$ and $x4$, with the following known VCV structure.

$$\Sigma_{4\times4} = \begin{bmatrix} \sigma_{x1x1} & \sigma_{x2x1} & \sigma_{x3x1} & \sigma_{x4x1} \\ \sigma_{x2x1} & \sigma_{x2x2} & \sigma_{x3x2} & \sigma_{x4x2} \\ \sigma_{x3x1} & \sigma_{x3x2} & \sigma_{x3x3} & \sigma_{x4x3} \\ \sigma_{x4x1} & \sigma_{x4x2} & \sigma_{x4x3} & \sigma_{x4x4} \end{bmatrix}. \tag{4.46}$$

Suppose variable $x3$ is of no interest anymore, then a new VCV matrix, Σ^{*}, can be realised by extracting the necessary elements from Σ. Additionally, the order of the variables does not matter because it would just be a case of relabelling. For example, let us denote $y1 = (x4, x2, x1)^T$ and $y2 = x3$. Then, the VCV matrix Σ can be rearranged and partitioned such that:

$$\Sigma_{4\times4} = \begin{bmatrix} \sigma_{y1y1} & \vdots & \sigma_{y1y2} \\ \cdots\cdots & \vdots & \cdots\cdots \\ \sigma_{y2y1} & \vdots & \sigma_{y1y2} \end{bmatrix} = \begin{bmatrix} \sigma_{x4x4} & \sigma_{x4x2} & \sigma_{x4x1} & \vdots & \sigma_{x4x3} \\ \sigma_{x2x4} & \sigma_{x2x2} & \sigma_{x2x1} & \vdots & \sigma_{x2x3} \\ \sigma_{x1x4} & \sigma_{x1x2} & \sigma_{x4x1} & \vdots & \sigma_{x1x3} \\ \cdots\cdots & \cdots\cdots & \cdots\cdots & \vdots & \cdots\cdots \\ \sigma_{x3x4} & \sigma_{x3x2} & \sigma_{x3x1} & \vdots & \sigma_{x3x3} \end{bmatrix} = \begin{bmatrix} \Sigma_{11} & \Sigma_{12} \\ \Sigma_{21} & \Sigma_{22} \end{bmatrix} \tag{4.47}$$

Therefore, ignoring variable $x3$ will result in a 3×3 matrix $\Sigma^{*}=\Sigma_{11}$. It is with this approach that the restriction on the fixed number of VCV components in the MINQUE estimation step is avoided. As V_{σ_j} ($j=1,\ 2,\ ..,\ q$) are direct results of the VCV matrix, they can also be managed in the same way.

Example 1:

Suppose satellites 1, 2, 3 and 4 were tracked for three epochs. In each epoch, satellite 2 was chosen to be the reference satellite. Furthermore, suppose the signal from satellite 1 was lost in the first epoch. Therefore, the DD observation vector L, which can be either pseudorange or phase measurements, is modelled as:

$$L=\begin{bmatrix} L^{2-3}(t_1)\\ L^{2-4}(t_1)\\ .....\\ L^{2-1}(t_2)\\ L^{2-3}(t_2)\\ L^{2-4}(t_2)\\ .....\\ L^{2-1}(t_3)\\ L^{2-3}(t_3)\\ L^{2-4}(t_3)\end{bmatrix}=AX+\begin{bmatrix} v_1\\ v_2\\ \cdots\\ v_3\\ v_4\\ v_5\\ \cdots\\ v_6\\ v_7\\ v_8\end{bmatrix} \tag{4.48}$$

The VCV matrix of all distinct satellite-pairs, 2-1, 2-3 and 2-4 can be written as:

$$\Sigma=\begin{bmatrix} \sigma^2_{2-1} & \sigma_{2-1,2-3} & \sigma_{2-1,2-4}\\ \sigma_{2-1,2-3} & \sigma^2_{2-3} & \sigma_{2-3,2-4}\\ \sigma_{2-1,2-4} & \sigma_{2-3,2-4} & \sigma^2_{2-4}\end{bmatrix} \tag{4.49}$$

Since the satellite pair 2-1 is missing in the first epoch, the VCV matrix at epoch t_1 will be a subset of Σ, that is,

$$\Sigma_{t_1}=\begin{bmatrix} \sigma^2_{2-3} & \sigma_{2-3,2-4}\\ \sigma_{2-3,2-4} & \sigma^2_{2-4}\end{bmatrix} \tag{4.50}$$

with $\Sigma_{t_2} = \Sigma_{t_3} = \Sigma$. Therefore the full VCV matrix for all DD observations is $\Sigma_{DD} = \mathrm{diag}(\Sigma_{t_1}, \Sigma_{t_2}, \Sigma_{t_3})$. Here also, there are six variance VCV components to be estimated. The *accompanying matrices* at the first epoch are:

$$V_{\sigma_1}(t_1) = \begin{bmatrix} 0 & 0 \\ 0 & 0 \end{bmatrix} \tag{4.51}$$

$$V_{\sigma_2}(t_1) = \begin{bmatrix} 1 & 0 \\ 0 & 0 \end{bmatrix} \tag{4.52}$$

$$V_{\sigma_3}(t_1) = \begin{bmatrix} 0 & 0 \\ 0 & 1 \end{bmatrix} \tag{4.53}$$

$$V_{\sigma_4}(t_1) = \begin{bmatrix} 0 & 0 \\ 0 & 0 \end{bmatrix} \tag{4.54}$$

$$V_{\sigma_5}(t_1) = \begin{bmatrix} 0 & 0 \\ 0 & 0 \end{bmatrix} \tag{4.55}$$

$$V_{\sigma_6}(t_1) = \begin{bmatrix} 0 & 1 \\ 1 & 0 \end{bmatrix} \tag{4.56}$$

where $\sigma = (\sigma_1, \sigma_2, \sigma_3, \sigma_4, \sigma_5, \sigma_6)^T = (\sigma^2_{2-1}, \sigma^2_{2-3}, \sigma^2_{2-4}, \sigma_{2-1,2-3}, \sigma_{2-1,2-4}, \sigma_{2-3,2-4})^T$; for epoch t_2 and t_3, the matrices V_{σ_j} ($j = 1,2,..,6$) are as represented by Eqs. (4.40) to (4.42). Finally, Σ_{DD} can be expressed as

$$\Sigma_{DD} = \mathrm{diag}(\Sigma_{t_1}, \Sigma_{t_2}, \Sigma_{t_3}) = \sum_{j=1}^{6} \sigma_j V^*_{\sigma_j} \tag{4.57}$$

where

$$V^*_{\sigma_j} = \mathrm{diag}(V_{\sigma_j}(t_1), V_{\sigma_j}(t_2), V_{\sigma_j}(t_3)) \tag{4.58}$$

Once V^*_{σ} has been properly defined, the MINQUE process can proceed without further complications.

Suppose that in the next few epochs there is a change in the reference satellite, say satellite 3. In this instance, a new set of ambiguities (i.e., $N^{3-1}, N^{3-2}, \text{and } N^{3-4}$) is formed. The corresponding VCV matrix for all epochs is a 6×6 matrix given by:

$$\Sigma = \begin{bmatrix} \sigma^2_{2-1} & \sigma_{2-1,2-3} & \sigma_{2-1,2-4} & \sigma_{2-1,3-1} & \sigma_{2-1,3-2} & \sigma_{2-1,3-4} \\ \sigma_{2-1,2-3} & \sigma^2_{2-3} & \sigma_{2-3,2-4} & \sigma_{2-3,3-1} & \sigma_{2-3,3-2} & \sigma_{2-3,3-4} \\ \sigma_{2-1,2-4} & \sigma_{2-3,2-4} & \sigma^2_{2-4} & \sigma_{2-4,3-1} & \sigma_{2-4,3-2} & \sigma_{2-4,3-4} \\ \sigma_{2-1,3-1} & \sigma_{2-3,3-1} & \sigma_{2-4,3-1} & \sigma^2_{3-1} & \sigma_{3-1,3-2} & \sigma_{3-1,3-4} \\ \sigma_{2-1,3-2} & \sigma_{2-3,3-2} & \sigma_{2-4,3-2} & \sigma_{3-1,3-2} & \sigma^2_{3-2} & \sigma_{3-2,3-4} \\ \sigma_{2-1,3-4} & \sigma_{2-3,3-4} & \sigma_{2-4,3-4} & \sigma_{3-1,3-4} & \sigma_{3-2,3-4} & \sigma^2_{3-4} \end{bmatrix} \tag{4.59}$$

Hence, there are 21 VCV components to be estimated instead. The derivation of the accompanying matrices is similar to the process outlined earlier. However, the increase in the dimension of the VCV matrix does significantly increase the computation time.

Previous to this work, MINQUE was thought to be only capable of processing GNSS data when the number of satellites does not change throughout the whole processing window. By restricting the length of the baseline, it ensures higher chances that both receivers are tracking the same set of satellites for a given period. However, it was shown that by correctly defining the VCV matrix and its corresponding *accompanying matrices* at each epoch, the issue of unequal number of observed satellites is no longer a problem. More specifically, this change allows MINQUE to be implemented for when there is a change in the number of distinct satellite-pairs (i.e. new ambiguity terms). Note that a change in the number of distinct satellite-pairs can occur either due to a change in the reference satellite, a new satellite appearing in the latter epochs of the processing window, or the disappearance of a tracked satellite within the observational period.

The proposed changes here will allow MINQUE to be implemented over larger data sets and longer baselines. This approach is also be used to construct the VCV matrix for SMINQUE in this study.

The number of distinct satellite-pairs will increase as the number of epochs increases for a given window session. Consequently, a 24-hour processing session may still be unrealistic for MINQUE. For a session with n_s distinct satellite-pairs, a $n_s \times n_s$ VCV matrix is to be stored. For large values of n_s, the storage of Σ will require significant memory space. To tackle this problem, one could suggest:

$$v_{DD_j} \sim \left(0, \sigma_j^2\right), \quad \text{for } j = 1, 2, \ldots, \max\{n_i\} \tag{4.60}$$

where n_i is the number of DD observations at epoch t_i for $i = 1, 2, \ldots, n_e$.

It is assumed here that the first DD observation of each epoch has a common variance σ_1^2, whilst the second DD observation of each epoch will have a variance σ_2^2, and so on. Therefore, if there is a maximum of n_{max} number of observations in any given epoch t_i, i.e. $n_{max} = \max_{i=1,2,..,n_e}\{n_i\}$, only a $n_{max} \times n_{max}$ VCV matrix is stored in memory instead. Hence, the dimension of Σ is significantly reduced. Additionally, the increase in redundancy level for each σ_j^2 will increase the likelihood of convergence and its non-negativity value (e.g., Fuller *et al.*, 2005). Thus, placing the assumption as defined in Eq. (4.60) on the DD observations is a more appropriate method of constructing the stochastic model in a practical sense.

4.5 CHAPTER SUMMARY

Stochastic modelling of GNSS observations is a well known, but complex issue. Stochastic models such as the EWM and the EADM ignore any existing spatial and temporal correlations between the raw GNSS observations, and are used to reduce the impact of low-quality signals on the final solution. Although the simplicity of these models also ensures the computational time does not become a hugely negative factor, the solution may suffer as a result. More sophisticated stochastic models such as MINQUE (Rao, 1970), generally require greater processing time and thus, are not routinely implemented in practice. However, Satirapod *et al.* (2002) provide a simplified MINQUE model, which significantly reduces the computation time. The simplification however, was not justified. The theoretical consequence of this

simplification was addressed in Section 4.3. MINQUE was initially only able to process data whereby equal number of satellites is observed at every epoch throughout the window session (Wang *et al.*, 1998; Wang *et al.*, 2002). This is the reason why MINQUE has generally been implemented over small window sessions (<1hr) and relatively short baselines (<15 km) in GNSS applications. However, this restriction can be avoided by redefining one of the processing steps. The modification is detailed in Section 4.4, along with an example. The revised approach, also applicable to SMINQUE, allows MINQUE to be implemented over larger data sets and longer baselines. In this study, the modified approach will be implemented in the data processing in Sections 6.2 to 6.4 of Chapter 6. The MINQUE and SMINQUE models will only be applied in static positioning mode in this thesis.

CHAPTER 5

ASSESSING THE PRECISION OF THE GNSS-ESTIMATED TROPOSPHERIC SOLUTIONS

5.0 INTRODUCTION

The optimality of LS estimates, described in Chapter 3, lies in minimising the model residuals (e.g., Johnson and Wichern, 2007; Walpole *et al.*, 2007). However, the final solution may not be reflective of the true solution if the defined stochastic models (see Chapter 4) are incorrect or due to a lack of quality observations. In general, reliable positioning can be achieved by introducing a certain level of observation redundancy (Kim and Langley, 2001). Tropospheric estimates will also improve as a result. To assess the *accuracy* of the LS solutions, positional estimates can be compared to known ITRF or local geodetic coordinates, whilst the ZTD/ZWD estimates can be compared to independent measurements from other atmospheric sensors such as a water vapour radiometer (WVR) and/or radiosonde (RS). This is one of the ways to assess the quality of the GNSS tropospheric estimates. It is worth noting that levels of uncertainty exist in these control data themselves (e.g., Nakamura *et al.*, 2004; Nilsson *et al.*, 2005), as discussed in Section 2.5.

The root mean squared error (RMSE) is often used to evaluate the accuracy of a set of GNSS tropospheric solutions. The RMSE evaluates the difference between GNSS and RS/WVR ZWD estimates (or any other comparable tropospheric estimates), and is computed as follows:

$$\text{RMSE} = \sqrt{\frac{\sum_{j=1}^{n_c}\left(\text{ZWD}_{\text{GPS}}^{(j)} - \text{ZWD}_{i}^{(j)}\right)^2}{n_c}} \quad \text{for i = RS or WVR} \tag{5.1}$$

where n_c refers to the number of data compared.

The general consensus from past studies (e.g., Bevis *et al.*, 1994; Businger *et al.*, 1996; Haase *et al.*, 2003; Snajdrova *et al.*, 2006; Heinkelmann *et al.*, 2007; Steigenberger *et al.*, 2007; Wang *et al.*, 2007) is that a set of GNSS ZWD (PWV) estimates is considered as good estimates if it has a RMSE value of less than 15-20 mm in ZWD (giving 2-3 mm in PWV using Eq.(2.31)) when compared to RS estimates, or any other reliable independent measurements such as WVR or VLBI solutions. For assimilation purposes, it is preferable that the accuracy of the GNSS ZWD estimates is within 7-15 mm, or 1-2 mm in PWV (Macpherson *et al.*, 2007).

Unfortunately, RS is the only atmospheric sensor in regular operational use within Australia for meteorological studies. Therefore at a specific site, there are at most two observations per day (at UTC 0:00 and 12:00) available for validating GNSS tropospheric solutions. However, in practice, tropospheric solutions are given hourly (i.e. 24 ZWD solutions a day) or two-hourly (i.e. 12 ZWD solutions a day). Consequently, the quality of the majority of the GNSS ZWD estimates remains unknown. In such a situation, the corresponding error estimates (i.e. the square root of the error variances) of the LS tropospheric solutions can be called upon to assess these remaining ZWD estimates. These error estimates are an indication of the *precision* of the tropospheric solutions. In order to evaluate the effectiveness of the error estimates of the LS ZWD solutions as a realistic source of quality-checking information, Section 5.1 will provide the statistical tests that can be used to perform such task.

It can also be observed from Eqs. (3.14) and (3.15) in Chapter 3, that the LS ZWD error estimates are dependent on the redundancy level, as well as the quality of the GNSS observations. Given a well-defined functional model of GNSS measurements, the ZWD and other parameter error estimates are generally very small when there is a high level of redundancy. Such small error estimates are generally not indicative of the dynamic nature of the ZWD in the atmosphere and thus, reliance on these error estimates for assessing the ZWD solutions can be unwise in many cases. Therefore, this chapter will also investigate the impact of high observation redundancy on the tropospheric error estimates. The discussions are provided in Section 5.2.

5.1 STATISTICAL INFERENCES FOR ZWD ESTIMATES

Although it is only implemented sparingly in practice, the error estimates (precision) from the LS adjustment process can be used for assessing the quality of the GNSS ZWD estimates in the absence of independent external measurements such as RS and WVR. To determine the adequacy of this approach, a statistical inference of the LS ZWD estimates is discussed.

The techniques of statistical inference can be categorized into two stages. The first stage involves the *estimation of the* ZWD *parameters*. The parameter estimation process was summarised in Chapter 3 (Sections 3.1 and 3.2). The second stage is realized by *hypothesis testing* of the ZWD parameter estimates (e.g., Montgomery, 2001; Walpole *et al.*, 2007).

In the hypothesis testing procedure, a statement is made with regards to the values of the parameters of a probability distribution (Montgomery, 2001). The statements in hypothesis testing are formally expressed as the *null hypothesis* (H_0) and the *alternative hypothesis* (H_A). By assuming true ZWD value is known beforehand, the GNSS ZWD can be deemed adequate (in a statistical sense) if H_0 is not rejected. For example, since RS ZWD estimates are often used as the benchmark, one may set up the hypothesis in such a way that the RS solutions are deemed as the *true* values. That is,

$$H_0 : \ ZWD_{GNSS} = ZWD_{RS} \tag{5.2}$$

$$H_A : ZWD_{GNSS} \neq ZWD_{RS} \tag{5.3}$$

The test statistic, i.e. a one-sample t-test, to help test the hypothesis is given as (e.g., Montgomery, 2005; Walpole *et al.*, 2007),

$$t_{OBS} = \frac{ZWD_{GNSS} - ZWD_{RS}}{s_{ZWD_{GNSS}}} \quad \text{with (n-1) degrees of freedom} \tag{5.4}$$

where $s_{ZWD_{GNSS}}$ is the error estimate of the LS GNSS ZWD estimate. The t-statistic is developed under the assumption that data is normally distributed, and that prior

information regarding the true variance σ^2 is unknown. The variance of the GNSS ZWD estimate ($s^2_{ZWD_{GPS}}$) is given by the diagonal entry of the covariance matrix, given by Eq. (3.27), corresponding to the (mean) ZWD estimate from the LS process. The null hypothesis H_0 in Eq. (5.2) is rejected if $|t_{OBS}| > t_{\alpha_s/2,n-1}$, where $t_{\alpha_s/2,n-1}$ denotes the upper $\alpha_s/2$ percentage point of the t-distribution. The quantity α_s is the level of significance.

If H_0 is not rejected, the test concludes that there is *no significant statistical difference* (NSSD) between the GNSS and RS ZWD estimates and thus, indicating that the error estimate provides a realistic measure of the quality of the LS ZWD solution. This error information can then be used to weight the ZWD observations in the NWP assimilation process. The hypothesis test can also be performed between the GNSS ZWD estimates and that of WVR or VLBI.

An alternative to a two-sided hypothesis test is through the use of a $(100-\alpha_s)\%$ confidence interval (CI) for the GNSS ZWD estimates. If the test value, ZWD_{RS} for example, falls within the CI, then H_0 is not rejected. A $(100-\alpha_s)\%$ CI forms the basis of a quality control chart (Montgomery, 2001). A control chart, given by Figure 5.1, consists of a centre line that represents the average value of the estimate, and two horizontal lines, called the *lower control limit* (LCL) and *upper control limit* (UCL), above and below the centre line. The control limits are chosen such that the majority of the sample points will fall between them.

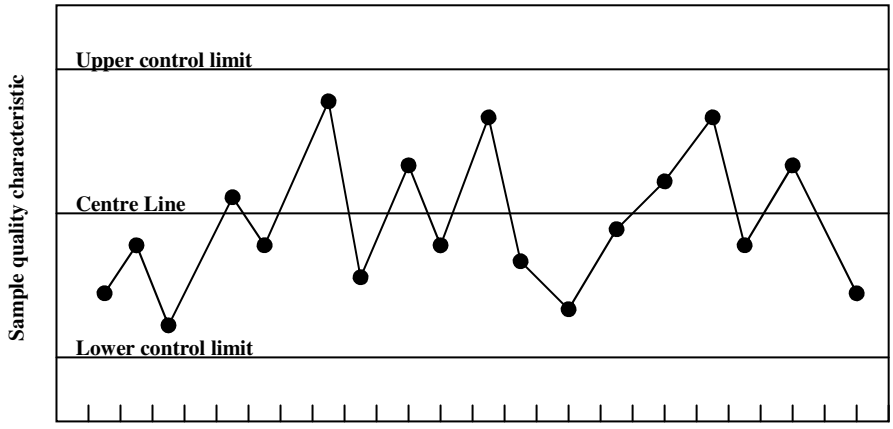

Figure 5.1 A typical control chart (source: Montgomery, 2001)

The mean and control limits, in reference to GNSS ZWD estimates, are given as:

$$\text{UCL} = \text{ZWD}_{\text{GNSS}} + t_{\alpha_s/2} s_{\text{ZWD}_{\text{GNSS}}} \tag{5.10}$$

$$\text{Centre Line} = \text{ZWD}_{\text{GNSS}} \tag{5.11}$$

$$\text{LCL} = \text{ZWD}_{\text{GNSS}} - t_{\alpha_s/2} s_{\text{ZWD}_{\text{GNSS}}} \tag{5.12}$$

In process control, the typical value chosen for $t_{\alpha_s/2}$ is three (e.g., Montgomery, 2001). The LCL and UCL are then referred to as the "*three-sigma*" control limits (Montgomery, 2001). Any points outside of these limits are considered as *outliers* and an investigation into the cause can be taken. Too many outliers may indicate the existence of a bias and corrective action such as re-sampling of the data points may be necessary (Montgomery, 2001). Therefore, if a RS ZWD point falls outside of a GNSS LS ZWD control limits, it may be necessary to obtain a more reliable mean estimate (with control limits) by increasing the window size. A set of inner limits at two-sigma, called the *warning limits*, is often constructed in conjunction to the control limits at three-sigma (Montgomery, 2001).

The use of the t-distribution in Eqs. (5.10) and (5.12) is an alternative to the Fisher distribution (commonly known as the F-distribution) when constructing the control limits (or the confidence interval). A confidence interval with the F-distribution is constructed in the "collective" sense in that the remaining LS parameter coefficients, i.e. the coordinate partials, the ambiguities, etc., are taken into consideration. However, the t-distribution is preferred over the F-distribution by practitioners when constructing the CI for individual parameter estimates as the precision of the interval is better (Johnson and Wichern, 2007). Therefore, the t-distribution will be used in this study when constructing the control limits for the ZWD or PWV estimates.

5.2 TROPOSPHERIC PARAMETER ERROR ESTIMATES

The impact of GNSS-estimated ZWD on weather forecasting is well documented (e.g., Kuo *et al.*, 1996; Vedel and Huang, 2003; Gutman *et al.*, 2004; Vedel and

Huang, 2004; Macpherson *et al.*, 2007). These studies reported small, but generally positive improvements in both the humidity and precipitation forecasts when GNSS ZWD estimates are assimilated into NWP models. However, a proper statistical description of the assimilated data is essential in improving NWP modelling (Vedel and Huang, 2004; Guo *et al.*, 2005). The estimation of the observation error covariance matrices is a very challenging prospect in data assimilation (Buehner *et al.*, 2005). The true impact of GNSS ZWD on NWP cannot be realised unless the error covariance matrix is correctly defined (Kuo *et al.*, 1996). Even if the quality of the assimilated data is poor, improvement in the NWP analysis can be expected as long as the error information is given correctly (Huang and Vedel, 2003).

A crude way to define the error structure of the to-be-assimilated GNSS ZWD estimates is to determine the statistical offsets (i.e. RMSE) between measurements of the GNSS-estimated ZWD and that of the NWP model analysis prior to the assimilation (Huang and Vedel, 2003). The resulting offsets provide the upper limits for error analysis. Koizumi and Sato (2004) similarly calculated the RMSE of the differences between the observed GNSS ZWD and the average ZWD estimates generated from the surface temperature and pressure profiles. The error estimates were taken as approximately half of the RMSE value. GNSS meteorology studies in recent times have assimilated slant wet delays (SWD) or slant ZWD into NWP models rather than the zenith measurements (e.g., Ha *et al.*, 2003; Eresmaa and Jarvinen, 2006; Eresmaa *et al.*, 2007; Järvinen *et al.*, 2007; Liu *et al.*, 2007). The GNSS SWD estimates are generated by mapping the ZWD, which is firstly estimated through the standard LS process, to various angles. The corresponding LS ZWD error estimates can also be used to provide a precision estimates for the slant delays (e.g., Ha *et al.*, 2003). Therefore, proper modelling of the zenith measurement errors structures are still important regardless. The error estimates of the GNSS ZWD data can also be derived from comparisons with measurements from other atmospheric sensors (Huang and Vedel, 2003) or from theoretical arguments (e.g., error estimates of the LS solutions).

The GNSS tropospheric solutions from several studies (e.g., Basili *et al.*, 2003; Wang *et al.*, 2007), including that of the IGS , are derived through the use of large networks. Error estimates resulting from the LS adjustment of large networks are

often very small and not reflective of the quality of the tropospheric solution. Section 5.2.1 will demonstrate such a scenario, and Sections 5.2.2 and 5.2.3 will investigate the cause of these small error estimates.

5.2.1 Assessing the Error Estimates of the GNSS ZWD Solutions

Figure 5.2 shows a plot of PWV in the atmosphere over the Townsville (TOW2) region in Australia. RS estimates (shown as triangles) from a nearby RS launch site (30 km from the GNSS station) are plotted along these GNSS PWV estimates. The RS PWV estimates were provided instead of ZWD for this campaign. The hourly GNSS PWV solutions (estimated at every major hour) for Townsville are generated as a part of a 24-h window solution for a network of stations. The processing strategy of the network is outlined in Chapter 6.

The relationship between the GNSS and RS PWV estimates is displayed in Figure 5.3. A regression correlation R_{reg} value of $\sqrt{0.8873} = 0.9420$ indicates a strong linear association. The RMSE of the PWV differences is 1.95mm.

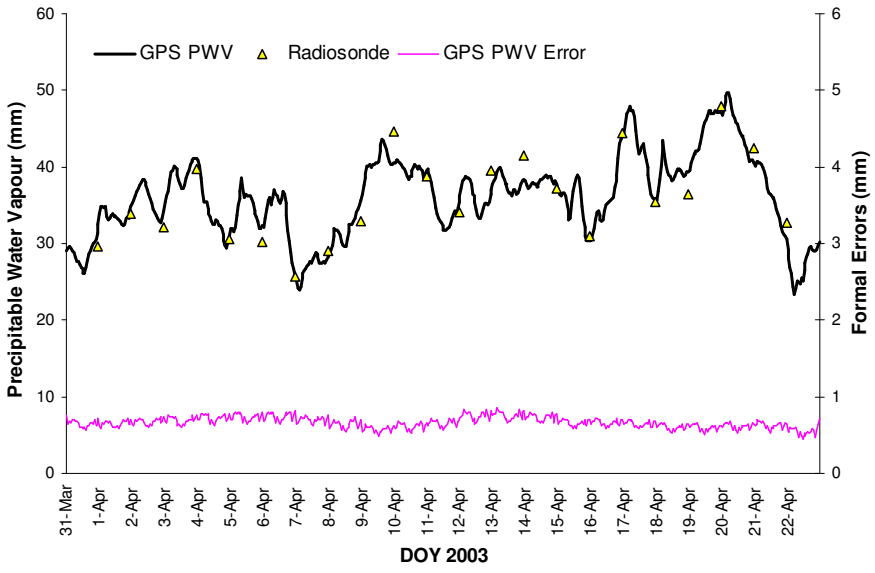

Figure 5.2 Comparison between GNSS (line) and RS (triangles) PWV estimates at Townsville (TOW2)

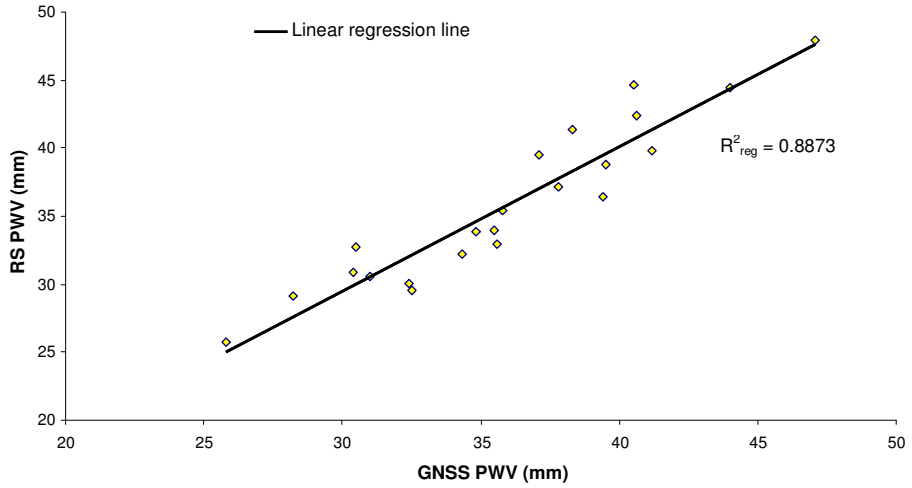

Figure 5.3 Regression plot between the GNSS and RS PWV estimates at TOW2

However, there is only one RS measurement available for comparison per day and as such, the number of GNSS PWV estimates that can be validated is limited. Unfortunately, there are no WVR data available at TOW2.

In the absence of independent RS data to assess these remaining GNSS PWV estimates, the only source of error information comes from the parameter error estimates generated via the LS adjustment process. Figure 5.4 and 5.5 indicates that according to the three-sigma control limits (see Eqs. (5.10) - (5.12)) only six out of the 22 GNSS PWV are in statistical agreement with the RS PWV). Hence, the majority of PWV solutions are biased. This also shows that the error estimates derived from the LS adjustment process are not a reliable a source of error information, which is essential in the NWP assimilation process.

The inadequacy of the error estimates from the LS adjustment process (see Eq. (3.31)) for assessing the quality of the GNSS PWV estimates may be attributed to the misspecification of the underlying stochastic model, and that a properly defined stochastic model should be able to provide more dynamic and realistic errors for the PWV estimates.

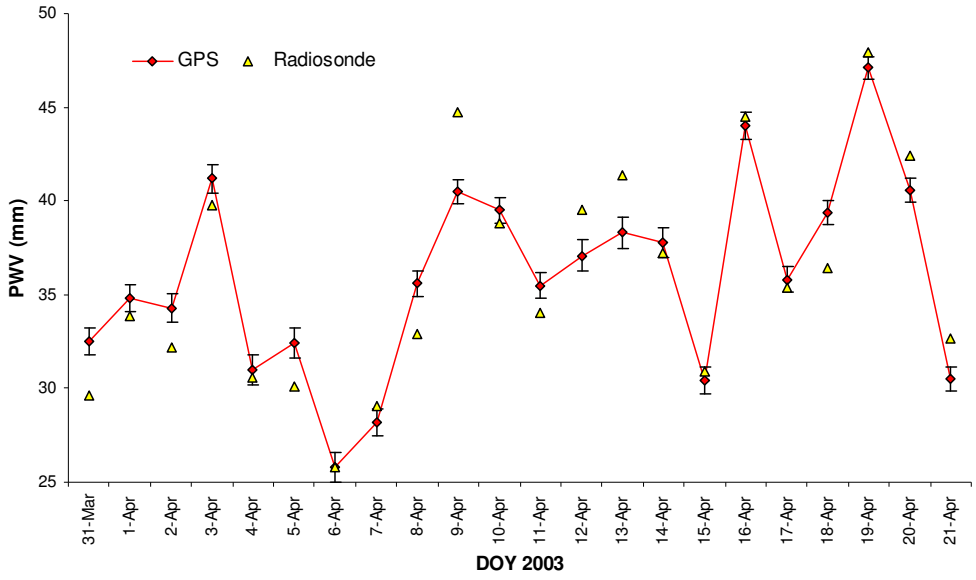

Figure 5.4 Plot of GNSS PWV with error bars at three-sigma against RS PWV

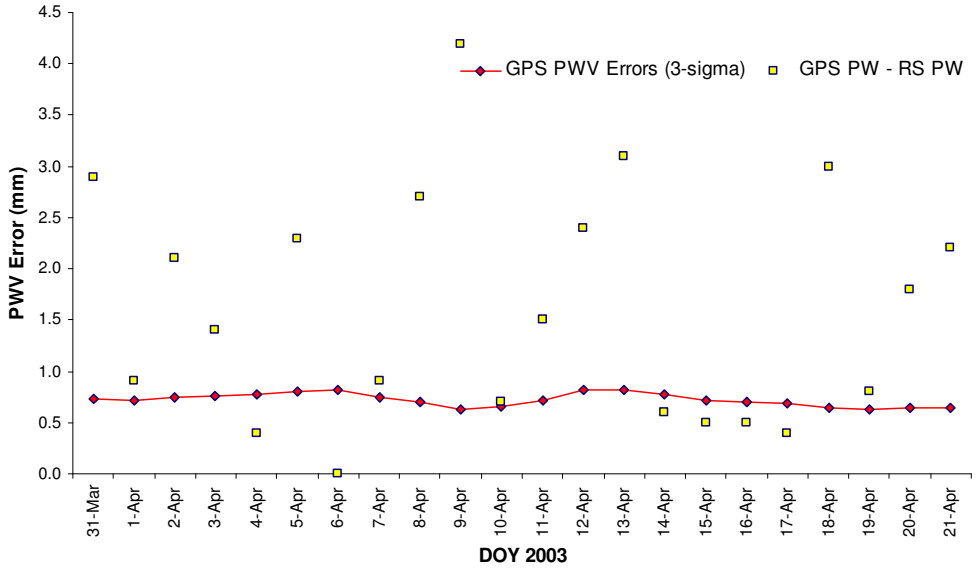

Figure 5.5 Plot indicating that only six out of 22 (below the 3-sigma error line) GNSS PWV estimates are in agreement with the RS PWV estimates

Larger error estimates however, imply lesser *precision* and therefore are not desirable. Greater redundancy is thus, often introduced to mitigate these errors so that the corresponding parameter estimates are applicable in practice (Seeber, 2003). For the coordinate correction and ambiguity parameters, this approach is justified since these parameters are theoretically time-invariant (in static GNSS applications). In an error-free environment, the station coordinate corrections will always be zero

(if the station is known) and the ambiguities are fixed integer values regardless of time. Each time a sample is taken, these values would not change. Therefore by increasing sample redundancy, the LS estimates of the corrections and ambiguity parameters should converge to the theoretical or "true" values.

On the other hand, the tropospheric delays vary over time, even for static GNSS positioning. If the tropospheric delay is resolved hourly, then the correct modelling of the corresponding error estimates should in essence capture the variability around the mean tropospheric delay during that period. However, when more observations are added to a session, information on the tropospheric parameters are generally not updated, but rather adjusted in accordance to better coordinate solutions. Though the accuracy of the tropospheric estimates may improve to an extent due to better coordinates, the tropospheric error estimates may be adversely affected if the redundancy level is too high. The theoretical bases of the above argument are discussed in the following sections.

5.2.2 Impact on the Error Estimates from the LS Adjustment Process by Varying Processing Window Sizes

Suppose there are two hours of data, each with n_1 and n_2 number of observations respectively, to be processed for a baseline between stations R1 and R2. Without loss of generality, the ambiguity terms are assumed to have been resolved. Furthermore, other error sources such as clock corrections and ionospheric delays are also assumed to have been accounted for either through differencing or external models (see Chapter 3). The coordinates of R1 are assumed to be known and fixed. If the ZTD parameter is to be estimated in each hour, then the corresponding design matrices $A^{(i)}\ (i = 1, 2)$ and $\tilde{N} = A^T W A$ (Eq. (3.21)) are as follows:

For the first hour:

$$A^{(1)} = \begin{bmatrix} \frac{\partial f_1^{(1)}}{\partial x_{R2}} & \frac{\partial f_1^{(1)}}{\partial y_{R2}} & \frac{\partial f_1^{(1)}}{\partial z_{R2}} & \frac{\partial f_1^{(1)}}{\partial T_{R1}} & \frac{\partial f_1^{(1)}}{\partial T_{R2}} \\ \frac{\partial f_2^{(1)}}{\partial x_{R2}} & \frac{\partial f_2^{(1)}}{\partial y_{R2}} & \frac{\partial f_2^{(1)}}{\partial z_{R2}} & \frac{\partial f_2^{(1)}}{\partial T_{R1}} & \frac{\partial f_2^{(1)}}{\partial T_{R2}} \\ \vdots & \vdots & \vdots & \vdots & \vdots \\ \frac{\partial f_{n_1}^{(1)}}{\partial x_{R2}} & \frac{\partial f_{n_1}^{(1)}}{\partial y_{R2}} & \frac{\partial f_{n_1}^{(1)}}{\partial z_{R2}} & \frac{\partial f_{n_1}^{(1)}}{\partial T_{R1}} & \frac{\partial f_{n_1}^{(1)}}{\partial T_{R2}} \end{bmatrix}$$

$$= \begin{bmatrix} \Delta x & \Delta y & \Delta z & \Delta m_{R1}^{1} & \Delta m_{R2}^{1} \end{bmatrix} \tag{5.13}$$

$$\tilde{N}^{(1)} = \left(A^{(1)}\right)^{T} W^{(1)} A^{(1)} = \begin{bmatrix} SSQ_{\Delta x}^{(1)} & SCP_{\Delta x\Delta y}^{(1)} & SCP_{\Delta x\Delta xz}^{(1)} & SCP_{\Delta x\Delta m_{R1}^{1}}^{(1)} & SCP_{\Delta x\Delta m_{R2}^{1}}^{(1)} \\ SCP_{\Delta x\Delta y}^{(1)} & SSQ_{\Delta y}^{(1)} & SCP_{\Delta y\Delta z}^{(1)} & SCP_{\Delta y\Delta m_{R1}^{1}}^{(1)} & SCP_{\Delta y\Delta m_{R2}^{1}}^{(1)} \\ SCP_{\Delta x\Delta xz}^{(1)} & SCP_{\Delta y\Delta z}^{(1)} & SSQ_{\Delta z}^{(1)} & SCP_{\Delta z\Delta m_{R1}^{1}}^{(1)} & SCP_{\Delta z\Delta m_{R2}^{1}}^{(1)} \\ SCP_{\Delta x\Delta m_{R1}^{1}}^{(1)} & SCP_{\Delta y\Delta m_{R1}^{1}}^{(1)} & SCP_{\Delta z\Delta m_{R1}^{1}}^{(1)} & SSQ_{\Delta m_{R1}^{1}}^{(1)} & SCP_{\Delta m_{R1}^{1}\Delta m_{R2}^{1}}^{(1)} \\ SCP_{\Delta x\Delta m_{R2}^{1}}^{(1)} & SCP_{\Delta y\Delta m_{R2}^{1}}^{(1)} & SCP_{\Delta z\Delta m_{R2}^{1}}^{(1)} & SCP_{\Delta m_{R1}^{1}\Delta m_{R2}^{1}}^{(1)} & SSQ_{\Delta m_{R2}^{1}}^{(1)} \end{bmatrix} \tag{5.14}$$

For the second hour:

$$A^{(2)} = \begin{bmatrix} \frac{\partial f_1^{(2)}}{\partial x_{R2}} & \frac{\partial f_1^{(2)}}{\partial y_{R2}} & \frac{\partial f_1^{(2)}}{\partial z_{R2}} & \frac{\partial f_1^{(2)}}{\partial T_{R1}} & \frac{\partial f_1^{(2)}}{\partial T_{R2}} \\ \frac{\partial f_2^{(2)}}{\partial x_{R2}} & \frac{\partial f_2^{(2)}}{\partial y_{R2}} & \frac{\partial f_2^{(2)}}{\partial z_{R2}} & \frac{\partial f_2^{(2)}}{\partial T_{R1}} & \frac{\partial f_2^{(2)}}{\partial T_{R2}} \\ \vdots & \vdots & \vdots & \vdots & \vdots \\ \frac{\partial f_{n_1}^{(2)}}{\partial x_{R2}} & \frac{\partial f_{n_1}^{(2)}}{\partial y_{R2}} & \frac{\partial f_{n_1}^{(2)}}{\partial z_{R2}} & \frac{\partial f_{n_1}^{(2)}}{\partial T_{R1}} & \frac{\partial f_{n_1}^{(2)}}{\partial T_{R2}} \end{bmatrix}$$

$$= \begin{bmatrix} \Delta x & \Delta y & \Delta z & \Delta m_{R1}^{2} & \Delta m_{R2}^{2} \end{bmatrix} \tag{5.15}$$

$$\tilde{N}^{(2)} = \left(A^{(2)}\right)^{T} W^{(2)} A^{(2)} = \begin{bmatrix} SSQ_{\Delta x}^{(2)} & SCP_{\Delta x\Delta y}^{(2)} & SCP_{\Delta x\Delta xz}^{(2)} & SCP_{\Delta x\Delta m_{R1}^{2}}^{(2)} & SCP_{\Delta x\Delta m_{R2}^{2}}^{(2)} \\ SCP_{\Delta x\Delta y}^{(2)} & SSQ_{\Delta y}^{(2)} & SCP_{\Delta y\Delta z}^{(2)} & SCP_{\Delta y\Delta m_{R1}^{2}}^{(2)} & SCP_{\Delta y\Delta m_{R2}^{2}}^{(2)} \\ SCP_{\Delta x\Delta xz}^{(2)} & SCP_{\Delta y\Delta z}^{(2)} & SSQ_{\Delta z}^{(2)} & SCP_{\Delta z\Delta m_{R1}^{2}}^{(2)} & SCP_{\Delta z\Delta m_{R2}^{2}}^{(2)} \\ SCP_{\Delta x\Delta m_{R1}^{2}}^{(2)} & SCP_{\Delta y\Delta m_{R1}^{2}}^{(2)} & SCP_{\Delta z\Delta m_{R1}^{2}}^{(2)} & SSQ_{\Delta m_{R1}^{2}}^{(2)} & SCP_{\Delta m_{R1}^{2}\Delta m_{R2}^{2}}^{(2)} \\ SCP_{\Delta x\Delta m_{R2}^{2}}^{(2)} & SCP_{\Delta y\Delta m_{R2}^{2}}^{(2)} & SCP_{\Delta z\Delta m_{R2}^{2}}^{(2)} & SCP_{T_1\Delta m_{R2}^{2}}^{(2)} & SSQ_{\Delta m_{R2}^{2}}^{(2)} \end{bmatrix} \tag{5.16}$$

Columns one, two and three of the design matrices $A^{(1)}$ and $A^{(2)}$ in Eqs. (5.13) and (5.15) are the partial derivatives of station R2 with columns four and five being the tropospheric parameters for stations R1 and R2, respectively. The forms of the tropospheric parameters, Δm_{R1} and Δm_{R2}, are as described by Eq. (3.16). $W^{(1)}$ and $W^{(2)}$ are the weight matrices generated through either standard models such as the SSM or the EADM described in Section 4.1, or a more sophisticated model such as MINQUE, given in Section 4.2. The $A^{T}WA$ matrix for each hour are given as $\tilde{N}^{(1)}$ and $\tilde{N}^{(2)}$, respectively. The diagonal entries of the $\tilde{N}$ matrices are given by SSQ (sum of squares) of each individual columns, whilst the off-diagonal entries of the $\tilde{N}$ matrices are defined by SCP_{ij}, which refers to the sum of cross-product between

columns i and j (see Section 3.2.1). If the two hours of data are processed together, then the corresponding combined design matrix A and $\tilde{N}$ matrix are typically of the forms:

$$A = \begin{bmatrix} \frac{\partial f_1^{(1)}}{\partial x_{R2}} & \frac{\partial f_1^{(1)}}{\partial y_{R2}} & \frac{\partial f_1^{(1)}}{\partial z_{R2}} & \frac{\partial f_1^{(1)}}{\partial T_{R1}} & \frac{\partial f_1^{(1)}}{\partial T_{R2}} & 0 & 0 \\ \frac{\partial f_2^{(1)}}{\partial x_{R2}} & \frac{\partial f_2^{(1)}}{\partial y_{R2}} & \frac{\partial f_2^{(1)}}{\partial z_{R2}} & \frac{\partial f_2^{(1)}}{\partial T_{R1}} & \frac{\partial f_2^{(1)}}{\partial T_{R2}} & 0 & 0 \\ \vdots & \vdots & \vdots & \vdots & \vdots & \vdots & \vdots \\ \frac{\partial f_{n_1}^{(1)}}{\partial x_{R2}} & \frac{\partial f_{n_1}^{(1)}}{\partial y_{R2}} & \frac{\partial f_{n_1}^{(1)}}{\partial z_{R2}} & \frac{\partial f_{n_1}^{(1)}}{\partial T_{R1}} & \frac{\partial f_{n_1}^{(1)}}{\partial T_{R2}} & 0 & 0 \\ \frac{\partial f_1^{(2)}}{\partial x_{R2}} & \frac{\partial f_1^{(2)}}{\partial y_{R2}} & \frac{\partial f_1^{(2)}}{\partial z_{R2}} & 0 & 0 & \frac{\partial f_1^{(2)}}{\partial T_{R1}} & \frac{\partial f_1^{(2)}}{\partial T_{R2}} \\ \frac{\partial f_2^{(2)}}{\partial x_{R2}} & \frac{\partial f_2^{(2)}}{\partial x_{R2}} & \frac{\partial f_2^{(2)}}{\partial z_{R2}} & 0 & 0 & \frac{\partial f_2^{(2)}}{\partial T_{R1}} & \frac{\partial f_2^{(2)}}{\partial T_{R2}} \\ \vdots & \vdots & \vdots & \vdots & \vdots & \vdots & \\ \frac{\partial f_{n_2}^{(2)}}{\partial x_{R2}} & \frac{\partial f_{n_2}^{(2)}}{\partial y_{R2}} & \frac{\partial f_{n_2}^{(2)}}{\partial z_{R2}} & 0 & 0 & \frac{\partial f_{n_2}^{(2)}}{\partial T_{R1}} & \frac{\partial f_{n_2}^{(2)}}{\partial T_{R2}} \end{bmatrix} \tag{5.17}$$

$$\tilde{N} = A^T W A$$

$$= \begin{bmatrix} SSQ_{\Delta x}^{(1+2)} & SCP_{\Delta x \Delta y}^{(1+2)} & SCP_{\Delta x \Delta z}^{(1+2)} & SCP_{\Delta x \Delta m_{R1}^1}^{(1+2)} & SCP_{\Delta x \Delta m_{R2}^1}^{(1+2)} & SCP_{\Delta x \Delta m_{R1}^2}^{(1+2)} & SCP_{\Delta x \Delta m_{R2}^2}^{(1+2)} \\ SCP_{\Delta x \Delta y}^{(1+2)} & SSQ_{\Delta y}^{(1+2)} & SCP_{\Delta y \Delta z}^{(1+2)} & SCP_{\Delta y \Delta m_{R1}^1}^{(1+2)} & SCP_{\Delta y \Delta m_{R2}^1}^{(1+2)} & SCP_{\Delta y \Delta m_{R1}^2}^{(1+2)} & SCP_{\Delta y \Delta m_{R2}^2}^{(1+2)} \\ SCP_{\Delta x \Delta z}^{(1+2)} & SCP_{\Delta y \Delta z}^{(1+2)} & SSQ_{\Delta z}^{(1+2)} & SCP_{\Delta z \Delta m_{R1}^1}^{(1+2)} & SCP_{\Delta z \Delta m_{R2}^1}^{(1+2)} & SCP_{\Delta z \Delta m_{R1}^2}^{(1+2)} & SCP_{\Delta z \Delta m_{R2}^2}^{(1+2)} \\ SCP_{\Delta x \Delta m_{R1}^1}^{(1+2)} & SCP_{\Delta y \Delta m_{R1}^1}^{(1+2)} & SCP_{\Delta z \Delta m_{R1}^1}^{(1+2)} & SSQ_{\Delta m_{R1}^1}^{(1)} & SCP_{\Delta m_{R1}^1 \Delta m_{R2}^1}^{(1)} & 0 & 0 \\ SCP_{\Delta x \Delta m_{R2}^1}^{(1+2)} & SCP_{\Delta y \Delta m_{R2}^1}^{(1+2)} & SCP_{\Delta z \Delta m_{R2}^1}^{(1+2)} & SCP_{\Delta m_{R1}^1 \Delta m_{R2}^1}^{(1)} & SSQ_{\Delta m_{R2}^1}^{(1)} & 0 & 0 \\ SCP_{\Delta x \Delta m_{R1}^2}^{(1+2)} & SCP_{\Delta y \Delta m_{R1}^2}^{(1+2)} & SCP_{\Delta z \Delta m_{R1}^2}^{(1+2)} & 0 & 0 & SSQ_{\Delta m_{R1}^2}^{(2)} & SCP_{T_z \Delta m_{R2}^2}^{(2)} \\ SCP_{\Delta x \Delta m_{R2}^2}^{(1+2)} & SCP_{\Delta y \Delta m_{R2}^2}^{(1+2)} & SCP_{\Delta z \Delta m_{R2}^2}^{(1+2)} & 0 & 0 & SCP_{\Delta m_{R1}^2 \Delta m_{R2}^2}^{(2)} & SSQ_{\Delta m_{R2}^2}^{(2)} \end{bmatrix} \tag{5.18}$$

where $SSQ_{ii}^{(1+2)} = SSQ_{ii}^{(1)} + SSQ_{ii}^{(2)}$ $\qquad$ $SCP_{ij}^{(1+2)} = SCP_{ij}^{(1)} + SCP_{ij}^{(2)}$

The key point to notice from Eq. (5.18) is that the SSQs of the tropospheric parameters are unaffected (assuming no temporal correlation) in the combined matrix. Only the SSQs and any cross-product terms involving only the coordinate partials are updated. In this instance, the accuracy of tropospheric estimates for the first hour will generally improve due to the expected improvement made to the coordinate partial estimates by addition of the second hour of data. The fact remains, however, that the second hour of data does not contribute directly to the variability of the tropospheric parameters in the first hour, as demonstrated by the SSQ values. The increase in SSQ for the coordinate partials will lead to smaller errors not just for the

variables themselves, but also for the tropospheric error estimates since from Eq. (3.27):

$$\Sigma_{\hat{X}} = \hat{\sigma}^2 \mathrm{inv}\left(\tilde{N}\right) \tag{5.19}$$

where $\hat{\sigma}^2$ is the model error defined by Eq. (3.28). If a 24-h window session was used, and the tropospheric parameters are estimated hourly, the accumulation of the normal matrix, i.e. $\tilde{N}_{24} = \sum_{i=1}^{24} \tilde{N}^{(i)}$, will ensure a substantial increase in the SSQs and SCPs corresponding to the coordinate partials. The tropospheric parameter SSQs are again unaffected. When the inverse $\tilde{N}_{24}$ is taken, the ensuing tropospheric error estimates will be even smaller. However, an increase in the accuracy of the tropospheric parameters is undeniable. Thus, the circumstance here requires a compromise between having good tropospheric estimates (through improving coordinate partial estimates) and realistic error estimates.

For the cases where the coordinates of both stations are fixed, the $\tilde{N}$ matrix in Eq. (5.18) reduces to:

$$\tilde{N}^* = \begin{bmatrix} SSQ_{T_1}^{(1)} & SCP_{T_1T_2}^{(1)} & 0 & 0 \\ SCP_{T_1T_2}^{(1)} & SSQ_{T_2}^{(1)} & 0 & 0 \\ 0 & 0 & SSQ_{T_3}^{(2)} & SCP_{T_3T_4}^{(2)} \\ 0 & 0 & SCP_{T_3T_4}^{(2)} & SSQ_{T_4}^{(2)} \end{bmatrix} \tag{5.20}$$

The covariance matrix of the corresponding parameter estimates $\hat{X}^*$ is:

$$\Sigma_{\hat{X}^*} = \hat{\sigma}^2_{\tilde{N}^*} \mathrm{inv}\left(\tilde{N}^*\right) \tag{5.21}$$

In such scenarios, the estimation of the tropospheric parameter of $\tilde{N}^*$ can be seen as uncorrelated. In other words, independent analyses of Eqs. (5.14) and (5.16) will yield solutions identical to those of Eq. (5.20). The error estimates of $\hat{X}^*$ (diagonal entries of $\Sigma_{\hat{X}^*}$ in Eq. (5.21)), which are dependent on the overall model error $\hat{\sigma}^2_{\tilde{N}^*}$,

are however different to those derived from $\tilde{N}^{(1)}$ and $\tilde{N}^{(2)}$. Suppose $\hat{\sigma}_1^2$ and $\hat{\sigma}_2^2$ are the model errors, given in Eq. (5.19), of $\tilde{N}^{(1)}$ and $\tilde{N}^{(2)}$. If $\hat{\sigma}_1^2 \approx \hat{\sigma}_2^2$ then the resulting tropospheric parameter error estimates will be similar to those derived from Eq. (5.21). However, if the model errors are vastly different, i.e. $\hat{\sigma}_1^2 >> \hat{\sigma}_2^2$, then the error estimates in Eq. (5.21) for one hour will be underestimated whilst errors will be overestimated for the other hour as compared to those of $\tilde{N}^{(1)}$and $\tilde{N}^{(1)}$. Therefore, it would make sense to perform independent analysis of the normal matrices to obtain more realistic error estimates.

5.2.3 Impact on the Error Estimates from the LS Adjustment Process: Baseline versus Network

Without loss of generality, suppose a 1-h session of data were processed for a network of three stations, namely R1, R2 and R3. For argument's sake, suppose station R1 was chosen as the station common to both independent baselines of the network. Thus, the designated baselines are from R1 to R2, i.e., (1-2), and from R1 to R3, i.e. (1-3). Furthermore, the coordinates of station R1 are deemed to be known (i.e., fixed). With the same assumptions as stated in Section 5.2.2, the corresponding combined design matrix for the baselines is:

$$A = \begin{bmatrix} \frac{\partial f_1^{(1-2)}}{\partial(x,y,z)_{R1}} & \frac{\partial f_1^{(1-2)}}{\partial(x,y,z)_{R2}} & 0 & \frac{\partial f_1^{(1-2)}}{\partial T_{R1}} & \frac{\partial f_1^{(1-2)}}{\partial T_{R2}} & 0 \\ \frac{\partial f_2^{(1-2)}}{\partial(x,y,z)_{R1}} & \frac{\partial f_2^{(1-2)}}{\partial(x,y,z)_{R2}} & 0 & \frac{\partial f_2^{(1-2)}}{\partial T_{R1}} & \frac{\partial f_2^{(1-2)}}{\partial T_{R2}} & 0 \\ \vdots & \vdots & \vdots & \vdots & \vdots & \vdots \\ \frac{\partial f_{n_1}^{(1-2)}}{\partial(x,y,z)_{R1}} & \frac{\partial f_{n_1}^{(1-2)}}{\partial(x,y,z)_{R2}} & 0 & \frac{\partial f_{n_1}^{(1-2)}}{\partial T_{R1}} & \frac{\partial f_{n_1}^{(1-2)}}{\partial T_{R2}} & 0 \\ \frac{\partial f_1^{(1-3)}}{\partial(x,y,z)_{R1}} & 0 & \frac{\partial f_1^{(1-3)}}{\partial(x,y,z)_{R3}} & \frac{\partial f_1^{(1-3)}}{\partial T_{R1}} & 0 & \frac{\partial f_1^{(1-3)}}{\partial T_{R3}} \\ \frac{\partial f_2^{(1-3)}}{\partial(x,y,z)_{R1}} & 0 & \frac{\partial f_2^{(1-3)}}{\partial(x,y,z)_{R3}} & \frac{\partial f_2^{(1-3)}}{\partial T_{R1}} & 0 & \frac{\partial f_2^{(1-3)}}{\partial T_{R3}} \\ \vdots & \vdots & \vdots & \vdots & \vdots & \vdots \\ \frac{\partial f_{n_2}^{(1-3)}}{\partial(x,y,z)_{R1}} & 0 & \frac{\partial f_{n_2}^{(1-3)}}{\partial(x,y,z)_{R3}} & \frac{\partial f_{n_2}^{(1-3)}}{\partial T_{R1}} & 0 & \frac{\partial f_{n_2}^{(1-3)}}{\partial T_{R3}} \end{bmatrix} \quad (5.22)$$

where $\frac{\partial f_i}{\partial(x,y,z)} = \begin{bmatrix} \frac{\partial f_i}{\partial x} & \frac{\partial f_i}{\partial y} & \frac{\partial f_i}{\partial z} \end{bmatrix}$.

By representing the columns of the design matrix in Eq. (5.22) as:

$$A = \begin{bmatrix} \Delta_{R1} & \Delta_{R2} & \Delta_{R3} & \Delta m_{R1} & \Delta m_{R2} & \Delta m_{R3} \end{bmatrix} \tag{5.23}$$

the $\tilde{N}$ matrix can be computed as:

$$\tilde{N} = A^T W A = \begin{bmatrix} SSQ_{\Delta_{R1}}^{(1-2)+(1-3)} & SCP_{\Delta_{R1}\Delta_{R2}}^{(1-2)} & SCP_{\Delta_{R1}\Delta_{R3}}^{(1-3)} & SCP_{\Delta_{R1}T_1}^{(1-2)+(1-3)} & SCP_{\Delta_{R1}T_2}^{(1-2)} & SCP_{\Delta_{R1}T_3}^{(1-3)} \\ SCP_{\Delta_{R1}\Delta_{R2}}^{(1-2)} & SSQ_{\Delta_{R2}}^{(1-2)} & 0 & SCP_{\Delta_{R2}T_1}^{(1-2)} & SCP_{\Delta_{R2}T_2}^{(1-2)} & 0 \\ SCP_{\Delta_{R1}\Delta_{R3}}^{(1-3)} & 0 & SSQ_{\Delta_{R3}}^{(1-3)} & SCP_{\Delta_{R3}T_1}^{(1-3)} & 0 & SCP_{\Delta_{R3}T_3}^{(1-3)} \\ SCP_{\Delta_{R1}T_1}^{(1-2)+(1-3)} & SCP_{\Delta_{R2}T_1}^{(1-2)} & SCP_{\Delta_{R3}T3}^{(1-3)} & SSQ_{T_1}^{(1-2)+(1-3)} & SCP_{T_1T_2}^{(1-2)} & SCP_{T_1T_3}^{(1-3)} \\ SCP_{\Delta_{R1}T_2}^{(1-2)} & SCP_{\Delta_{R2}T_2}^{(1-2)} & 0 & SCP_{T_1T_2}^{(1-2)} & SSQ_{T_2}^{(1-2)} & 0 \\ SCP_{\Delta_{R1}T_3}^{(1-3)} & 0 & SCP_{\Delta_{R3}T_3}^{(1-3)} & SCP_{T_1T_3}^{(1-3)} & 0 & SSQ_{T_3}^{(1-3)} \end{bmatrix} \tag{5.24}$$

Eq. (5.24) shows that the SSQ of the coordinate partials (i.e. $SSQ_{\Delta_{R1}}^{(1-2)+(1-3)}$) and tropospheric parameter (i.e. $SSQ_{T_1}^{(1-2)+(1-3)}$) estimates of station R1 are updated and benefits from the addition of data from baseline (1-3). The LS estimates for the remaining two stations will adjust accordingly to the estimates of station R1. Improvements in the estimates of station R1 will impact the estimates of stations R2 and R3 similarly. It is also noticeable from Eq. (5.24) that the SSQ of the tropospheric parameters for stations R2 and R3 are unaffected by the merging of the baseline data sets. Therefore, the corresponding tropospheric error estimates are likely to be underestimated. Network constraints for the coordinates can be implemented to stabilise the network solutions. Inclusion of these constraints can improve the geodetic solution and hence, reduce the model error $\hat{\sigma}^2$. The tropospheric estimates will improve as a by-product of the improved coordinate solutions. The corresponding tropospheric error estimates will reflect this improvement and become smaller. However, the fact remains that the tropospheric estimates are only adjusting to better resolution of the coordinate solutions. The tropospheric SSQ terms of stations R2 and R3 still remain unchanged. Relative tropospheric constraints between subsequent tropospheric parameters of the same station can also be used, though it is not necessary for tropospheric estimation intervals longer than 1-h (e.g., Hugentobler *et al.*, 2001).

The impact on the error estimates may not be as great for a small network as demonstrated here. However, for a large network, the formal errors will become even smaller. The stations that will benefit from a large network are those that appear multiple times amongst the designated baselines. However, it is likely that one or more of the stations will appear in only one of the baselines. Although the LS geodetic and tropospheric solutions of such stations will adjust and profit from the improvement in the estimates of other stations, the error estimates will nevertheless be grossly affected by the increased redundancy level. Given that precise coordinates are available from external sources for most GNSS stations, a large network may not be necessary in GNSS processing. Chapter 6 will explore whether or not a simple baseline with known station coordinates will suffice in providing good tropospheric parameter and realistic error estimates.

5.3 CHAPTER SUMMARY

GNSS processing is often implemented over a large network with a 24-h processing window to obtain highly precise tropospheric estimates (e.g., Wang *et al.*, 2007). However, the magnitudes of the resulting error estimates of GNSS PWV/ZWD are often very small, and thus are not appropriate for assimilation in NWP models. From Eqs. (3.27) and (3.28), the tropospheric error estimates are dependent on (1) the model error $\hat{\sigma}^2$, and (2) the stochastic model. Issues regarding the specified stochastic model were addressed earlier in Chapter 4. The model error in turn is dependent on the number of observations. The dependence of the LS error estimates on the observation number is a fact that is often overlooked. GNSS ZTD estimates are traditionally estimated with a rigid 24-h window data in a large network of stations (e.g., Wang *et al.*, 2007). In a 24-hr window, the number of observations can exceed the thousands for a network. Consequently, it is expected that the tropospheric parameter error estimates are statistically small. It is also not uncommon that larger windows (72-h) are considered (e.g., Glowacki *et al.*, 2006).

Given that the coordinates of the majority of the GNSS stations worldwide are accurately known, it is feasible to acquire sensible ZTD results with a smaller network of highly constrained stations, or even just a single baseline. The combination of downgrading window size and network thus may have a positive

impact on the error estimates without severely impacting the quality of the ZTD estimates in a negative manner. The impact of a smaller window across different stochastic models on the GNSS PWV/ZWD estimates, and the corresponding error estimates, are investigated and discussed in Chapter 6.

CHAPTER 6

GNSS ZWD ESTIMATION - RESULTS AND ANALYSES

6.0 INTRODUCTION

The issues put forward in Chapters 4 and 5 are tested in this chapter. They are:

(1) To investigate the estimation of GNSS tropospheric delay and its error estimates using a baseline and a reduced processing window size;
(2) To investigate the impact of stochastic modelling on the GNSS tropospheric estimation over long processing windows and long baselines.

Section 6.1 provides the analysis using an Australian-wide GNSS network over a 3-week campaign carried out in 2004. The LS solutions from this network analysis will provide some insight into the appropriateness of the corresponding tropospheric error estimates as a dependable source of error information, in periods where there are no external data readily available for validation purposes. Section 6.2 investigates the impact of reducing the size of the session window, as discussed in Section 5.2.2, on the LS estimation of the ZWD and its error estimates via the use of *simulation* data. In addition, the MINQUE method, given in Chapter 4, will be implemented to analyse its impact on GNSS height and tropospheric solutions. Results from MINQUE and its variations, will be compared to the more conventional models such as EWM and EADM.

Next, the assessment of these stochastic methods is performed based on *real* GNSS data are summarised in Section 6.3. These investigations were carried out on Australian GNSS stations. RS data are chiefly used by Australian meteorologists for atmospheric profiling. Thus, the number of comparisons is limited in the third study. To further emphasise the results in Section 6.3, a follow-up study was conducted using a baseline campaign between two European stations where WVR data were

available, and multiple comparisons can be made daily. The results of this study are presented in Section 6.4.

Assessment of the error estimates of the GNSS LS tropospheric solutions from each of the aforementioned stochastic models was also performed. The error estimates of the GNSS solutions were gathered and used to construct the confidence (or error) intervals. These intervals are used to determine if the error estimates were adequate as a dependable source of error information to assess the invalidated tropospheric estimates. Behrend *et al.* (2002) briefly commented on the statistical aspects of error analysis between independent atmospheric sensors (VLBI, GNSS, WVR and NWP models) but no values were actually presented. The error analysis presented here will hopefully provide some insights into the extent in which the error estimates can be considered useful.

6.1 ANALYSIS OF THE AUSTRALIAN GNSS STATIONS

Australia boasts many different climatic regions, including the tropical north of Australia, the Mediterranean of the south-west, the humid and cool subtropical of the east, and the arid centre of Australia (BoM, 2008a). Atmospheric profiling in Australia is heavily dependent on RS soundings to provide accurate upper air temperature and humidity measurements (BoM, 2008b). According to the Integrated Global Radiosonde Archive (IGRA), there are currently around 45 established RS sites in Australia (NOAA, 2008), which is fairly low in comparison with the size of the country. The aims of this section are:

- To demonstrate the potential of GNSS as a reliable atmospheric sensor to complement RS;
- To determine the appropriateness of the error estimates of the LS PWV solutions as a dependent source of error information at times where there are no RS data to validated the GNSS PWV solutions.

Data from a three-week period were selected for the analyses of the Australian campaigns. The chosen period dates from the 31st March to 21st April 2003,

corresponding to the autumn season. This period has high diurnal variation and it allows GNSS to demonstrate its capability under varying atmospheric conditions. Geoscience Australia (http://www.ga.gov.au), IGS and Land Victoria, provided the GNSS data sets for the campaign. The Australian Fiducial Network (AFN) and Land Victoria are the sources of all GNSS data. The AFN consists of eight geodetic quality GNSS receivers distributed over the whole of Australia. The Darwin, Melbourne, Townsville, Alice Spring and Karratha station are among the tested locations. Moreover, additional data from the GNSS stations around the State of Victoria were incorporated in the analysis process to strengthen the network analysis, as well as providing a glimpse into the potential of the Victorian network as a major source of GPSMet (GPS Meteorology) data given its density (see Figure 6.2). The Australian Bureau of Meteorology (BoM) also supplied the corresponding PWV estimates retrieved via RS (at 0:00 and/or 12:00 UTC) for validation purposes, together with other relevant surface meteorological data such as temperature and pressure data. These atmospheric data allow the ZHD to be extracted from the LS ZTD via Eq. (2.30), and what remains is assumed to be the ZWD, which will then be converted to PWV (see Eqs. (2.31) and (2.32)), thus enabling a direct comparison to the RS PWV data.

All data were processed with the Bernese GNSS software (version 4.2) package (Hugentobler *et al.*, 2001). Data included in the processing also comprises the IGS products concerning the monitoring stations, satellite ephemerides, Earth Orientation Parameters (EOPs), coordinates and velocity of ground stations, antenna phase centre offsets and variations. During processing, the station coordinates, satellite and receiver clock offsets and the tropospheric zenith delay were estimated. The processing parameters include a cut-off elevation angle of 15^0, the Niell (1996) MFs, and the Saastamoinen (1972) tropospheric model, which was used to provide *a-priori* ZTD estimates. The *ionosphere-free* linear combination (e.g., Leick, 2004) was implemented to mitigate the ionospheric residual errors. Data from 34 GNSS stations were analysed (See Figures 6.1 and 6.2).

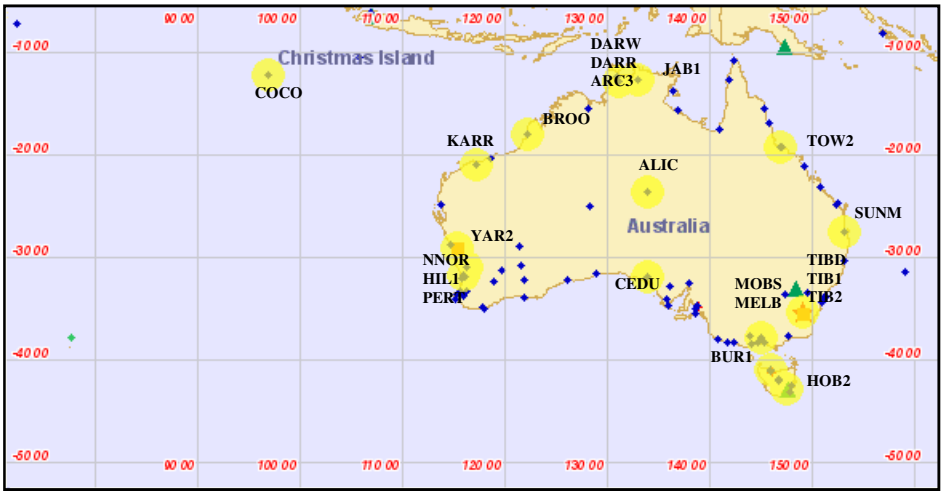

Figure 6.1 IGS Stations around Australia (http://itrf.ensg.ign.fr/)

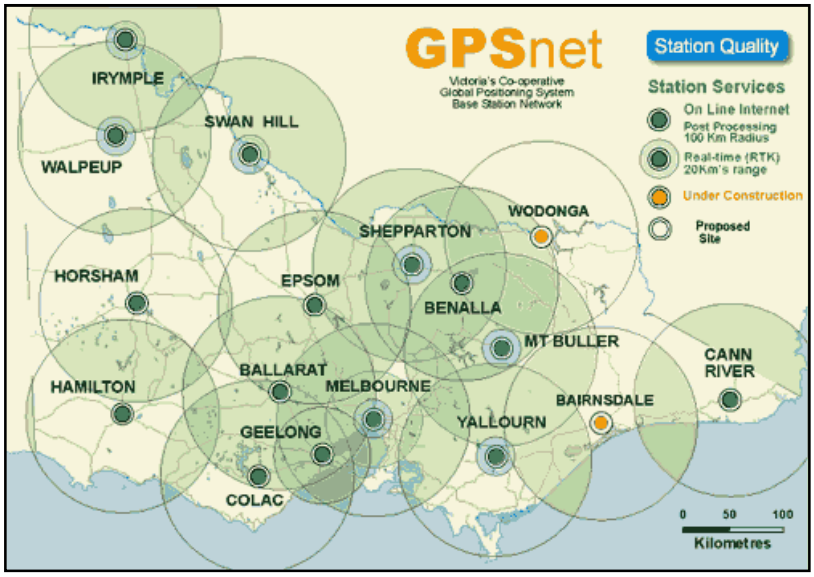

Figure 6.2 GNSS stations in the state of Victoria (http://www.land.vic.gov.au/)

These stations were divided into three separate campaigns depending on to their locations, which will be referred to as: (1) the Southern Campaign (2) the North-eastern Campaign, and (3) the Western Campaign. The North-eastern and the Western campaigns each consist of seven stations. The Southern campaign involved the remaining 23 stations, where the majority of the selected sites are from the state of Victoria, as shown in Figure 6.2. The division of the stations is for reducing the computational workload whilst ensuring the accuracy and precision of the parameter solutions are not negatively impacted (e.g., Haase *et al.*, 2003). The processing strategy is similarly to that which is recommended by Hugentobler *et al.* (2001).

The raw GNSS code pseudorange and carrier phase data (in RINEX format) were firstly converted to Bernese (Version 4.2) format prior to any post-processing. After the data conversion, the clock errors were then estimated with the code observables by the built-in *CODSPP* program. The estimated (approximate) clock errors were later accounted for in the carrier phase observables. The *CODSPP* program provided *a-posteriori* positional error estimates to check if the quality of the measurements warrants further processing. Single-difference (SD) code and phase observations were then generated with the *SNGDIF* program and stored as files. These SD observations, and not the raw data, were used to generate DD observations (Eq. (3.6)) in the parameter estimation process. If the campaign involved m receivers, the program *SNGDIF* generates m-1 independent baselines from which the SD observations (Eq. (3.4)) were determined. The SD observations then underwent a cycle-slip detection/repair process in *MAUPRP* and corrected for large discontinuities in the receiver clock on a SD level. The triple-differencing technique (e.g., Goad *et al.*, 1996; Leick, 2004; Chen *et al.*, 2005) was also employed for the detection of cycle-slips that were more subtle. Once the SD data is "cleaned", the post-processing of the DD observations began by implementing the *GPSEST* program. The *GPSEST* program utilised the LS principle in the parameter estimation process (see Section 3.2). The parameter estimation procedure involved three stages. In the initial stage, the ionospheric-free observations and the Saastamoinen (1972) model, given by Eq. (2.37), was used to account for the tropospheric delays in the initial stage so that the float ambiguities can be estimated. The ambiguities, which are dependent on the baseline length and observation window, for all baselines are then resolved (if possible) to their integer values separately in the succeeding processing stage with the aid of the QIF (Quasi-Ionosphere-Free) ambiguity resolution method. Details of the QIF, and other ambiguity resolution techniques (e.g., LAMDA, SIGMA, ROUND, etc.) are provided in Hugentobler *et al.* (2001). The integer ambiguities were then incorporated into the DD observations, from which the absolute tropospheric delay were estimated and mapped to the zenith direction (i.e. ZTD) with the NMF, given by Eq. (3.64), in the final stage. The final positional coordinates were also estimated in the LS adjustment process, given in Eq. (3.25). The processing procedure is summarised in Figure 6.3.

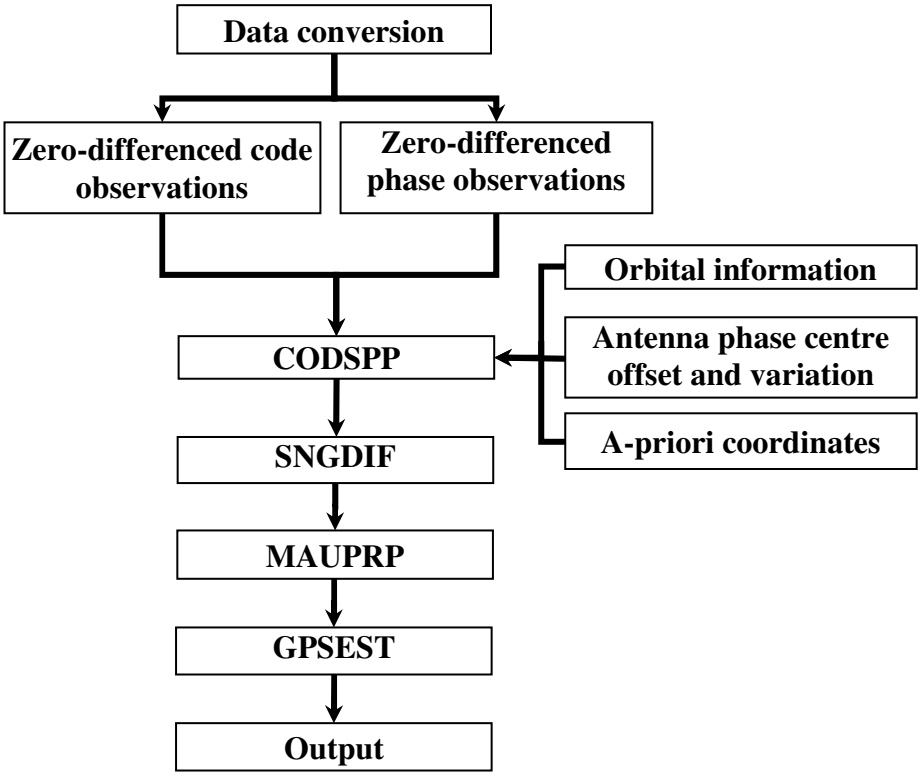

Figure 6.3 Data processing with Bernese GNSS software

Once estimated, the ZTD is then converted to PWV estimates using Eqs. (2.30) and (2.31), which can then be compared to the RS PWV estimates. Figures 6.4 to 6.9 illustrate the good agreement between the GNSS PWV (line) and RS PWV (triangles) solutions for some of the selected stations in each campaign.

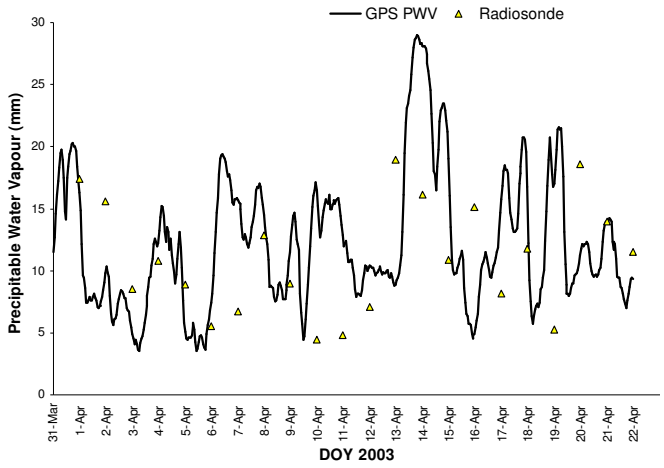

Figure 6.4 PWV plots at MAC1 for the Southern Campaign

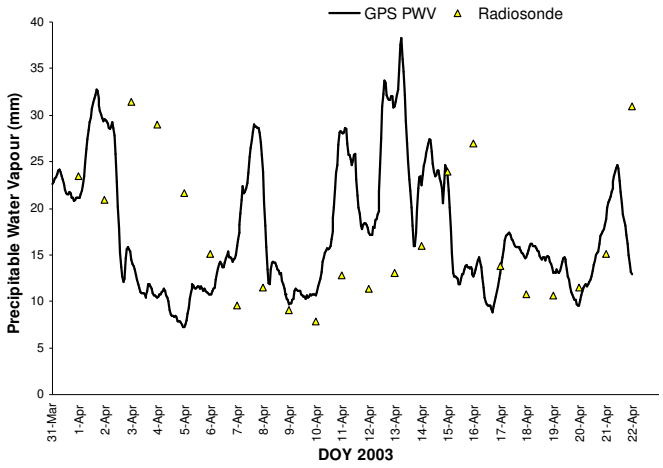

Figure 6.5 PWV plots at MOBS for the Southern Campaign

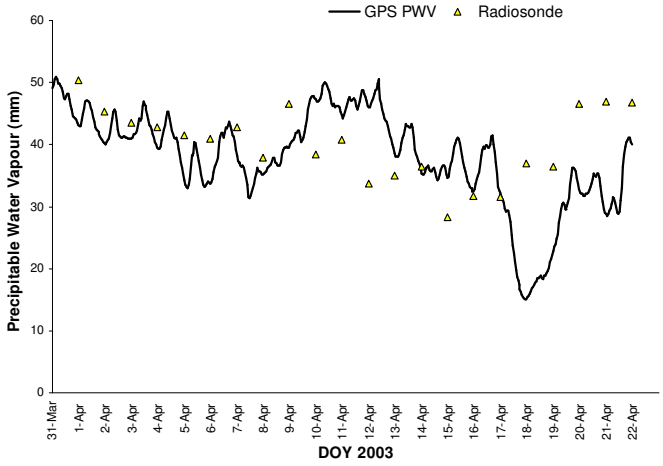

Figure 6.6 PWV plots at DARW for the North-eastern Campaign

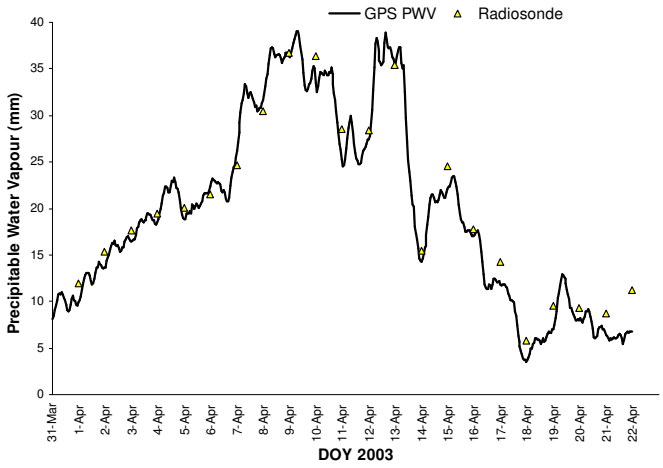

Figure 6.7 PWV plots at ALIC for the North-eastern Campaign

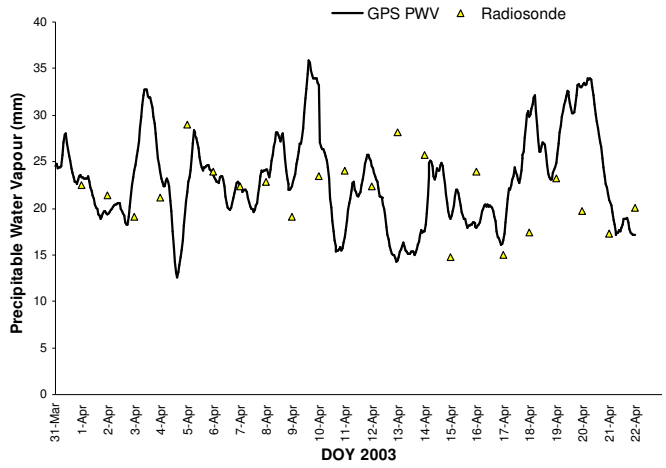

Figure 6.8 PWV plots at YAR2 for the Western Campaign

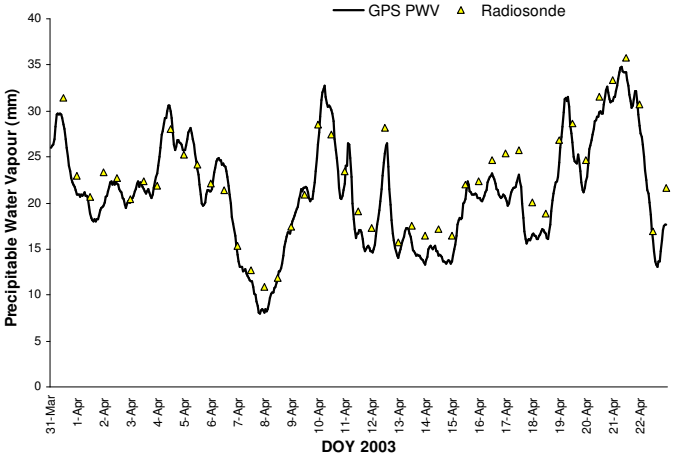

Figure 6.9 PWV plots at PERT for the Western Campaign

Using the RS PWV as the validation data, the quality of the GNSS-estimated PWV is defined by the RMSE expression given in Eq. (5.1). The number of RS data available each day for most stations is two. However, Townsville (TOW2) and Alice Springs (ALIC), for instance, have only one daily RS observation for comparison. The RMSE of the differences between the GNSS and RS PWV estimates for all stations are given in Tables 6.1 to 6.3. The distances between each of the GNSS stations and the nearest RS launch site are also presented in these tables. Note that the RS may rise and drift further away from the GNSS stations before any measurements are taken.

Table 6.1 RMSE of the GNSS-RS PWV differences for the Southern Campaign

Station	PWV RMSE (mm)	Approximate distance between the GNSS and radiosonde sites (km)	Number of RS per day
BALL	2.38	87	2
BENA	3.59	162	2
BUR1	3.29	237	2
CANN	3.41	306	1
CEDU	4.62	293	2
CLAY	2.14	37	2
COLA	2.14	132	2
EPSO	2.37	115	2
HAMI	1.74	109	1
HOB2	1.35	6	2
HORS	3.01	168	1
MAC1	1.28	1	2
MELB	1.51	18	2
MOBS	1.46	21	2
MTBU	2.06	154	2
SHEP	3.38	153	2
TID1	1.65	140	1
TID2	1.73	140	1
TIDB	1.47	140	1
YALL	2.91	142	2

Table 6.2 RMSE of the GNSS-RS PWV differences for the Northern Campaign

Station	PWV RMSE (mm)	Approximate distance between the GNSS and radiosonde site (km)	Number of RS per day
ALIC	2.04	14	1
ARC3	2.50	0.1	2
DARW	3.47	53	2
DARR	3.37	53	2
JAB1	5.39	218	2
SUNM	6.24	381	2
TOW2	1.95	30	1

Table 6.3 RMSE of the GNSS-RS PWV differences for the Western Campaign

Station	PWV RMSE (mm)	Approximate distance between the GNSS and radiosonde site (km)	Number of RS per day
BROO	1.58	0.2	1
COCO	3.16	0.1	2
HIL1	1.92	25	2
KARR	6.00	172	2
NNOR	3.08	99	2
PERT	2.16	16	2
YAR2	2.10	69	1

For the most part in Tables 6.1 to 6.3, the results from the analyses generally agree with previous studies such as Bevis *et al.* (1992) and Wang *et al.* (2007), whereby the RMSE*s* between the GNSS and RS PWV estimates are usually less than 2.5 mm, or at worst 3 mm. Stations attributed with relatively large (>3 mm) PWV RMSE can be justified by the fact that the distances between the GNSS and RS sites (with drifts) are large (>100km), therefore significant biases are not unexpected. KARR, SUNM and JAB1 are the main culprits. Although the RMSEs for COCO, DARW and DARR (co-located with DARW) are relatively high (considering the distance between the GNSS and RS sites are small), this is not unexpected. The COCO station is located on the Cocos Island and DARW and DARR are situated in the tropics, hence the atmospheric conditions are much more unstable than for the other stations. However, these values are consistent with the RMSEs reported by Glowacki *et al.* (2006).

Table 6.4 indicates that once the distance between a GNSS station and a RS launch sites reaches more than 150km, the discrepancy between the estimates becomes significant. Thus, RS data becomes unreliable as a source of validation data.

Table 6.4 RMSE of PWV estimates for various distances between the GNSS and RS sites

Distance (D) between the GNSS and RS site (km)	PWV RMSE (mm)
0<=D<=50	2.00
50<D<=100	2.98
100<D<=150	2.10
150<D<=200	3.97
D>200	4.78

Figures 6.10 to 6.14 show that the overall PWV differences become larger as the distances between the sites increases.

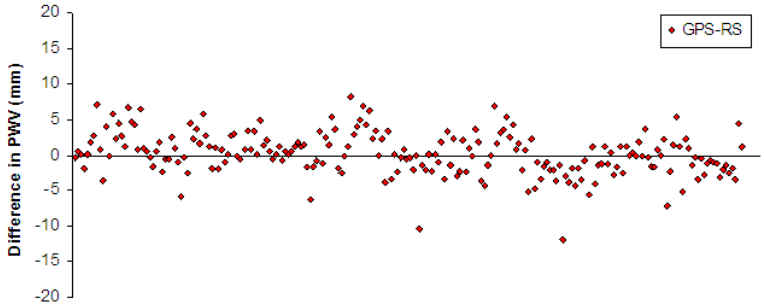

Figure 6.10 Plot of the differences between the GNSS and RS PWV whereby the distance between the GNSS and RS sites ranges from 0-50km

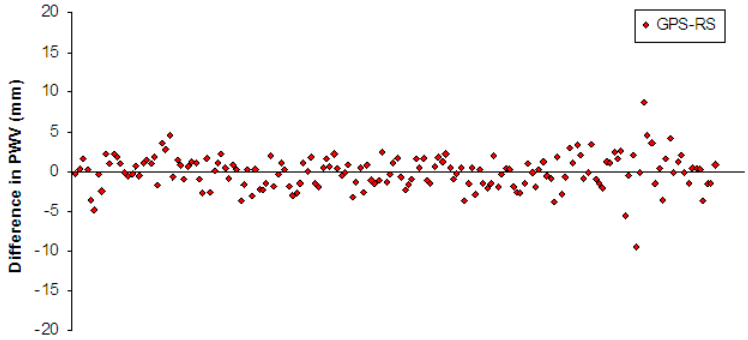

Figure 6.11 Plot of the differences between the GNSS and RS PWV whereby the distance between the GNSS and RS sites ranges from 50-100km

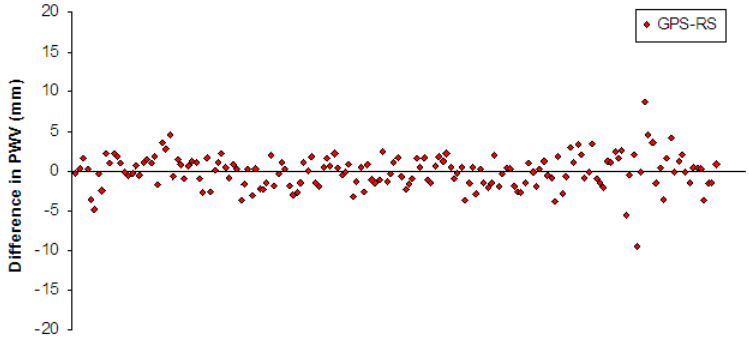

Figure 6.12 Plot of the differences between the GNSS and RS PWV whereby the distance between the GNSS and RS sites ranges from 100-150km

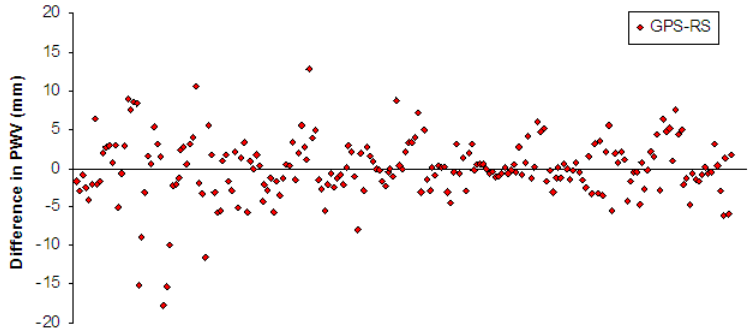

Figure 6.13 Plot of the differences between the GNSS and RS PWV whereby the distance between the GNSS and RS sites ranges from 150-200km

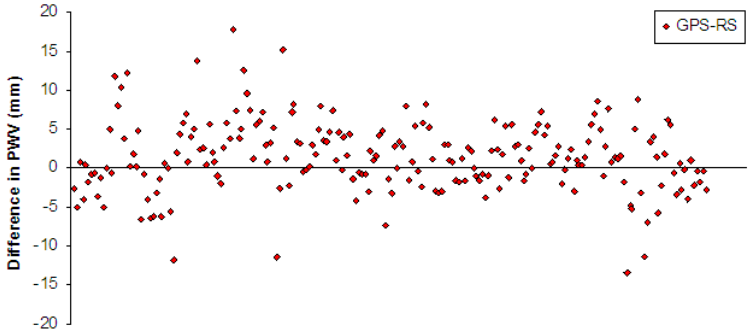

Figure 6.14 Plot of the differences between the GNSS and RS PWV whereby the distance between the GNSS and RS sites are greater than 200km

Results from the Australia-wide campaigns have demonstrated the capability of GNSS to produce reliable PWV estimates for stations across various climatic regions. However, at times where there are no RS or WVR data, the only other way to assess the GNSS PWV estimates is through its error estimates. Figure 6.15 is a plot of the error estimates of the GNSS PWV corresponding to the stations given by Figures 6.4 to 6.9.

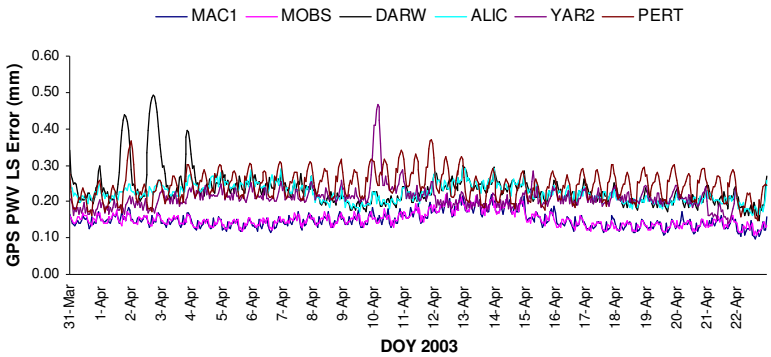

Figure 6.15 A plot of the error estimates of the GNSS PWV for various stations

As illustrated by Figure 6.15 and the case considered in Section 5.2.1, the error estimates of the GNSS PWV are very small (<0.5 mm in PWV) in comparison and, in general, are fairly constant over the time window, and thus, not very indicative of the dynamic nature of the atmospheric water vapour. Thus, Sections 6.2 to 6.4 aim to explore the impact of stochastic modelling and varying window session lengths on the error estimates of the GNSS tropospheric solutions to assess whether it is possible to obtain a set of error estimates that can be considered as a dependable source of error information for the actual GNSS tropospheric estimates.

6.2 WET DELAYS RECOVERY WITH SIMULATED DATA

Results from Section 6.1 shows that although GNSS can provide quality tropospheric solutions, however, the resulting tropospheric error (precision) estimates do not provide an adequate source of error information. One of the aims of this study is to explore whether or not the error estimates of the tropospheric estimates can be made more realistic to adequately reflect the quality of the GNSS tropospheric estimates without the aid of external measurements such as RS and WVR. Thus, the objectives of this section are to explore:

- The impact of stochastic modelling (as discussed in Chapter 4) on the error estimates of the GNSS LS tropospheric solutions;
- The effects of varying window session lengths on the error estimates of the GNSS LS tropospheric solutions.

The significance of their impacts on the error estimates of the GNSS tropospheric solutions is determined by constructing error or confidence intervals at one, two and three standard error as outlined in Section 5.1. Furthermore, the objectives are carried out with the view that the actual accuracies of the tropospheric estimates and the coordinate height solutions are not severely compromised. The investigations were carried out via simulation data initially as it allows the "observation noise" component to be controlled, and thus, the direct impact of various stochastic models and varying window sizes on the ZWD estimation can be assessed.

The simulation data used here were generated by simulating the satellite coordinates for a specified session, using the software developed at Curtin University by Penna and Stewart (2003). The software is GNSS orbital simulator that simulates a satellite's path with no perturbations. Therefore, for a particular location, the exact geometric range between the satellite and the receiver can be calculated, and the effect of different individual error sources readily assessed. The GNSS simulation software used can perform weighting by using the EWM, the EADM models, or any other arbitrary weighting schemes. Tropospheric delays, and/or any other error sources (e.g., multipath or random errors) determined through external functions, can also be accommodated.

In this test, simulated ZWD (SimZWD) values were also used. These SimZWDs were actual wet delay values determined from a 24-h GIPSY version 2.6 software in precise point positioning mode, estimating them every 5 minutes together with horizontal gradients, whilst holding fixed 'legacy' JPL (Jet Propulsion Laboratory) 'fiducial-free' orbital and Earth rotation products, and using the NMFs. SimZWD values were generated for the HOB2 IGS station from 1999 to 2004. A five-day period in 2004 from June 15th to 19th was chosen for this analysis as there was a large ZWD variability over these five days, ranging from 5mm to 16mm. As the SimZWDs were given at every 5-minute interval, the orbital simulator was also used to sample at the same interval length. For each observation of every epoch, the SimZWDs were added to the simulated LoS geometric ranges with the aid of the NMFs. Once all the SimZWDs have been incorporated into the simulated data, the LS analysis is then performed. Figure 6.16 shows a flowchart that describes the main procedure in the simulator.

Along with the coordinate partials, the weighted one-hourly LS ZWDs estimates were retrieved in the analyses. These LS ZWDs were then compared to the "averaged" SimZWDs across six different processing windows, selected to be 1-h, 2-h, 4-h, 6-h, 12-h and 24-h, and using the five different stochastic methods discussed in Chapter 4. These models are the EWM, the EADM, the MINQUE, the SMINQUE and the non-negative definite MINQUE (NND_MINQUE) models.

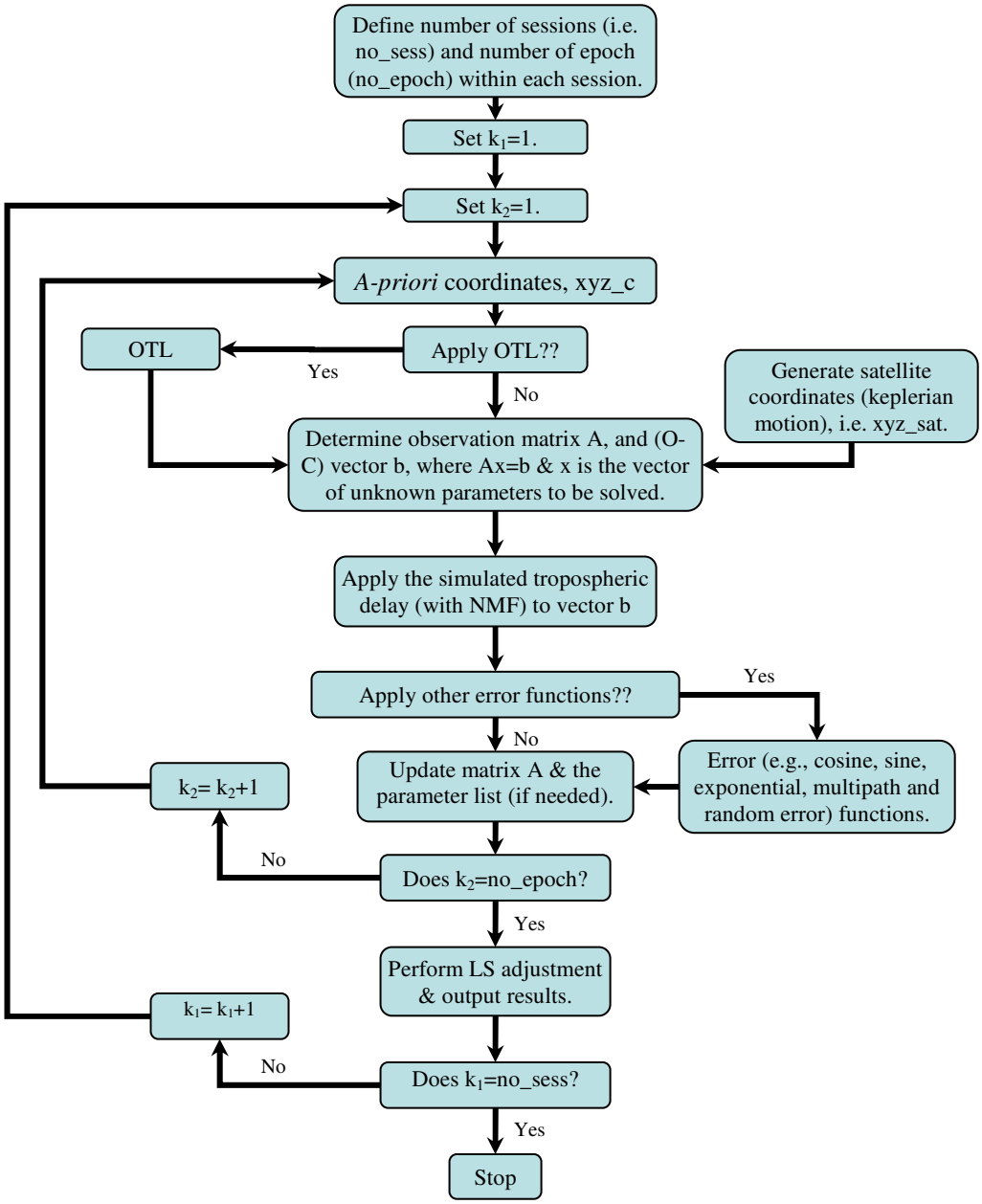

Figure 6.16 A flowchart describing the data simulation and analysis process

The non-negative MINQUE (NND_MINQUE) model is similar to that of EWM and EADM in that it involves only the estimation of the variances among the ZD observations. The NND_MINQUE is defined by Eq. (4.26). In discussing the results, MINQUE and SMINQUE will be referred to collectively as (S)MINQUE. The most important aspect of this simulation analysis is that no errors were applied to the observations besides tropospheric delay, i.e. the only present "error source" is the variability among the SimZWDs themselves within the hour. If the stochastic model is correctly chosen, one would expect the coordinate correction estimates to be

approximately zero and the output ZWD estimates to be similar to the (averaged) SimZWDs values for the processing window considered.

The height component of the coordinates is most affected by atmospheric delay (e.g., Bock *et al.*, 2001). As such, the height offsets resulting from the analysis were closely looked at. Figures 6.17 to 6.22 show the height offsets of each stochastic model resulting from varying the processing window size from 1-h to 24-h.

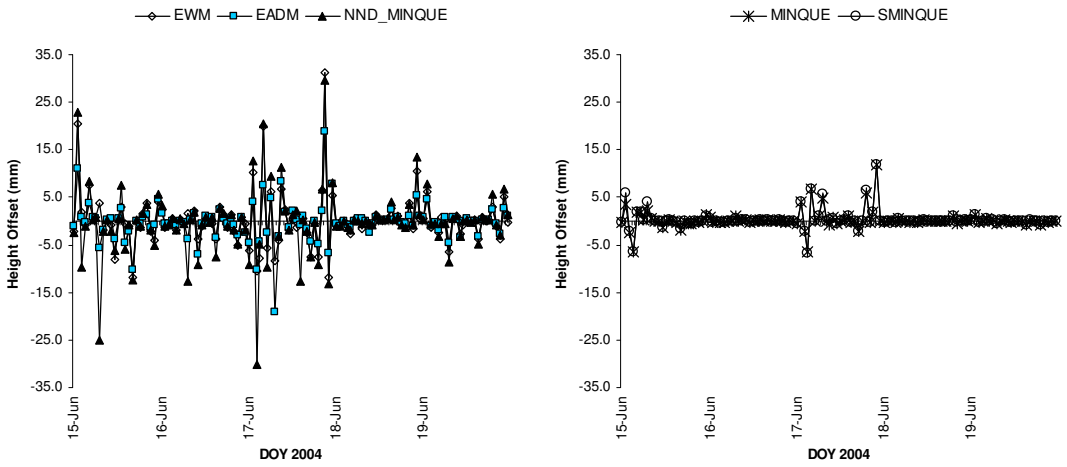

Figure 6.17 Height offsets resulting from the LS analysis with a 1-h processing window

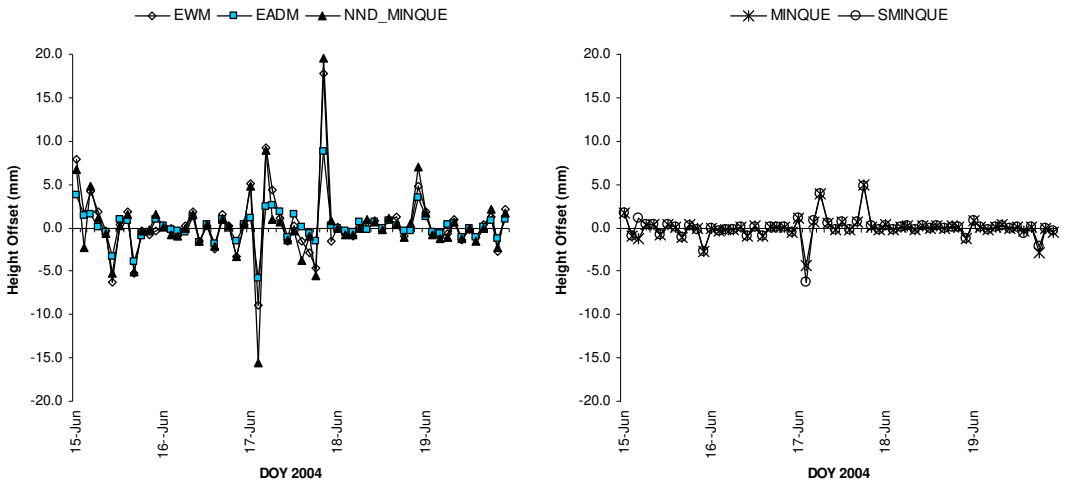

Figure 6.18 Height offsets resulting from the LS analysis with a 2-h processing window

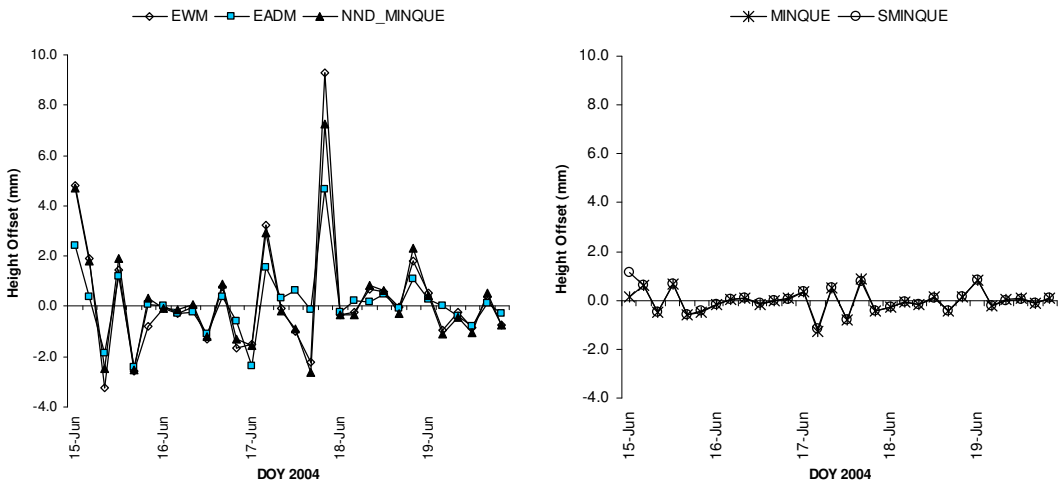

Figure 6.19 Height offsets resulting from the LS analysis with a 4-h processing window

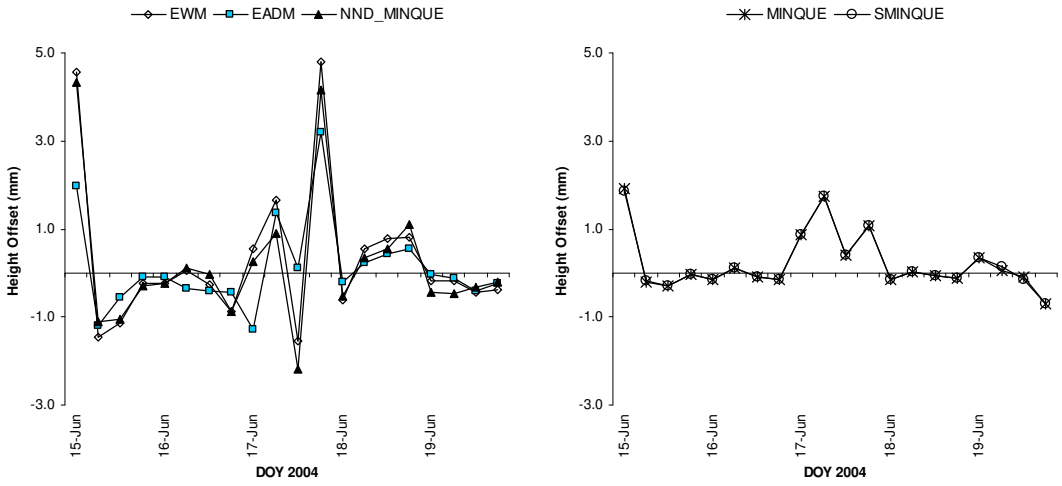

Figure 6.20 Height offsets resulting from the LS analysis with a 6-h processing window

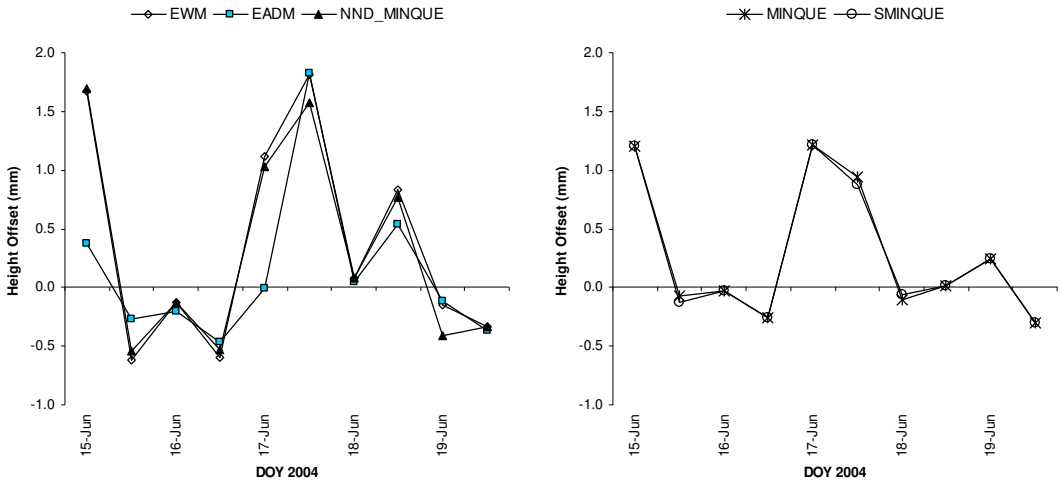

Figure 6.21 Height offsets resulting from the LS analysis with a 12-h processing window

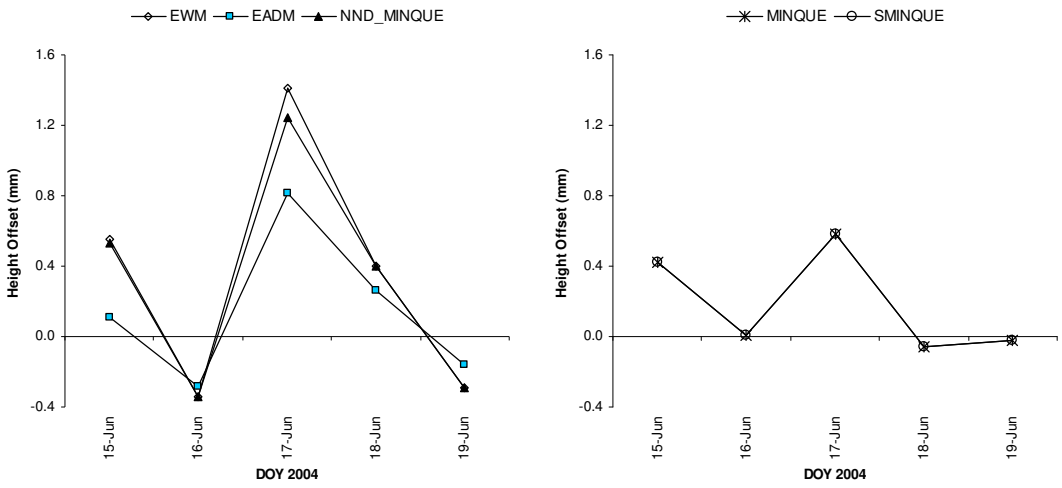

Figure 6.22 Height offsets resulting from the LS analysis with a 24-h processing window

It can be observed from Figure 6.17 that the residual wet delays, coupled with the stochastic model that was used, can incur a height offset of up to 30 mm in some instances. As the size of the processing window increases, the residual effects on the heights will decrease due to increased observation redundancy (Kim and Langley, 2001).

Over the six different window sizes, both MINQUE and SMINQUE consistently produced the smallest height offsets. The RMSE of the height offsets (in mm) over the 5-day campaign is present in Table 6.5. The superiority of (S)MINQUE is especially evident for the smaller processing window sizes (1-h, 2-h, and 4-h). The NND_MINQUE was the worst performer over the 5-day period. The variance factor, given by Eq. (3.28), of the linear model produced by the NND_MINQUE model is unity. A variance factor of one indicates that the stochastic model is correctly chosen (e.g., Dodson, 1993; Wang *et al.*, 1998). Given that this is the case, and coupled with the fact that NND_MINQUE produced the worst results, the underlying notion here signifies the importance of proper modelling of the correlation between the observations. The mean and standard deviation of the height offsets are presented in Tables 6.6 and 6.7, respectively. The corresponding plots for the table values are given by Figures 6.23 to 6.25.

Table 6.5 RMSEs of the height offsets (mm) over the 5-day campaign

Window	EWM	EADM	MINQUE	SMINQUE	NND_MINQUE
1-h	5.35	3.90	1.84	1.94	8.57
2-h	2.59	1.35	0.86	0.94	2.90
4-h	1.17	0.66	0.23	0.25	1.03
6-h	0.68	0.41	0.28	0.28	0.63
12-h	0.27	0.19	0.18	0.18	0.26
24-h	0.73	0.41	0.32	0.32	0.66

Table 6.6 Mean height offsets (mm) over the 5-day campaign

Window	EWM	EADM	MINQUE	SMINQUE	NND_MINQUE
1-h	0.19	-0.19	0.20	0.26	-0.77
2-h	0.38	0.16	-0.03	-0.02	0.17
4-h	0.24	0.11	-0.03	-0.01	0.25
6-h	0.31	0.12	0.22	0.22	0.20
12-h	0.37	0.13	0.29	0.28	0.32
24-h	0.35	0.15	0.19	0.19	0.31

Table 6.7 Standard deviation of the height offsets (mm) over the 5-day campaign

Window	EWM	EADM	MINQUE	SMINQUE	NND_MINQUE
1-h	5.36	3.92	1.84	1.93	8.57
2-h	3.67	1.92	1.23	1.34	4.14
4-h	2.36	1.33	0.47	0.50	2.08
6-h	1.69	1.04	0.67	0.67	1.56
12-h	0.92	0.67	0.60	0.59	0.87
24-h	0.72	0.43	0.29	0.29	0.65

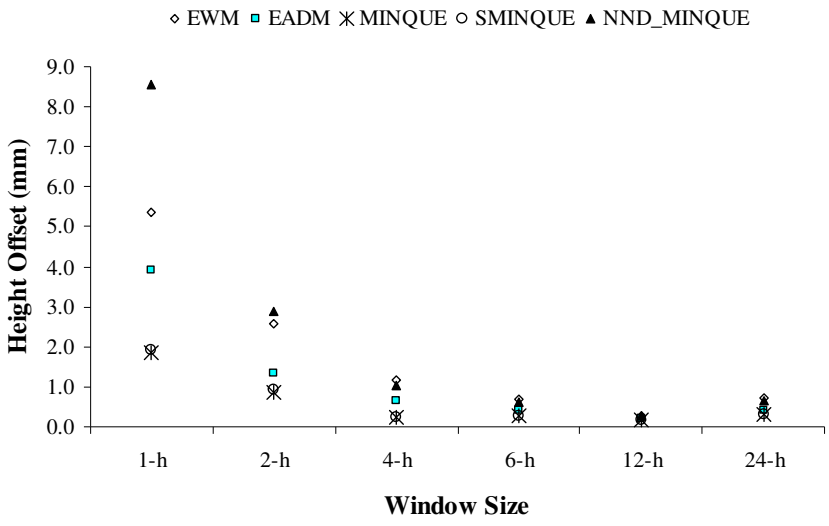

Figure 6.23 Height offset RMSEs (mm) for various stochastic models over varying window sizes

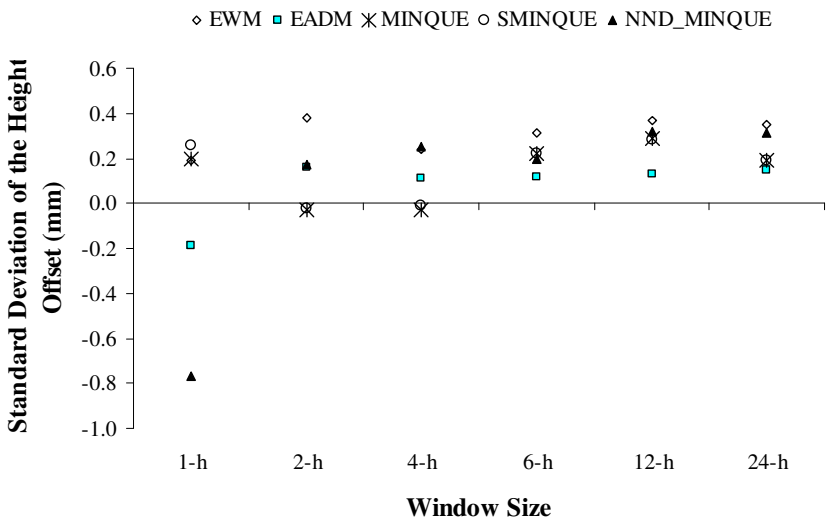

Figure 6.24 Mean height offset (mm) for various stochastic models over varying window sizes

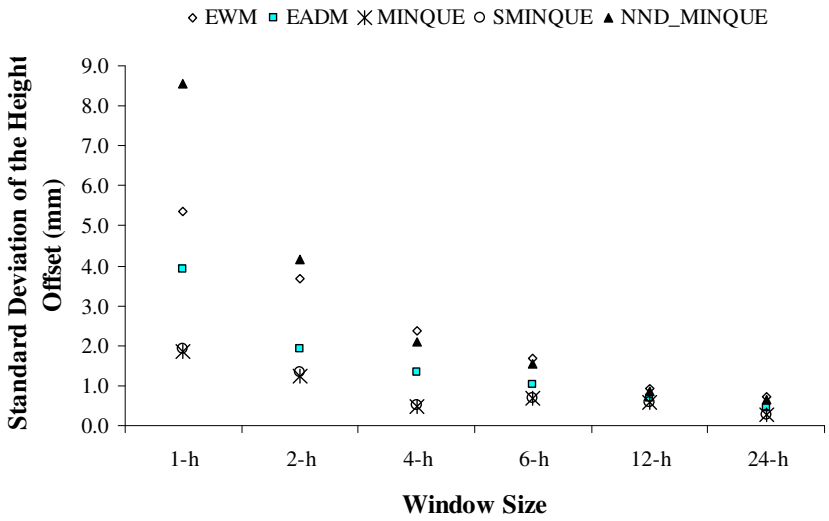

Figure 6.25 Standard deviation of the height offsets (mm) for various stochastic models over varying window sizes

Table 6.8 compares the MINQUE's RMSE in the height component to those of the other stochastic models. The relative improvement (RI) of MINQUE over the other models is calculated as follows:

$$\mathrm{RI} = \frac{\mathrm{RMSE}_i - \mathrm{RMSE}_{\mathrm{MINQUE}}}{\mathrm{RMSE}_i} * 100, \tag{6.1}$$

where

$$i = \{\mathrm{EWM}, \mathrm{EADM}, \mathrm{SMINQUE}, \mathrm{NND\_MINQUE}\}$$

The advantage of MINQUE over the other models that ignore spatial correlation among the raw observations is fairly substantial. The average height improvements made by MINQUE are 60%, 36%, and 61% when compared to EWM, EADM and NND_MINQUE, respectively. However, the difference between MINQUE and SMINQUE is marginal.

Table 6.8 Relative improvement in the height estimates for HOB2 over the five-day data set as a result of using MINQUE

Window Size	EWM	EADM	MINQUE	SMINQUE	NND_MINQUE
1-h	66%	53%	-	5%	79%
2-h	67%	36%	-	9%	70%
4-h	80%	65%	-	8%	78%
6-h	66%	53%	-	5%	79%
12-h	67%	36%	-	9%	70%
24-h	80%	65%	-	8%	78%

In the analysis of the ZWD estimation, the differences between the SimZWDs and the LS-estimated ZWDs over the five days are illustrated by Figures 6.26 to 6.31. It can be observed from these figures that there are minimal changes between the ZWD trends for the 4-h, 6-h, 12-h and the 24-h processing window. The RMSE of the differences, given by Eq.(5.1), are given in Table 6.9.

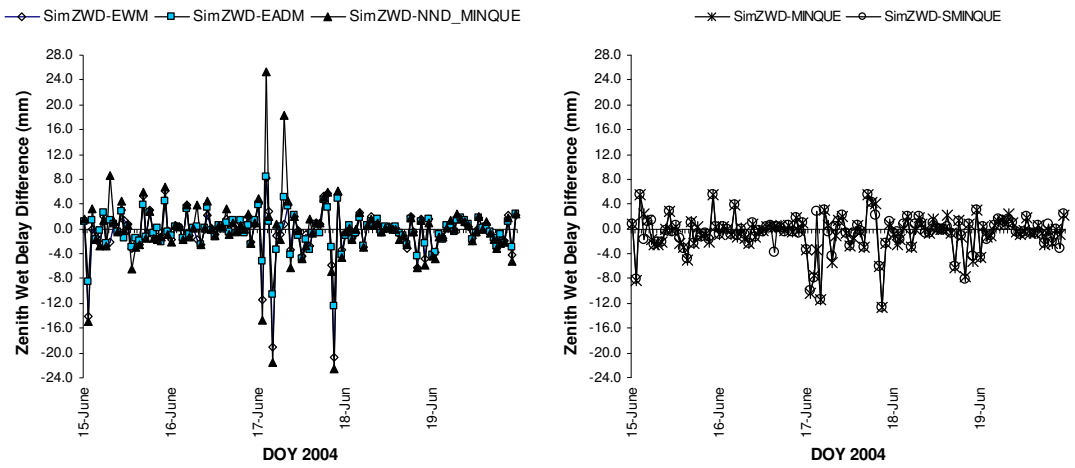

Figure 6.26 Wet delay differences between the LS (acquired with a 1-h processing window) and SimZWD estimates

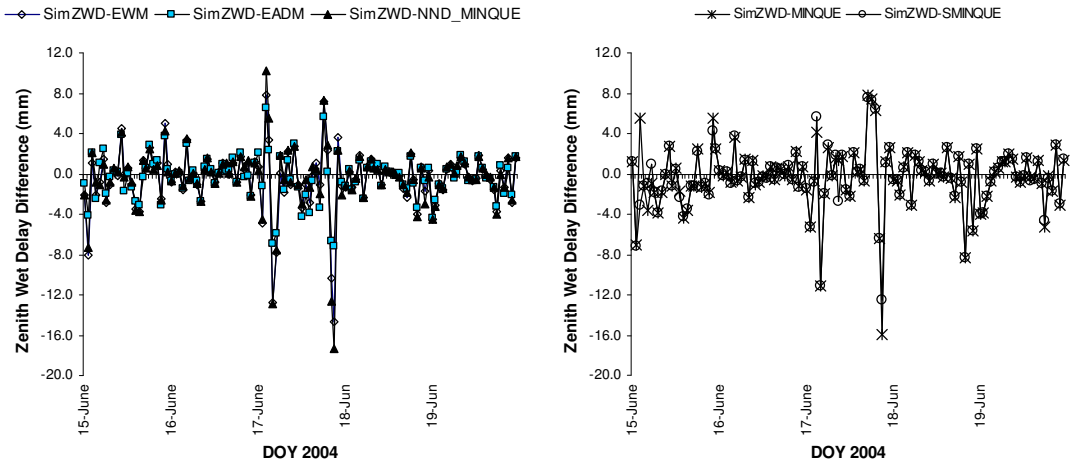

Figure 6.27 Wet delay differences between the LS (acquired with a 2-h processing window) and SimZWD estimates

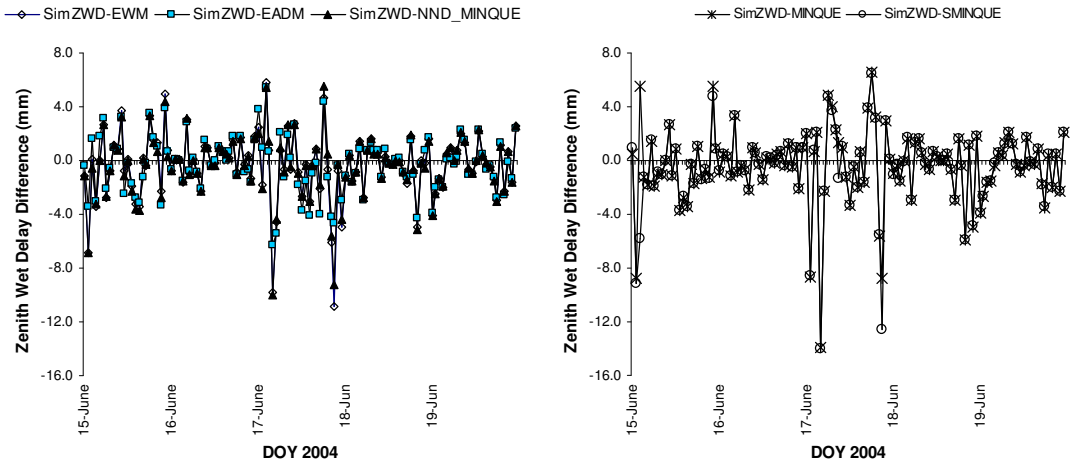

Figure 6.28 Wet delay differences between the LS (acquired with a 4-h processing window) and SimZWD estimates

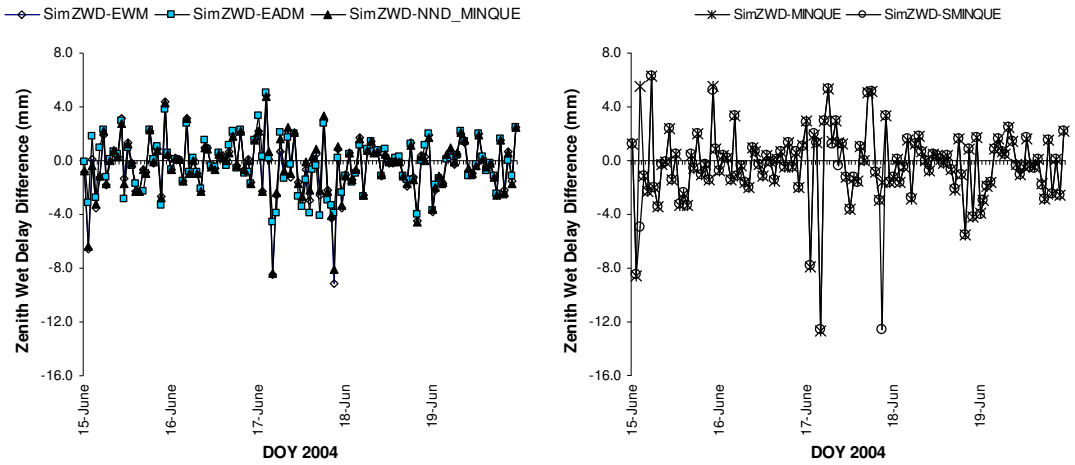

Figure 6.29 Wet delay differences between the LS (acquired with a 6-h processing window) and SimZWD estimates

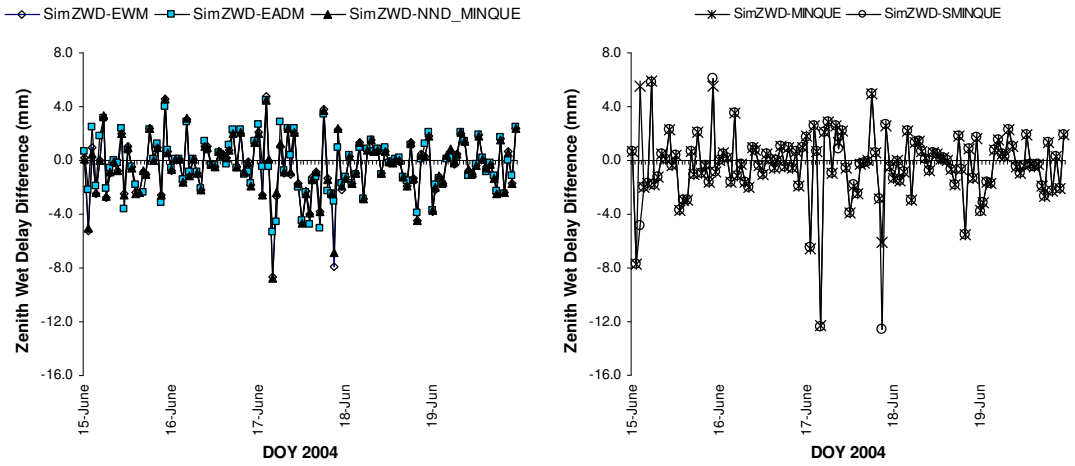

Figure 6.30 Wet delay differences between the LS (acquired with a 12-h processing window) and SimZWD estimates

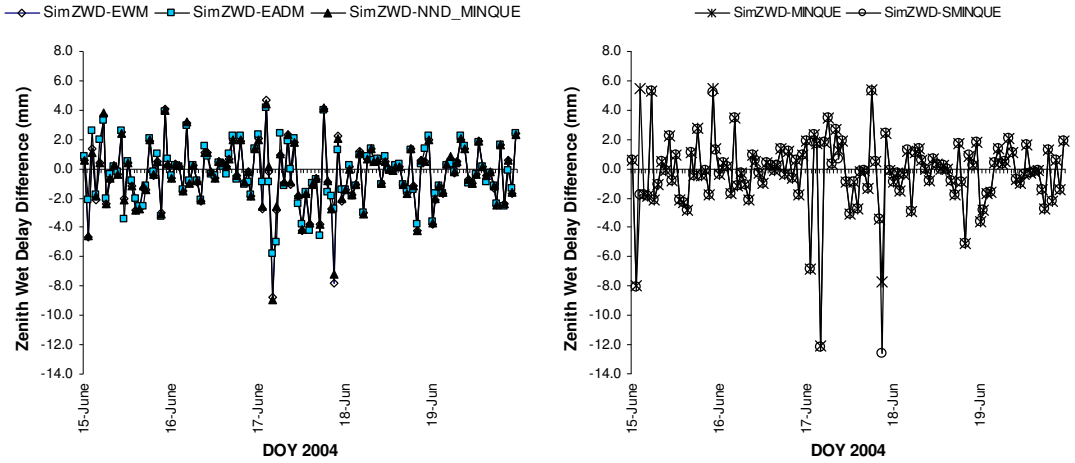

Figure 6.31 Wet delay differences between the LS (acquired with a 24-h processing window) and SimZWD estimates

Table 6.9 RMSE of the wet delay differences (mm) at HOB2

Window	EWM	EADM	MINQUE	SMINQUE	NND_MINQUE
1-h	3.88	2.80	3.07	3.02	5.24
2-h	3.03	2.22	3.08	3.08	3.25
4-h	2.46	2.10	2.74	2.78	2.39
6-h	2.14	1.89	2.60	2.60	2.08
12-h	2.14	1.97	2.45	2.46	2.10
24-h	2.12	1.93	2.38	2.39	2.08

Unexpectedly, better height recovery did not yield better ZWD estimates, contradicting many previous studies (e.g., Dodson *et al.*, 1996; Bock and Doerflinger, 2001; Bock *et al.*, 2001; Tregoning and Herring, 2006). The EADM was

the best stochastic model over all window sizes in the recovery of the wet delay estimates. The EADM recovered the ZWD with a better accuracy than EWM, MINQUE, SMINQUE and NND_MINQUE, by an average of 23%, 20%, 20%, and 30%, respectively, over the smaller windows (1-h, 2-h and 4-h). When estimating the ZWD, GNSS observations that are closer to the zenith have more significant impact as compared to those at low elevations, and therefore should have greater weights. The EADM is reflective of this, and this could explain why it had out-performed (S)MINQUE. Thus, the solutions may have been driven in favour of the EADM. The dependence of NMFs on the elevation angle could also exaggerate the results of the EADM.

For larger windows sizes (6-h, 12-h and 24-h), the relative improvement of the EADM over the EWM and the NNE_MINQUE models are consistently around 10%. On other hand, the advantage of the EADM over the (S)MINQUE techniques is still around 20%. The (S)MINQUE approach produced the least precise estimates overall.

The corresponding wet delay error estimates were also analysed. To determine whether a set of error estimates can be considered as a dependable source of error information, error (confidence) intervals at $1\sigma_{SE}$, $2\sigma_{SE}$ and $3\sigma_{SE}$, where σ_{SE} represents one SE, were constructed for each of ZWD estimates (see Section 5.2). Two and three standard errors represent approximately, a 95% and a 99.7% error interval, respectively. An error estimates for a LS ZWD is deemed adequate if there is a statistical agreement between the LS ZWD and SimZWD estimates according to the error intervals.

Figures 6.32 to 6.36 illustrate the number of LS ZWD that are statistically in agreement with the SimZWD at 1σ, 2σ and 3σ , corresponding to each of the tested stochastic models with a 1-h processing window. For these plots, a statistical agreement between a LS ZWD and the simulated ZWD estimates is achieved if their difference (blue circles) falls below the error intervals (black line).

All these figures display similar trend, whereby comparatively larger peaks are observed on the 15th and the 17th of June 2004, in each of the respective plot. It can

also be observed that the (S)MINQUE produced smaller LS ZWD error intervals, i.e. more precise, than the EWM, EADM and NND_MINQUE. However, there is a greater portion of statistical disagreement between the SimZWD and LS ZWD, and thus, indicating that the majority of the LS ZWD estimates are biased. On the other hand, the majority of the LS ZWD and SimZWD are in statistical agreement with one another. Hence, the corresponding error estimates provide useful error information for any future NWP data assimilation process.

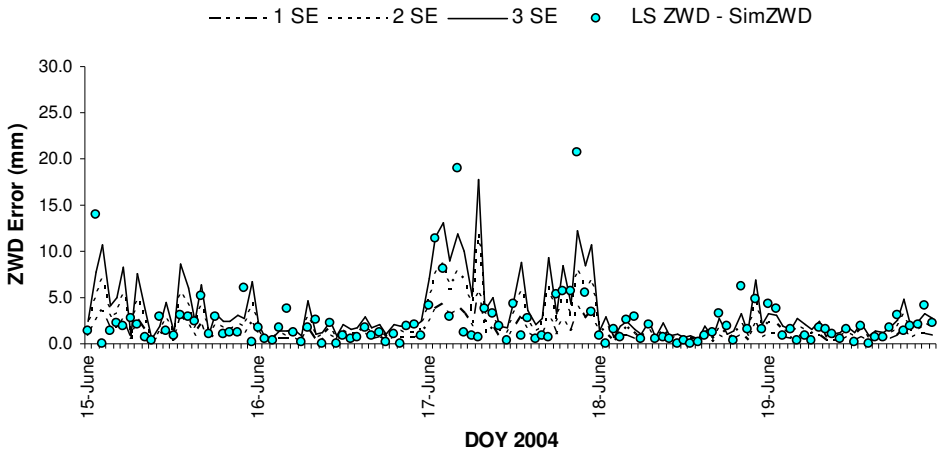

Figure 6.32 Error intervals (black line) of the LS ZWD at 1σ, 2σ and 3σ for EWM and with a 1-h processing window.

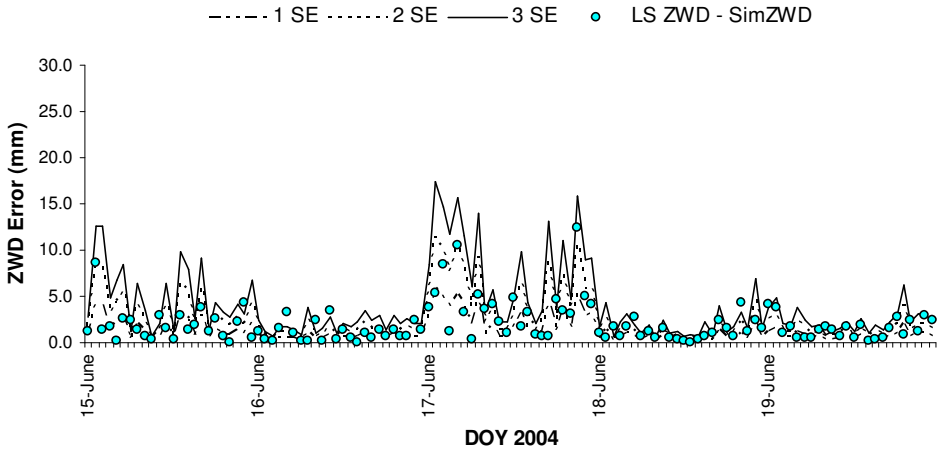

Figure 6.33 Error intervals (black line) of the LS ZWD at 1σ, 2σ and 3σ for EADM and with a 1-h processing window.

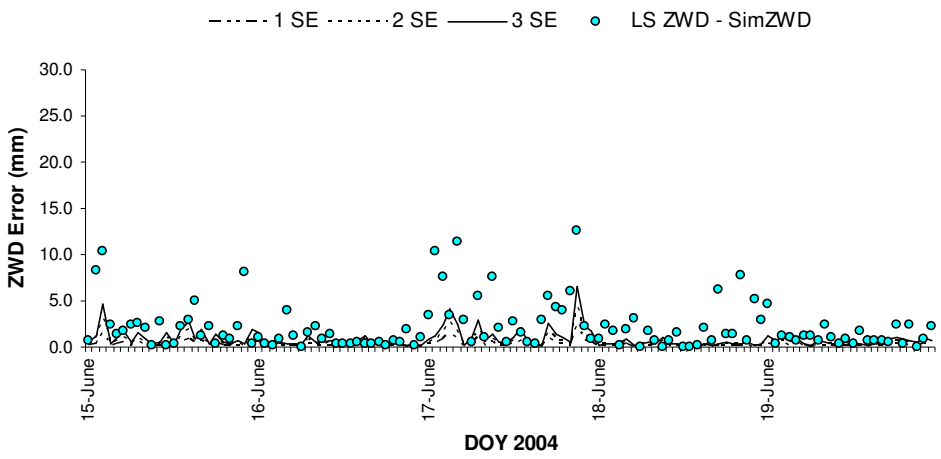

Figure 6.34 Error intervals (black line) of the LS ZWD at 1σ, 2σ and 3σ for MINQUE and with a 1-h processing window.

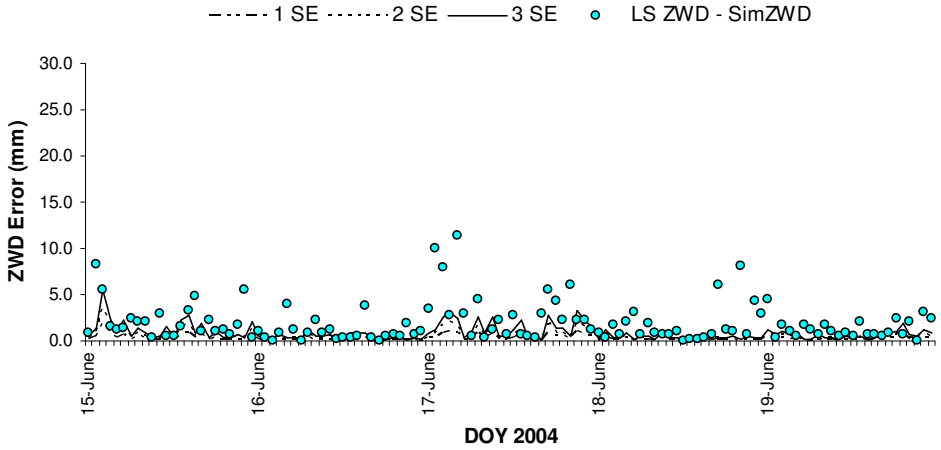

Figure 6.35 Error intervals (black line) of the LS ZWD at 1σ, 2σ and 3σ for SMINQUE and with a 1-h processing window.

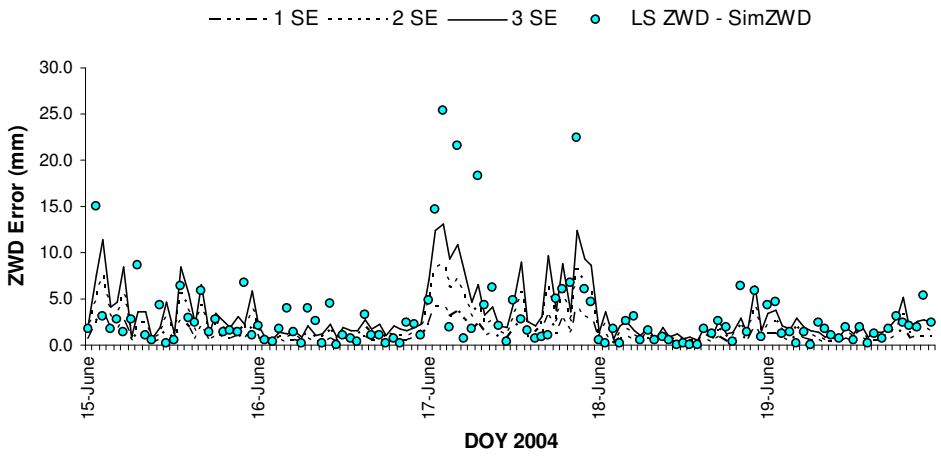

Figure 6.36 Error intervals (black line) of the LS ZWD at 1σ, 2σ and 3σ for NND_MINQUE and with a 1-h processing window.

Tables 6.10 to 6.12 illustrate the actual percentages of LS ZWD estimates that are in statistical agreement with the SimZWD measurements at $1\sigma_{SE}$, $2\sigma_{SE}$ and $3\sigma_{SE}$, respectively over various processing window sizes. The total number of comparisons in each case is 120.

Table 6.10 Number (percentage) of LS ZWD solutions that are in statistical agreement with actual ZWD at $1\sigma_{SE}$

Window	EWM	EADM	MINQUE	SMINQUE	NND_MINQUE
1-h	35 (29%)	41 (34%)	10 (8%)	8 (6%)	28 (23%)
2-h	37 (30%)	46 (38%)	9 (7%)	8 (6%)	36 (30%)
4-h	35 (29%)	30 (25%)	14 (11%)	14 (11%)	38 (31%)
6-h	32 (26%)	35 (29%)	17 (14%)	17 (14%)	34 (28%)
12-h	26 (21%)	31 (25%)	26 (21%)	26 (21%)	30 (25%)
24-h	30 (25%)	31 (25%)	29 (24%)	29 (24%)	33 (27%)

Table 6.11 Number (percentage) of LS ZWD solutions that are in statistical agreement with actual ZWD at $2\sigma_{SE}$

Window	EWM	EADM	MINQUE	SMINQUE	NND_MINQUE
1-h	66 (55%)	78 (65%)	22 (18%)	22 (18%)	55 (45%)
2-h	66 (55%)	70 (58%)	20 (16%)	24 (20%)	63 (52%)
4-h	55 (45%)	60 (50%)	32 (26%)	32 (26%)	56 (46%)
6-h	58 (48%)	58 (48%)	36 (30%)	36 (30%)	57 (47%)
12-h	57 (47%)	53 (44%)	45 (37%)	45 (37%)	56 (46%)
24-h	58 (48%)	50 (41%)	54 (45%)	53 (44%)	58 (48%)

Table 6.12 Number (percentage) of LS ZWD solutions that are in statistical agreement with actual ZWD at $3\sigma_{SE}$

Window	EWM	EADM	MINQUE	SMINQUE	NND_MINQUE
1-h	91 (75%)	98 (81%)	30 (25%)	37 (30%)	79 (65%)
2-h	84 (70%)	95 (79%)	41 (34%)	36 (30%)	84 (70%)
4-h	77 (64%)	87 (72%)	56 (46%)	56 (46%)	76 (63%)
6-h	83 (69%)	83 (69%)	56 (46%)	55 (45%)	83 (69%)
12-h	69 (57%)	73 (60%)	67 (55%)	67 (55%)	68 (56%)
24-h	71 (59%)	74 (61%)	68 (56%)	68 (56%)	72 (60%)

From Tables 6.10-6.12, the EADM is again the top performer across all window sizes with respect to producing realistic error estimates. For the 1-h and 2-h processing windows, approximately 60% and 80% of LS ZWD estimates are in

agreement with SimZWD at $2\sigma_{SE}$ and $3\sigma_{SE}$, respectively. The (S)MINQUE models are inferior to the other methods in this regard. The performance of (S)MINQUE did improve as the size of the processing window increases. The differences between the stochastic models are negligible for larger window sizes.

In summary, the results from the simulation study indicate that although (S)MINQUE did resolve the station heights (with respect to RMSE, mean and standard deviation of the offsets) better than the EWM, EADM and NND_MINQUE, this superiority was not evident in the recovery of the SimZWD. In fact, EADM recovered the SimZWD better than the other models (EWM, MINQUE, SMINQUE and NND_MINQUE) by an average of 16%, 21%, 21% and 19%, respectively, across all window sizes, respectively. Error analysis for EWM, EAD and NND_MINQUE suggests that smaller processing windows will produce a set of LS ZWD estimates that are statistically less biased (i.e. statistically not different to the actual ZWD estimates). Hence, the corresponding error estimates can provide useful information for the eventual assimilation of the LS ZWD estimates. The error intervals produced by the EADM were able to successfully capture 82% of the SimZWD (at three standard errors) with a 1-h window, with EWM not far behind at 76%. Overall, the EADM came out as the top performer.

6.3 PWV ESTIMATION WITH REAL DATA AND VALIDATED WITH RS

Results from the simulation study in Section 6.3 indicated that a reduction in the processing window size (session length) can potentially have a positive impact on the ZWD error estimates without negatively impacting the accuracy of the LS ZWD estimates significantly. Thus, in this section, further investigation is carried out to:

- Determine whether or not the encouraging results in the simulation study can carry over to real practical application, and
- Investigate the impact of a reduced network (i.e. smaller number of stations) on the tropospheric solutions and the corresponding error estimates (theoretical discussion given in Section 5.2.3).

Data from a baseline between the Alice Springs (ALIC) and Hobart (HOB2) were chosen for testing. The tropospheric solution from the baseline-campaign will be compared to those of the network solutions in Section 6.1. The close proximity of the RS launching sites from ALIC (~14 km from RS site) and HOB2 (~6 km from RS site) stations is the reason for choosing these stations for this investigation. The distance between the two stations is approximately 2447 km. The long baseline length between the two stations also ensures that "absolute" tropospheric delays can be estimated appropriately (Kouba, 2009). Tregoning (1998) also indicated that a baseline length of more than 2000 km is more appropriate in providing sufficient decorrelation of the observations between the two baseline stations to enable better absolute estimation of the PWV.

A week of data, from March 31st to April 6th in 2004, was used for this study. The processing strategy is identical to that outlined in the Australian campaigns (Section 6.1). As it was difficult to incorporate the (S)MINQUE programs into the original Bernese GNSS software, the DD design matrices, which contained the parameter coefficients, were instead outputted as text files and analysed externally to Bernese. The analysis was performed twice. The first involves only constraining the coordinates of ALIC, whereas the coordinates of both stations are constrained in the second analysis. The coordinates of the stations are constrained to within 0.1 mm from the ITRF2000 coordinate solutions. The *a-priori* ITRF coordinates remained unchanged throughout the test.

6.3.1 Baseline Analysis – ALIC Constrained

The accuracy (in comparison to the ITRF solutions) and precision of the final coordinates of HOB2 for the first analysis are summarised in Tables 6.13 to 6.16. The mean, standard deviation and RMSE of the coordinate and height offsets at various window sizes were presented as the three main columns for each of these tables. The values in these tables are determined from all solutions over the whole week.

Table 6.13 Summary of the coordinate offsets (cm) at HOB2 with the EWM

EWM												
Window	Mean				Std Deviation				RMSE			
	X	Y	Z	HGHT	X	Y	Z	HGHT	X	Y	Z	HGHT
1-h	-3.8	0.4	-2.7	4.3	23.0	22.4	10.1	20.6	23.3	22.4	10.4	21.0
2-h	1.6	-1.7	0.2	-1.8	10.0	11.9	6.5	12.6	10.1	12.0	6.5	12.7
3-h	3.4	-3.4	0.8	-4.0	7.0	5.7	3.4	7.6	7.7	6.6	3.5	8.6
6-h	2.3	-4.7	1.1	-4.0	3.4	2.9	2.1	4.4	4.0	5.5	2.3	5.9
12-h	3.2	-3.6	1.2	-4.2	2.1	2.4	1.9	3.5	3.7	4.3	2.2	5.3
24-h	2.6	-3.4	1.0	-3.6	2.0	2.4	1.8	3.3	3.2	4.0	1.9	4.7

Table 6.14 Summary of the coordinate offsets (cm) at HOB2 with the EADM

EADM												
Window	Mean				Std Deviation				RMSE			
	X	Y	Z	HGHT	X	Y	Z	HGHT	X	Y	Z	HGHT
1-h	-1.8	-0.7	-0.4	1.1	15.9	16.4	8.0	16.0	16.0	16.4	8.0	16.0
2-h	2.6	-1.4	0.9	-2.8	6.7	6.3	4.5	8.7	7.1	6.4	4.6	9.1
3-h	1.8	-1.7	0.6	-2.2	3.7	3.5	2.5	5.0	3.3	3.1	2.1	4.4
6-h	1.9	-2.6	1.0	-2.9	2.7	3.1	2.3	4.1	1.9	2.3	1.4	2.9
12-h	2.1	-1.9	1.0	-2.7	2.6	2.6	2.2	4.1	1.3	1.3	1.0	2.0
24-h	2.0	-1.8	0.9	-2.6	2.6	2.5	2.3	4.1	0.9	0.9	0.7	1.3

Table 6.15 Summary of the coordinate offsets (cm) with the MINQUE model

MINQUE												
Window	Mean				Std Deviation				RMSE			
	X	Y	Z	HGHT	X	Y	Z	HGHT	X	Y	Z	HGHT
1-h	-2.4	1.7	-1.6	3.2	17.6	18.2	8.9	17.2	17.7	18.3	9.0	17.4
2-h	1.3	-0.6	0.1	-1.1	6.8	7.8	4.9	8.9	6.9	7.8	4.9	8.9
3-h	1.3	-2.4	0.4	-2.0	4.5	4.7	2.4	5.6	4.6	5.2	2.4	6.0
6-h	1.9	-3.2	0.9	-3.0	2.9	3.0	1.9	3.7	3.4	4.4	2.1	4.7
12-h	2.3	-2.4	0.8	-2.9	2.7	2.7	2.2	4.2	3.5	3.6	2.3	5.0
24-h	2.5	-2.9	0.9	-3.3	2.6	2.6	2.2	4.1	3.4	3.8	2.2	5.0

Table 6.16 Summary of the coordinate offsets (cm) with the SMINQUE model

SMINQUE												
Window	Mean				Std Deviation				RMSE			
	X	Y	Z	HGHT	X	Y	Z	HGHT	X	Y	Z	HGHT
1-h	-2.5	2.3	-1.9	3.7	17.7	17.9	8.5	16.9	17.8	18.0	8.6	17.3
2-h	1.5	-0.6	0.2	-1.3	8.0	8.1	5.0	9.6	8.0	8.1	5.0	9.7
3-h	2.0	-2.9	1.0	-3.0	4.7	4.6	2.8	5.8	5.1	5.4	3.0	6.5
6-h	1.8	-3.3	0.9	-3.0	3.1	3.0	2.3	4.0	3.5	4.4	2.4	5.0
12-h	2.2	-2.4	0.8	-2.9	2.7	2.8	2.3	4.2	3.4	3.6	2.3	5.0
24-h	2.5	-2.9	0.9	-3.3	2.6	2.6	2.2	4.1	3.4	3.8	2.2	5.0

From Tables 6.13 to 6.16, the EADM consistently produced the best results among the four presented stochastic models with respect the mean, standard deviation and RMSE of the coordinate offsets. The EWM was the worst performer, which is not unexpected since all raw GNSS measurements are assumed to have equal weighting (e.g., Wang *et al.*, 2002; Jin *et al.*, 2005). The MINQUE method did perform marginally better with the 2-h processing window than the EADM, with mixed results when a 3-h window is applied. The differences between the MINQUE and SMINQUE are generally in the sub-millimetre range, a result consistent with Satirapod *et al.*, 2002. However, differences of up to a few millimeters are also observed. The magnitude of the offsets may be attributed to the large baseline length (e.g., King and Bock, 2002; Schön and Kutterer, 2006). Additionally, HOB2 is located at low latitude (see Figure 6.1) and thus, the geometry of the satellites is biased towards the north.

The corresponding GNSS PWV estimates, which were estimated along with the coordinate partials in LS, were validated against the RS data. The RMSE of the differences for ALIC and HOB2 are summarised in the Tables 6.17 and 6.18. The corresponding plots for the RMSEs are given by Figures 6.37 and 6.38. GNSS estimates of less than 3 mm are achieved with a 3-h or a larger window with all four stochastic models. With EADM and MINQUE, a 2-h window seems to suffice. Differences between the models are minimal for large (12-h and 24-h) processing windows, a result consistent with previous studies by Baker *et al.* (2001) and Gutman *et al.* (2004).

Table 6.17 RMSE (mm) of GNSS-RS PWV at Alice Springs

Window	EWM	EADM	MINQUE	SMINQUE
1-h	5.7	3.2	5.8	5.6
2-h	4.9	2.2	3.0	4.1
3-h	2.3	1.1	1.6	2.2
6-h	2.1	2.3	1.2	1.2
12-h	2.9	3.0	3.0	2.9
24-h	2.5	2.8	2.6	2.6

Table 6.18 RMSE (mm) of GNSS-RS PWV at Hobart

Window	EWM	EADM	MINQUE	SMINQUE
1-h	3.3	2.3	3.7	2.2
2-h	2.0	1.6	2.0	2.0
3-h	2.0	2.2	2.4	2.2
6-h	1.8	2.5	2.5	2.8
12-h	2.1	2.5	2.3	2.3
24-h	1.4	1.8	1.6	1.6

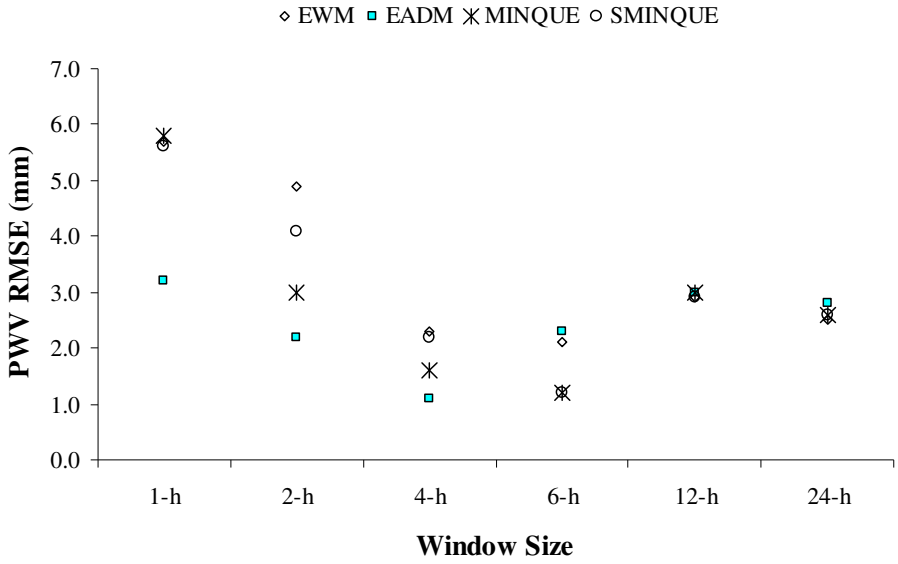

Figure 6.37 A plot of the GNSS-RS RMSE at Alice Springs

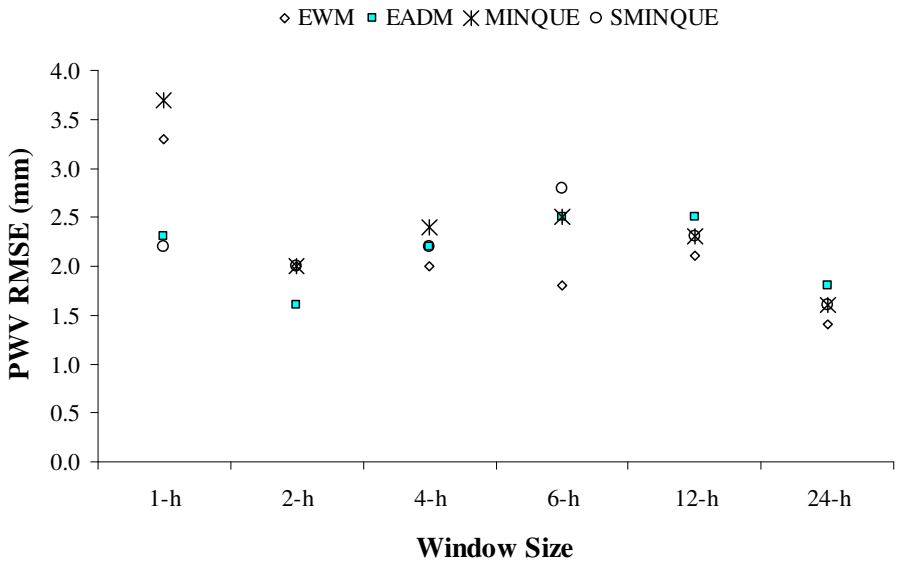

Figure 6.38 A plot of the GNSS-RS RMSE at Hobart

The error estimates of the GNSS LS PWV are assessed to determine whether or not they can be considered as dependable error information through the use of confidence intervals at $2\sigma_{SE}$ and $3\sigma_{SE}$ (as discussed in Chapter 5). There are seven RS data (one per day) available during this period at ALIC, whilst there are fourteen RS data (two per day) available at HOB2. Figures 6.39 and 6.40 show the percentages of GNSS LS PWV that are in agreement with the RS PWV estimate at two and three standard errors (σ_{SE}), respectively, over various window sizes at ALIC, whist Figures 6.41 and 6.42 are for HOB2.

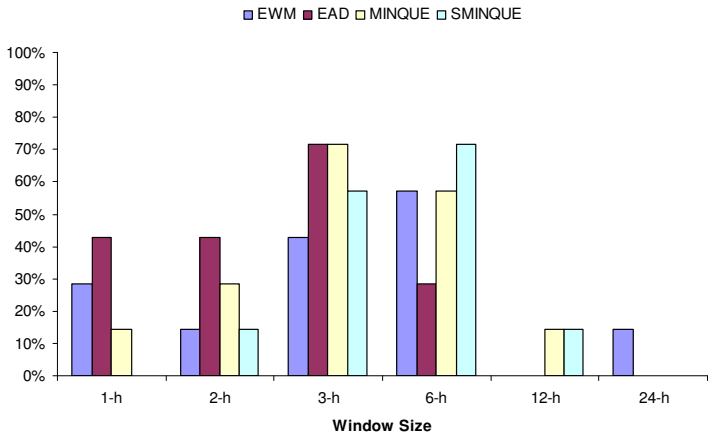

Figure 6.39 Percentages of GNSS LS PWV estimates that are in agreement with the RS PWV at $2\sigma_{SE}$ for each of the tested stochastic model at ALIC

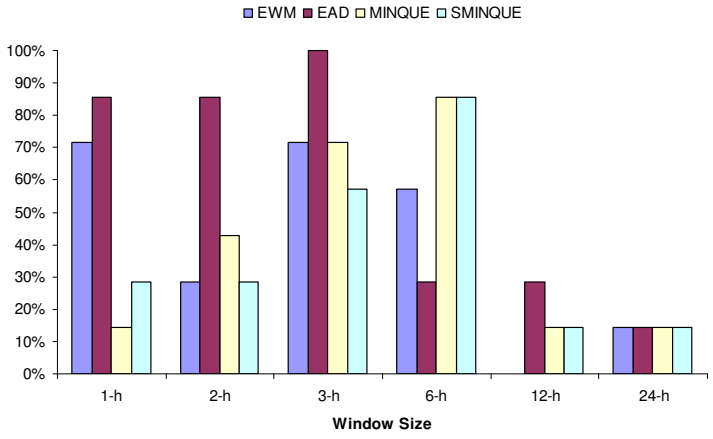

Figure 6.40 Percentages of GNSS LS PWV estimates that are in agreement with the RS PWV at $3\sigma_{SE}$ for each of the tested stochastic model at ALIC

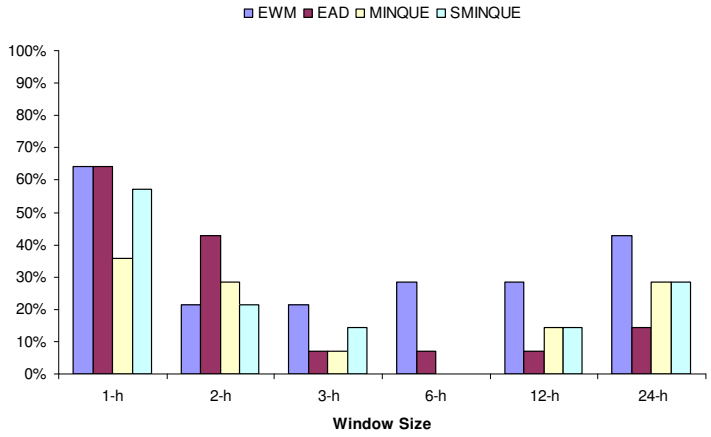

Figure 6.41 Percentages of GNSS LS PWV estimates that are in agreement with the RS PWV at $2\sigma_{SE}$ for each of the tested stochastic model at HOB2

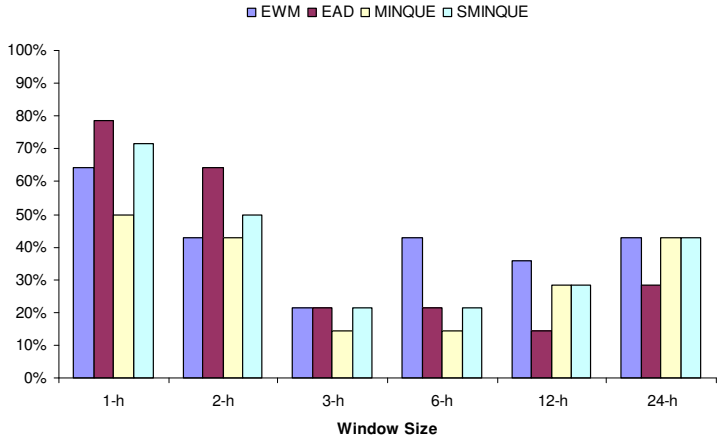

Figure 6.42 Percentages of GNSS LS PWV estimates that are in agreement with the RS PWV at $3\sigma_{SE}$ for each of the tested stochastic model at HOB2

As can been seen from Figures (6.39) to (6.42), the window size that achieved the best overall results with respect to the proportion of LS PWV that are in agreement with the RS PWV, appears to be the 2-h processing window. The 3-h window is also worth considering as it produced the best set of results at ALIC. The error estimates of the LS PWV realised with the 1-h processing window did particularly well at HOB2 and for the EADM model. Across the 1-h and 2-h processing windows, the EADM yielded the best results.

MINQUE and SMINQUE are iterative procedures that provide global optimal solutions when convergence is achieved. The difference in height between using the MINQUE and SMINQUE methods is less than 1 mm in approximately 43% of the

sessions where both MINQUE and SMINQUE simultaneously converged to their optimal solutions. The proportion of differences that are greater than 3 mm, 5 mm, and 10 mm, is approximately 27%, 12% and 7% respectively. These differences are likely due to the simplification imposed on SMINQUE (Section 4.3). The difference in the overall mean and RMSE of the offsets are however, at the sub-millimetre level. It is further noted that achieving convergence in MINQUE does not necessarily imply the same will happen with SMINQUE in the same session, and vice-versa. Such occurrences happened 6% of the time when either one of both MINQUE and SMINQUE converged. When MINQUE does converge, the variance factor is always "one" or thereabouts depending on the tolerance level set between the solutions successive iteration. The variance factor values for SMINQUE conversely are generally between the range of 0.96 and one under the same tolerance level.

6.3.2 Baseline Analysis – ALIC and HOB2 Constrained

GNSS data from a large network are generally processed with the majority of the station coordinates being tightly constrained to ensure highly precise tropospheric solutions (e.g., Hugentobler *et al.*, 2001; Haase *et al.*, 2003). If ITRF (or any other precise reference frame) coordinates are available, a question may arise about the possibility of attaining similar accuracy with a smaller network or even a baseline whilst constraining all stations. In additional, the error estimates of the LS PW would likely to be more realistic as a result (see Section 5.2.3). To investigate this, both stations from the ALIC-HOB2 baseline are constrained (0.1 mm). The determination of the GNSS PWV estimates, using different stochastic models as discussed earlier, are summarised by Tables 6.19 and 6.20.

Table 6.19 RMSE*s* and biases of GNSS-RS PWV at Alice Springs

Window	RMSE (mm)				BIAS (mm)			
	EWM	EADM	MINQUE	SMINQUE	EWM	EADM	MINQUE	SMINQUE
1-h	1.4	1.3	1.4	1.8	-0.8	-0.3	-0.9	-0.5
2-h	1.2	1.1	1.4	1.4	-0.4	0.2	-0.3	-0.3
3-h	1.0	1.2	1.2	1.2	-0.2	0.5	0.4	0.6
6-h	1.1	1.2	1.2	1.2	-0.2	0.5	0.1	0.0
12-h	1.0	1.2	0.8	1.0	-0.1	0.5	0.5	0.2
24-h	1.0	1.3	1.0	1.0	-0.1	0.6	0.3	0.2

Table 6.20 RMSE*s* and biases of GNSS-RS PWV at Hobart

Window	RMSE (mm)				BIAS (mm)			
	EWM	EAD	MINQUE	SMINQUE	EWM	EAD	MINQUE	SMINQUE
1-h	2.1	2.6	2.4	2.3	-1.9	-2.4	-2.2	-2.0
2-h	2.1	2.8	2.7	2.7	-1.9	-2.6	-2.5	-2.5
3-h	2.1	2.7	2.5	2.5	-2.0	-2.5	-2.3	-2.3
6-h	2.2	2.8	2.4	2.4	-2.0	-2.5	-2.2	-2.1
12-h	2.2	2.8	2.5	2.6	-2.0	-2.5	-2.3	-2.3
24-h	1.6	1.9	1.9	1.9	-1.5	-1.7	-1.7	-1.8

The RMSEs shown in Tables 6.19 and 6.20 demonstrate that good GNSS PWV estimates can be achieved even with a baseline. From the results of the network given in Section 6.1, the PWV RMSE of ALIC in the North-eastern Campaign was 1.43 mm in the same one-week period. Correspondingly, the PWV RMSE of HOB2 in the Southern Campaign was 1.10 mm. Both stations were constrained to 0.0001 m in their respective network. The baseline tropospheric solutions for ALIC in this scenario are better than the network solution. Although the same cannot be said for HOB2, the baseline solutions are still reliable (<2.8 mm). The difference is decreased for the 24-h window with a maximum difference of 0.8 mm.

Glowacki *et al.* (2006) performed an independent study of a single campaign (with discrete 24-h processing window) involving 17 GNSS stations over the Australian region for the entire year 2000. The reported RMSEs of the GNSS-RS PWV differences for ALIC and HOB2 were 2.7 mm and 2.5 mm, respectively. Although the studied period of this baseline campaign is only one week, the results demonstrate the potential of the baseline approach to produce quality PWV solutions. In the corresponding error analysis of the PWV error estimates, Figures 6.43 to 6.46 show the percentage of the LS PWV estimates that are in agreement with the corresponding RS PWV at $2\sigma_{SE}$ and $3\sigma_{SE}$, for ALIC and HOB2 respectively. The majority of the LS PWV estimates for ALIC were in agreement with the RS PWV at $3\sigma_{SE}$, as shown in Figure 6.43. The results however, were not as good for HOB2 with around 20% of the LS PWV estimates corresponding well with the RS PWV estimates. Comparatively, the network solutions at HOB2 are similar to that of the baseline approach. Therefore, there is no real advantage to the network approach in estimating the PWV/ZWD.

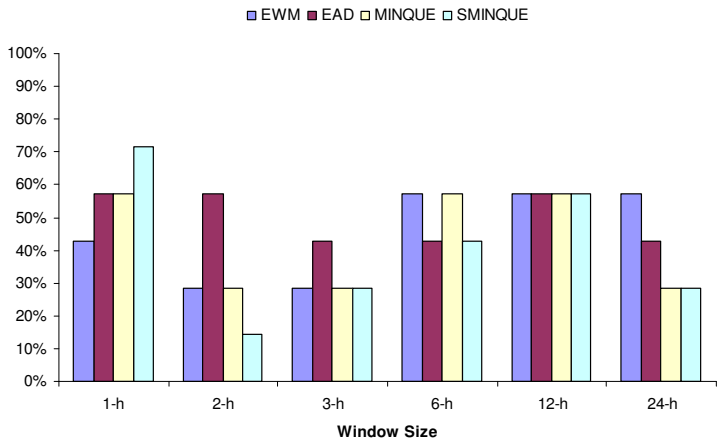

Figure 6.43 Percentages of GNSS LS PWV estimates that are in agreement with the RS PWV at $2\sigma_{SE}$ for each of the tested stochastic model at ALIC

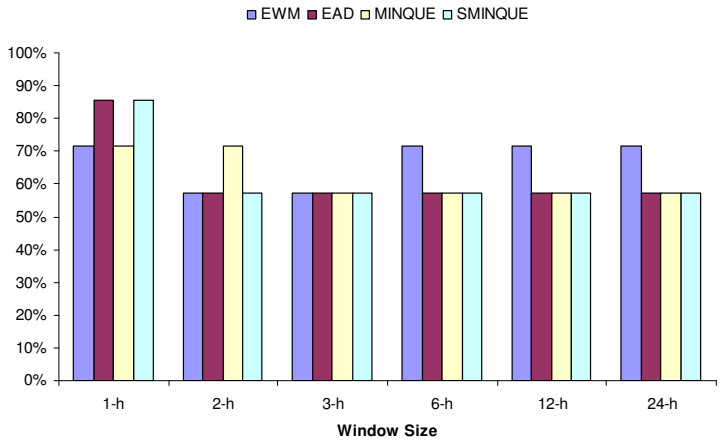

Figure 6.44 Percentages of GNSS LS PWV estimates that are in agreement with the RS PWV at $3\sigma_{SE}$ for each of the tested stochastic model at ALIC

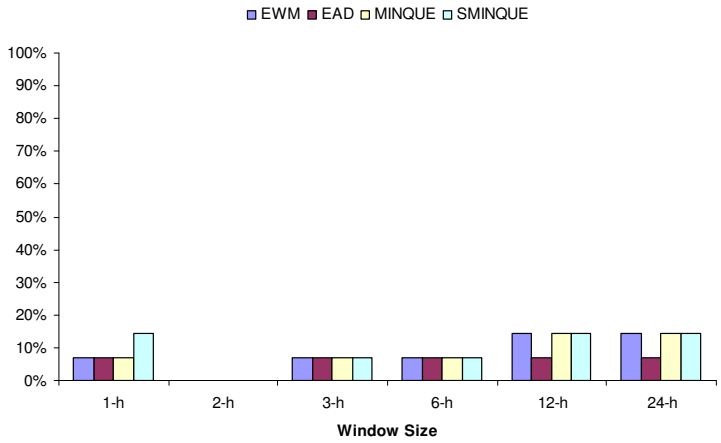

Figure 6.45 Percentages of GNSS LS PWV estimates that are in agreement with the RS PWV at $2\sigma_{SE}$ for each of the tested stochastic model at HOB2

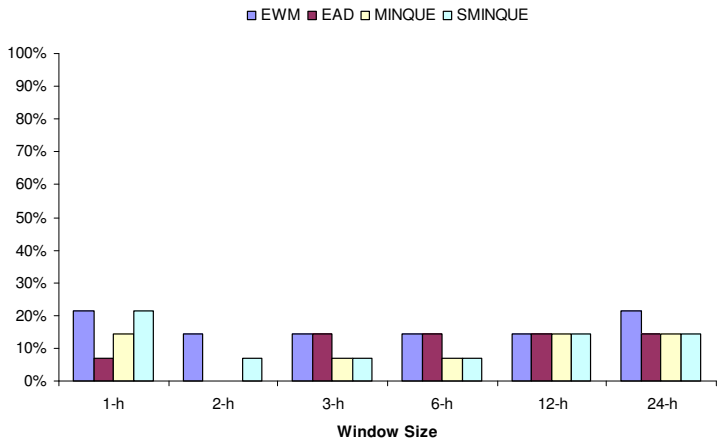

Figure 6.46 Percentages of GNSS LS PWV estimates that are in agreement with the RS PWV at $3\sigma_{SE}$ for each of the tested stochastic model at HOB2

On the other hand, not a single LS GNSS PWVfor the network solution at ALIC (Section 6.1) was in agreement with the corresponding RS PWV measurement, even though the RMSE of the GNSS PWV estimates for the baseline and network solutions were similar. The results of the analysis have demonstrated that modelling the tropospheric delays with the baseline approach, does have its merits in providing good solution and error estimates.

In summary, analysis of the *unconstrained-baseline* has indicated that the EADM is the best model in terms of coordinate RMSEs, mean offsets and standard deviations, across all processing window sizes. This superiority in coordinate resolution has also translated into better PWV estimates for the EADM. Statistical analysis of the LS PWV shows that smaller windows of sizes 1-h, and 2-h will provide more tropospheric estimates that are statistically in agreement with the RS PWV estimates than larger window sizes (i.e. 6-h, 12-h and 24-h), as shown in Figures 6.39 to 6.42. The 3-h window performed quite well at ALIC, but less so at HOB2. The increased level of observation redundancy associated with larger windows has reduced the magnitude of the error estimates, as discussed in Chapter 5, to such an extent that it consistently underestimates the error associated with the LS PWV estimates. The EADM yielded the best results within the smaller windows whereby 80%-100% of LS PWV are in agreement with the RS PWV at both ALIC and at HOB2.

The results of the *constrained-baseline* analysis have shown that the corresponding PWV estimates (of all window sizes) are very much comparable to those of the network approach (24-h window). Additionally, the resulting LS PWV derived with a 1-h window session are statistically equal to the RS PWV measurement at 90% of the time, as compared to 0% for those at ALIC in the network analysis. The results of the statistical analysis at HOB2 are similar for both the baseline and network approach. Overall, the results show that the constrained-baseline approach is a dependable strategy when resolving the tropospheric parameters.

6.4 ESTIMATION OF ZWD WITH REAL DATA AND VALIDATED WITH WVR DATA

Results from the Section 6.3 are based on comparisons with limited RS profiles. Furthermore, no WVR were available in the tested period. To provide further insight into the impact of different stochastic models and the shortening of window sizes, a baseline campaign was set up between the European GNSS stations of Onsala (ONSA) and Wettzell (WTZR). A two-week interval from the 10^{th} to 23^{rd} of September in 2003 was chosen as it represents an autumn period where significant atmospheric water vapour variation can be observed. The baseline length between the two stations is approximately 920km, which allows the "absolute" tropospheric estimation to be determined. RS data were not available for this period; however, WVR data were accessible for comparisons. The WVR data at Onsala were available at every 60 seconds whilst hourly WVR data were provided at Wettzell. However, the WVR data Onsala were taken at every hour to ensure that comparisons can be made with the hourly GNSS ZWD estimates. The WVR at Onsala can measure the slant wet delay with an accuracy of 0.01 cm^2 to 0.04 cm^2 (Nilsson *et al.*, 2005).

A WVR however is only able to sense the water vapour (i.e. wet delay) in the atmosphere. In order for the comparisons to be made, the ZWD had to be extracted from the GNSS ZTD estimates. The extraction process is given in Figure 3.1. The WVR data at both locations are given in the zenith direction and thus, direct comparison can be made after the ZWDs have been extracted from the ZTDs. The ONSA-WTZR campaign was processed with EWM, EADM, MINQUE and SMINQUE across three different window sizes (1-h, 2-h and 3-h). Only smaller

window sizes are considered here since the previous results from the simulated data and ALIC-HOB2 baseline analyses suggest more realistic error estimates are achieved through such window sizes. Two scenarios will be presented. The coordinates of the Onsala station was constrained (0.0001 m) in the first, and both stations are constrained in the second. The stations coordinates were calculated with ITRF2000 positional solutions. The processing strategy of the GNSS baseline data here is similar to the one outlined in Section 6.3.

6.4.1 Baseline Analysis – ONSA Constrained

The results of the final coordinate solutions at WTZR for each stochastic model are summarised in Tables 6.21-6.24. The mean, standard deviation and RMSE (with respect to ITRF2000 solutions) of the coordinate and height offsets at various window sizes were presented as the three main columns for each of these tables. The values in these tables are determined from the all solutions over the 2-week period.

Table 6.21 Coordinate offsets (cm) at WTZR with the EWM

EWM												
Window	**MEAN**				**STD DEVIATION**				**RMSE**			
	X	Y	Z	HGHT	X	Y	Z	HGHT	X	Y	Z	HGHT
1-h	-0.2	0.4	-0.2	-0.2	7.1	6.7	6.3	8.5	12.2	11.5	10.9	14.6
2-h	1.9	0.2	1.0	2.0	4.5	3.6	4.3	5.7	5.9	4.4	5.4	7.3
3-h	1.9	0.1	1.3	2.2	3.4	4.9	3.3	4.5	3.9	4.9	3.6	5.0

Table 6.22 Coordinate offsets (cm) at WTZR with the EADM

EADM												
Window	**MEAN**				**STD DEVIATION**				**RMSE**			
	X	Y	Z	HGHT	X	Y	Z	HGHT	X	Y	Z	HGHT
1-h	-0.4	0.3	-0.4	-0.5	4.4	4.9	3.2	4.8	7.5	8.4	5.5	8.2
2-h	1.8	0.4	1.1	2.0	4.0	3.6	3.1	4.4	5.2	4.4	3.9	5.9
3-h	1.5	0.7	1.1	1.9	2.8	3.0	2.5	3.7	3.2	3.1	2.7	4.1

Table 6.23 Coordinate offsets (cm) at WTZR with the MINQUE model

MINQUE												
Window	MEAN				STD DEVIATION				RMSE			
	X	Y	Z	HGHT	X	Y	Z	HGHT	X	Y	Z	HGHT
1-h	-0.8	0.3	-0.8	-1.1	6.2	6.0	6.5	8.6	10.7	10.3	11.1	14.8
2-h	1.0	0.1	0.4	0.9	3.5	2.8	2.6	3.9	4.4	3.4	3.2	4.9
3-h	1.2	0.4	0.7	1.3	2.5	1.8	2.4	3.3	2.7	1.8	2.5	3.5

Table 6.24 Coordinate offsets (cm) at WTZR with the SMINQUE model

SMINQUE												
Window	MEAN				STD DEVIATION				RMSE			
	X	Y	Z	HGHT	X	Y	Z	HGHT	X	Y	Z	HGHT
1-h	-0.5	0.6	-0.5	-0.6	6.9	6.8	6.4	9.1	11.8	11.8	11.1	15.7
2-h	1.1	0.0	0.5	1.0	3.5	2.8	2.7	3.9	4.4	3.3	3.3	4.9
3-h	1.0	0.4	0.5	1.1	2.5	2.1	2.3	3.1	2.6	2.2	2.3	3.3

Results for the 1-h processing window are similar to that of the ALIC-HOB2 baseline in that the (S)MINQUE models performed relatively poorly in comparison to that of EADM. However, the (S)MINQUE models show drastic improvements for the 2-h and 3-h windows. In fact, the (S)MINQUE models have produced better outcomes in terms of coordinate biasedness, repeatability and RMSE. The more favourable results from the ONSA-WTZR campaign (as compared to ALIC-HOB2) can be attributed to the shorter distance, as well as a smaller difference in latitudes between the two stations and thus, both stations experienced similar satellite geometry. The EWM have again, but not unexpectedly, yielded the worst results.

Results of the ZWD comparisons for ONSA and WTZR are summarised in Tables 6.25 and 6.26, respectively. The bias and RMSE, given by Eq. (5.1), of the GNSS and WVR ZWD differences are presented in each of these tables for each of the aforementioned stochastic models. Additionally, the adjusted RMSEs were given in brackets alongside the RMSE values. The adjusted RMSE are calculated by subtracting the corresponding bias value from each of the (GNSS-WVR) ZWD-differences. The RMSE for the adjusted differences is then recalculated. The adjusted RMSE has zero bias.

Table 6.25 RMSEs and biases (cm) of WVR-GNSS ZWD at ONSA

Window	RMSE (Adj RMSE)				BIAS			
	EWM	EADM	MINQUE	SMINQUE	EWM	EADM	MINQUE	SMINQUE
1-h	2.8 (2.8)	2.4 (2.3)	2.8 (2.8)	2.8 (2.8)	0.4	0.6	0.5	0.4
2-h	2.1 (2.1)	1.7 (1.7)	1.8 (1.7)	1.8 (1.7)	0.4	0.3	0.5	0.5
3-h	1.8 (1.5)	1.4 (1.4)	1.7 (1.7)	1.7 (1.7)	1.0	0.2	0.1	0.1

Table 6.26 RMSEs and biases (cm) of WVR-GNSS ZWD at WTZR

Window	RMSE (Adj RMSE)				BIAS			
	EWM	EADM	MINQUE	SMINQUE	EWM	EADM	MINQUE	SMINQUE
1-h	5.5 (3.1)	5.2 (3.0)	5.5 (3.2)	5.6 (3.5)	4.5	4.3	4.5	4.5
2-h	3.5 (2.4)	3.3 (2.1)	3.9 (2.3)	3.9 (1.7)	2.6	2.5	3.1	3.6
3-h	3.2 (2.0)	3.2 (1.9)	3.5 (2.0)	3.5 (2.0)	2.5	2.6	2.9	2.9

There is no significant ZWD difference between the EWM and (S)MINQUE. The EADM achieved the lowest RMSE across all three processing window. The RMSE of 1.4 cm given by the EADM with a 3-h window is comparable to that of 24-h solutions (not given in Tables 6.25 and 6.26), which has a RMSE of 1.1 cm, or that of the GNSS tropospheric solutions, which has a RMSE of 1.0 cm for the same period. Figure 6.42 demonstrates the agreement that exists between the WVR and GNSS estimates. For the 1-h processing window, the RMSE values of the ZWD differences at ONSA are relatively high in comparison to past studies (e.g., Pottiaux *et al.*, 2003; Wang *et al.*, 2007). This is not unexpected since the height component was not resolved accurately enough as shown in Tables 6.21 to 6.24. The mean differences (biases) at ONSA are generally less than 0.5 cm, which is consistent with the values given by Wang *et al.* (2007). The biases at ONSA were not significant since there were no real difference between the RMSE and the adjusted RMSE values.

The RMSEs at the WTZR station are, however, particularly high. It was later discovered that the WVR operated at the time at WTZR was a prototype and that an offset of a few centimetres may exist. The offsets can be observed in Figures 6.49 and 6.50, with majority of the differences indicating a dry bias in the WVR estimates at WTZR. Comparison with the GNSS solution also gave a high RMSE value of 3.2 cm, and thus, reinforcing the existence of a bias in the WVR solutions. The adjusted

RMSEs at WTZR corresponded quite well with those at ONSA. The WVR was not operating for the period between the 11th to the 13th of September at WTZR.

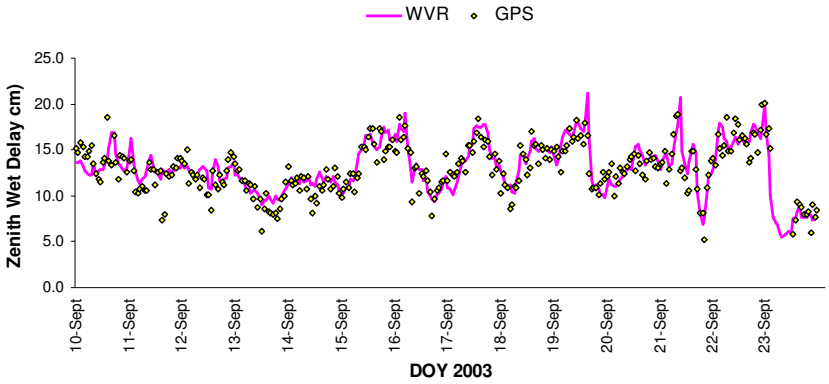

Figure 6.47 Wet delay plot of WVR vs GNSS at the Onsala (ONSA) station with a 3-h processing window

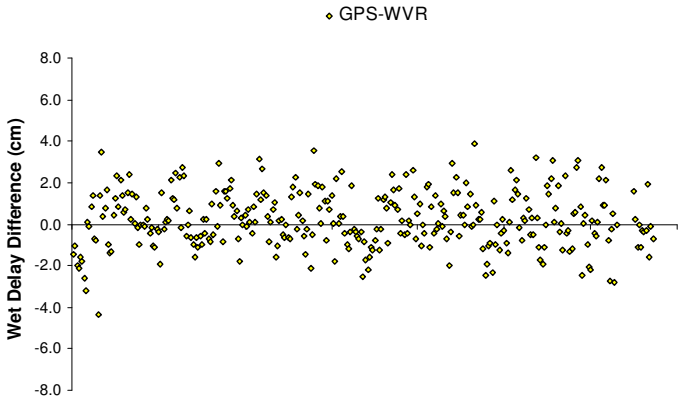

Figure 6.48 GNSS-WVR wet delay difference plot at the Onsala (ONSA) station

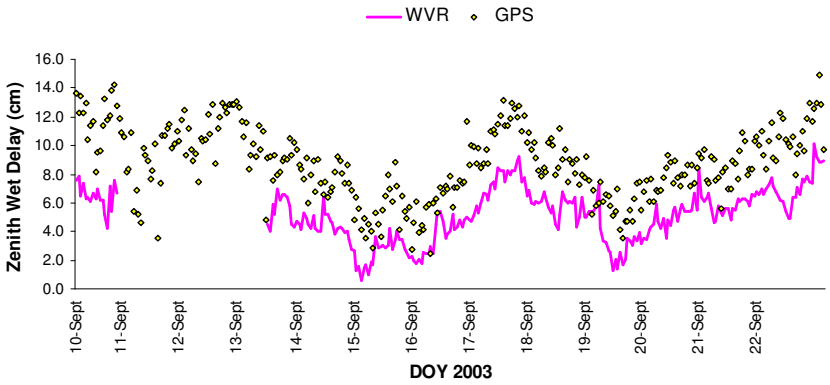

Figure 6.49 Wet delay plot of WVR vs GNSS at the Wettzell (WTZR) station

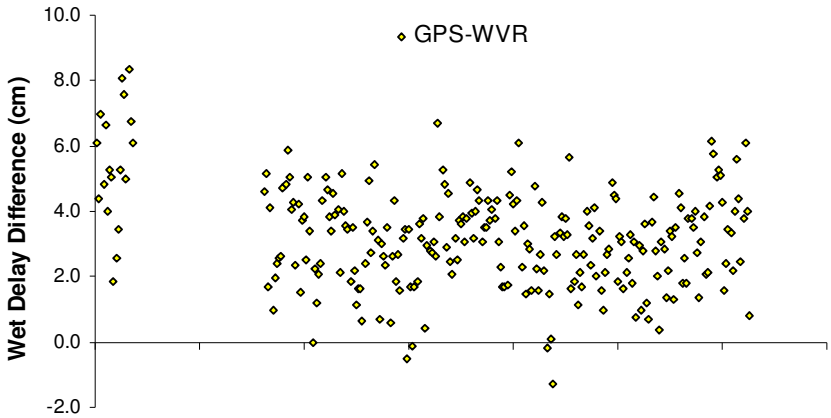

Figure 6.50 GNSS-WVR wet delay difference plot at the Wettzell (WTZR) station

Error intervals are then constructed to determine whether the error estimates of the LS ZWD are dependable error measures. Figures 6.51 and 6.52 illustrate the percentage of LS ZWD that is statistically in agreement with the WVR ZWD. Incidentally, the result of the analysis for EWM and EADM are comparatively similar to that of the simulation study. Although the performance of the (S)MINQUE models did not fare as well, it was still reasonably comparable to those of EWM and the EADM.

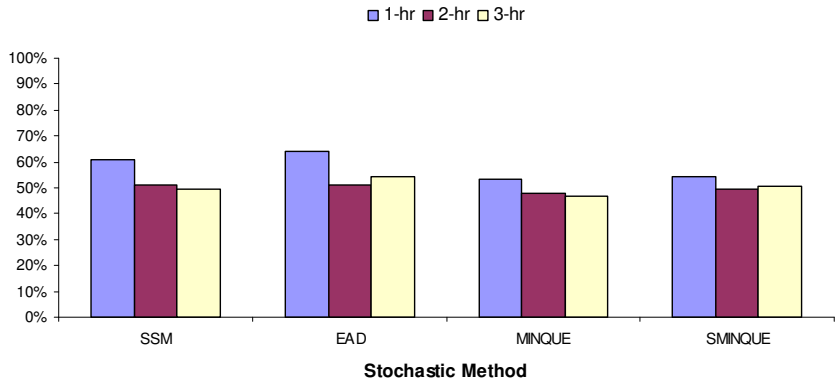

Figure 6.51 Percentages of GNSS LS ZWD estimates that are in agreement with the WVR ZWD at $2\sigma_{SE}$ for each of the tested stochastic model at ONSA

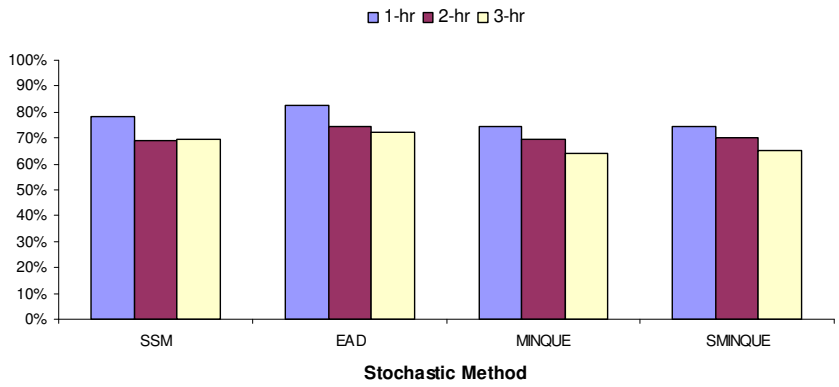

Figure 6.52 Percentages of GNSS LS ZWD estimates that are in agreement with the WVR ZWD at $3\sigma_{SE}$ for each of the tested stochastic model at ONSA

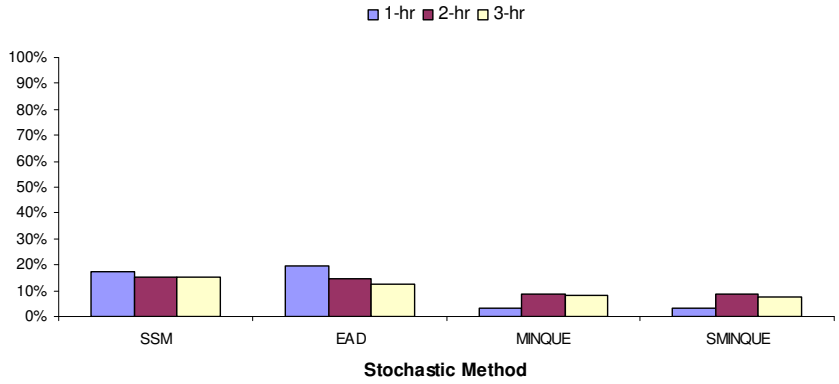

Figure 6.53 Percentages of GNSS LS ZWD estimates that are in agreement with the WVR ZWD at $2\sigma_{SE}$ for each of the tested stochastic model at WTZR

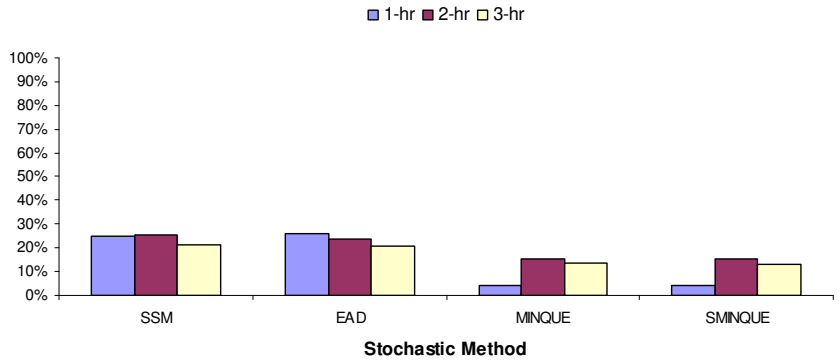

Figure 6.54 Percentages of GNSS LS ZWD estimates that are in agreement with the WVR ZWD at $3\sigma_{SE}$ for each of the tested stochastic model at WTZR

Given that large offsets that exist in the WVR measurements for WTZR, it is not surprising that the percentage of successful agreement is relatively low (see Figures 6.53 and 6.54). Since the true offset is not known, error analysis on the adjusted values can be wrongly interpreted and therefore, was not performed.

6.4.2 Baseline Analysis – ONSA and WTZR Constrained

With the coordinates of ONSA and WTZR tightly constrained to 0.0001 m, the results of the ZWD analysis are presented in the Tables 6.26 and 6.27. The RMSE are presented along with the adjusted RMSE, and as well as the biases.

Table 6.26 RMSEs and biases (cm) of WVR-GNSS ZWD at ONSA

Window	RMSE (Adj RMSE)				BIAS			
	EWM	EAD	MINQUE	SMINQUE	EWM	EAD	MINQUE	SMINQUE
1-h	2.1 (2)	1.7 (1.6)	1.9 (1.8)	1.9 (1.8)	-0.5	-0.6	-0.5	-0.5
2-h	1.6 (1.6)	1.2 (1.2)	1.6 (1.6)	1.5 (1.5)	-0.1	0.0	-0.1	-0.1
3-h	1.4 (1.4)	1.2 (1.1)	1.3 (1.3)	1.5 (1.5)	0.1	-0.1	-0.2	-0.1

Table 6.27 RMSEs and biases (cm) of WVR-GNSS ZWD at WTZR

Window	RMSE (Adj RMSE)				BIAS			
	EWM	EAD	MINQUE	SMINQUE	EWM	EAD	MINQUE	SMINQUE
1-h	5.0 (2.7)	4.6 (2.2)	4.8 (2.6)	4.8 (2.4)	4.2	4.1	4.1	4.1
2-h	3.7 (2.0)	3.6 (1.7)	4.0 (1.9)	3.9 (1.8)	3.1	3.1	3.5	3.4
3-h	3.6 (1.8)	3.6 (1.5)	3.9 (1.7)	3.9 (1.7)	3.1	3.2	3.5	3.5

The differences between the stochastic models are small at ONSA. The largest difference observed at WTZR is approximately 4 mm between EADM and EWM. This offset corresponds to less than 1 mm in PWV. The mean differences (bias) in ZWD are once again very low at ONSA, corresponding well with the aforementioned studies. With a 2-h and 3-h window, the EADM (with a RMSE value of 1.2 cm for both window sizes) again performed almost just as well as the 24-h processing window, which yielded a RMSE value of 1.1 cm. The RMSE for the ONSA GNSS solutions is 1.0 cm when compared with the WVR data for the tested period. Offset in the RMSEs WTZR can again be observed. The EADM provided the lowest RMSEs in all processing window sizes. Although not shown in the Table 6.27, the RMSEs for the 2-h and 3-h windows are in fact, identical to that of the 24-h solution. The adjusted RMSE of the 24-h solution is 1.5 cm, which is the same as that of the 3-h window session. Furthermore, the RMSEs (3.6cm for the 2-h and 3-h window) for the EADM and EWM are comparable to the RMSE for the GNSS solutions, which was 3.2 cm.

Statistical analysis of the LS ZWD at ONSA was performed and the results are presented in Figures 6.55 and 6.56. The proportions of LS ZWD that are in agreement with the WVR ZWD measurements in the constrained network are slightly less than that of the free baseline network. However, each of the models is still able to provide ZWD estimates that statistically agree with the WVR ZWD at least 65% (at $3\sigma_{SE}$) of the time at ONSA. The EADM model was again the top performer with around 80% success rate. The results for WTZR are presented in Figures 6.57 and 6.58, though no definitive interpretation of the results can be made due to the large offset in the WVR data, which is not accurately known.

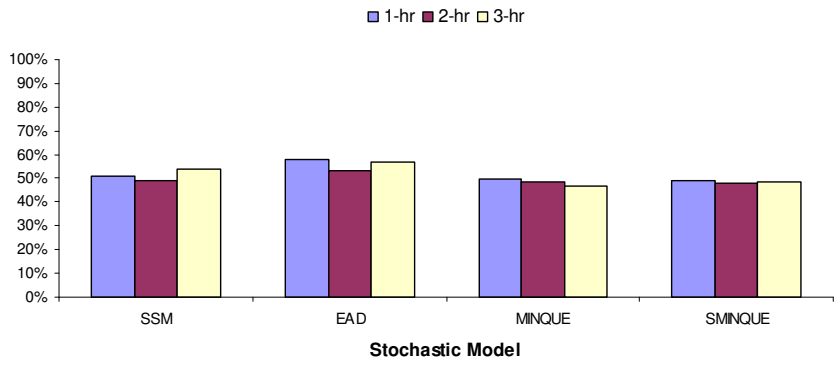

Figure 6.55 Percentages of GNSS LS ZWD estimates that are in agreement with the WVR ZWD at $2\sigma_{SE}$ for each of the tested stochastic model at ONSA

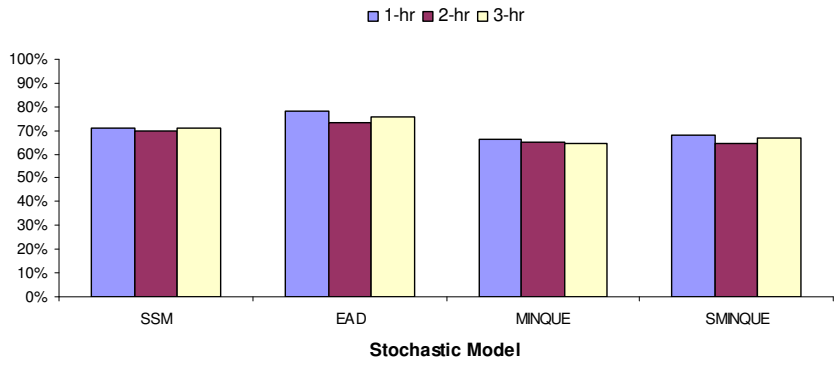

Figure 6.56 Percentages of GNSS LS ZWD estimates that are in agreement with the WVR ZWD at $3\sigma_{SE}$ for each of the tested stochastic model at ONSA

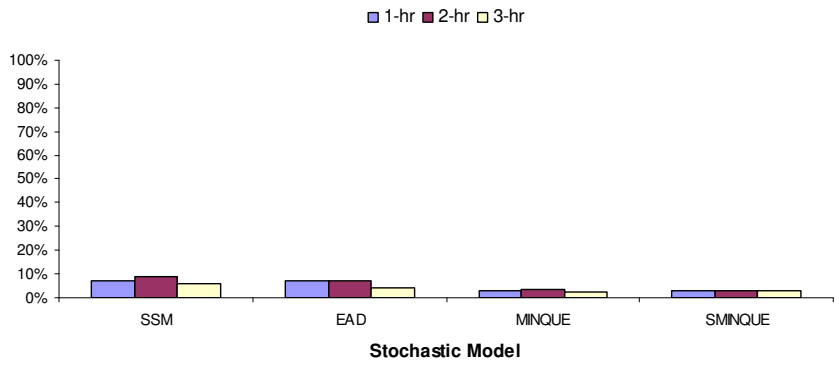

Figure 6.57 Percentages of GNSS LS ZWD estimates that are in agreement with the WVR ZWD at $2\sigma_{SE}$ for each of the tested stochastic model at WTZR

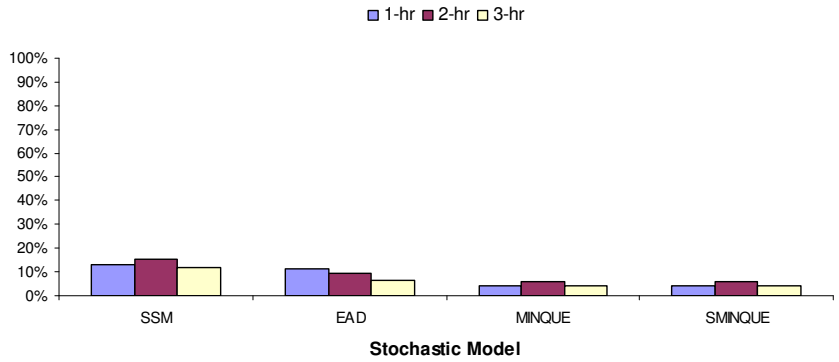

Figure 6.58 Percentages of GNSS LS ZWD estimates that are in agreement with the WVR ZWD at $3\sigma_{SE}$ for each of the tested stochastic model at WTZR

In summary, the results of the *unconstrained-baseline* show that the EADM yielded by far the best results in terms of the mean, the standard deviation and the RMSE of the coordinate offsets, for a 1-h processing window. The (S)MINQUE models however, performed marginally better for 2-h and 3-h processing windows. The performance of one model over another in the coordinate recovery is also translated to the retrieval of the GNSS ZWD estimates at ONSA. Biases between the GNSS and WVR estimates at ONSA are in the order of a few millimetres, which are consistent with previous studies (e.g., Wang *et al.*, 2007). Additionally, the EADM produced ZWD estimates (1.4 cm in RMSE) with a 3-h window that are comparable to the solution yielded with a 24-h window, which had a RMSE of 1.2 cm, as well as the GNSS solution (1.0 cm in RMSE). Due to the calibration problems, the comparison between the GNSS ZWD and the WVR estimates at WTZR are tainted with large biases ranging from 3-4 cm. However, the ZWD results for WTZR (3.3 cm and 3.2 cm in RMSEs for the EADM with a 2-h and 3-h window) are consistent

with that of the GNSS solutions, which yield a RMSE of 3.2 cm when compared to the same WTZR WVR data set.

Statistical analysis of the LS ZWD estimates for all stochastic models has indicated that at least 60% (at $3\sigma_{SE}$) of the GNSS estimates are in agreement with the WVR ZWD estimates across all window sizes. The 1-h window produced the highest success rate with at least 70% for all models, with the EADM achieving a success rate of 80%. This also shows that the error estimates from the LS adjustment process are adequate measures as a source of error information. In fact, the EADM was the top performer among all the stochastic models across all window sizes. Although with slightly lesser success rate, the same conclusion applies to the GNSS ZWD estimates for the *constrained-baseline* across all models and window sizes. Furthermore, the EADM (with a 2-h and a 3-h window), once again, was able to produce ZWD estimates (with a RMSE of 1.2 cm for both cases) that are more than comparable to that of the 24-h window (a RMSE 1.1 cm) and the GNSS solution. Although the results for WTZR are biased due to an obvious offset in the WVR data (see Figure 6.44 and Table 6.27), the RMSE of the GNSS ZWD solutions are similar to the RMSE value given by the GNSS solution.

6.5 NEAR REAL-TIME ESTIMATION OF THE ZENITH WET DELAY AT A SINGLE STATION

The first-order Gauss-Markov (GM) model given in Eq. (3.49) takes advantage of the temporal correlations that exist among the ZWD estimates to provide near real-time (NRT) wet delay estimates in the Kalman filter (KF) process. However, it was shown in Chapter 3 that the corresponding GM autocorrelation function (Eq. (3.50)), does not adequately represent the autocorrelation trend as it consistently underestimates the actual ZWD autocorrelation values. An alternative autocorrelation function was therefore proposed and is given in Eq. (3.58). The proposed autocorrelation function was shown to follow the ZWD autocorrelation trend significantly more closely than that of the GM function. However, its effect on the NRT estimation of the ZWD is still not known. Hence, in this section, the impact of the proposed model (PM) on the NRT estimation of the ZWD was investigated. The

corresponding results were then compared to that of the GM model, as well as the random-walk (RW) model (Eq. (3.47)).

In this investigation, GNSS data (1st of February, March and May) from a Western Australian IGS station, namely Yarragadee (YAR2), were used to test the models. IGS products, including the IGS final orbital file, satellite clock information, Earth Orientation Parameters (EOPs), the coordinates of the ground station and the antenna phase centre offsets and variations were used in the analysis. The station was processed in Precise Point Positioning (PPP) mode. The processing strategy includes an elevation angle cut-off of 5^0 and the Niell (1996) MFs (see Eqs. (3.64) - (3.67)). The ionosphere-free linear combination was implemented to mitigate the ionospheric residual errors. In conjunction with the standard surface meteorological data, i.e. 20 ^{0}C in temperature, 50 % humidity and 1010 millibars in pressure, the Saastamoinen (1973) hydrostatic model given in Eq. (2.37) was used to provide *a-priori* ZHD estimates. These ZHD estimates, with the aid of the NMFs, were then subtracted from the observation equations and thus, leaving behind the ZWD parameters, which were to be estimated. The KF process, which models the state vector as defined by the RW model, the GM model and the PM in Chapter 3, was used to estimate the ZWD at every 30-second interval, along with the station coordinate partials, ambiguities and receiver clock error in PPP mode. The station coordinates were not fixed as this investigation was carried out to simulate kinematic positioning. For the RW, GM and the PM models, the ZWD parameter was estimated as a random process in the form by Eq. (3.51). The *a-priori* standard deviations (SD) for the RW, GM and PM models were given as 1 mm, 5 mm and 10 mm, respectively, to represent the precision of the phase observations. Based on the autocorrelation analysis of the PWV estimates across 10 Australian stations (Section 6.1), the correlation time τ for both the GM model and the proposed model was empirically given as 4800 seconds. The empirical β value for the PM was $3/4$. Once the ZWD was estimated, it was then added to the estimated ZHD, and thus, yielding an estimate for ZTD. The estimated ZTD from each of the models was averaged at every 5 min and at every 2-h periods, respectively, during the course of the 24-h day and was then compared to the IGS tropospheric solutions.

Table 6.28 presents the RMSE of the differences between the estimated ZTD and the 5-min IGS ZTD solution, whilst Table 6.29 provides the RMSE of the estimated ZTD when compared with the 2-h IGS solution.

Table 6.28 RMSE (mm) of the differences between the estimated ZTD and the IGS tropospheric solution at 5-min resolution

DOY in 2010	1 mm SD		
	RW	GM	PM
Feb 1	17	10	10
Mar 1	22	18	18
May 1	29	7	7

DOY in 2010	5 mm SD		
	RW	GM	PM
Feb 1	17	10	10
Mar 1	22	18	18
May 1	29	7	7

DOY in 2010	10 mm SD		
	RW	GM	PM
Feb 1	17	10	10
Mar 1	22	18	18
May 1	29	7	7

Table 6.29 RMSE (mm) of the differences between the estimated ZTD and the IGS tropospheric solution at 2-h resolution

DOY in 2010	1 mm SD		
	RW	GM	PM
Feb-01	14	5	5
Mar-01	16	14	14
May-01	25	5	5

DOY in 2010	5 mm SD		
	RW	GM	PM
Feb-01	14	5	5
Mar-01	16	14	14
May-01	25	5	5

DOY in 2010	10 mm SD		
	RW	GM	PM
Feb-01	14	5	5
Mar-01	16	14	14
May-01	25	5	5

Tables 6.28 to 6.29 indicate that the RMSE differences for when the estimated ZTD were compared to the 5-min and the 2-h IGS solution ranged from 2-6 mm, which

was within the expected RMSE reported by Kouba (2009). The average RMSE difference when compared with the 5-min and 2-h IGS solutions was around 3.9 mm.

One notable observation from Tables 6.28 and 6.29 was that there was no difference in the RMSE results for when the *a-priori* standard deviation was 1 mm, 5 mm, and 10 mm. The best results were achieved with GM and PM. Moreover, there was virtually no difference between two models. This is likely due to the short sampling interval (i.e. 30 s) and estimation period (every 5 min) whereby there were minimal differences in the correlation coefficients generated by the PM and GM models. Over the 3 days, the RMSE results for GM and PM ranged from 7 to 18 mm, and with an average RMSE of 12 mm when compared to the 5-min IGS solutions. This showed an average improvement of 11 mm in ZWD when compared to the RW model.

6.6 CHAPTER SUMMARY

Results from Sections 6.2 to 6.4 suggested that reliable ZWD or PWV estimates can be obtained from smaller processing window sizes (1-h, 2-h and 3-h), especially when the station coordinates are known beforehand. When the coordinates are known, the tropospheric solutions from the baselines analyses are comparable to that of the network tropospheric solutions (Section 6.1) or the IGS estimates. In addition, the combination of shorter window size and a single-baseline processing had resulted in 80% of the LS tropospheric estimates in statistical agreement with the external RS/WVR data. In other words, there is no obvious bias for the set of LS tropospheric estimates and that the corresponding error estimates from the LS adjustment process provided a set of realistic error measures, which is essential in the weighting of the tropospheric estimates in the NWP assimilation process.

Section 6.5 provided the real data analysis of the proposed autocorrelation model given in Chapter 3. The PM was tested against the RW and GM models in the KF process in PPP mode at YARR. The RMSE results showed that GM and the PM model produced better NRT ZWD estimates than the RW model, with minimal difference between each other.

CHAPTER 7

INTERPOLATION AND PREDICTION OF ZENITH WET DELAYS

7.0 INTRODUCTION

Temporary breakdowns of GNSS stations result in missing ZWD observations. Therefore, a reliable interpolation model can be used to estimate these missing values in post-processing. In addition, a properly-chosen interpolation method can be useful in providing reliable ZWD estimates for missing RS or WVR data when GNSS is co-located with these techniques. Thus, one of the aims of this chapter is to investigate the best approach for interpolating missing ZWD data. On the other hand, prediction of ZWD values is important for some GNSS applications. For instance, a reliable real-time prediction model can provide practical ZWD estimates, which has major importance for real-time kinematic (RTK) applications. In RTK, tropospheric estimates are transmitted every couple of minutes. However, a reliable prediction model is required to produces these ZWD during transmission breaks, which can lasts several minutes. Thus, the prediction of ZWD values from a number of time-series (TS) models is also investigated.

The necessary data for the investigation of these aims are provided by the one-hourly GNSS ZWD solutions at ONSA (discussed in Section 6.4). To investigate possible interpolation and prediction methods that can be used efficiently with the ZWD data, the autocorrelation of the ZWD observations must first be studied. Hence, Section 7.1 will investigate the temporal correlations that exist among the GNSS tropospheric delays. The autocorrelation study of the tropospheric delays is carried out over the ONSA station, as well as several other Australian GNSS stations. Results show that a high autocorrelation exists between successive tropospheric measurements.

Based on this finding, Section 7.2 will discuss a number of possible interpolation models that can be used to estimate missing ZWD observations. The high

autocorrelation that exist between successive ZWD estimates and their time sequence behaviour indicates that even a simple model, such as linear interpolation, may prove useful. Thus, the linear model, along with other more sophisticated models, is investigated. Results of the investigation are summarised in Section 7.3. Using the same data set, the performances of a number of possible prediction models are also assessed. Section 7.4 briefly outlines the prediction models used in the investigation. Section 7.5 discusses the findings.

7.1 AUTOCORRELATION OF THE ZENITH WET DELAY ESTIMATES

A well-defined statistical description for the GNSS-derived tropospheric estimates is important for NWP modelling. The autocorrelations, defined in Eqs. (3.58) and (3.59), describe the temporal correlations between pairs of GNSS tropospheric estimates TS, as a function of time differences (Borre and Tiberius, 2000). These correlations need to be defined for the eventual assimilation of the GNSS tropospheric estimates into NWP model, especially for the weighting of past data in a bias reduction scheme (e.g., Stoew *et al.*, 2007). Furthermore, the autocorrelation time length can be used in recursive data processing procedures such as GM Kalman filtering (KF) with state vector augmentation (e.g., Borre and Tiberius, 2000).

To better understand the temporal correlations that exist among the GNSS tropospheric delay estimates, autocorrelation analysis of the GNSS PWV data from 14 of the Australia GNSS stations provided in Section 6.1 were performed. As there is not sufficient data available in this study to perform a long-term autocorrelation analysis, the investigation is restricted to a 12-h window. A smaller window, such as the 12-h window, would seem a logical choice for a RTK application, as it is generally dependent on the most recent data. Furthermore, the 12-h window ensures a first-order *stationarity* in the TS. Stationary TS refers to a process whose parameters, such as the mean and variance, remain fairly constant over time and space (Wei, 2006). Hence, the corresponding autocorrelation of a stationary TS value can then be deemed constant in any time interval within the 12-h window.

In this investigation, hourly GNSS PWV estimates are analysed over a 12-h interval at each station on three different dates in 2003 (Mar 31st, Apr 3rd and 6th). Figures 7.1 to 7.3 illustrate the autocorrelation of the PWV estimates over ALIC on each of these three days. Likewise, Figures 7.4-7.6 provide the autocorrelation plot of the PWV estimates over Cocos Island (COCO). In these figures, autocorrelation values that lie between the red dotted lines, which represent a 95% confidence interval, are deemed insignificant. Over the three days, the average time lengths (lags) in hours, where significant autocorrelations are observed, are summarised for each of the 14 stations in Table 7.1, whilst Figure 7.7 provides a graphical illustration for the corresponding results.

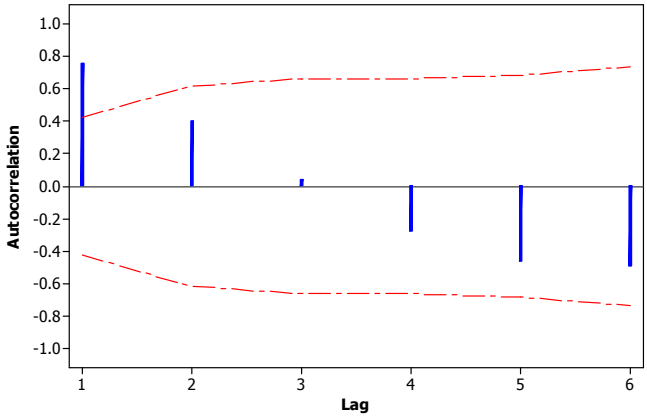

Figure 7.1 Autocorrelation plot of the PWV estimates over ALIC on Mar 31st

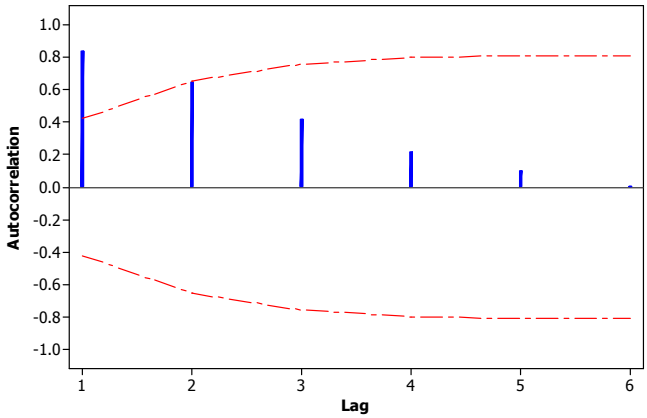

Figure 7.2 Autocorrelation plot of the PWV estimates over ALIC on Apr 3rd

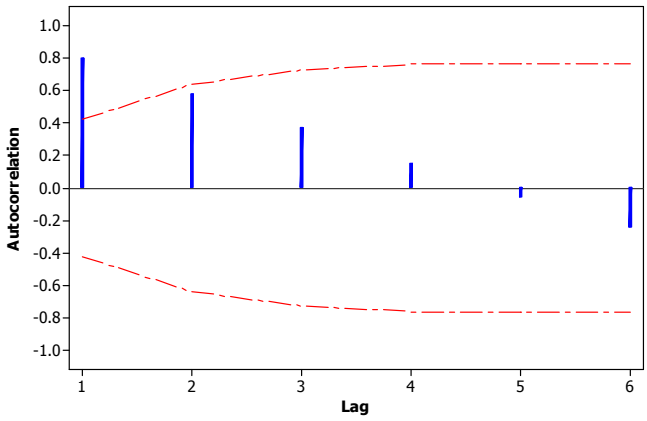

Figure 7.3 Autocorrelation plot of the PWV estimates over ALIC on Apr 6th

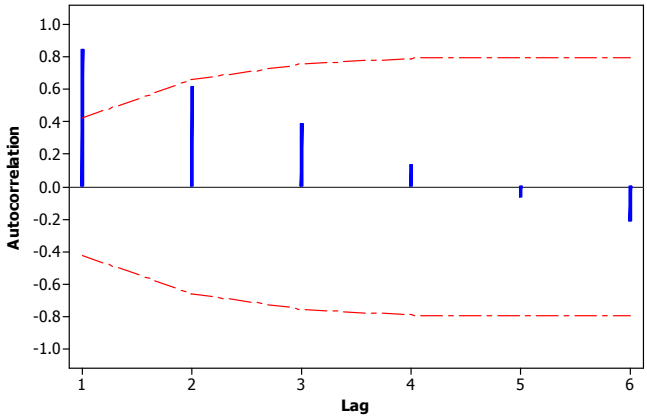

Figure 7.4 Autocorrelation plot of the PWV estimates over COCO on Mar 31st

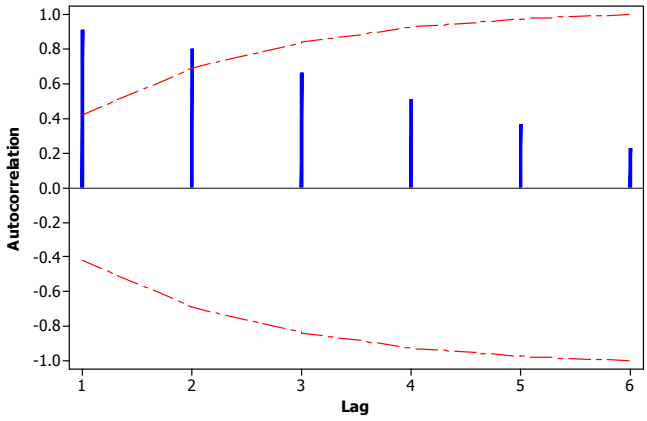

Figure 7.5 Autocorrelation plot of the PWV estimates over COCO on Apr 3rd

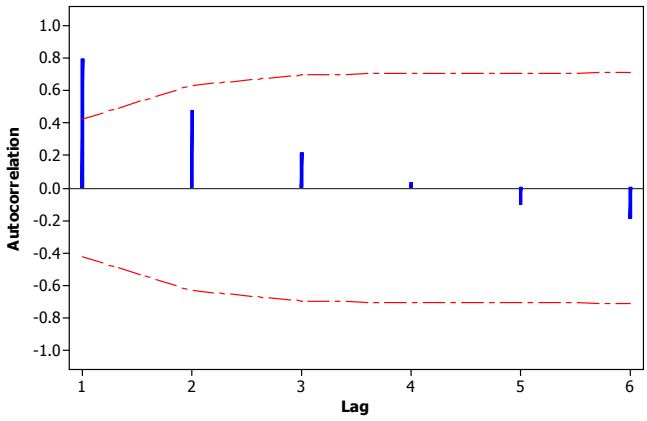

Figure 7.6 Autocorrelation plot of the PWV estimates over ALIC on Apr 6th

Table 7.1 Average time length (in hours) where significant autocorrelation is observed

Station	Time Length (h)
ALIC	1.3
ARC3	2.0
BALL	1.7
BENA	1.3
BUR1	2.0
CANN	1.3
CEDU	1.7
CLAY	1.3
COCO	1.3
COLA	1.7
DARR	2.0
DARW	2.0
EPSO	1.7
HAMI	1.7
Overall Mean (Std Dev)	1.6 (0.3)

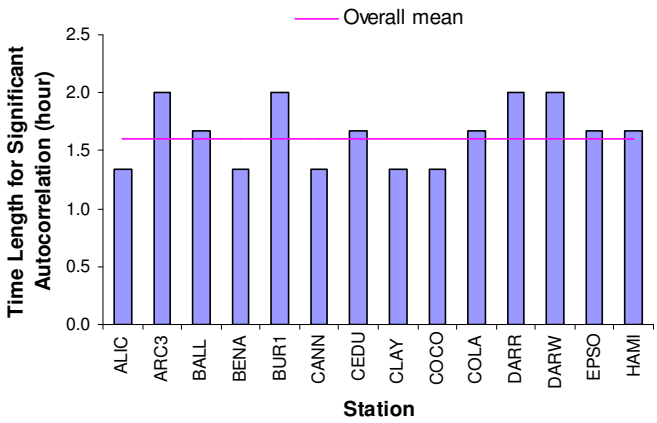

Figure 7.7 A graphical display of the average time lengths (in hours) where significant autocorrelations are observed for each of the 14 Australian stations

From Table 7.1, it can be observed that the average time lengths are fairly consistent across all stations. The overall mean of the time lengths, given as 1.6 hours in Table 7.1, can be used to provide an estimate for the time correlation constant in a GM model for RTK application.

An investigation of the WVR ZWD estimates over ONSA (as used in section 6.4) is also performed. The WVR at ONSA was appropriate for this study as it provided ZWD data at a very high frequency (every 8 seconds). In this autocorrelation study, hourly WVR ZWD were analysed with a 12-h time interval and over three different days on September 10th, 13th and 16th in 2003. The autocorrelation plots are given by Figures 7.8-7.10. Correspondingly over the same 12-h periods in these three days, the WVR ZWD estimates, sampled at every 10-min interval, were also analysed and the autocorrelation plots are given in Figures 7.11-7.13. Each unit of lag in Figures 7.11-7.13 represents a 10-min period. The summary statistics for both the 1-h ZWD and 10-min ZWD data sets are given in Table 7.2. The results of the autocorrelation analysis between the ZWDs, sampled at different rates, were then compared and summarised in Table 7.3.

Table 7.2 Mean and standard deviation (cm) of the WVR ZWD sampled at different time intervals

Sampling Rate	Mean and Standard Deviation (cm)		
	Sept 10	Sept 13	Sept 16
10 min	13.5 (1.3)	10.4 (1.0)	13.0 (2.8)
1-h	13.6 (1.5)	10.4 (1.0)	13.1 (3.1)

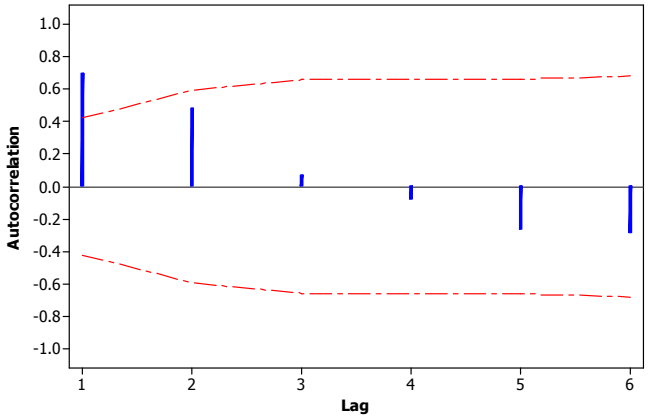

Figure 7.8 Autocorrelation plot of the 1-hrly WVR ZWDs over ONSA on Sept 10

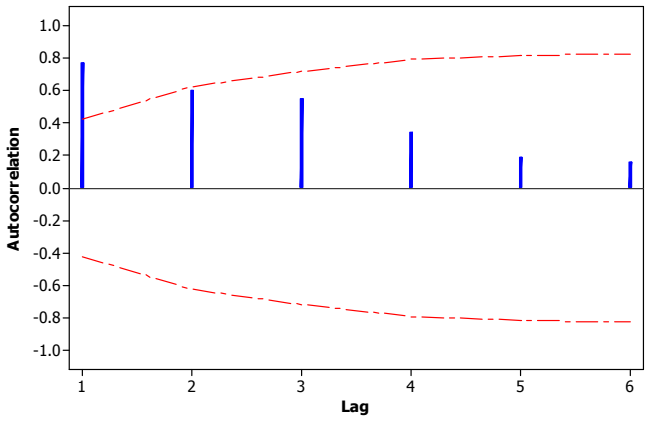

Figure 7.9 Autocorrelation plot of the 1-hrly WVR ZWDs over ONSA on Sept 13

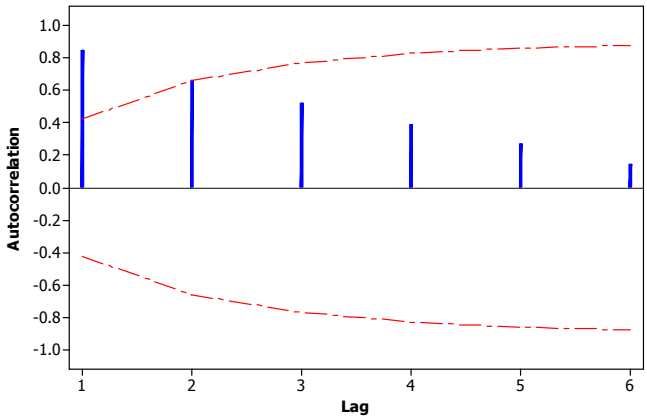

Figure 7.10 Autocorrelation plot of the 1-hrly WVR ZWDs over ONSA on Sept 16

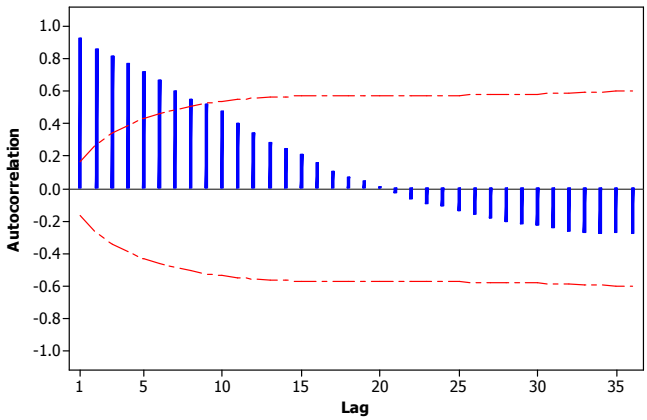

Figure 7.11 Autocorrelation plot of the 10-min WVR ZWDs over ONSA on Sept 10

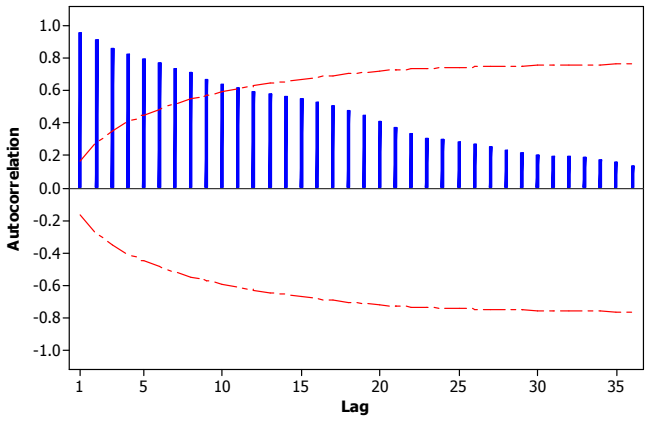

Figure 7.12 Autocorrelation plot of the 10-min WVR ZWDs over ONSA on Sept 13

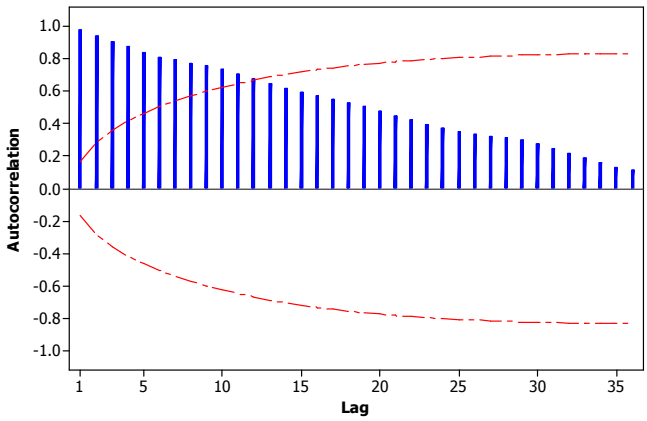

Figure 7.13 Autocorrelation plot of the 10-min WVR ZWDs over ONSA on Sept 16

Table 7.3 Comparison between the time lengths for significant autocorrelation of the WVR ZWD sampled at different time intervals

Sampling Rate	Time length with Significant Autocorrelation		
	Sept 10	Sept 13	Sept 16
10 min	1-h 30-min	1-h 50-min	2-h
1-h	1-h	1-h	2-h

Although the analysis of 10-min WVR ZWDs involved a greater number of observations than the hourly ZWDs (6 per hour as compared to 1 per hour), there are minimal differences between the means and standard deviations of the two sets of

data (Table 7.2). Comparison between Figures 7.8 to 7.13 also shows that the shape of the autocorrelation plots are maintained even when greater number of observations is sampled within the same period. Similarities between the time lengths for significant correlation are also observed for both sets of data in Table 7.3. On Sept 10^{th} and 13^{th}, both data sets agreed that the autocorrelations are insignificant when the lag is greater than 2-h. However, the 10-min ZWD data set appeared to provide a more precise estimate of the autocorrelation time lag due to the higher sampling rate. The autocorrelation results here agree well with those of the Australian stations.

Overall, the results of this study show that the existence of autocorrelations among the tropospheric estimates is evident. The autocorrelations are generally significant for estimates that are within the 1-h to 2-h lag. An average lag value of 1.6 hours is observed for the 14 Australian stations, whilst the results at ONSA are similar at around 1.7 hours. In considering the autocorrelation results, the following sections will investigate several interpolation and prediction methods for modelling the ZWD estimates over ONSA. The correlation plots at ONSA, given by Figures 7.8-7.13, will provide some insights into possible models that are appropriate for this study.

7.2 INTERPOLATION OF MISSING ZENITH WET DELAYS

Six interpolation models are considered in this study for interpolating ZWDs. The descriptions of these models are outlined briefly in the following sub-sections. The models range from the easy-to-implement linear interpolant, to the more sophisticated Kriging model. For the purpose of this investigation, the actual and estimated ZWD at time t_i (where i = 0, 1, …, n) are denoted as $ZWD(t_i)$ and $\hat{ZWD}(t_i)$, respectively, where (n+1) is the total number of ZWD values. A set of (n+1) ZWD observations is denoted by $\{ZWD(t_i)\}_{i=0}^{n}$; t_k denotes the time corresponding to a missing ZWD observation.

7.2.1 Linear Interpolation

The linear interpolation (LI) method fits a linear function between each pair of ZWD points $\{ZWD(t_i), ZWD(t_{i+1})\}$ and returns the values of the estimated ZWD,

$\hat{ZWD}(t_k)$, at a specified value of time t_k, where $t_i < t_k < t_{i+1}$ (e.g., Benesty *et al.*, 2004). The estimated ZWD can be formulated as:

$$\hat{ZWD}(t_k) = m(t_k - t_i) + ZWD(t_i) \tag{7.1}$$

where

$$m = \frac{ZWD(t_{i+1}) - ZWD(t_i)}{t_{i+1} - t_i} \tag{7.2}$$

7.2.2 Cubic Spline Interpolation

Suppose a set of $\{ZWD(t_i)\}_{i=0}^{n}$ observations are given from a reference time t_0 until t_n. A cubic spline (CS) ZWD interpolant, $\hat{ZWD}(t)$, over the time interval $[t_i, t_{i+1}]$ can be given as (e.g., Burden and Faires, 2004):

$$\hat{ZWD}(t) = a_i + b_i(t - t_i) + c_i(t - t_i)^2 + d_i(t - t_i)^3, \text{ for } i = 0,\ 1,\ ..,\ n\text{-}1 \tag{7.3}$$

where,

$$a_i = ZWD(t_i) \tag{7.4}$$

$$b_i = \frac{(a_{i+1} - a_i)}{h_i} - \frac{h_i(2c_i + c_{i+1})}{3} \tag{7.5}$$

$$d_i = \frac{(c_{i+1} - c_i)}{3h_i} \tag{7.6}$$

$$h_i = t_{i+1} - t_i \tag{7.7}$$

The coefficients $\{c_i\}_{i=0}^{n-1}$ are determined by solving a linear system of equations given by:

$$h_{i-1}c_{i-1} + 2(h_{i-1}h_i)c_i + h_i c_{i+1} = \frac{3(a_{i+1} - a_i)}{h_i} - \frac{3(a_i - a_{i-1})}{h_{i-1}}, \text{ for } i = 0, 1, ..., n-1 \tag{7.8}$$

If a ZWD observation is missing at time t_k, such that $t_i < t_k < t_{i+1}$, the interpolated value, $\hat{ZWD}(t_k)$ can be calculated via Eq. (7.3) once the coefficients a_i, b_i, c_i and d_i have been determined. To implement the CS interpolant requires at least three observations.

7.2.3 Cubic Hermite Polynomial Interpolation

For any pair of epochs $[t_i, t_{i+1}]$, the cubic Hermite polynomial (CHP) interpolant, $\hat{ZWD}(t)$, between the given points can be estimated as (e.g., Burden and Faires, 2004):

$$\hat{ZWD}(t) = ZWD(t_i) + f_1(t - t_i) + f_2(t - t_i)^2 + f_3(t - t_i)^2(t - t_{i+1}) \tag{7.9}$$

where,

$$f_1 = \Delta ZWD(t_i) = \frac{ZWD(t_i) - ZWD(t_{i-1})}{t_i - t_{i-1}}, \tag{7.10}$$

$$f_2 = \frac{f_4 - f_1}{t_{i+1} - t_i}, \tag{7.11}$$

$$f_3 = \frac{f_6 - f_2}{t_{i+1} - t_i} \tag{7.12}$$

$$f_4 = \frac{ZWD(t_{i+1}) - ZWD(t_i)}{t_{i+1} - t_i}, \tag{7.13}$$

$$f_5 = \frac{ZWD(t_{i+2}) - ZWD(t_{i+1})}{t_{i+2} - t_{i+1}}, \text{ and} \tag{7.14}$$

$$f_6 = \frac{f_5 - f_4}{t_{i+1} - t_i} \tag{7.15}$$

7.2.4 Lagrange Polynomial Interpolation

For a set of $\{ZWD(t_i)\}_{i=0}^{n}$ observations given at (n+1) epochs, then there exists a unique polynomial $P(t)$ of a degree $\leq n$ such that (Burden and Faires, 2004)

$$ZWD(t_i) = P(t_i) \text{ for each } i = 0, 1, \ldots, n\text{-}1 \tag{7.16}$$

For each epoch i = 0, 1, …, n-1, the Lagrange polynomial (LP) is given by:

$$P(t) = ZWD(t_0)L_{n,0}(t) + \cdots + ZWD(t_n)L_{n,n}(t) = \sum_{i=0}^{n} ZWD(t_i)L_{n,i}(t) \tag{7.17}$$

where

$$L_{n,i}(t) = \frac{(t-t_0)(t-t_1)\cdots(t-t_{i-1})(t-t_{i+1})\cdots(t-t_n)}{(t_i-t_0)(t_i-t_1)\cdots(t_i-t_{i-1})(t_i-t_{i+1})\cdots(t_i-t_n)} = \prod_{\substack{j=0 \\ j\neq i}}^{n} \frac{(t-t_j)}{(t_i-t_j)} \quad (7.18)$$

The estimated value of ZWD at time t_k can be given as:

$$\hat{ZWD}(t_k) = P(t_k) \quad (7.19)$$

7.2.5 Fast Fourier Transform Interpolation

To use the fast Fourier transform (FFT) method for the interpolation of the ZWDs, a vector of ZWD observations $[ZWD] = \{ZWD(t_i)\}_{i=1}^{n}$ of length n (sampled at equally spaced points) is firstly transformed to the discrete Fourier transform vector F_{ZWD} using the algorithm (Frigo and Johnson, 1998) given by:

$$F_{ZWD} = \sum_{i=1}^{n} ZWD(t_i) v_n^{(i-1)(t-1)} \quad (7.20)$$

where v_n is the complex n^{th} root of unity (with $j = \sqrt{-1}$) defined by,

$$v_n = e^{-2\pi\pi/n} \quad (7.21)$$

The next step of the process is to calculate the inverse Fourier transform vector $[\hat{ZWD}] = \{\hat{ZWD}(t_i)\}_{i=1}^{N}$, i.e. the interpolated values), by using the following expression for a user-specified value of N:

$$[\hat{ZWD}] = \left(\frac{1}{N}\right) \sum_{i=1}^{N} F_{ZWD} v_N^{-(i-1)(t-1)} \quad (7.22)$$

If $n < N$, the vector F_{ZWD} is padded with trailing zeros to a length of N, prior to applying the inverse transformation defined by Eq. (7.22). If $n > N$, then F_{ZWD} is truncated to the specified length. In this investigation, N is given as:

$$N = n \times (\text{number of missing observations}) \quad (7.23)$$

7.2.6 Ordinary Kriging Interpolation

Kriging is a spatial technique that can be used for interpolating tropospheric delays from reference stations in a GNSS network to a user in an unknown location within the region (e.g. Zeng *et al.*, 2004). Kriging is known as best linear unbiased estimator as it estimates the value of a random function at a point as a linear combination of the values at the sample points whilst minimizing the error variance. In essence, Kriging is a weighted linear combination of all observations. It assumes that the closer the input parameters are, the more correlated the observations are. With this concept, it is then worthwhile exploring whether Kriging is appropriate as ZWD interpolator whereby time *t* is the input parameter. More precisely, the use of *ordinary* Kriging is investigated in its simplest one-dimensional form to determine its usefulness for interpolating ZWD.

Ordinary Kriging interpolation is performed by using a two-component predictor. The first component can be viewed as the generalised LS estimate while the second component is treated as the realisation of a Gaussian process. The ZWD can be modelled as (Sacks *et al.*, 1989):

$$\mathrm{ZWD}(t) = \sum_{j=1}^{p} \beta_j h_j(t) + Z(t) \tag{7.24}$$

where h_j's are the pre-determined functions of time; p is the number of unknown parameter; β_j's are unknown coefficients to be estimated. The Gaussian process, $Z(t)$, is assumed to have zero mean and a covariance that can be estimates as:

$$V_t = \mathrm{Cov}(t_{i1}, t_{i2}) = \sigma^2 R(t_{i1}, t_{i2}) \tag{7.25}$$

between times t_{i1} and t_{i2}; σ^2 is the a-priori variance of the model and $R(t_{i1}, t_{i2})$ is the correlation, whose form can be given by:

$$R_t = R(t_{i1}, t_{i2}) = e^{\left(-\theta |t_{i1} - t_{i2}|^q\right)} \quad 0 < q \le 2 \tag{7.26}$$

In this study, the variable q is selected to equal two to indicate Euclidian norm, whilst the unknown parameter θ is to be estimated. Additionally, the first component of Eq. (7.24) can be simplified as an unknown coefficient $\hat{\mu}$, and the ordinary Kriging model can be formulated as (Morris, 1995):

$$\hat{ZWD}(t) = \hat{\mu} + Z(t) \tag{7.27}$$

The use of $\hat{\mu}$, instead of $\sum_{j=1}^{p} \beta_j h_j(t)$, will result in less computational effort with no significant model degradation (Sacks *et al.*, 1989).

Given a set of times $t = \{t_0, t_2, ..., t_n\}$ and the corresponding $(n+1)\times 1$ vector of ZWD estimates, $ZWD(t) = \{ZWD(t_0), ZWD(t_2), ..., ZWD(t_n)\}^T$, the best linear unbiased predictor (BLUP) at time t_k can be written as (Sacks *et al.*, 1989):

$$\hat{ZWD}(t_k) = \hat{\mu} + v_{t_k}^T V_t^{-1} (ZWD(t) - H\hat{\mu}) \tag{7.28}$$

where

$$(V_t)_{ij} = Cov[Z(t_i),\ Z(t_j)]\ , \tag{7.29}$$

$$v_{t_k}^T = \{Cov[Z(t_k), Z(t_1)] ...., Cov[Z(t_k), Z(t_n)]\} \tag{7.30}$$

$$\hat{\mu} = \left((H^T V H)^{-1} H^T V\right) ZWD(t) \tag{7.31}$$

and H being a $(n+1)\times 1$ vector of ones.

In general, σ^2 and θ in Eqs. (7.25) and (7.26) are unknowns. They can be estimated by a method equivalent to the empirical Bayes approach (Koehler and Owen, 1996), which finds the parameters that are most consistent with the observed data. Since $Z(t)$ is Gaussian, the maximum likelihood estimation (MLE) method can be used to estimate σ^2 and θ (Koehler and Owen, 1996). The MLE of σ^2 is given as:

$$\hat{\sigma}^2 = \frac{(ZWD(t) - \hat{\mu}H)^T R_t^{-1} (ZWD(t) - \hat{\mu}H)}{n+1} \tag{7.32}$$

The maximum likelihood estimation of θ is a one-dimensional optimisation problem of the form:

$$\max_{\theta \in R^1} (-1/2)\left[\left(n \ln \hat{\sigma}^2\right) + \ln\left(\det\left(R_t\right)\right)\right], \tag{7.33}$$

subject to $0 \le \theta \le \infty$

A nonlinear optimisation subroutine can usually solve Eq. (7.33) with respect to the parameter θ (Koehler and Owen, 1996). Once the optimal value of θ is obtained, it can then be substituted back into Eq. (7.26), and be used to determine V_t and $\hat{\mu}$. The predictor $ZWD(t_k)$ in Eq. (7.28) can then be completely determined.

7.2.7 Least-Squares Modelling

For a set of $(n+1)$ GNSS ZWDs corresponding to time $t = \{t_0, t_1, \ldots, t_n\}$, a least-squares model can be formulated in a polynomial form using these observations such that:

$$\hat{ZWD}(t_i) = a_0 + a_1 t_i + a_2 t_i^2 + \cdots + a_p t_i^p = a_0 + \sum_{j=1}^{p} a_j t_i^j \tag{7.34}$$

where p is the order of the polynomial and a_i (for i = 0, 1, …, p) are the unknown coefficients to be estimated. The LS solution for the coefficients $\{a_j\}_{j=0}^{p}$ can be calculated by using Eq. (3.25) in Chapter 3. Once the coefficients are solved, Eq. (7.34) can then be used to estimate the missing observation and time t_k. The principle of LS is described in Chapter 4.

The LS approach models the data by minimising the sum of squares of the residual errors, which may or may not pass through the data points. The LS differs from the interpolation models considered here, in that the latter passes through all the observation points.

7.3 TESTING AND ANALYSIS OF METHODS FOR ESTIMATING MISSING ZENITH WET DELAY OBSERVATIONS

The purpose of this section is to identify the best method of interpolating missing GNSS ZWD data. The performances of all the aforementioned interpolation methods given in Section 7.2 are assessed and inter-comparisons between the models are made using the GNSS ZWD data at ONSA in Section 6.4. These GNSS ZWD data were estimated with a fully constrained ONSA-WTZR baseline and a 3-h processing window. The GNSS ZWD data has a RMSE of 12 mm (or < 2 mm in PWV) in comparison to the WVR ZWD for the corresponding period. Figure 7.14 shows the time sequence of the GNSS ZWD data used in this study.

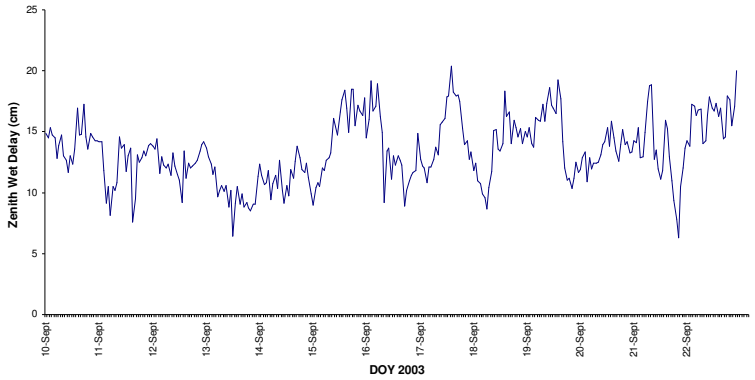

Figure 7.14 GNSS ZWD estimates at ONSA

The number of ZWD observations used to generate the IM and LS models will impact the determination of the model coefficients, and consequently the accuracy of the missing GNSS ZWD observations. Thus, in this investigation, different sets of observations will be used to construct these models. The number of pre-determined data points, m_{ZWD}, used to generate these models will range from 4 to 48, i.e. $m_{ZWD} \in \{4, 6, 8, 12, 18, 24, 30, 36, 40, 44, 48\}$. Additionally, in each of these runs, the tested models will be used to estimate one, two-consecutive, three-consecutive and four-consecutive missing observations, i.e. $1 \le k_{mis} \le 4$. The models are generated and analysed using the following procedure:

(1) Assuming a total of n observations in the data set, let k_{mis} be the pre-determined number of missing data points, and m_{ZWD} the number of data points used to generate the model;

(2) Set $i = {}^{m_{ZWD}}\!/_{2}$;

(3) Let $ZWD_{mis}(t) = \{t_j, ZWD(t_j)\}_{j=i+1}^{i+k_{mis}}$ be the consecutively selected missing ZWD data set;

(4) Let $ZWD_{obs} = \{ZWD(t_{i-k_{mis}+1}),\ ZWD(t_i),\ ZWD(t_{i+k_{mis}+1}),\ ...,\ ZWD(t_{2i+k_{mis}})\}$ be the selected data set used to generate the models;

(5) Generate the IM or LS model based on the data set ZWD_{obs} and estimate the wet delay, $\hat{ZWD}(t_j)$, for $\{t_j\}_{j=i+1}^{i+k_{mis}}$;

(6) To assess the model used at any epoch, the difference between the "true" GNSS ZWD (ONSA-WEZ ZWD data set) and the estimated ZWD, i.e. $\Delta ZWD_{diff}(t) = \hat{ZWD}(t) - ZWD_{mis}(t)$, is computed;

(7) Similarly, the next missing data points are estimated by shifting one position in time, i.e. $\{t_{j+1}, ZWD(t_{j+1})\}$ becomes $\{t_j, ZWD(t_{j+1})\}_{j=i+2}^{i+k_{mis}+1}$, until the last missing data point has been reached.

The above procedure places the set of missing ZWD observations, $ZWD_{mis}(t)$, in the centre of the modelling data set, $ZWD_{obs}(t)$. The first set of missing data begins at time $\{t_{i+1}, \ldots, t_{i+k_{mis}}\}$ and the last set finishes at time $\{t_{n-i-k_{mis}+1}, \cdots, t_{n-i}\}$. In all, a total of $(n - m_{ZWD} - k_{mis})$ missing data sets are considered. Given that there are k_{mis} missing observations in each of these sets, the total number of comparisons is therefore, $k_{mis}(n - m_{ZWD} - k_{mis})$.

When all cases of missing data sets for a given model have been considered, the RMSE of the $k_{mis}(n - m_{ZWD} - k_{mis})$ ZWD differences are then calculated by:

$$RMSE_I = \sqrt{\frac{\sum_{j=1}^{k_{mis}(n-m_{ZWD}-k_{mis})} [\Delta ZWD_{diff}(t_j)]^2}{k_{mis}(n - m_{ZWD} - k_{mis})}} \tag{7.35}$$

The overall estimation (interpolation) error E_I, as a percentage, is defined as the RMSE divided by the total number of comparisons:

$$E_I = \left(\frac{RMSE_I}{\left(\frac{1}{k_{mis}\left(n - m_{ZWD} - k_{mis}\right)} \right)^{k\left(n - m_{ZWD} - k_{mis}\right)} \sum_{j=1} ZWD_{mis}\left(t_j\right)} \right) * 100\% \qquad (7.36)$$

7.3.1 Interpolation Models

In an effort to determine a suitable model for the purpose of estimating missing ZWDs, the interpolation models outlined in Section 7.1 were tested. The RMSEs, calculated via Eq. (7.35), of these models for $m_{ZWD} \in \{4, 6, 8, 12, 18, 24, 30, 36, 40, 44, 48\}$ are summarised in Tables 7.4 to 7.7.

The results show that the Lagrange polynomials (LP) method is the poorest performer. As the number of data points increases, the LP exhibits what is known as Runge's phenomenon (Runge, 1901; Fornberg and Zuev, 2007), and thus produces poor outcomes. Runge's phenomenon is an error problem for a high-order polynomial interpolant on equidistant intervals, whereby the polynomial oscillates towards the end of the interval, as shown in Figure 7.15, resulting in poor ZWD estimation between the intervals. This effect was more prominent when estimating two, three and four missing ZWD observations.

Table 7.4 RMSEs (cm) of the interpolated ZWDs for the case of a single missing observation

Num of Data Pts	Linear	Spline	CHP	FFT	Lagrange	Kriging
4	1.27	1.39	1.30	1.35	1.39	1.27
6	1.27	1.45	1.30	1.36	1.49	1.35
8	1.27	1.47	1.30	1.36	1.56	1.40
12	1.27	1.47	1.30	1.35	1.65	1.37
18	1.27	1.47	1.30	1.33	1.72	1.40
24	1.27	1.47	1.30	1.32	1.76	1.41
30	1.27	1.47	1.30	1.32	1.78	1.41
36	1.27	1.47	1.30	1.32	1.81	1.43
40	1.27	1.47	1.30	1.32	1.82	1.43
44	1.27	1.47	1.30	1.32	1.84	1.42
48	1.27	1.47	1.30	1.32	1.85	1.42

Table 7.5 RMSEs (cm) of the interpolated ZWDs for the case of two-successive missing observations

Num of Data Pts	Linear	Spline	CHP	FFT	Lagrange	Kriging
4	1.41	1.66	1.46	1.48	1.66	1.41
6	1.41	1.79	1.46	1.51	1.96	1.58
8	1.41	1.87	1.46	1.52	2.28	1.54
12	1.41	1.89	1.46	1.54	2.88	1.58
18	1.41	1.89	1.46	1.54	3.65	1.59
24	1.41	1.89	1.46	1.54	4.26	1.65
30	1.41	1.89	1.46	1.54	4.78	1.68
36	1.41	1.89	1.46	1.54	5.22	1.71
40	1.41	1.89	1.46	1.54	5.48	1.73
44	1.41	1.89	1.46	1.54	5.73	1.75
48	1.41	1.89	1.46	1.53	5.97	1.75

Table 7.6 RMSEs (cm) of the interpolated ZWDs for the case of three-successive missing observations

Num of Data Pts	Linear	Spline	CHP	FFT	Lagrange	Kriging
4	1.50	1.76	1.53	1.55	1.76	1.54
6	1.50	1.88	1.53	1.55	2.12	1.53
8	1.50	1.94	1.53	1.55	2.54	1.55
12	1.50	1.96	1.53	1.55	3.59	1.66
18	1.50	1.96	1.53	1.54	5.57	1.72
24	1.50	1.96	1.53	1.54	7.76	1.82
30	1.50	1.96	1.53	1.54	10.01	1.88
36	1.50	1.96	1.53	1.54	12.29	1.93
40	1.50	1.96	1.53	1.54	13.81	1.95
44	1.50	1.96	1.53	1.54	15.31	1.98
48	1.50	1.96	1.53	1.54	16.81	1.99

Table 7.7 RMSEs (cm) of the interpolated ZWDs for the case of four-successive missing observations

Num of Data Pts	Linear	Spline	CHP	FFT	Lagrange	Kriging
4	1.62	2.12	1.68	1.68	2.12	1.65
6	1.62	2.35	1.68	1.70	2.99	1.71
8	1.62	2.48	1.68	1.71	4.02	1.73
12	1.62	2.51	1.68	1.71	6.45	1.81
18	1.62	2.51	1.68	1.71	11.03	1.87
24	1.62	2.51	1.68	1.70	16.62	1.98
30	1.62	2.51	1.68	1.70	23.04	2.06
36	1.62	2.51	1.68	1.71	30.20	2.10
40	1.62	2.51	1.68	1.71	35.42	2.13
44	1.62	2.51	1.68	1.70	41.04	2.16
48	1.62	2.51	1.68	1.70	47.04	2.17

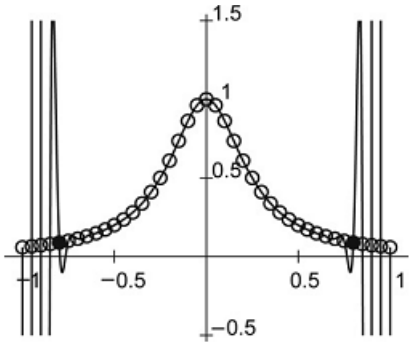

Figure 7.15 Runge's phenomenon (Fornberg and Zuev, 2007)

Tables 7.4 to 7.7 also indicate that the linear interpolation (LI), the cubic Hermite polynomial (CHP) and fast Fourier transform (FFT) models (interpolants that are dependent only on the most recent pair of data points) produce better estimates than splines and ordinary Kriging, which estimate the missing data points by giving greater weights to more recent data points, and lesser weights to those that are further away. Kriging did, however, produce comparable results to these models when the number of modelling data is low. The LI model, which was the simplest of all to use, produced the best results across all scenarios. The LI was able to provide, on average, ZWD estimates to within 1.3 cm to 1.6 cm from the actual ZWD data, which corresponds to a PWV error of about 2 mm to 2.5 mm. This level of discrepancy is comparable to many GNSS PWV studies (e.g., Basili *et al.*, 2001; Snajdrova *et al.*, 2006; Wang *et al.*, 2007). Note that both LI and CHP are methods that only utilise the two most recent observations, with one on either side of the missing data set.

The favourable results for LI, CHP and FFT models can be explained by the autocorrelation study in Section 7.1, whereby significant correlations occur among the estimates within a 1h to 2-h period. Successive 1-h ZWD estimates have an autocorrelation value as high as 0.8. Inclusion of several data points that are, time-wise, distant from the estimation time may have introduced noise into the splines and Kriging models.

7.3.2 Least-Squares Polynomials

A higher-order polynomial will generally model the behaviour of the data better if there is a weak linear trend between the observations. However, it is also possible that the data is over-parameterised. For example, a data set that exhibits a parabolic behaviour is best modelled by a quadratic function. In this instance, the model will not benefit from a polynomial of an order higher than two. In some cases, over-parameterisation of the observations may reduce the reliability of the model (Walpole *et al.*, 2007). In this study into the LS modelling of m_{ZWD} observations, polynomials $P_{m_{ZWD}}$ of an order up to (m_{ZWD}-2) are analysed for each run, with the maximum order of 18 allowed. Tables 7.8 to 7.11 summarise the results of estimating one, two-consecutive, three-consecutive and four-consecutive missing observations. The polynomial with the lowest RMSE, given by Eq. (7.35), in each of these runs, is presented. The fourth and fifth columns in these tables are the percentages of the interpolated ZWD that are not statistically significant different to the GNSS ZWD at $2\sigma_{SE}$ and $3\sigma_{SE}$, respectively. These corresponding error estimates can be useful as error measures in an assimilation process.

From Tables 7.8 to 7.11, it can be seen that the best results are achieved with polynomials of order greater than two when $m \geq 6$. This is always the likely case since greater variations are observed in the data sets as m increases. Therefore, it is expected that higher-order polynomials are more appropriate in following the data trends.

Table 7.8 The LS polynomial in the estimation of a single missing observation

Polynomial	Order of Polynomial	RMSE (cm)	% of agreement at 2 SE	% of agreement at 3 SE
P_4	1	1.32	68%	77%
P_6	3	1.32	76%	85%
P_8	3	1.30	82%	91%
P_{12}	7	1.30	87%	94%
P_{18}	6	1.30	88%	95%
P_{24}	9	1.30	87%	96%
P_{30}	13	1.30	86%	96%
P_{36}	15	1.31	89%	97%
P_{40}	15	1.30	87%	96%
P_{44}	16	1.30	88%	96%
P_{44}	18	1.30	87%	97%

Table 7.9 The LS polynomial in the estimation of two-successive missing observations

Polynomial	Order of Polynomial	RMSE (cm)	% of agreement at 2 SE	% of agreement at 3 SE
P_4	1	1.44	68%	80%
P_6	3	1.46	78%	87%
P_8	3	1.45	81%	91%
P_{12}	5	1.48	85%	95%
P_{18}	7	1.42	87%	97%
P_{24}	9	1.43	87%	97%
P_{30}	12	1.43	89%	98%
P_{36}	15	1.46	88%	97%
P_{40}	15	1.44	89%	97%
P_{44}	17	1.44	88%	97%
P_{44}	18	1.42	89%	97%

Table 7.10 The LS polynomial in the estimation of three-successive missing observations

Polynomial	Order of Polynomial	RMSE (cm)	% of agreement at 2 SE	% of agreement at 3 SE
P_4	1	1.55	69%	79%
P_6	3	1.63	79%	87%
P_8	3	1.54	82%	92%
P_{12}	4	1.57	87%	96%
P_{18}	7	1.54	88%	96%
P_{24}	7	1.58	88%	95%
P_{30}	13	1.58	89%	97%
P_{36}	14	1.59	89%	97%
P_{40}	16	1.59	89%	97%
P_{44}	18	1.58	91%	98%
P_{44}	18	1.62	89%	96%

Table 7.11 The LS polynomial in the estimation of four-successive missing observations

Polynomial	Order of Polynomial	RMSE (cm)	% of agreement at 2 SE	% of agreement at 3 SE
P_4	1	1.65	67%	79%
P_6	2	1.73	85%	92%
P_8	3	1.66	82%	92%
P_{12}	5	1.72	86%	95%
P_{18}	7	1.70	88%	96%
P_{24}	9	1.76	88%	95%
P_{30}	13	1.77	90%	97%
P_{36}	16	1.77	90%	98%
P_{40}	6	1.77	75%	88%
P_{44}	18	1.74	91%	98%
P_{44}	9	1.77	76%	89%

However, the polynomial with maximum polynomial order allowed, did not always yield the best results. This is a classic case of over-parameterisations. Figure 7.16 is a

graphical illustration of this issue, for $m_{ZWD} \in \{4, 6, 8, 12, 18, 24, 30, 36, 40, 44, 48\}$, in the case of estimating a single missing ZWD observation.

Among the best polynomials of these runs, the differences, in regards to the ZWD RMSEs, are marginal. On the other hand, the performance of the error estimates improves as m increases from four to 18, but gave similar results for $m_{ZWD} > 18$. Overall for this data set, one can make the case that the best LS polynomial model for the estimation of missing ZWDs is generated with 18 data points, denoted as P_{18}, with results in Table 7.11 being the only exception. Although P_4 and P_8 have yielded lower ZWD RMSE results in this case, P_{18} provided ZWD estimates that are statistically more agreeable to the GNSS ZWD estimates (with 96% success rate at three SE, as compared to 79% and 92% with P_4 and P_8, respectively). The corresponding error estimates can be useful if the nature of the user's work requires not just the actual ZWD estimates, but the corresponding precisions as well.

Comparisons of the performances of the LS polynomials and IMs were also made. Figures 7.17 to 7.20 illustrate the estimation errors, given by Eq. (7.36), for each of the modelling techniques given in Section 7.2 at each $m_{ZWD} \in \{4, 6, 8, 12, 18, 24, 30, 36, 40, 44, 48\}$. As can be seen from Tables 7.9 to 7.12, the results of the LP were comparatively large, and thus were excluded from Figures 7.17 to 7.20.

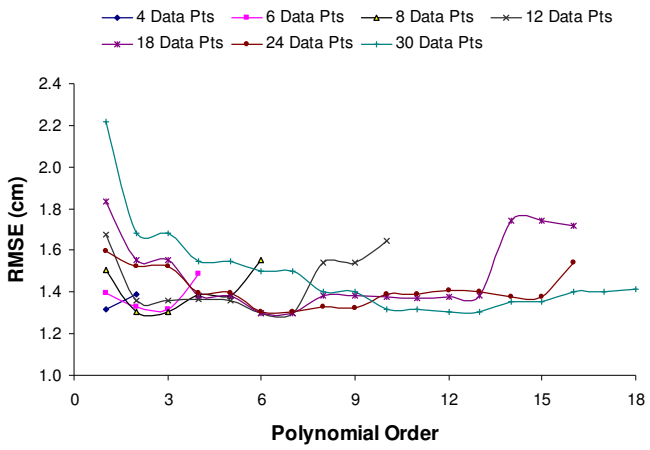

Figure 7.16 Variation in the RMSEs as the order of the polynomial increases

Based on the results of the above tests, the LS polynomials have outperformed all the investigated interpolation models, except for the linear interpolation model. The LI was marginally better than the LS model. The average difference between the interpolation errors of the linear interpolation and the least-squares approach is about 0.2%, which corresponds to less than a millimetre difference in estimating the ZWDs. The advantage of the former approach is in its simplicity, whereas the LS model has the added benefit of (standard) error estimation as a measure of precision for the estimates. If the error estimates is of no interest to the user, the linear interpolant suffices.

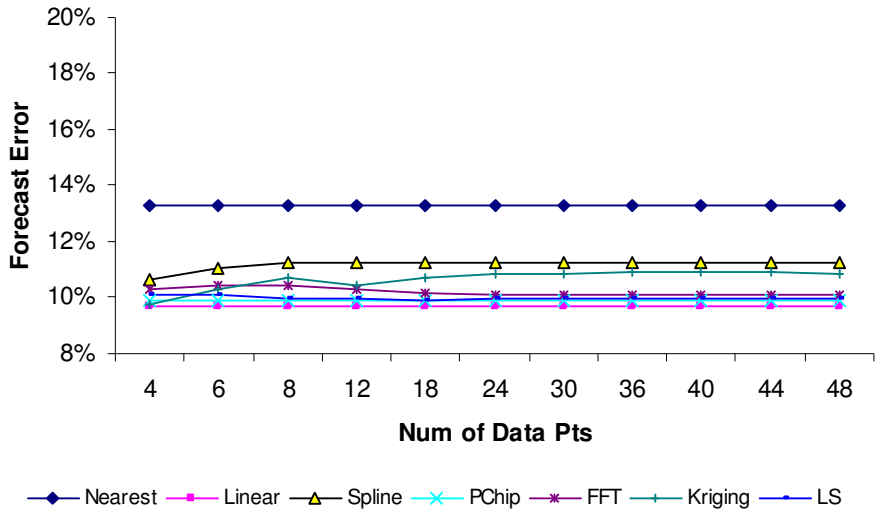

Figure 7.17 Comparison between the estimation errors of different modelling techniques for the case of one missing observation

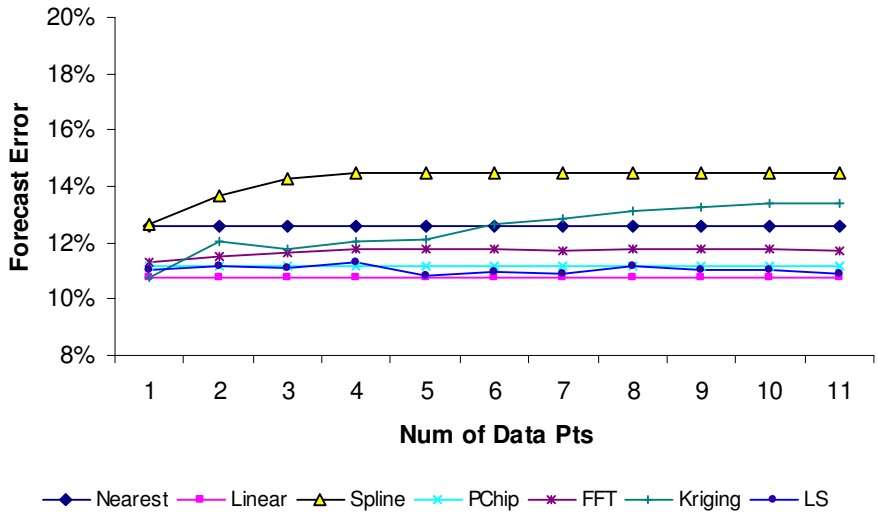

Figure 7.18 Comparison between the estimation errors of different modelling techniques for the case of two-successive missing observations

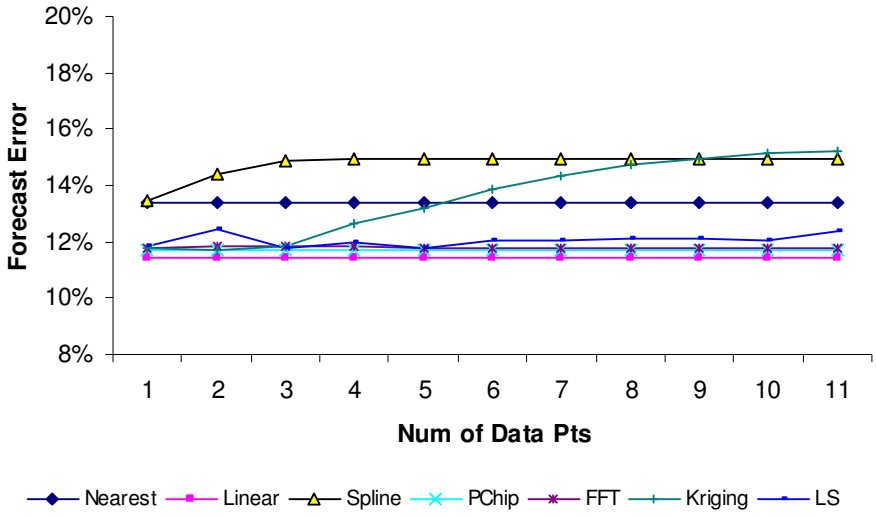

Figure 7.19 Comparison between the estimation errors of different modelling techniques for the case of three-successive missing observations

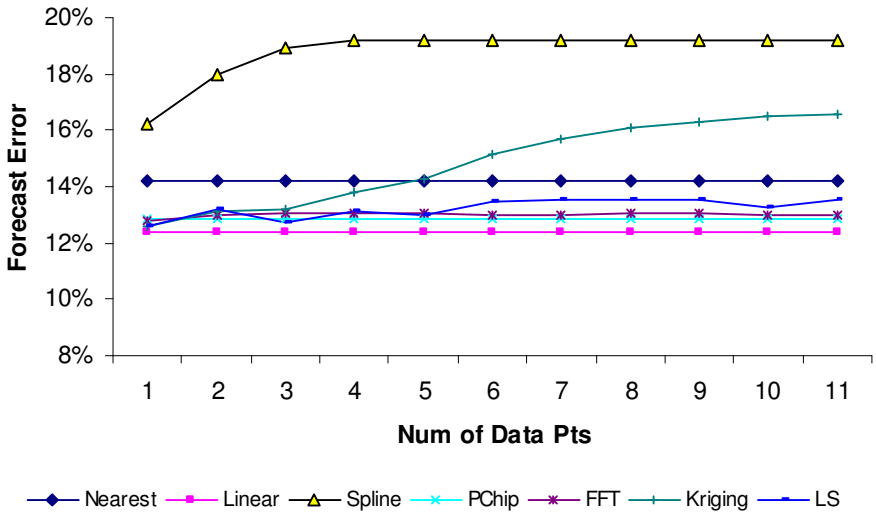

Figure 7.20 Comparison between the estimation errors of different modelling techniques for the case of four-successive missing observations

7.4 PREDICTION OF ZENITH WET DELAYS

In GNSS positioning, reliable prediction of ZWD estimates can play an important role in improving RTK precision by mitigating the tropospheric effect. In this section, several TS models are examined to investigate their performance in predicting ZWDs with the objective of recommending the best model that follows the characteristics of the ZWDs. The TS models can be categorised as trend models

and smoothing models. The trend models are implemented with the LS principle. Descriptions of these models are outlined in the following sub-sections.

7.4.1 Linear Trend (LT) Model

The LT model describes the relationship between the ZWD observations, $\{ZWD(t_i)\}_{i=1}^{n}$ and time $\{t_i\}_{i=1}^{n}$, in the following linear form (e.g., Johnson and Wichern, 2007):

$$ZWD(t_i) = \beta_0 + \beta_1 t_i + e_{t_i} \tag{7.37}$$

where β_0 and β_1 are coefficients to be determined in a least-squares estimation process and e_{t_i} is the model error.

7.4.2 Quadratic Trend (QT) Model

The QT Model attempts to model the association between the ZWD observations, $\{ZWD(t_i)\}_{i=1}^{n}$, and time $t = \{t_1, t_2, .., t_n\}$ as a quadratic function, which can be formulated as (e.g., Farnum and Stanton, 1989):

$$ZWD(t_i) = \beta_0 + \beta_1 t_i + \beta_2 t_i^2 + e_{t_i} \tag{7.38}$$

where β_0, β_1 and β_2 are coefficients to be determined in a LS estimation process as above, and e_{t_i} is the model error.

7.4.3 Exponential Growth Trend (EGT) Model

The EGT model expresses the relationship between the ZWD observations, $\{ZWD(t_i)\}_{i=1}^{n}$, and time $t = \{t_1, t_2, .., t_n\}$, in the form (e.g., Farnum and Stanton, 1989):

$$ZWD(t_i) = \beta_0 \times (\beta_1)^{t_i} \times e_{t_i} \tag{7.39}$$

Eq. (7.39) can be redefined in its linearised form by taking the natural logarithm of both sides of the equation, resulting in:

$$\ln(\mathrm{ZWD}(t_i)) = \ln(\beta_0) + \ln(\beta_1)t_i + \ln(e_{t_i}) \tag{7.40}$$

By letting $z = \ln(\mathrm{ZWD}(t_i))$ and taking $\ln(\beta_0) = \alpha$ and $\ln(\beta_1) = \gamma$, this translates to:

$$z = \alpha + \gamma t_i + \varepsilon_t \tag{7.41}$$

The coefficients α and γ can then be resolved via the LS process and $\beta_0 = e^{\alpha}$ and $\beta_1 = e^{\gamma}$ can subsequently be determined.

7.4.4 Decomposition (DCP) Model

The decomposition model represents the ZWD data as a TS with a linear trend and seasonal components, along with the errors. The multiplicative decomposition TS model can be given as (e.g., Bowerman and O' Connell, 1993; Makridakis *et al.*, 1998):

$$\mathrm{ZWD}(t_i) = \mathrm{Trend} \times \mathrm{Seasonal} \times \mathrm{Error} \tag{7.42}$$

The multiplicative decomposition model involves the following steps:

(i) The ZWD data is initially fitted by a linear regression trend line.

(ii) The data is then detrended by dividing the data by the trend component.

(iii) The detrended data is then smoothed using a centred moving average.

(iv) Once the moving average is obtained, it is divided by the detrended data to obtain what is referred to as raw seasonals.

(v) Within each seasonal period, the median value of the raw seasonals is found. The medians are then adjusted so that the mean is one. These adjusted medians constitute the seasonal indices.

(vi) The seasonal indices are then used to seasonally adjust the data.

7.4.5 Moving Average (MA) Model

The moving average time-series model smoothes the ZWD data by averaging consecutive observations in a series and provides a short-term prediction. The procedure is a likely choice if the ZWD data exhibits neither a trend nor a seasonal component. The smoothed statistic at time t_i, $MA(t_i)$, for the previous m ZWD observations, $\{ZWD(t_j)\}_{j=0}^{m-1}$, where $i > j$, is given by (e.g., Bowerman and O' Connell, 1993; Makridakis *et al.*, 1998):

$$MA(t_i) = \frac{1}{m}\sum_{j=0}^{m-1} ZWD(t_j) \tag{7.43}$$

For a set of $(n+1)$ ZWD observations given by $\{ZWD(t_j)\}_{j=0}^{n}$, the forecasted value, $\hat{ZWD}(t_{n+k})$, for k epochs after time t_n can be given as:

$$\hat{ZWD}(t_{n+k}) = MA(t_n) \tag{7.44}$$

7.4.6 Single-Exponential Smoothing (SES) Model

The SES model smoothes the n ZWD data, at $t = \{t_1, t_2, .., t_n\}$, by computing exponentially weighted averages, allowing it to provide short-term predictions. The SES model is (e.g., Bowerman and O' Connell, 1993; Makridakis *et al.*, 1998):

$$SES_{t_i} = \alpha_w w_{t_i} + (1-\alpha_w) SES_{t_{i-1}} = SES_{t_{i-1}} + \alpha_w (w_{t_i} - SES_{t_{i-1}}) \tag{7.45}$$

with an initial value SES_{t_0} at time t_0 given by:

$$SES_{t_1} = ZWD(t_1) \tag{7.46}$$

where $0 < \alpha_w < 1$ is the weight factor. Values of α_w closer to one will result in rapid changes in the fitted line as more weights are given to recent changes in the data, whilst smaller values have greater smoothing effects and are less responsive to recent data. Thus, smaller values for α_w are recommended for data with a high noise level.

The Auto-Regressive Integrated Moving Average (ARIMA) (Box and Jenkins, 1994) procedure is used to determine the optimal value for α_w. The forecasted value, $\hat{ZWD}(t_{n+k})$, for k epochs after time t_n is given by:

$$\hat{ZWD}(t_{n+k}) = SES_{t_n} \tag{7.47}$$

7.4.7 Double-Exponential Smoothing (DES) Model

If the ZWD data exhibits a trend, the SES method may not model the $\{ZWD(t_i)\}_{i=1}^{n}$ observations adequately. The DES model overcomes this deficiency by introducing a second equation to capture the trend component and provide short-term predictions. The two associated equations at time t_i, defined as the level (Lv_{t_i}) and trend (Tr_{t_i}) components, are (LaViola, 2003):

$$Lv_{t_i} = \alpha_w (ZWD(t_i)) + (1-\alpha_w)(Lv_{t_{i-1}} - Tr_{t_{i-1}}) \tag{7.48}$$

$$Tr_{t_i} = \gamma_w (Tr_{t_i} - Tr_{t_{i-1}}) + (1-\gamma_w) Tr_{t_{i-1}} \tag{7.49}$$

where α_w and γ_w are the weight factors, and γ_w has to be chosen in conjunction with α_w. The chosen values for both γ_w and α_w have to be between zero and one. The ARIMA method can be used to obtain the optimal values for the weights. The initial value for Lv_{t_i} at $t_{i=1}$ is generally set to the value of the first observation, i.e. $Lv_{t_1} = ZWD(t_{t_{i=1}})$, whilst Tr_{t_1} may be chosen in one of the following ways:

$$\text{(i)}\ Tr_{t_1} = ZWD(t_2) - ZWD(t_1) \tag{7.50}$$

$$\text{(ii)}\ Tr_{t_1} = \frac{1}{3}\sum_{i=1}^{3}[ZWD(t_{i+1}) - ZWD(t_i)] \tag{7.51}$$

$$\text{(iii)}\ Tr_{t_i} = [ZWD(t_m) - ZWD(t_1)]/m\text{, for a selected period m} \tag{7.52}$$

The forecasted value, $\hat{ZWD}(t_{n+k})$, for k epochs after time t_n is given by:

$$\hat{ZWD}(t_{n+k}) = Lv_{t_n} + kTr_{t_n} \tag{7.53}$$

7.4.8 Winters' Method (WM)

WM smoothes the data by utilising the Holt-Winters exponential smoothing technique and provide short- to medium-range predictions (Chatfield and Yar, 1988). WM is appropriate when trend and seasonality are present. Thus, WM calculates dynamic estimates for three components, namely; level $\left(\mathrm{Lv}_{t_i}\right)$, trend $\left(\mathrm{Tr}_{t_i}\right)$ and seasonal $\left(\mathrm{Sn}_{t_i}\right)$. The *multiplicative* WM model can be defined as (Chatfield and Yar, 1988):

$$\mathrm{Lv}_{t_i} = \alpha_w \left(\frac{\mathrm{ZWD}_{t_i}}{\mathrm{Sn}_{t_{i-1}}} \right) + (1-\alpha_w)\left(\mathrm{Lv}_{t_{i-1}} + \mathrm{Tr}_{t_{i-1}}\right) \tag{7.54}$$

$$\mathrm{Tr}_{t_i} = \gamma_w \left(\mathrm{Lv}_{t_i} - \mathrm{Lv}_{t_{i-1}}\right) + (1-\gamma_w)\mathrm{Tr}_{t_{i-1}} \tag{7.55}$$

$$\mathrm{Sn}_{t_i} = \zeta_w \left(\frac{\mathrm{ZWD}_{t_i}}{\mathrm{Lv}_{t_i}} \right) + (1-\zeta_w)\mathrm{Sn}_{t_i-\varpi} \tag{7.56}$$

where α_w, γ_w and ζ_w are the weights for the level, trend and seasonal components, respectively; ϖ is the seasonal period. Unlike the SES and the DES models, the optimal values for the weights $(\alpha_w, \gamma_w, \zeta_w)$ cannot be computed with the ARIMA model. The magnitudes of the weights are, however, similar to that of SES and DES methods, i.e. greater smoothing is achieved through smaller weights, which is recommended for noisy data.

The forecasted value, $\hat{\mathrm{ZWD}}(t_{n+k})$, for k epochs after time t_n can be given by:

$$\hat{\mathrm{ZWD}}(t_{n+k}) = \mathrm{Sn}_{t_n}\left(\mathrm{Lv}_{t_n} + k\mathrm{Tr}_{t_n}\right) \tag{7.57}$$

7.5 Testing and Analysis of Methods for Predicting Zenith Wet Delay Observations

In order to assess the accuracy and reliability of the TS prediction models given in Section 7.4, ZWD estimates were predicted using each of these models separately, on ZWD data from days Sept 13th, 15th and 18th of the ONSA data set (see Figure 7.14

in Section 7.3). The models were generated based on the previous 24-h of data for each of these dates. For each model, ZWD were forecasted for the next 24-h from each of the above dates. The forecasted values, $\hat{ZWD}(t)$, were then compared to the actual GNSS ZWD estimates. Based on the combined differences between the forecasted and the actual GNSS ZWD estimates for each of the dates, the RMSE (cm) for a given prediction model is:

$$RMSE_F = \frac{1}{n_c}\sum_{j=1}^{n_c}\left(\hat{ZWD}(t_j) - ZWD(t_j)\right)^2 \tag{7.58}$$

where n_c is the total number of comparisons. For a better perspective of the RMSEs, the overall forecast error (%), E_F, is also calculated for each of the prediction models:

$$E_F = \left(\frac{RMSE_F}{\frac{1}{n_c}\sum_{j=1}^{n_c} ZWD(t_j)}\right) * 100\% \tag{7.59}$$

The complete results of the investigation are presented in Tables 7.12, which shows the average forecast errors up to the j^{th} hour of prediction, for j = 1-h, 2-h, …, 24-h. Correspondingly, Figure 7.21 provides a graphical illustration of the forecast error trend for each of the tested models.

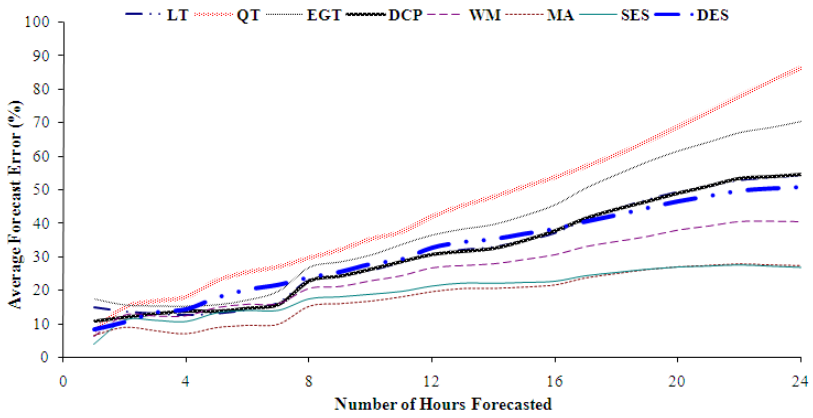

Figure 7.21 Forecast error trend exhibited by each of the tested model

Table 7.12 Forecast errors (%) of the next 24-h of prediction for each of the tested models

Number of hours forecasted	LT	QT	EGT	DCP	WM	MA	SES	DES
1	15%	8%	17%	11%	6%	6%	4%	8%
2	13%	15%	16%	12%	13%	9%	11%	11%
3	13%	17%	15%	13%	12%	8%	11%	13%
4	12%	18%	15%	14%	12%	7%	11%	14%
5	13%	23%	16%	14%	15%	9%	13%	18%
6	14%	25%	17%	15%	16%	9%	14%	20%
7	16%	27%	20%	16%	16%	10%	14%	22%
8	23%	30%	27%	23%	20%	15%	17%	24%
9	24%	32%	29%	24%	21%	16%	18%	25%
10	26%	35%	31%	26%	23%	17%	19%	28%
11	28%	37%	34%	29%	24%	18%	19%	29%
12	31%	42%	37%	31%	27%	19%	21%	33%
13	32%	45%	38%	32%	27%	20%	22%	34%
14	33%	48%	40%	32%	28%	20%	22%	35%
15	35%	51%	42%	35%	29%	21%	22%	37%
16	37%	54%	46%	38%	30%	21%	23%	38%
17	41%	57%	51%	41%	33%	24%	24%	40%
18	44%	60%	55%	44%	34%	25%	25%	42%
19	47%	64%	58%	46%	36%	26%	26%	44%
20	49%	69%	62%	49%	38%	27%	27%	46%
21	51%	73%	64%	51%	39%	27%	27%	48%
22	53%	78%	67%	53%	40%	28%	27%	50%
23	53%	82%	69%	54%	40%	27%	27%	50%
24	54%	86%	70%	54%	40%	27%	27%	51%

As expected, the accuracy of all the forecast models decreases with forecast time as shown in Figure 7.21. This behaviour is somewhat anticipated from the autocorrelation analysis in Section 7.1, whereby the correlations among the ZWD estimates decays over time and are only really significant within the first two hours. The QT and the DES models are the worst-performing models.

Previous studies (e.g., El-Mowafy, 2006) had shown that the DES model is very effective in providing real-time GNSS ZWD solutions for short-term prediction (15 min). However, for the longer periods considered here, its performance was bettered by the MA, the SES, and the WM prediction models. The MA and SES were able provide ZWD estimates with a forecast error of less than 10% for the first 4 hours of prediction. Within these 4 hours, the percentages of predicted ZWD that are in statistical agreement with the actual GNSS ZWD values are 100% and 92% for MA

and SES, respectively. As the forecast time increases, the proportion of agreements between the predicted and actual ZWD estimates for SES deteriorates significantly after 4 hours to around 43% at the end of the 24-h period. On the other hand, the MA model is still able to maintain the level of statistical agreement at 75% mark at the end of the 24-h period.

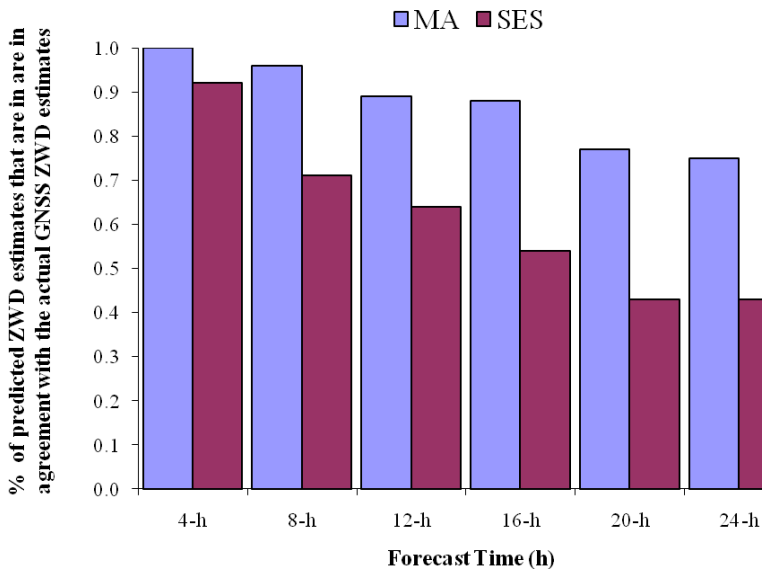

Figure 7.22 Percentage of predicted ZWD estimates that are in good agreement with the actual GNSS ZWD estimates

Overall, the MA model was the best performer and is recommended for practical applications such as RTK. The SES model is also worth considering.

7.6 CHAPTER SUMMARY

In the efforts to determine the most appropriate models for the interpolation and prediction of ZWD estimates, an autocorrelation analysis of the tropospheric estimates TS was initially carried out. The autocorrelation study was restricted to a 12-h time interval to ensure a degree of stationarity in the time series. It was found that for 14 of the Australian GNSS stations, the average time lag for significant autocorrelation was observed at 1.6 hours. If a Gauss Markov model is assumed, this value can be of significant help in KF processing with state augmentation.

With the autocorrelation study in mind, an investigation into the accuracy and precision of several modelling techniques was carried out to determine the best approach for estimating missing data points for a set of ZWD observations. Such interpolation processes are needed for post processing applications. For the investigated data set, results indicate that the LI model and an 18-point polynomial model, P_{18}, of order seven, are the best interpolant and regression model, respectively. The favourable results for the LI model, which only depends on the two most recent data points, were reflected in the autocorrelation plot of the GNSS ZWD estimates, whereby significant autocorrelation values were observed for up to 2-h only. The advantage of the regression model approach to the LI model is in the added benefit of precision estimation, which acts as a source of quality indication. The errors of the P_{18} model were able to successfully summarise over 95% of the GNSS ZWD differences between the estimated and the actual values at three standard errors for all of the investigated cases of missing data.

A ZWD prediction study was also implemented over several prediction models. From Figure 7.21, the MA and the SES models appear to produce the most accurate ZWD predictions with forecast error of less than 10% up to 4 hours, and increasing to around 27% at the end of the 24-h period. This is expected as the ZWD autocorrelation is only significant to 1.6 hours. With at least 75% statistical agreement between the predicted and the actual ZWD estimates within the 24-h period, the MA model has outperformed the SES model in this respect. Overall, the MA is recommended model for predicting ZWD.

CHAPTER 8

CONCLUSIONS AND RECOMMENDATIONS

8.0 INTRODUCTION

The major conclusions and recommendations that can be drawn from the developments and the test results of this study are outlined in this Chapter. The study began by discussing the use of GNSS measurements for the estimation of the ZWD in static mode. Next, factors that can impact the ZWD estimation process were identified. These include the choice of stochastic model, the length of the processing session, and the number of stations involved in the data processing. By examining these factors, a strategy was proposed to estimate the ZWD more efficiently for practical use. The impact of proposed strategy on the ZWD estimation was tested with a statistical procedure that includes cross-validation with external data, and the analysis of the error (precision) estimates. An autocorrelation study on the ZWD estimates was also performed. By observing the autocorrelations at various stations, it was found that the commonly-used Gauss-Markov (GM) autocorrelation model does not effectively model the autocorrelation trends. Therefore, a new autocorrelation model was proposed and tested. The study concluded with an investigation into various ZWD interpolation and prediction models that can provide estimates during data breaks in network real-time applications and other practical considerations. The following section presents the main conclusions drawn from the numerical results of the study.

8.1 Conclusions

The GM KF process utilises the first-order GM autocorrelation function, given in Eq. (3.50). However, for the purpose of ZWD or PWV estimation, it has been shown in Section 3.2 that the GM autocorrelation function decays much too rapidly and thus, it often fails to properly follow the actual ZWD autocorrelation trend. Therefore, a new

autocorrelation function was proposed for the KF process. The following provides a summary of the performances for the proposed model:

- The hyperbolic function is the basis of the proposed autocorrelation function, which is generated based on the small number of autocorrelation values determined with the standard autocorrelation formula given by Eqs. (3.58) and (3.59). With these estimates, the LS method is then used to determine the parameter coefficient of the proposed model. Once solved, the proposed model is then fully defined;
- This study has shown that the proposed model is able to follow the autocorrelation closely for a significant number of time lags, unlike the GM function;
- Real data analysis had also shown that the proposed model is able to provide near real-time ZTD estimates to within 1-2 cm accuracy, and had performed just as well as the GM model. The marginal difference between the proposed model and the GM model is likely due to the short sampling interval (30 s) and estimation period (every 5 min), whereby minimal differences were observed in the estimated correlation coefficients from the two models. However, the proposed model demonstrated an average improvement of around 11 mm in ZWD when compared to the RW model.

The functional model of a GNSS observation, given in Chapter 3, is not particularly controversial and is widely accepted by the GNSS community. However, the stochastic modelling of the GNSS measurements remains a challenging prospect, and a properly-defined stochastic model is essential in providing highly accurate ZWD and geodetic solutions.

A stochastic model of interest here is a rigorous method known as the Minimum Norm Quadratic Unbiased Estimator (MINQUE). The MINQUE method was shown to improve coordinate solution over short-baselines (e.g., Wang *et al.*, 1998). However, prior to this study, the impact of MINQUE on the estimation of the ZWD was still unclear. Therefore, one contribution of this research is the investigation into the MINQUE method and its effect on the ZWD estimates (Sections 6.2 to 6.4).

Results from the MINQUE technique was compared to typical methods such as the equal-weighting model (EWM) and the elevation-angle dependent model (EADM). A simplified version of MINQUE, known as the SMINQUE (Satirapod *et al.*, 2002), was also studied and tested. In Section 4.4, a simple, but significant adjustment was made to the original MINQUE and SMINQUE algorithms. The following gives a summary of developments and conclusions drawn from the simulation and real data studies:

- The adjustment made to the MINQUE and SMINQUE methods increases the flexibility of these methods to accommodate uneven numbers of satellites in the observing epochs of the processing session. The modification is given in Chapter 4;
- Previous studies mentioned that the differences in the coordinate solution between MINQUE and SMINQUE are of the sub-millimetre level, a theoretical investigation into their formulations suggests that it is not always the case. This was demonstrated by the results of the Australian baseline campaign whereby sub-millimetre differences in the height offsets between the two methods were observed at only 43% of the time. In 7% of the results, the height solutions of MINQUE differ to that of SMINQUE by over 10 mm;
- The simulation study has shown that although both MINQUE and SMINQUE produced better height solutions than the EWM and the EADM (by an average of 71% and 51 % respectively) in point positioning. For the long-baseline campaigns, it was demonstrated that there is not real advantage in using MINQUE or SMINQUE over the EADM;
- Although using MINQUE and SMINQUE resulted in better height resolution, this superiority did not translate into better ZWD estimation in the simulation study. The EADM was the best model in this case. The baseline-campaigns have also shown that the EADM is the preferred stochastic model when estimating the ZWD or PWV. In addition, error analysis of the corresponding tropospheric LS error estimates has shown that the EADM is able to provide better precision or error estimates that are agreeable to the true accuracy of the LS tropospheric estimates. For the purpose of ZWD and LS error

estimation, the study concludes that the EADM is the optimal stochastic model among all the tested methods.

Another contribution of this research work is to propose the use of a baseline strategy with a reduced processing window in estimating the ZWD and the error parameters, instead of the network approach. The solutions from the baseline strategy were compared to the solutions from multi-station networks, IGS solutions or 24-h solutions. Statistical analysis was performed to determine the validity of the baseline approach.

- Analysis of 35 Australian stations over a 3-week campaign was initially performed. This campaign resulted in quality PWV estimates when compared to the corresponding RS data. The accuracies of the PWV estimates (less than 3 mm in most cases) corresponded well with past studies. However, the corresponding error estimates (i.e. square root of the LS error variance of the tropospheric delay estimates) were inadequate as a source of error information for the NWP data assimilation;
- The simulation study has shown that a reduced processing window can have a positive impact on the error estimates of the LS ZWD as a dependable source of error measures, whilst providing ZWD estimates that are more than comparable to that of the 24-h solutions. Results also show that for the EADM, a 2-h processing window was able to provide ZWD estimates with a root mean squared error (RMSE) that is only 15% bettered by the 24-h solution. In addition, more than 80% (at 3 standard deviations) of the GNSS ZWD estimates determined with the 2-h processing window were in statistical agreement with the actual WVR ZWD values. The proportion of agreement for the 24-h solution was only at 50%;
- Two baseline studies were conducted in Australia and Europe with real data, which showed that if the station coordinates in each baseline are known and are constrained, a 2-h processing window is sufficient in providing ZWD and PWV estimates that are in good agreement with the IGS solutions, the network solutions and the 24-h solution. In addition, the baseline approach was able to generate ZWD and PWV estimates that are in statistical agreement with tropospheric measurements from RS and WVR. If there is

only one reference station in the baseline, a 3-h window is necessary to increase the redundancy level so that the coordinates of the other unknown station can be resolved adequately, and subsequently the estimation of tropospheric parameter will improve.

The final contribution of the study is to provide insight into several interpolation and prediction (trend and smoothing) models for ZWD estimation. An autocorrelation analysis of the ZWD data was initially carried out to provide insight into possible models which may aid the study. The findings are as follows:

- Results of the autocorrelation analysis of the ONSA ZWD data indicated that the ZWDs are significantly correlated to each other for approximately 2-h;
- The interpolation models considered in the missing ZWD study in Section 7.3 include the linear interpolation (LI) model, the cubic spline models, the cubic Hermite and Lagrange polynomial interpolation models, the fast-Fourier-transform model, the simple Kriging model, and the LS regression models. The results have shown that the LI model provided the most accurate ZWD estimation for when there are up to 4-h of missing data. The LI model only relies on the two most recent observed data surrounding the missing values. This outcome is in agreement with the ZWD autocorrelation analysis;
- The linear trend model (LT), the quadratic trend model (QT), the exponential growth trend (EGT) model, along with the smoothing models such as the decomposition (DECOMP) model, the moving average (MA) models, the single-exponential-smoothing model (SES) and the double-exponential-smoothing (DES) model, were used in the study to determine the best model for predicting ZWD. Results given in Section 7.5 indicated that the MA and the SES models are able to provide ZWD estimates with forecast errors of less than 10% for the first 4 hours of prediction. Beyond that the results are significantly worse. This outcome is expected as the autocorrelation analysis of the ZWD estimates indicated that the ZWDs are only significantly correlated up to 1.6 hours. Furthermore, the ZWD values predicted from the MA model were able to be in statistical agreement (at three standard deviations) with the actual ZWD estimates at a rate of at least 75% within the 24-h period (see Figure 7.22).

8.2 RECOMMENDATIONS

Based on the theoretical and experimental results in this study, the following recommendations are made for future research. Note that although the experimental data in this thesis were from GPS, the proposed recommendations are applicable to other GNSS systems such as Glonass and Galileo.

- The new autocorrelation function proposed in Chapter 3 was shown to be able to produce good NRT ZWD estimates in PPP mode. Further studies are required to determine how well the model can when the receiver is in roving mode, and whether or not the model can be improved;
- The choice of stochastic model is an important issue in GNSS data adjustment. An incorrectly defined stochastic model can lead to unrealistic ZWD results, as well as LS error estimates. The MINQUE and SMINQUE methods considered in this study model the spatial correlations among the observations in reference to the satellites (or satellite pairs for DD observations). However, the study has shown that MINQUE and SMINQUE are unable to improve the estimation of the tropospheric and error parameter estimates. In fact, the EADM, a model that depends on the satellite elevation angles and ignores all correlations, produced better tropospheric estimates. Therefore further research is required to investigate the impact of other spatial and temporal models on the determination of the tropospheric parameter, and whether or not the outcome for MINQUE and SMINQUE is just an isolated case;
- The proposed strategy in this study for estimating the tropospheric delays at reference stations is via a baseline approach with a shortened processing window session. If the coordinates of all stations are known, results show that the baseline strategy will suffice in estimating the tropospheric parameter to a degree of accuracy comparable to that of the network solution, whilst producing realistic error estimates that are able to correspond well with the true accuracy of the parameter estimates. The chosen stations for this study are located at mid to low latitudes where the atmospheric conditions are considered as mild. However, for stations that are located in tropical and sub-tropical regions, the quality of the GNSS signals in these regions can be

severely degraded due to the constant changes in the weather activities, as well as heavy humidity on a day to day basis. Therefore, further research is required to determine how well this baseline strategy will work in regions that experience more volatile weather conditions and greater atmospheric delay;

- The study has shown that good LS tropospheric estimates and realistic error estimates can be achieved with a baseline approach. To fully realise the effects of the GNSS tropospheric and the corresponding error estimates on weather forecasts, further research should be directed to assimilating these baseline-generated tropospheric solutions into NWP models to determine its full impact;
- The tropospheric estimates generated through the appropriate prediction model should be tested to determine the effectiveness of the predicted estimates, in different locations and under various measuring conditions, and as well as its impact on the results of network RTK applications.

APPENDIX

Table A1 Formulations of the established hydrostatic delay models.

Model	Formulation	Parameters
Davis *et al.* (1985)	$ZHD = \frac{0.0022768 P_s}{1 - 0.00266\cos 2\phi - 0.00028H}$	P_s = surface pressure (hPa) ϕ = geocentric latitude of the station H = station height (km)
Baby *et al.* (1988)	$ZHD = \frac{0.022277 P_s}{g_s}\left(1 + \frac{2}{r_s\vartheta(\mu+1)}\right)$ where, $\vartheta = \frac{\alpha}{T_s}$ and $\mu = \frac{g_s}{\alpha R_d}\left(1 - \frac{2}{r_s\vartheta}\right)$	P_s = surface pressure (hPa) T_s = surface temperature (K) g_s = surface gravity (ms^{-2}) α = lapse rate r_s = mean geocentric radius (m) R_d = specific gas constant for dry air
Hopfield (1969)	$ZHD = 77.607\times10^{-6}\frac{P_s H_d^e}{5T_s}$, where $H_d^e = 40136 + 148.72(T_s - 273.16)$	P_s = surface pressure (hPa) T_s = surface temperature (K)

Table A2 Formulations of established wet delay models.

Model	Formulation	Parameters
Askne and Nordius (1987)	$ZWD = 10^{-6}\left(k_2' + \frac{k_3}{T_m}\right)\frac{R_d}{(\lambda+1)g_m}P_{wv}^s$ where, $P_{wv} = P_{wv}^s\left(\frac{T}{T_s}\right)^{(\lambda+1)(\mu+1)}$, $\left(\frac{P}{P_s}\right) = \left(\frac{T}{T_s}\right)^{(\mu+1)}$ $T_m = T_s\left[1 - \frac{1}{(\mu_1+1)(\mu_2+1)}\right]$	(k_2', k_3) = pre-specified constants R_d = specific gas constant for dry air T_m = mean temperature (K) P_s = surface pressure (hPa) T_s = surface temperature (K) g_m = mean gravity $\mu_{1,2}$ = a site- and season-dependent constant.
Baby *et al.* (1988)	$ZWD = 10^{-6}k_3'\frac{U_s P_{wv,s}}{C_0\beta}$, where $C_0 = \begin{cases}5327.1157K,\\6162.3496K,\end{cases}$, with $T(H) = T_s - \beta(H - H_s)$, $P_{wv} = U_s \times P_{wv,s}$	$k_3' = 3.81\times10^2\ K^2mbar^{-1}$ U_s = relatively humidity (%) $P_{wv,s}$ = saturated vapour pressure
Hopfield (1969)	$ZWD = 10^{-6}N_{ws}\frac{H_w^e}{5}$, where $N_{ws} = 3.73 + 10^5\frac{P_{wv}^s}{T_s^2}$, H_w^e = 11000m.	P_{wv}^s = surface partial pressure of water vapour
Ifadis (1986)	$ZWD = 0.00554 - A + B + C$, where $A = 0.88\times10^{-4}(P_s - 1000.0)$ $B = 0.272\times10^{-4}P_{wv}^s$, $C = 2.771\left(\frac{P_{wv}^s}{T_s}\right)$	P_{wv}^s = surface partial pressure of water vapour P_s = surface pressure (hPa) T_s = surface temperature (K)

Table A3 Formulations of different mapping functions

MF	Formulation	Parameters
Chao (1974)	$m_H(\theta)=\frac{1}{\sin(\theta)+\frac{a}{\tan(\theta)+b}}$ $m_W(\theta)=\frac{1}{\sin(\theta)+\frac{c}{\tan(\theta)+d}}$	$a = 0.00143$ $b = 0.0445$ $c = 0.00035$ $d = 0.017$
Davis *et al.* (1985)	$m(\theta)=\frac{1}{\sin(\theta)+\frac{a}{\tan(\theta)+\frac{b}{\sin(\theta)+c}}}$	$a = 0.001185\begin{bmatrix}1+0.6071\times10^{-4}(P_s-1000)-0.1471\times10^{-3}P_{wv}+\\0.3072\times10^{-2}(T_s-20)+0.01965(6.5-\alpha)-\\5.645\times10^{-6}(H_T-11231)\end{bmatrix}$ $b = 0.001144\begin{bmatrix}1+0.1164\times10^{-4}(P_s-1000)-0.2795\times10^{-3}P_{wv}+\\0.3109\times10^{-2}(T_s-20)+0.03038(6.5-\alpha)-\\0.1217\times10^{-6}(H_T-11231)\end{bmatrix}$ $c = -0.0090$
Ifadis (1986)	$m_{H,W}(\theta)=\frac{1+\frac{a_{H,W}}{1+\frac{b_{H,W}}{1+c_{H,W}}}}{\sin(\theta)+\frac{a_{H,W}}{\sin(\theta)+\frac{b_{H,W}}{\sin(\theta)+c_{H,W}}}}$	$a_H = 0.001237+\begin{bmatrix}0.01316(P_s-1000)+0.8057\sqrt{P_{wv}}+\\0.1378(T_s-15)\end{bmatrix}\times10^{-5}$ $b_H = 0.003333+\begin{bmatrix}0.1946(P_s-1000)+0.1747\sqrt{P_{wv}}+\\0.1040(T_s-15)\end{bmatrix}\times10^{-6}$ $c_H = 0.078$ $a_W = 0.0005236+\begin{bmatrix}0.2471(P_s-1000)+13.28\sqrt{P_{wv}}+\\0.1724(T_s-15)\end{bmatrix}\times10^{-6}$ $b_W = 0.001705+\begin{bmatrix}0.7384(P_s-1000)+21.47\sqrt{P_{wv}}+\\0.3767(T_s-15)\end{bmatrix}\times10^{-6}$ $c_W = 0.05917$
Herring (1992)	$m_{H,W}(\theta)=\frac{1+\frac{a_{H,W}}{1+\frac{b_{H,W}}{1+c_{H,W}}}}{\sin(\theta)+\frac{a_{H,W}}{\sin(\theta)+\frac{b_{H,W}}{\sin(\theta)+c_{H,W}}}}$	$a_H = \begin{bmatrix}1.2320+0.0139\cos\phi-0.0000209H_s+\\0.00215(T_s-10)\end{bmatrix}\times10^{-3}$ $b_H = \begin{bmatrix}3.1612-0.1600\cos\phi-0.0000331H_s+\\0.002106(T_s-10)\end{bmatrix}\times10^{-3}$ $c_H = \begin{bmatrix}71.244-4.293\cos\phi-0.000149H_s-\\0.0021(T_s-10)\end{bmatrix}\times10^{-3}$ $a_W = \begin{bmatrix}0.583-0.011\cos\phi-0.000052H_s+\\0.0014(T_s-10)\end{bmatrix}\times10^{-3}$ $b_W = \begin{bmatrix}1.402-0.102\cos\phi-0.000101H_s+\\0.0020(T_s-10)\end{bmatrix}\times10^{-3}$ $c_W = \begin{bmatrix}45.85-1.91\cos\phi-0.00129H_s+\\0.015(T_s-10)\end{bmatrix}\times10^{-3}$

Table A4 Formulations of IMF and VMF1

MF	Formulation	Parameters
IMFs (Niell, 2000)	$m_H(\theta)=\dfrac{1+\dfrac{a_{dry}}{1+\dfrac{b_{dry}}{1+c_{dry}}}}{\sin(\theta)+\dfrac{a_{dry}}{\sin(\theta)+\dfrac{b_{dry}}{\sin(\theta)+c_{dry}}}}+\Delta H$ $m_W(\theta)=\dfrac{1+\dfrac{a_{wet}}{1+\dfrac{b_{wet}}{1+c_{wet}}}}{\sin(\theta)+\dfrac{a_{wet}}{\sin(\theta)+\dfrac{b_{wet}}{\sin(\theta)+c_{wet}}}}$	ΔH is as defined in Niell (1996) $z200 = 200\text{hPa}$ $a_{dry} = \Psi(\ell)+\Pi(\ell)\times(z200 - z_{ref})$ $b_{dry} = 0.002905$ $c_{dry} = 0.0634 + 0.0014\cos(\ell)$ $\Psi(\ell) = 0.00124 + 4.0\times10^{-5}\cos[2(\ell - 2.0)]$ $\Pi(\ell) = 7.4\times10^{-8} - 1.6\times10^{-8}\cos[2\ell]$ $z_{ref} = 11836 + 619\cos[2(\ell - 3.0)]$ $a_{wet} = 6.8827\times10^{-4} - 2.0795\times10^{-4}(\Omega - 15.5) - 1.6580\times10^{-7}H$ $b_{wet} = 1.3503\times10^{-3} + 1.8882\times10^{-4}(\Omega - 15.5)$ $c_{wet} = 3.9647\times10^{-2} + 4.8581\times10^{-3}(\Omega - 15.5)$ $\Omega = \dfrac{\tau(3.3^0)}{\tau(90^0)}$, where $\tau(\ell) = \dfrac{k_3\int\frac{e_v(s)}{T^2(s)}ds}{k_3\int\frac{e_v(H)}{T^2(H)}dH}$
VMF1 (Boehm and Schuh, 2004)	$m_H(\theta)=\dfrac{1+\dfrac{a_{dry}}{1+\dfrac{b_{dry}}{1+c_{dry}}}}{\sin(\theta)+\dfrac{a_{dry}}{\sin(\theta)+\dfrac{b_{dry}}{\sin(\theta)+c_{dry}}}}+\Delta H$ $m_W(\theta)=\dfrac{1+\dfrac{a_{wet}}{1+\dfrac{b_{wet}}{1+c_{wet}}}}{\sin(\theta)+\dfrac{a_{wet}}{\sin(\theta)+\dfrac{b_{wet}}{\sin(\theta)+c_{wet}}}}$	(b_{dry}, c_{dry}) are as defined in the IMF. $(b_{wet}, c_{wet}) = (1.4572752\times10^{-3}, 4.3908931\times10^{-2})$ a_{dry} and a_{wet} are determined by inverting the continued fractions.

REFERENCES

Aonashi, K., T. Iwabuchi, and Y. Shoji. 2004. Statistical study on precipitable water content variations observed with ground-based microwave radiometers. *Journal of the Meteorological Society of Japan* 82 (1B): 269-275.

Askne, J., and H. Nordius. 1987. Estimation of tropospheric delay for microwaves from surface weather data. *Radio Science* 22 (3): 379-386.

Awange, J. L., Y. Fukuda, S. Takemoto, J. Wickert, and Y. Aoyama. 2004. Analytic solution of GPS atmospheric sounding refraction angles. *Earth Planets Space* 56 (6): 573-587.

Baby, H. B., P. Gole, and J. Lavergnat. 1988. A model for the tropospheric excess path length of radio waves from surface meteorological measurements. *Radio Science* 23 (6): 1023-1038.

Baker, T. F., D. J. Curtis, and A. H. Dodson. 1995. Ocean tide loading and GPS. *GPS World* 6 (3): 54-59.

Baker, H. C., A. H. Dodson, N. T. Penna, M. Higgins, and D. Offiler. 2001. Ground-based GPS water vapour estimation: potential for meteorological forecasting. *Journal of Atmospheric and Solar-Terrestrial Physics* 63 (12): 1305-1314.

Barnes, J. B., and P. A. Cross. 1998. Processing models for very high accuracy GPS positioning. *Journal of Navigation* 51 (2): 180-193.

Basili, P., S. Bonafoni, R. Ferrara, P. Ciotti, E. Fionda, and R. Ambrosini. 2001. Atmospheric water vapor retrieval by means of both a GPS network and a microwave radiometer during an experimental campaign in Cagliari, Italy, in 1999. *IEEE Transactions on Geoscience and Remote Sensing* 39 (11): 2436-2443.

Basili, P., S. Bonafoni, V. Mattioli, P. Ciotti, and E. Fionda. 2002. A ground-based microwave radiometer and a GPS network for the remote sensing of atmospheric water vapour content: a year of experimental results. In *1st COST720 Workshop: Integrated groundbased remote sensing stations for atmospheric profiling*, June 18-21, L'Aquila, Italy.

Beamson, G. A. 1995. Precise height determination of tide gauges using GPS. PhD Thesis, University of Nottingham, Nottingham.

Behrend, D., R. Haas, D. Pino, L. P. Gradinarsky, S. J. Keihm, W. Schwarz, L. Cucurull, and A. Rius. 2002. MM5 derived ZWDs compared to observational results from VLBI, GPS and WVR. *Physics and Chemistry of the Earth* 27 (4-5): 301-308.

Benesty, J., J. Chen, and Y. Huang. 2004. Time-delay estimation via linear interpolation and cross correlation. *IEEE Transactions on Speech and Audio Processing* 12 (5): 509-519.

Bétaille, D. F., P. A. Cross, and H. J. Euler. 2006. Assessment and improvement of the capabilities of a window correlator to model GPS multipath phase errors. *IEEE Transactions on Aerospace and Electronic Systems* 42 (2): 705-717.

Beutler, G., I. Bauersima, W. Gurtner, and M. Rothacher. 1987. Correlations between simultaneous GPS double difference carrier phase observations in the multistation mode: Computation considerations and first experiences. *Manuscripta Geodetica* 11: 40-44.

Beutler, G., G. Jäggi, U. Hugentobler, and L. Mervart. 2006. Efficient satellite orbit modeling using psuudo-stochastic parameter. *Journal of Geodesy* 80 (7): 353-372.

Bevis, M., S. Businger, S. Chiswell, T. A. Herring, R. A. Anthes, C. Rocken, and R. H. Ware. 1994. GPS meteorology: mapping zenith wet delays onto precipitable water. *Journal of Applied Meteorology* 33 (3): 379-386.

Bevis, M., S. Businger, T. A. Herring, C. Rocken, R. A. Anthes, and R. H. Ware. 1992. GPS meteorology: remote sensing of atmospheric water vapor using the global positioning system. *Journal of Geophysical Research* 97 (D14): 15787-15801.

Bischoff, W., B. Heck, J. Howind, and A. Teusch. 2006. A procedure for estimating the variance function of linear models and for checking the appropriateness of estimated variances: A case study of GPS carrier-phase observations. *Journal of Geodesy* 79 (12): 694-704.

Bock, O., and E. Doerflinger. 2001. Atmospheric modeling in GPS data analysis for high accuracy positioning. *Physics and Chemistry of the Earth, Part A: Solid Earth and Geodesy* 26 (6-8): 373-383.

Bock, O., J. Tarniewicz, C. Thom, J. Pelon, and M. Kasser. 2001. Study of external path delay correction techniques for high accuracy height determination with

GPS. *Physics and Chemistry of the Earth, Part A: Solid Earth and Geodesy* 26: 165-171.

Boehm, J., and H. Schuh. 2004. Vienna mapping functions in VLBI analyses. *Geophysical Research Letters* 31: L01603.

Boehm, J., B. Werl, and H. Schuh. 2006. Troposphere mapping functions for GPS and very long baseline interferometry from European Centre for Medium-Range Weather Forecasts operational analysis data. *Journal of Geophysical Research* 111: B02406.

Bolton, D. 1980. The computation of equivalent potential temperature. *Monthly Weather Review* 108: 1046-1053.

BoM. 2008a. *Australian climate zones*. http://www.bom.gov.au/lam/climate/levelthree/ausclim/koeppen2.htm (accessed 26/11/09).

BoM. 2008b. *Meteorological and related data*. http://www.bom.gov.au/inside/eiab/reports/ar07-08/Meteorological-and-related-data.pdf (accessed 26/11/09).

Borre, K., and C. Tiberius. 2000. *Proceedings of the 13th International Technical Meeting of the Satellite Division of The Institute of Navigation, September 19-22: Time series analysis of GPS observables.* Salt Lake City, Utah: ION GPS-2000

Bowerman, B. L., and R. T. O' Connell. 1993. *Forecasting and Time Series: An Applied Approach*. 3rd ed: Duxbury Press.

Box, G. E. P., and G. M. Jenkins. 1994. *Time Series Analysis: Forecasting and Control*. 3rd ed. New Jersey: Prentice-Hall.

Brandt, S. 1999. *Datenanalyse: Mit Statistischen Methoden Und Computerprogrammen*, 4th ed. Spektrum Akademischer Verlag.

Brunner, F. K., H. Hartinger, and L. Troyer. 1999. GPS signal diffraction modelling: the stochastic SIGMA- Δ model. *Journal of Geodesy* 73 (5): 259-267.

Buehner, M., P. Gauthier, and Z. Liu. 2005. Evaluation of new estimates of background- and observation-error covariances for variational assimilation. *Quarterly Journal of the Royal Meteorological Society* 131 (613): 3373–3383.

Burden, R. L., and J. D. Faires. 2004. *Numerical analysis*. 8th ed. Pacific Grove: Brooks/Cole Publishing Company.

Businger, S., S. R. Chiswell, M. Bevis, J. Duan, R. A. Anthes, C. Rocken, R. H. Ware, M. Exner, T. Van Hove, and F. S. Solheim. 1996. The promise GPS in atmospheric monitoring. *Bulletin of the American Meteorological Society* 77 (1): 5-18.

Chao, C. C. 1974. The tropospheric calibration model for Mariner Mars 1971. *JPL Technical Report* 32-1587: 61-76.

Chatfield, C., and M. Yar. 1988. Holt-Winters forecasting: some practical issues. *The Statistician* 37 (2): 129-140.

Chen, H. Y., L. Dai, C. Rizos, and S. Han. 2005. Ambiguity recovery using the triple-differenced carrier phase type approach for long-range GPS kinematic positioning *Marine Geodesy* 28 (2): 119 - 135.

Collins, J. P., and R. B. Langley. 1997. *Proceedings of the 10th International Technical Meeting of the Satellite Division of the Institute of Navigation*, *September 16-19: Estimating the residual tropospheric delay for airborne differential GPS positioning*. Kansas City, MO: ION GPS-97.

Comp, C. J., and P. Axelrad. 1996. *Proceedings of the 9th International Technical Meeting of the Satelite Division of the U.S. Instititute of Navigation*, *September 17-20: An adaptive SNR-based carrier phase multipath mitigation technique*. Kansas City, Missouri, USA: ION GPS-96.

Coster, A. J., A. E. Niell, F. S. Solheim, V. B. Mendes, P. C. Toor, K. P. Buchmann, and C. A. Upham. 1996. *Proceedings of the 9th International Technical Meeting of the Satellite Division of The Institute of Navigation*, *September 17-20: Measurements of precipitable water vapor by GPS, radiosondes, and a microwave water vapor radiometer*. Kansas City, Kansas: ION GPS-96.

Cui, X., Z. Yu, B. Tao, and D. Liu. 1982. *Adjustment in surveying*. Beijing, China: Surveying Press.

Dach, R., and R. Dietrich. 2001. The ocean tide loading effect in the GPS analysis: a case study in the Antarctica peninsula region. *Marine Geodesy* 24 (1): 13-25.

Davis, J. L., T. A. Herring, I. I. Shapiro, A. E. E. Rogers, and G. Elgered. 1985. Geodesy by radio interferometry - effects of atmospheric modeling errors on estimates of baseline length. *Radio Science* 20: 1593-1607.

Dodson, A. H. 1993. Analysis of Control Networks and their Application to Deformation Monitoring. In *Engineering Surveying Technology*, ed. T. J. M. Kennie and G. Petrie, 146-173. Blackie A&P Glasgow.

Dodson, A. H., W. Chen, H. C. Baker, N. T. Penna, G. W. Roberts, R. J. Jeans, and J. Westbrook. 1999. *Proceedings of the 12th International Technical Meeting of the Satellite Division of the Institute of Navigation*, *September 14-17 Assessment of EGNOS tropospheric correction model*. Nashville, Tennese, USA: ION GPS-99.

Dodson, A. H., P. J. Shardlow, L. C. M. Hubbard, G. Elgered, and P. O. J. Jarlemark. 1996. Wet tropospheric effects on precise relative GPS height determination. *Journal of Geodesy* 70 (4): 188-202.

Duan, J., M. Bevis, P. Fang, Y. Bock, S. Chiswell, S. Businger, C. Rocken, F. Solheim, T. van Hove, R. Ware, S. McClusky, T. A. Herring, and R. W. King. 1996. GPS meteorology: direct estimation of the absolute value of precipitable water. *Journal of Applied Meteorology* 35: 830-838.

Ebner, R., and W. E. Featherstone. 2008. How well can online GPS PPP post-processing services be used to establish geodetic survey control networks? *Journal of Applied Geodesy* 2 (3): 149-157.

Elgered, G. 1993. Tropospheric radio path delay from ground-based microwave radiometry. In *Atmospheric Remote Sensing by Microwave Radiometry*, ed. M. A. Janssen, New York: Wiley.

El-Mowafy, A. 2006. Precise real-time prediction of the wet tropospheric corrections during reception gaps in RTK positioning. *Journal of Geospatial Engineering* 8 (1/2): 31-40.

El-Rabanny, A. 2002. *Introduction to GPS: the Global Positioning System*. Boston: Artech House.

Eresmaa, R., and H. Jarvinen. 2006. An observation operator for ground-based GPS slant delays. *Tellus* 58A: 131-140.

Eresmaa, R., H. Järvinen, S. Niemelä, and K. Salonen. 2007. Asymmetricity of ground-based GPS slant delay data. *Atmospheric Chemistry and Physics* 7 (12): 3143-3151.

Erol, B., S. Erol, and R. N. Çelik. 2008. Height transformation using regional geoids and GPS/levelling in Turkey. *Survey Review* 40 (307): 2-18.

Farah, A., T. Moore, and C. J. Hill. 2005. High spatial variation tropospheric model for GPS-data simulation. *Journal of Navigation* 58 (3): 459-470.

Farnum, N. R., and L. W. Stanton. 1989. *Quantitative Forecasting Methods*: PWS-Kent.

Fornberg, B., and J. Zuev. 2007. The Runge phenomenon and spatially variable shape parameters in RBF interpolation. *Computers & Mathematics with Applications* 54 (3): 379-398.

Fotopoulos, G. 2005. Calibration of geoid error models via a combined adjustment of ellipsoidal, orthometric and gravimetric geoid height data. *Journal of Geodesy* 79 (1-3): 111-123.

Frigo, M., and S. G. Johnson. 1998. *Proceedings of the International Conference on Acoustics, Speech, and Signal Processing*, *May 12-15: FFTW: An adaptive software architecture for the FFT*. Seattle, USA: IEEE.

Fu, E., K. Zhang, F. Wu, X. Xu, and K. Marion. 2007. An evaluation of GNSS radio occultation technology for Australian meteorology. *Journal of Global Positioning Systems* 6 (1): 74-79.

Fuller, S., P. Collier, and A. Kealy. 2005. Real time quality assessment for CORS networks. *Journal of Global Positioning Systems* 4 (1-2): 223-229.

Geng, Y. and J. Wang 2008. Adaptive estimation of the multiple fading factors in Kalman filter for navigation applications. *GPS Solutions* 12(4): 273-279.

Glowacki, T. J., N. T. Penna, and W. P. Bourke. 2006. Validation of GPS-based estimates of integrated water vapour for the Australian region and identification of diurnal variability. *Australian Meteorological Magazine* 55 (2): 131-148.

Goad, C. C., D. A. Grejner-Brzezinska, and M. Yang. 1996. Determination of high-precision GPS orbits using triple differencing technique *Journal of Geodesy* 70 (11): 655-662.

Gotthardt, E. 1978. *Einführung in die ausgleichungsrechnung*. Karlsruhe, Germany: Herbert Wichmann Verlag.

Guo, Y.-R., H. Kusaka, D. M. Barker, Y.-H. Kuo, and A. Crook. 2005. Impact of ground-based GPS PW and MM5-3DVar background error statistics on forecast of a convective case. *SOLA* 1 (0): 73-76.

Gutman, S. I., S. R. Sahm, S. G. Benjamin, B. E. Schwartz, K. L. Holub, J. Q. Stewart, and T. L. Smith. 2004. Rapid retrieval and assimilation of ground based GPS precipitable water observations at the NOAA forecast systems laboratory: Impact on weather forecasts. *Journal of the Meteorological Society of Japan* 82 (1B): 351-360.

Ha, S.-Y., Y.-H. Kuo, Y.-R. Guo, and G.-H. Lim. 2003. Variational assimilation of slant-path wet delay measurements from a hypothetical ground-based GPS network. Part I: Comparison with precipitable water assimilation. *Monthly Weather Review* 131 (11): 2635.

Haase, J. S., M. Ge, H. Vedel, and E. Calais. 2003. Accuracy and variability of GPS tropospheric delay measurements of water vapor in the western Mediterranean. *Journal of Applied Meteorology* 42 (11): 1547-1568.

Haefele, P., L. Martin, M. Becker, E. Brockmann, J. Morland, S. Nyeki, C. Matzler, and M. Kirchner. 2004. *ION GNSS-04 Proceedings*, *September 21-24: Impact of radiometric water vapor measurements on troposphere and height estimates by GPS*. Long Beach, California: ION GNSS.

Hajj, G. A., E. R. Kursinski, L. J. Romans, W. I. Bertiger, and S. S. Leroy. 2002. A technical description of atmospheric sounding by GPS occultation. *Journal of Atmospheric and Solar-Terrestrial Physics* 64 (4): 451-469.

Han, S., and C. Rizos. 1995. Standardization of variance-covariance matrix for GPS rapid static positioning. *Geomatics Research Australia* 62: 37-54.

Hartinger, H., and F. K. Brunner. 1999. Variances of GPS phase observations: The SIGMA-e model *GPS Solutions* 2 (4): 35-43.

Hay, C., and J. Wong. 2000. Enhancing GPS: tropospheric delay prediction at the master control station. *GPS World* 11 (1): 56-62.

Healy, S. B., A. M. Jupp, and C. Marquardt. 2005. Forecast impact experiment with GPS radio occultation measurements. *Geophysical Research Letters* 32: L03804.

Heinkelmann, R., J. Boehm, H. Schuh, S. Bolotin, G. Engelhardt, D. S. MacMillan, M. Negusini, E. Skurikhina, V. Tesmer, and O. Titov. 2007. Combination of long time-series of troposphere zenith delays observed by VLBI. *Journal of Geodesy* 81 (6-8): 483-501.

Herring, T. A. 1992. Modeling atmospheric delays in the analysis of space geodetic data. In *Symposium on Refraction of Transatmospheric Signals in Geodesy*, ed. J. C. De Munck and T. A. Spoelstra, 36:157-164. Delft: Netherlands Geodetic Commission.

Hill, R. J., R. S. Lawrence, and J. T. Priestly. 1982. Theoretical and calculational aspects of the radio refractive index of water vapor. *Radio Science* 17: 1251-1257.

Hofmann-Wellenhof, B., H. Lichtenegger, and J. Collins. 2001. *GPS theory and practice*. 5th ed. New York: Springer-Verlag Wien.

Hopfield, H. S. 1971. Tropospheric effects on electromagnetically measured range: prediction from surface weather data. *Radio Science* 6 (3): 357-367.

Huang, X. Y., and H. Vedel. 2003. *Proceedings of 2nd EUMETSAT GRAS-SAF user workshop*, *June 11-13: An introduction to data assimilation*. Helsingør, Denmark: EUMETSAT.

Hugentobler, U., S. Schaer, and P. Fridez, eds. 2001. *Bernese GPS software version 4.2*: Astronomical Institute University of Berne.

Ichikawa, R. 1995. Estimation of atmosphere excess path delay based on three-dimensional numerical prediction model data. *Journal of the Geodetic Society of Japan* 41 (4): 379-408.

Ifadis, I. M. 1986. *The atmospheric delay of radio waves: modeling the elevation dependence on a global scale*. Goteborg, Sweden: School of Electrical and Computer Engineering, Chalmers University of Technology.

Jacobson, M. Z. 1999. *Fundamentals of atmospheric modeling*. Cambridge, UK: Cambridge University Press.

Janes, H. W., R. B. Langley, and S. P. Newby. 1991. Analysis of tropospheric delay prediction models: comparisons with ray-tracing and implications for GPS relative positioning. *Journal of Geodesy* 65 (3): 151-161.

Järvinen, H., R. Eresmaa, H. Vedel, K. Salonen, S. Niemelä, and J. de Vries. 2007. A variational data assimilation system for ground-based GPS slant delays. *Quarterly Journal of the Royal Meteorological Society* 133: 969-980.

Jin, S., J. Wang, and P. H. Park. 2005. An improvement of GPS height estimations: stochastic modeling. *Earth Planets Space* 57 (4): 253-259.

Jin, X. X., and C. D. de Jong. 1996. Relationship between satellite elevation and precision of GPS code observations. *Journal of Navigation* 49 (22): 253-265.

Johnson, R. A., and D. W. Wichern. 2007. *Applied multivariate statistical analysis*. 6th ed. London, UK: Prentice-Hall.

Kaniuth, K., and S. Vetter. 2006. Estimating atmospheric pressure loading regression coefficients from GPS observations *GPS Solutions* 10 (2): 126-134.

Kaplan, E. D., ed. 1996. *Understanding GPS: Principles and applications*. Norwood, MS: Artech House.

Khan, S. A., and H. G. Scherneck. 2003. The M2 ocean tide loading wave in Alaska: vertical and horizontal displacements, modelled and observed. *Journal of Geodesy* 77 (3-4): 117-127.

Kim, D., S. Bisnath, R. B. Langley, and P. Dare. 2004. *Proceedings of the 17th International Technical Meeting of The Institute of Navigation, September 21-24: Performance of long-baseline real-time kinematic applications by improving tropospheric delay modeling*. Long Beach, California, USA: ION GNSS-04.

Kim, D., and R. B. Langley. 2001. Quality control techniques and issues in GPS applications: Stochastic modeling and reliability test. In *International Symposium on GPS/GNSS (the 8th GNSS Workshop)*. Novermber 7-9, Jeju Island, Japan.

King, R. W., and Y. Bock. 2002. *Documentation for the GAMIT GPS software version 4.2*. Cambridge, Massachusetts: Massachusetts Institute of Technology.

Kleijer, F. 2004. Troposphere modeling and filtering for precise GPS leveling. PhD, Department of Mathematical Geodesy and Positioning, Delft University of Technology, Netherlands

Klobuchar, J. A. 1986. *Proceedings of the Position Location & Navigation Symposium, November 4-7: Design characteristics of the GPS ionospheric time-delay algorithm for single frequency users*. Las Vegas, Nevada, USA: PLANS-86

Koehler, J. R., and A. B. Owen. 1996. Computer experiments. In *Handbook of Statistics*, ed. S. Ghosh and C. R. Rao, 261-305. New York: Elsevier Science.

Koizumi, K., and Y. Sato. 2004. Impact of GPS and TMI precipitable water data on mesoscale numerical weather prediction model forecasts. *Journal of Meteorological Society of Japan* 82 (1B): 453-457.

Kouba, J. 2009. A guide to using International GNSS Service (IGS) Products. http://acc.igs.org/UsingIGSProductsVer21.pdf. (last accessed 21/9/09)

Krügel, M., D. Thaller, V. Tesmer, M. Rothacher, D. Angermann, and R. Schmid. 2007. Tropospheric parameters: combination studies based on homogeneous VLBI and GPS data *Journal of Geodesy* 81 (6-8): 515-527.

Kuo, Y. H., W. S. Schreiner, J. Wang, J. L. Rossiter, and Y. Zhang. 2005. Comparison of GPS radio occultation soundings with radiosondes. *Geophysical Research Letters* 32: L05817.

Kuo, Y. H., X. Zou, and Y. R. Guo. 1996. Variational assimilation of precipitable water using a nonhydrostatic mesoscale adjoint model. *Monthly Weather Review* 124 (1): 122-147.

Kwon, H. T., T. Iwabuchi, and G. H. Lim. 2007. Comparison of precipitable water derived from ground-based GPS measurements with radiosonde observations over the Korean peninsula. *Journal of the Meteorological Society of Japan* 85 (6): 733-746.

Lachapelle, G. 1990. GPS observables and error sources for kinematic positioning. In *Kinematic Systems in Geodesy, Surveying, and Remote Sensing*, ed. K. P. Schwarz and G. Lachapelle, 17-26. New York Berlin Heidelberg Tokyo: Springer.

Larson, K. M., A. Bilich, and P. Axelrad. 2007. Improving the precision of high-rate GPS. *Journal of Geophysical Research* 112: B05422.

Lau, L., and P. Cross. 2007. Development and testing of a new ray-tracing approach to GNSS carrier-phase multipath modelling. *Journal of Geodesy* 81 (11): 713-732.

Lau, L., and E. Mok. 1999. Improvement of GPS Relative Positioning Accuracy by Using SNR. *Journal of Surveying Engineering* 125 (4): 185-202.

LaViola, J. J. 2003. *Proceedings of Immersive Projection Technology and Virtual Environments, May 22-23: Double exponential smoothing: an alternative to Kalman filter-based predictive tracking*. Zurich, Germany. ACM Press 39:199-206.

Leick, A. 2004. *GPS Satellite Surveying*. 3rd ed. New Jersey, USA: John Wiley & Sons, Inc.

Liu, H., M. Xue, J. R. Purser, and D. F. Parrish. 2007. Retrieval of moisture from simulated GPS slant-path water vapor observations using 3DVAR with anisotropic recursive filters *Monthly Weather Review* 135 (4): 1506-1520.

Liu, J., Z. Sun, H. Liang, X. Xu, and P. Wu. 2005. Precipitable water vapor on the Tibetan plateau estimated by GPS, water vapor radiometer, radiosonde, and numerical weather prediction analysis and its impact on the radiation budget. *Journal of Geophysical Research* 110: D17106.

Ljung, G. M., and G. E. P. Box. 1978. On a measure of a lack of fit in time series models. *Biometrika* 65: 297-303.

Lyard, F., F. Lefevre, T. Letellier, and O. Francis. 2006. Modelling the global ocean tides: modern insights from FES2004. *Ocean Dynamics* 56 (5-6): 394-415.

Macpherson, S. R., G. Deblonde, J. M. Aparicio, and B. Casati. 2007. Impact of NOAA ground-based GPS observations on the Canadian regional analysis and forecast system. *Monthly Weather Review* 136 (7): 2727-2745.

Mäkinen, J., H. Koivula, M. Poutanen, and V. Saaranen. 2003. Vertical velocities in Finland from permanent GPS networks and from repeated precise levelling *Journal of Geodynamics* 35 (4-5): 443-456.

Makridakis, S., S. C. Wheelwright, and R. J. Hyndman. 1998. *Forecasting methods and applications*. 3rd ed. New York: Wiley.

Martin, L., C. Matzler, T. J. Hewison, and D. Ruffieux. 2006. Intercomparison of integrated water vapor measurements. *Meteorologische Zeitschrift* 15 (1): 57-64.

Mattioli, V., E. R. Westwater, S. I. Gutman, and V. R. Morris. 2005. Forward model studies of water vapor using scanning microwave radiometers, global positioning system, and radiosondes during the cloudiness intercomparison experiment. *IEEE Transactions on Geoscience and Remote Sensing* 43 (5): 1012-1021.

McMillin, L. M., J. Zhao, M. K. Rama Varma Raja, S. I. Gutman, and J. G. Yoe. 2007. Radiosonde humidity corrections and potential atmospheric infrared sounder moisture accuracy. *Journal of Geophysical Research* 112: D13S90.

Melachroinos, S. A., R. Biancale, M. Llubes, F. Perosanz, F. Lyard, M. Vergnolle, M. N. Bouin, F. Masson, J. Nicolas, L. Morel, and S. Durand. 2008. Ocean tide loading (OTL) displacements from global and local grids: comparisons to GPS estimates over the shelf of Brittany, France. *Journal of Geodesy* 82 (6): 357-371.

Mendes, V. B. 1999. Modeling the neutral-atmosphere propagation delay in radiometric space techniques. PhD, Department of Geodesy and Geomatics Engineering, University of New Brunswick, Fredericton.

Mendes, V. B., and R. Langley. 1999. Tropospheric zenith delay prediction accuracy for height-precision GPS positioning and navigation. *Navigation* 46 (1): 25-34.

Mervart, L. 1995. *Ambiguity resolution techniques in geodetic and geodynamic application of the Global Positioning System*. Vol. 53, *Geodätisch-geophys*. Switzerland: Arbeiten in der Schweiz, Schweizerische Geodätische Kommission.

Miloshevich, L. M., H. Vömel, D. N. Whiteman, B. M. Lesht, F. J. Schmidlin, and F. Russo. 2006. Absolute accuracy of water vapor measurements from six operational radiosonde types launched during AWEX-G and implications for AIRS validation *Journal of Geophysical Research* 111: D09S10.

Möller, F. 1973. Einführung in die Meteorologie Mannheim: B.I. Hochschultaschenbücher.

Montgomery, D. C. 2001. *Introduction to statistical quality control*. 4th ed. New York, USA: Wiley & Sons.

Montgomery, D. C. 2005. *Design and analysis of experiments*. 6th (revised) ed. New York, USA: Wiley & Sons.

Morris, M. D. a. M., T.J. 1995. Exploratory designs for computational experiments. *Journal of Statistical Planning and Inference* 43 (3): 381-402.

Musa, T. A., J. Wang, C. Rizos, and Y. J. Lee. 2004. Mitigating residual tropospheric delay to improve user's network-based positioning. *Journal of Global Positioning Systems* 3 (1-2): 322-320.

Musa, T. A., J. Wang, C. Rizos, and C. Satirapod. 2003. *Proceeding of the 6th International Symposium on Satellite Navigation Technology Including Mobile Positioning & Location Services*, *July 22-25: Stochastic modelling for network-based positioning*. Melbourne, Australia: SatNav-03.

Nakamura, H., H. Seko, and Y. Shoji. 2004. Dry biases of humidity measurements from the Vaisala RS80-A and Meisei RS2-91 radiosondes and from ground-based GPS. *Journal of Meteorological Society of Japan* 82 (1B): 277-299.

Nicholson, N. A., S. Skone, M. E. Cannon, G. Lachapelle, and N. Luo. 2005. *ION GNSS-05 Proceedings*, *September 13-16: Regional tropospheric tomography based on real-time double difference observables*. Long Beach, California: ION GNSS.

Niell, A. E. 1996. Global mapping functions for the atmosphere delay at radio wavelenghts. *Journal of Geophysical Research* 101 (B2): 3227-3246.

Niell, A. E. 2000. Improved atmospheric mapping functions for VLBI and GPS. *Earth Planets Space* 52 (10): 699-702.

Nilsson, T., L. Gradinarsky, and G. Elgered. 2005. Correlations between slant wet delays measured by microwave radiometry. *IEEE Transactions on Geoscience and Remote Sensing* GE-43 (5): 1028-1035.

NOAA. 2008. *National Climatic Data Center: Integrated global radiosonde archive*. http://www.ncdc.noaa.gov/oa/climate/igra/index.php (last accessed 26/11/08).

Owens, J. C. 1967. Optical refractive index of air: Dependence on pressure, temperature, and composition. *Applied Optics* 6 (1): 51-59.

Özlüdemir, M. T. 2004. The stochastic modeling of GPS observatios. *Turkish Journal of Engineering & Environmental Sciences* 28: 223-231.

Peixoto, J. P., and A. H. Oort. 1992. *Physics of climate*. New York: American Institute of Physics.

Penna, N. T., and T. F. Baker. 2002. Ocean tide loading considerations for GPS processing around Australia. *Geomatics Research Australasia* 77: 1-26.

Penna, N. T., A. H. Dodson, and W. Chen. 2001. Assessment of EGNOS tropospheric correction model. *Journal of Navigation* 54 (11): 37-55.

Penna, N. T., J. Lo, and G. Luton. 2005. Geodetic GPS analysis of Land Victoria's GPSnet. *Journal of Spatial Science* 50 (1): 45-57.

Penna, N. T., and M. P. Stewart. 2003. Aliased tidal signatures in continuous GPS height time series. *Geophysical Research Letters* 30 (23): 2184.

Pervan, B., and F. C. Chan. 2003. Detecting global positioning satellite orbit errors using short-baseline carrier-phase measurements. *Journal of Guidance, Control and Dynamics* 16 (1): 122-131.

Pottiaux, E., M. Becker, B. B., R. Gyger, P. Häfele, C. Plötz, W. Schlüter, W. Schwarz, A. Somieski, and R. Warnant. 2003. Calibration and quality assessment of water vapor radiometer observations using radiosonde, GPS, and VLBI. *Geophysical Research Abstracts* 5: 05745.

Pradel, N., P. Charlot, and J.-F. Lestrade. 2006. Astrometric accuracy of phase-referenced observations with the VLBA and EVN *A&A* 452 (3): 1099-1106.

Rao, C. R. 1970. Estimation of heterogeneous variances in linear models. *Journal of American Statistical Association* 65: 161-172.

Rao, C. R. 1971. Estimation of variance and covariance components - MINQUE. *Journal of Multivariate Analysis* 1: 257-275.

Rao, C. R. 1979. MINQUE theory and its relation to ML and MML estimation of variance components. *Sankhya* 1 (Series B): 138-153.

Rao, C. R., and J. Kleffe. 1980. Estimation of variance components. In *Handbook of Statistics*, ed. P. R. Krishnaiah, 1-40. Amsterdam: North-Holland Publishing Company.

Rao, C. R., and J. Kleffe. 1988. *Estimation of variance components and applications*. Netherlands: Elsevier Science Publishers B.V.

Resch, G. M. 1984. Water vapor radiometry in geodetic applications. In *Geodetic aspects of electromagnetic wave propagation through the atmosphere*, ed. F. K. Brunner, 53-84. New York: Springer-Verlag.

Rocken, C., R. A. Anthes, M. Exner, D. Hunt, S. Sokolovskiy, R. Ware, M. Gorbunov, W. Schreiner, D. Feng, B. Herman, Y. H. Kuo, and X. Zou. 1997. Analysis and validation of GPS/MET data in the neutral atmosphere *Journal of Geophysical Research* 102 (D25): 29849.

Rocken, C., J. M. Johnson, R. E. Neilan, M. Cerezo, J. R. Jordan, M. J. Falls, L. D. Nelson, R. H. Ware, and M. Hayes. 1991. The measurement of atmospheric water vapor: radiometer comparison and spatial variations. *IEEE Transactions on Geoscience and Remote Sensing* 29 (1): 3-8.

Rocken, C., T. van Hove, J. Johnson, F. Solheim, R. Ware, M. Bevis, S. Chiswell, and S. Businger. 1995. GPS/Storm-GPS sensing of atmospheric water vapor meteorology. *Journal of Atmospheric and Oceanic Technology* 12: 468-478.

Ross, R. J., and S. Rosenfeld. 1997. Estimating mean weighted temperature of the atmosphere for Global Positioning System applications. *Journal of Geophysical Research* 102 (D18): 21,719–21,730.

Runge, C. 1901. Über empirische Funktionen und die Interpolation zwischen äquidistanten Ordinaten. *Zeitschrift für Mathematik und Physik* 46: 224-243.

Saastamoinen, J. 1973. Contributions to the theory of atmospheric refraction. *Bullétin Géodésique* 105, 106, 107: 279-298, 383-397, 13-34.

Sacks, J., W. J. Welsh, T. J. Mitchell, and H. P. Wynn. 1989. Design and analysis of computer experiments. *Statistical Science* 4 (4): 409-423.

Saha, K., K. Parameswaran, and C. Suresh Raju. 2007. Tropospheric delay in microwave propagation for tropical atmosphere based on data from the Indian subcontinent. *Journal of Atmospheric and Solar-Terrestrial Physics* 69 (8): 875-905.

Sapucci, L. F., L. A. T. Machado, J. F. G. Monico, and A. Plana-Fattori. 2007. Intercomparison of integrated water vapor estimates from multisensors in

Amazonian regions. *Journal of Atmospheric and Oceanic Technology* 24 (11): 1880-1893.

Satirapod, C., and P. Chalermwattanachai. 2005. Impact of different tropospheric models on GPS baseline accuracy: case study in Thailand. *Journal of Global Positioning Systems* 4 (1-2): 36-40.

Satirapod, C., and J. Wang. 2000. Comparing the quality Indicators of GPS carrier phase observations. *Geomatics Research Australasia* 73: 75-92.

Satirapod, C., J. Wang, and C. Rizos. 2002. A simplified MINQUE procedure for the estimation of variance-covariance components of GPS observables. *Survey Review* 36 (286): 582–590.

Satoh, M. 2004. *Amospheric circulation dynamics and general circulation models*. Chichester, UK: Praxis Publishing.

Saucier, W. J. 1955. *Principles of meteorological analysis*. Chicago: The University of Chicago Press.

Schmid, R. 2005. Absolute phase center corrections of satellite and receiver antennas: impact on global GPS solutions and estimation of azimuthal phase center variations of the satellite antenna. *GPS Solutions* 9 (4): 283-293.

Schmid, R., and M. Rothacher. 2003. Estimation of elevation-dependent satellite antenna phase center variations of GPS satellites. *Journal of Geodesy* 77 (7-8): 440-446.

Schmid, R., P. Steigenberger, G. Gendt, M. Ge, and M. Rothacher. 2007. Generation of a consistent absolute phase-center correction model for GPS receiver and satellite antennas *Journal of Geodesy* 81 (12): 781-798.

Schön, S., and H. Kutterer. 2006. Uncertainty in GPS networks due to remaining systematic errors: the interval approach. *Journal of Geodesy* 80 (3): 150-162.

Schön, S., A. Wieser, and K. Macheiner. 2004. *Proceedings of the 18th International Technical Meeting of the Satellite Division*, *September 13-16: Accurate tropospheric correction for local GPS monitoring networks with large height differences*. Long Beach, California, USA: ION GNSS-04.

Schupler, B. R., and T. A. Clark. 1991. How different antennas affect the GPS observable. *GPS World* 2 (10): 32-36.

Seeber, G. 2003. *Satellite geodesy: foundations, methods, and applications*. 2nd ed. Berlin, Germany: Walter de Gruyter.

Shoji, Y., H. Nakamura, K. Aonashi, A. Ichiki, and H. Seko. 2000. Semi-diurnal and diurnal variation of errors in GPS precipitable water vapor at Tsukuba, Japan caused by site displacement due to ocean tide loading. *Earth Planets Space* 52 (10): 685-690.

Sjöberg, L. 1984. Non-negative variance component estimation in the Gauss-Helmert adjustment model. *Manuscripta Geodaetica* 9: 247-280.

Smith, T. L., S. G. Benjamin, S. I. Gutman, and S. Sahm. 2006. Short-range forecast impact from assimilation of GPS-IPW observations into the Rapid Update Cycle. *Monthly Weather Review* 135 (8): 2914–2930.

Snajdrova, K., J. Boehm, P. Willis, R. Haas, and H. Schuh. 2006. Multi-technique comparison of tropospheric zenith delays derived during the CONT02 campaign. *Journal of Geodesy* 79 (10-11): 613–623.

Soden, B. J., D. D. Turner, B. M. Lesht, and L. M. Miloshevich. 2004. An analysis of satellite, radiosonde, and lidar observations of upper tropospheric water vapor from the atmospheric radiation measurement program *Journal of Geophysical Research* 109: D04105.

Spilker, J. J. 1996. GPS signal structure and theoretical performance. In *Global Positioning System: Theory and Applications*, 57-119. Washington: American Institute of Aeronautics and Astronautics, Inc.

Steigenberger, P., V. Tesmer, M. Krügel, D. Thaller, R. Schmid, S. Vey, and M. Rothacher. 2007. Comparisons of homogeneously reprocessed GPS and VLBI long time-series of troposphere zenith delays and gradients *Journal of Geodesy* 81 (6-8): 503-514.

Stoew, B., T. Nilsson, G. Elgered, and P. O. J. Jarlemark. 2007. Temporal correlations of atmospheric mapping function errors in GPS estimation. *Journal of Geodesy* 81 (5): 311-323.

Sun, H. P., B. Ducarme, and V. Dehant. 1995. Effect of the atmospheric pressure on surface displacements *Journal of Geodesy* 70 (3): 131-139.

Takiguchi, H., T. Kato, H. Kobayashi, and T. Nakaegawa. 2000. GPS observations in Thailand for hydrological applications. *Earth Planets Space* 52: 913-919.

Tesmer, V., J. Boehm, R. Heinkelmann, and H. Schuh. 2007. Effect of different tropospheric mapping functions on the TRF, CRF and position time-series estimated from VLBI. *Journal of Geodesy* 81 (6-8): 409-421.

Teunissen, P. J. G., and A. R. Amiri-Simkooei. 2007. Least-squares variance component estimation *Journal of Geodesy* 82 (2): 65-82.

Teunissen, P. J. G., P. J. de Jong, and C. Tiberius. 1997. The least-squares ambiguity decorrelation adjustment: its performance on short GPS baselins and short observation spans. *Journal of Geodesy* 71 (10): 589-602.

Teunissen, P. J. G., and A. Kleusberg. 1998. *GPS for geodesy*. 2nd ed. New York: Springer-Verlag.

Thayer, D. 1974. An improved equation for the radio refractive index of air. *Radio Science* 9: 803-807.

Tiberius, C., and F. Kenselaar. 2003. Variance component estimation and precise GPS positioning: Case study. *Journal of Surveying Engineering* 129 (1): 11-18.

Tregoning, P., R. Boers, D. O'Brien, and M. Hendy. 1998. Accuracy of absolute precipitable water vapor estimates from GPS observations. *Journal of Geophysical Research* 103 (D22): 28,701-28,710.

Tregoning, P., and T. A. Herring. 2006. Impact of a priori zenith hydrostatic delay errors on GPS estimates of station heights and zenith total delays. *Geophysical Research Letters* 33: L23303.

Tregoning, P., and T. M. Van Dam. 2005. Atmospheric pressure loading corrections applied to GPS data at the observation level. *Geophysical Research Letters* 32: L22310.

Urschl, C., R. Dach, U. Hugentobler, S. Schaer, and G. Beutler. 2005. Validating ocean tide loading models using GPS, *Journal of Geodesy* 78 (10): 616-625.

Van Dam, T. M., G. Blewitt, and M. B. Heflin. 1994. Atmospheric pressure loading effects on global positioning system coordinate determinations. *Journal of Geophysical Research* 99 (B12): 23,939-23,950.

Van Dam, T. M., and J. M. Wahr. 1987. Displacements of the earth's surface due to atmospheric loading - effects of gravity and baseline measurements. *Journal of Geophysical Research* 92 (B2): 1281-1286.

Van Nee, R. D. J. 1992. Multipath effects on GPS code phase measurements. *Navigation* 39 (2): 177-190.

Vedel, H., and X. Y. Huang. 2003. A NWP impact study with ground based GPS data. In *The International Workshop on GPS Meteorology*. January 13-17, Tsubaka, Japan.

Vedel, H., and X. Y. Huang. 2004. Impact of ground-based GPS data on numerical weather prediction. *Journal of Meteorological Society of Japan* 82 (1B): 459-472.

Vedel, H., X. Y. Huang, J. Haase, M. Ge, and E. Calais. 2004. Impact of GPS zenith tropospheric delay data on precipitation forecasts in Mediterranean France and Spain. *Geophysical Research Letters* 31: L02102.

Vey, S., E. Calais, M. Llubes, N. Florsch, G. Woppelmann, J. Hinderer, M. Amalvict, M. F. Lalancette, B. Simon, F. Duquenne, and J. S. Haase. 2002. GPS measurements of ocean loading and its impact on zenith tropospheric delay estimates: a case study in Britanny, France. *Journal of Geodesy* 76 (8): 419-427.

Walpole, R. E., R. Myers, and S. L. Myers. 2007. *Probability and Statistics for Engineers and Scientists*. 8th ed. London, UK: Prentice-Hall.

Wang, J. 1999. Modelling and quality control for precise GPS and GLONASS satellite positioning. PhD, Department of Spatial Sciences, Curtin University of Technology, Perth.

Wang, J. 2000, Stochastic modelling for RTK GPS/Glonass positioning, Navigation. *Journal of the US institute of Navigation*, 46(4): 297-305.

Wang, J., D. J. Carlson, D. B. Parsons, T. F. Hock, D. Lauritsen, H. L. Cole, K. Beierle, and E. Chamberlain. 2003. Performance of operational radiosonde humidity sensors in direct comparison with a chilled mirror dew-point hygrometer and its climate implication. *Geophysical Research Letters* 30 (16): 1860.

Wang, J., C. Satirapod, and C. Rizos. 2002. Stochastic assessment of GPS carrier phase measurements for precise static relative positioning. *Journal of Geodesy* 76 (2): 95-104.

Wang, J., M. P. Stewart, and M. Tsakiri. 1998. Stochastic modeling for static GPS baseline data processing. *Journal of Surveying Engineering* 124 (4): 171-181.

Wang, J., and L. Zhang. 2008. Systematic errors in global radiosonde precipitable water data from comparisons with ground-based GPS measurements. *Journal of Climate* 21 (10): 2218-2235.

Wang, J., L. Zhang, A. Dai, T. van Hove, and J. van Baelen. 2007. A near-global, 2-hourly data set of atmospheric precipitable water from ground-based GPS measurements. *Journal of Geophysical Research* 112: D11107.

Watson, C., P. Tregoning, and R. Coleman. 2006. The impact of solid Earth tide models on GPS coordinate and tropospheric time series. *Geophysical Research Letters* 33: L08306.

Wei, W. 2006. *Time series analysis - Univariate and multivariate methods*. 2nd ed. USA: Peason Education, Inc.

Wells, D. E., N. Beck, D. Delikaraoglou, A. Kleusberg, E. J. Krakiwsky, G. Lachapelle, R. B. Langley, M. Nakiboglu, K. P. Schwarz, J. M. Tranquilla, and P. Vanicek. 1987. *Guide to GPS Positioning*. Fredericton, Canada: Canadian GPS Associates.

Wickert, J., C. Reigber, G. Beyerle, R. König, C. Marquardt, T. Schmidt, L. Grunwaldt, R. Galas, T. K. Meehan, W. G. Melbourne, and K. Hocke. 2001. Atmosphere sounding by GPS radio occultation: First results from CHAMP. *Geophysical Research Letters* 28 (17): 3263–3266.

Wieser, A., and F. K. Brunner. 2000. An extended weight model for GPS phase observations. *Letter of Earth Planets Space* 52: 777–782.

Xu, G. 2003. *Theory, Algorithms and Applications*. Berlin: Springer.

Yoneyama, K., M. Mikiko Fujita, N. Sato, M. Fujiwara, Y. Inai, and F. Hasebe. 2008. Correction for radiation dry bias found in RS92 radiosonde data during the MISMO field experiment. *SOLA* (4): 13-16.

Zhang, J., and G. Lachapelle. 2001. Precise estimation of residual tropospheric delays using a regional GPS network for real-time kinematic applications. *Journal of Geodesy* 75 (5-6): 255-266.

Zhang, K., B. Biadeglgne, F. Wu, Y. Kuleshov, A. Rea, G. de Hodet, and E. Fu. 2007. A comparison of atmospheric temperature and moisture profiles derived from GPS radio occultation and radiosone in Australia. In *Workshop for Space, Aeronautical and Navigational Electronics*. Perth.

Zhang, K., E. Fu, F. Wu, X. Xu, A. Rea, Y. Kuleshov, and B. Biadeglgne. 2007. *International Global Navigation Satellite Systems*, *December 4-6: GNSS radio occultation for weather and climate research - A case study in Australia*. Sydney.